University of Alberta

Concrete Deep Beams Reinforced with Internal FRP

by

Matthias Franz Andermatt

A thesis submitted to the Faculty of Graduate Studies and Research
in partial fulfillment of the requirements for the degree of

Master of Science

in

Structural Engineering

Department of Civil and Environmental Engineering

Fall 2010
Edmonton, Alberta

Examining Committee

Adam Lubell, Civil and Environmental Engineering

Gilbert Grondin, Civil and Environmental Engineering

P.-Y. Ben Jar, Mechanical Engineering

Abstract

Concrete deep beams with small shear span-to-depth (a/d) ratios are common elements in structures. However, there are few experimental results on the behaviour of FRP reinforced concrete deep beams and no specific modelling techniques exist in design codes for such members. The objectives of this study were to examine the shear behaviour of FRP reinforced concrete deep beams containing no web reinforcement and to develop a modelling technique.

Test results of 12 large-scale specimens are reported where the primary variables included the a/d ratio, reinforcement ratio, member height, and concrete strength. The results showed that an arch mechanism was able to form in FRP reinforced concrete beams having $a/d \leq 2.1$. A strut and tie modelling procedure adapted from CSA A23.3-04 was capable of accurately predicting the capacity of FRP reinforced concrete deep beams containing no web reinforcement while sectional shear models gave poor, but conservative, predictions.

Acknowledgements

There are several individuals who assisted in various ways throughout the research program which was carried out in the Department of Civil and Environmental Engineering at the University of Alberta.

The guidance, support, encouragement, and advice from Professor Adam Lubell is very much appreciated.

Many people contributed to the laboratory work. The structural engineering laboratory technologists, Sean Watt and Michael Frost, instrumentation technologist Greg Miller, and construction technologist Rizaldy Mariano provided invaluable assistance in casting the 12 test specimens. Colleagues Andrew Neilson and Sylwester Zagaj also assisted with the casting of the specimens. The assistance of Sean Watt and Greg Miller in the preparation and testing of the specimens is also greatly appreciated.

A special thanks goes to Samarium Zhao who provided assistance for all the laboratory work including instrumentation of the FRP bars, specimen casting, preparation of the specimens prior to testing, and testing of the specimens. In addition, Samarium went out of her way to beautify the ends of the specimens with artwork. Samarium's help made the long days in the laboratory much more enjoyable.

Personal financial support from the Natural Sciences and Engineering Research Council of Canada (NSERC), Alberta Ingenuity, and the University of Alberta is gratefully acknowledged. The material donation of glass FRP reinforcement from BP Composites (Edmonton) and concrete from Lehigh Inland Concrete is also acknowledged.

Finally, I thank my family, especially my parents, for all the encouragement they have provided.

Table of Contents

List of Tables

List of Figures

List of Abbreviations

AFRP - aramid fibre reinforced polymer

CFRP - carbon fibre reinforced polymer

COV - coefficient of variation

FRP - fibre reinforced polymer

GFRP - glass fibre reinforced polymer

MCFT - modified compression field theory

STM - strut and tie model

List of Symbols

A_{cs} = cross-sectional area at one end of a strut in a strut and tie model, taken perpendicular to the axis of the strut, mm^2

A_{FRP} = area of FRP reinforcing bars on the flexural tension side of a member, mm^2

A_s = area of longitudinal steel reinforcement on the flexural tension side of a member, mm^2

A_{si} = total area of surface reinforcement at spacing s_i in the i-th layer crossing a strut with reinforcement at an angle α_i to the axis of the strut, mm^2

$A_{v,min}$ = minimum required area of transverse shear reinforcement perpendicular to the axis of a member, mm^2

a = dimension of the shear span measured from the centerline of the loading and reaction plates, mm

a_g = nominal maximum size of coarse aggregate, mm

a/d = shear span-to-depth ratio

b_s = width of strut, mm

b_w = width of a member, mm

C = compression force, N

c = distance from the extreme compression fibre to the neutral axis, mm

d = effective depth, the distance from the extreme compression fibre to the centroid of the tensile force, mm

d_s = diameter of an FRP stirrup, mm

d_v = effective shear depth, mm

E_c =modulus of elasticity of concrete, MPa

E_{FRP} = modulus of elasticity of FRP reinforcement, MPa

E_s = modulus of elasticity of steel reinforcement, MPa

E_{vFRP} = modulus of elasticity of the FRP stirrups, MPa

F_{ns} = nominal strength of a strut, N

f_c' = compressive strength of concrete, MPa

f_{ce} = effective compressive strength of the concrete in a strut or nodal zone, MPa

f_{cr} = cracking strength of concrete, MPa

$f_{FRPbend}$ = specified tensile strength of the straight portion of an FRP bent stirrup, MPa

f_{FRPs} = stress in the FRP at the equivalent service load, MPa

f_{FRPu} = ultimate tensile strength of FRP, MPa

f_{cu} = limiting compressive stress in a strut, MPa

f_u = ultimate tensile strength of steel reinforcement, MPa

f_y = yield strength of steel reinforcement, MPa

h = overall height of member, mm

k = ratio of depth of neutral axis to reinforcement depth

k_a = factor representing effect of arch action

k_m = factor representing effect of moment at a section

k_r = factor representing effect of reinforcement rigidity

k_s = factor representing effect of beam size

L_b = bearing plate dimension in the direction of the span, mm

M_f = moment due to factored loads, N·mm

n_f = ratio of modulus of elasticity of FRP bars to modulus of elasticity of concrete

P = point load applied on a member, N

P_c = inclined cracking load, N

P_{max} = maximum applied point load on a member, N

P_s = point load applied on a member corresponding to the equivalent service load, N

R = nominal resistance of a structural element

r = radius of curvature of the bend of an FRP stirrup, mm

S_n = load effect under specified loads

s = spacing of shear reinforcement, mm

s_i = center to center spacing of transverse reinforcement in the i-th layer adjacent to the surface of the member, mm

s_{ze} = crack spacing parameter that allows for influence of aggregate size, mm

T = tension force, N

V_{exp} = experimental shear resistance of a reinforced concrete member, N

V_c = shear resistance attributed to concrete, N

V_{cs} = shear capacity prediction calculated using a strut and tie model, N

V_f = factored shear force, N

V_{pre} = predicted shear capacity, N

Δ = mid-span deflection, mm

Δ_{max} = mid-span deflection corresponding to a load of P_{max}, mm

Δ_s = mid-span deflection corresponding to a load of P_s, mm

α_i = angle between the axis of a strut and the bars in the i-th layer of reinforcement crossing a strut, degrees

α_n = load factor

β = factor accounting for shear resistance of cracked concrete

β_n = factor to account for the effect of the anchorage of ties on the effective compressive strength of a nodal zone

β_s = factor to account for the effect of cracking and confining reinforcement on the effective compressive strength of the concrete in a strut

ε_c' = measured compressive concrete strain at a stress of f_c'

ε_{exp} = measured mid-span tensile strain in the FRP reinforcement at the centroid of the reinforcement layers at peak load

ε_{frp} = tensile strain in the tie reinforcement at mid-span

$\varepsilon_{frp,c}$ = tensile strain in the tie reinforcement at the center of the diagonal strut, taken as ½ of ε_{frp}

ε_s = tensile strain in tie reinforcement due to loads

ε_v = strain in an FRP stirrup

ε_x = longitudinal strain at mid-depth of the member due to loads

ε_1 = principal tensile strain in cracked concrete due to loads

θ = angle of inclination of diagonal compressive stresses to the longitudinal axis of the member, degrees

λ = factor to account for low-density concrete

ν = concrete efficiency factor

ρ = longitudinal reinforcement ratio, A_{FRP}/bd_w

ρ_{vFRP} = ratio of the total cross-sectional area of the legs of an FRP stirrup to the product of the width of the beam and the spacing of the stirrups

σ_n = stress in concrete due to axial load, MPa

ϕ = resistance factor

ϕ_c = resistance factor for concrete

1 Introduction

1.1 FRP Reinforced Concrete Beams

Steel reinforced concrete structures have been built for over a century and numerous research programs have been conducted to understand the behaviour of such structures. However, one unfortunate aspect of steel reinforcement is its susceptibility to corrosion. Many steel reinforced concrete structures such as marine structures, bridges, and parking garages are exposed to aggressive environments which over time can cause extensive damage and the need for costly rehabilitation due to corrosion of the steel reinforcement. Fibre reinforced polymers (FRP), which are a composite material consisting of fibres embedded in a resin, are an alternative type of reinforcement that can be used instead of steel. Not only is FRP non-corrosive, but it is also non-magnetic making it useful in many applications were corrosion and electromagnetic interference are problematic.

FRP reinforcement exhibits high tensile strength, up to six times higher than the tensile strength of Grade 400 steel (ISIS 2007) and has linear elastic stiffness up to brittle failure. FRP reinforcement is also an anisotropic material with high tensile strength only in the direction of the fibres. Since FRP bars have linear elastic behaviour with no yielding, the lack of material ductility must be accounted for in the design of FRP reinforced concrete members. In addition, the most common type of FRP reinforcement (glass FRP) has a lower stiffness than steel reinforcement, which must be accounted for at the ultimate and serviceability conditions, including the impact on member deflection and crack widths.

The shear behaviour of steel reinforced concrete members has been well documented and many design procedures have been developed (ACI 445R-99). In general, concrete members can be classified in two categories based on shear behaviour. Slender members are commonly defined as having a shear span-to-depth (a/d) ratio greater than 2.5 and are designed using sectional shear design methods and flexural design methods based on the principle that plane sections remain plane. Contrary to slender members, in deep members (a/d < 2.5) the strain distribution in sections perpendicular to the axis of bending is nonlinear over the height and sectional shear and flexural design methods do not apply. The shear capacity of deep members increases rapidly as the a/d ratio decreases due to the formation of an arch mechanism. Strut and tie models (STM) have been developed as one technique to design steel reinforced deep members (Marti 1985b, Rogowsky and MacGregor 1986, and Schlaich et al. 1987).

Strut and tie modelling of steel reinforced concrete deep members is an analysis technique where the flow of forces in the member is idealized using a pin-jointed truss model consisting of compression struts and tension ties as shown in Figure 1-1. Zones of

high unidirectional compressive stresses are modelled as struts while ties are used to model the tension reinforcement. Nodes are formed at the intersection of the truss elements and represent areas of multidirectional stresses in the concrete. All three elements of the STM (struts, ties, and nodes) must be properly proportioned to resist the applied loading. The STM is discussed further in Chapter 2.

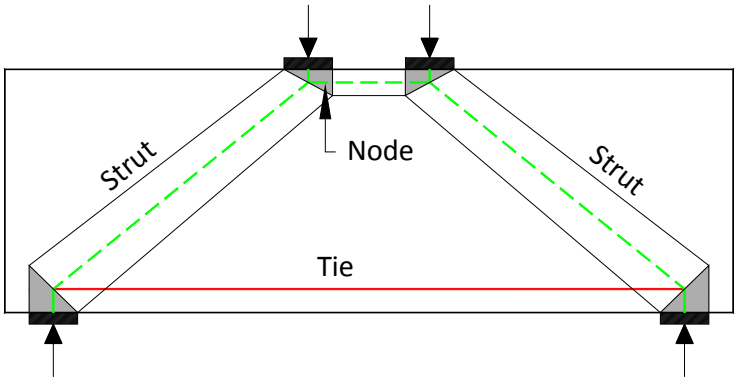

Figure 1-1: Strut and tie model for a deep beam subjected to four-point bending.

The shear behaviour of slender FRP reinforced beams has also been studied albeit to a lesser extent than steel reinforced beams. Sectional design models have been proposed and incorporated into codes and design documents such as CSA S806-02, CSA S6-06, ISIS 2007 and ACI 440.1R-06. Very little research has been conducted on members having small a/d ratios and reinforced internally with FRP. Of the 25 specimens tested in two prior test programs (El-Sayed 2006 and Nehdi et al. 2008), all had small dimensions when compared to the common sizes of beams used in industry. All the specimens had effective depths, d, less than 350 mm and 11 specimens had effective depths of 150 mm. However, the results indicated that arch action can form in FRP reinforced beams having small a/d ratios and the capacities were in excess of that predicted by sectional shear models for FRP reinforced concrete members.

Normal strength concrete, f_c' = 35-50 MPa, was used for most of the specimens in the research programs by El-Sayed (2006) and Nehdi et al. (2008). Only one beam had concrete strength in excess of 60 MPa. Limited values of a/d ratios and reinforcement ratios were used due to the small number of specimens and large number of variables.

The current design codes and guides (CSA S806-02, S6-06, ISIS 2007, and ACI 440.1R-06) provide no shear design method specifically for deep concrete members reinforced with FRP. Designers only have guidance on using sectional models, which may result in uneconomical designs in instances where large members are used, as is the case when steel reinforced deep beams are designed using sectional models. CSA S806-02 even states that “analysis by strut and tie models is not permitted.”

Therefore, it was identified that additional research was needed to develop a better understanding of the behaviour of FRP reinforced concrete deep beams and to develop a modelling technique that accurately predicts the shear capacity. This thesis describes an experimental research program involving the design, fabrication, and testing of large-scale FRP reinforced concrete deep beams that more realistically represent the member sizes used in structures. A modelling technique for predicting the capacity of FRP reinforced concrete deep members is developed and validated using data from the experimental program and from the literature.

1.2 Hypothesis

The experimental work in this study was conducted to test the hypotheses:

> FRP reinforced concrete deep beams have similar shear behaviour to what has been documented for steel reinforced concrete deep beams. More specifically, FRP reinforced concrete deep beams will develop an arch mechanism after the formation of diagonal cracks.
>
> The strut and tie modelling procedure developed for steel reinforced concrete members (CSA A23.3-04) based on the modified compression field theory (Vecchio and Collins, 1986) is capable of accurately predicting the load carrying capacity of FRP reinforced concrete deep beams.

The latter hypothesis would also serve to provide validation of modified compression field theory based design models at high strain ranges. Since glass FRP has a lower Young's modulus than steel reinforcement, it is expected that higher strains will be present in the FRP reinforcement than in the reinforcement of comparable steel reinforced concrete members at the same load level.

1.3 Project Objectives and Scope

This thesis reports on the experimental and analytical results of the shear behaviour of large-scale FRP reinforced concrete deep beams containing no distributed web reinforcement. The main objectives of the study were to:

- Determine the behaviour of FRP reinforced concrete deep beams containing no web reinforcement.
- Assess the design parameters that influence the strength and behaviour of FRP reinforced concrete deep beams containing no web reinforcement.

- Determine if existing sectional design methods for FRP reinforced members are capable of accurately predicting the shear capacity of FRP reinforced concrete deep beams.
- Evaluate the ability of strut and tie models to predict the capacity of FRP reinforced concrete deep beams.

To address these objectives, a test program consisting of 12 concrete deep beams longitudinally reinforced with glass FRP (GFRP) and containing no distributed web reinforcement was developed. The primary test variables included the a/d ratio, longitudinal reinforcement ratio (ρ), effective depth (d), and concrete strength (f_c'). The test results together with published data from other researchers were analyzed to identify an appropriate design approach for FRP reinforced concrete deep members.

1.4 Thesis Organization

Chapter 2 provides background material on the properties of FRP reinforcement, an overview of the shear mechanisms, and strut and tie modelling procedures. Review of previous research on FRP reinforced concrete deep beams and a summary of the shear design models given in codes and guides are also presented. Chapter 3 describes the design, fabrication, instrumentation, and testing of 12 new specimens. The experimental results along with a description of the behaviour of the specimens are given in Chapter 4. Chapter 5 contains the analysis of the specimens using different sectional shear models and the strut and tie modelling techniques. Discussions of the behaviour of the specimens and the suitability of each shear model are also included in Chapter 5. Chapter 6 summarizes the conclusions developed from this study and identifies areas for future research.

Appendix A contains test results from the tensile testing of FRP bars. Appendix B includes details on the concrete properties for each deep beam specimen. Appendix C contains details related to the instrumentation and testing of each specimen along with a subset of experimental data.

2 Background

2.1 Overview

This chapter presents a summary of the background and references that are applicable to the current study. Section 2.2 provides general information regarding FRP reinforcement. Subsequently, the shear behaviour of slender and deep beams is summarized in section 2.3. A review of the literature pertaining to the shear behaviour of FRP reinforced deep members is presented in section 2.4. Finally, sectional shear models for FRP reinforced members and strut and tie models used in the analysis of steel reinforced deep members are discussed in section 2.5.

2.2 Fibre Reinforced Polymer (FRP) Bars

FRP reinforcing bars are composed of longitudinal fibres embedded in a resin matrix. The most common types of fibres are carbon, glass, and aramid. In general, the weight of FRP bars is one-fourth to one-sixth the weight of steel which increases the ease of on-site handling and placing of FRP reinforcement when compared to steel reinforcement (ACI 440.1R-06). In addition to being lightweight, FRP is non-corrosive and magnetically neutral. Glass FRP (GFRP) is the most common FRP reinforcement while carbon FRP (CFRP) and aramid FRP (AFRP) are less common.

The mechanical properties of FRP reinforcement vary considerably depending on the type of fibre, fibre volume fraction, and manufacturing process (ACI 440.1R-06). FRP bars in tension exhibit a linear elastic stress-strain response up to failure as seen in Figure 2-1. Unlike steel, no plastic behaviour such as yielding occurs in FRP bars and failure is sudden and brittle with a large release of energy. The tensile strength typically ranges between one to six times the tensile capacity of common steel (i.e. Grade 400) reinforcement (ACI 440.1R-06, ISIS 2007). CFRP reinforcement generally has the highest tensile capacity and GFRP reinforcement has the lowest. The modulus of elasticity of GFRP reinforcement is significantly lower than the steel modulus of elasticity and typically ranges between 35 to 51 GPa (ACI 440.1R-06). CFRP is stiffer than GFRP and in some cases stiffer than steel as the modulus of elasticity of the CFRP can be as high as 580 GPa (ACI 440.1R-06).

Unlike steel, FRP bars cannot be bent after manufacturing unless the bars contain a thermoplastic resin, which enables reshaping of the bars under heat. Therefore, bends for most types of bars are created during manufacturing. In addition, the tensile strength of the bend is reduced by 40 to 50% when compared to the straight bar (ACI 440.1R-06).

FRP reinforcing bars can experience creep rupture; failure resulting from a sustained load. The time required for rupture depends on the magnitude of the sustained load and

the type of FRP. CFRP are the least susceptible to creep rupture while GFRP are the most susceptible (ACI 440.1R-06, ISIS 2007). To avoid creep rupture, design codes impose a limit on the allowable sustained stress in the FRP (i.e. ACI 440.1R-06, ISIS 2007, CSA S6-06, and CSA S806-02). The sustainable stress limit in GFRP reinforcement varies from $0.2f_{FRPu}$ (ACI 440.1R-06) to $0.30f_{FRPu}$ (CSA S806-02).

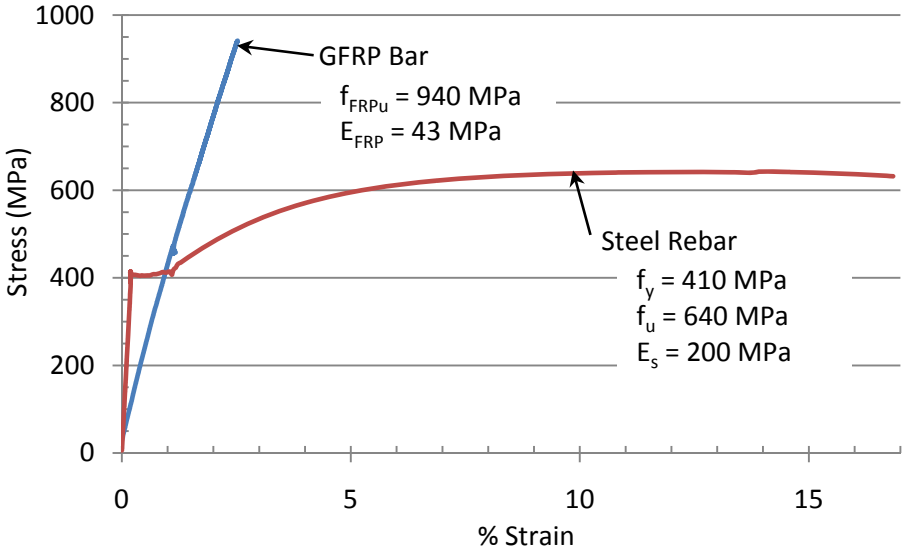

Figure 2-1: Comparison of the tensile stress-strain responses of a No. 7 GFRP bar used in this study and a steel rebar (20M).

Bonding of the internal FRP bars to the concrete is achieved through friction or mechanical interlock (ISIS 2007). Force transfer through friction is achieved by coating the bar in a layer of sand prior to complete curing of the bar. Force transfer by mechanical interlock is achieved by the formation of indentations on the bar surface by one of many methods such as wrapping of fibres around the bar or grinding of grooves.

Additional information relating to the physical and mechanical properties and durability of FRP reinforcement can be found in ISIS Design Manual No. 3 (2007), ISIS durability monograph (2006), ACI 440.1R-06, and CSA S806-02.

2.3 Shear Behaviour of Members without Web Reinforcement

The shear behaviour of reinforced concrete members has been studied extensively by many researchers over the last century. Of particular interest in this study is the shear behaviour of concrete members without transverse reinforcement, especially the behaviour of deep members with small shear span-to-depth (a/d) ratios ($a/d < 2.5$). This section provides an overview of the shear behaviour of steel and FRP reinforced concrete members.

2.3.1 Shear Transfer Mechanisms

Shear failure of reinforced concrete members containing no web reinforcement occurs after the formation of diagonal tension cracks and is typically brittle. Prior to cracking, the shear resistance mechanism consists of a series of diagonal compressive stresses and diagonal tensile stresses utilizing the entire beam cross-section (Collins and Mitchell 1997). Once the tensile stresses exceed the tensile capacity of the concrete, a crack forms. Subsequent to the formation of a crack, the shear stresses are transmitted by a combination of mechanisms.

Five shear force transfer mechanisms have been identified in cracked concrete members without transverse reinforcement (ACI 445R-99). The uncracked regions of a reinforced concrete member continue to carry shear stresses through inclined principal compression and tensile stresses. In the cracked regions, the uncracked flexural compression zone does not contribute a significant amount to the shear capacity due to the small depth of this zone. Aggregate interlock permits the transfer of shear stresses across the diagonal cracks due to the mechanical interlock of the rough crack surface which provides resistance to slip along the crack. The effectiveness of aggregate interlock depends on the width and roughness of the crack. As the crack width increases or the roughness of the crack interface decreases, the maximum shear stress transmitted through aggregate interlock decreases. Dowel action, or the resistance to "kinking" of the main longitudinal reinforcement, provides resistance to the relative shearing displacement along the crack. However, this mechanism is limited to the tensile strength of the concrete cover and is not significant in members without transverse reinforcement (ACI 445R-99). Residual tensile stresses across cracks have also been identified as a shear transfer mechanism while the crack widths remain small (less than 0.15 mm as reported by ACI-ASCE Committee 445 (1999)). Arch action is the final shear force transfer mechanism where shear is transmitted directly to the support by diagonal compression. Arch action is the dominant force transfer mechanism in steel reinforced concrete members having a shear span-to-depth (a/d) ratio less than 2.5. Complete arch action occurs when there is no bond between the reinforcement and concrete between the support points. The arch mechanism is the main focus in this study and is discussed in detail in section 2.3.2.2.

2.3.2 Slender Members vs. Deep Members

Major changes occur in the shear behaviour of steel reinforced concrete members at an a/d ratio of 2.0 to 2.5 which affects the mode of failure (Wight and MacGregor 2009). Reinforced concrete members having an a/d ratio greater than 2.5 are commonly referred to as slender members while deep or non-slender members have an a/d ratio less than 2.5. The a/d ratio has a major impact on the shear capacity of a reinforced concrete member as determined by Kani (1966) and shown in Figure 2-2. As the a/d ratio becomes less than 2.5, the shear stress at failure increases rapidly indicating a

change in the shear transfer mechanism. Due to these differences in observed behaviour, different analysis approaches are used for steel reinforced concrete members depending on the a/d ratio. For slender members with a/d > 2.5, sectional flexural and shear models are typically used in analysis. Strut and tie models are one method of analyzing deep members with a/d < 2.5 as further discussed in section 2.5.3. It is unknown whether the transition from slender behaviour to deep behaviour occurs at a similar a/d ratio in FRP reinforced concrete members as in steel reinforced concrete members.

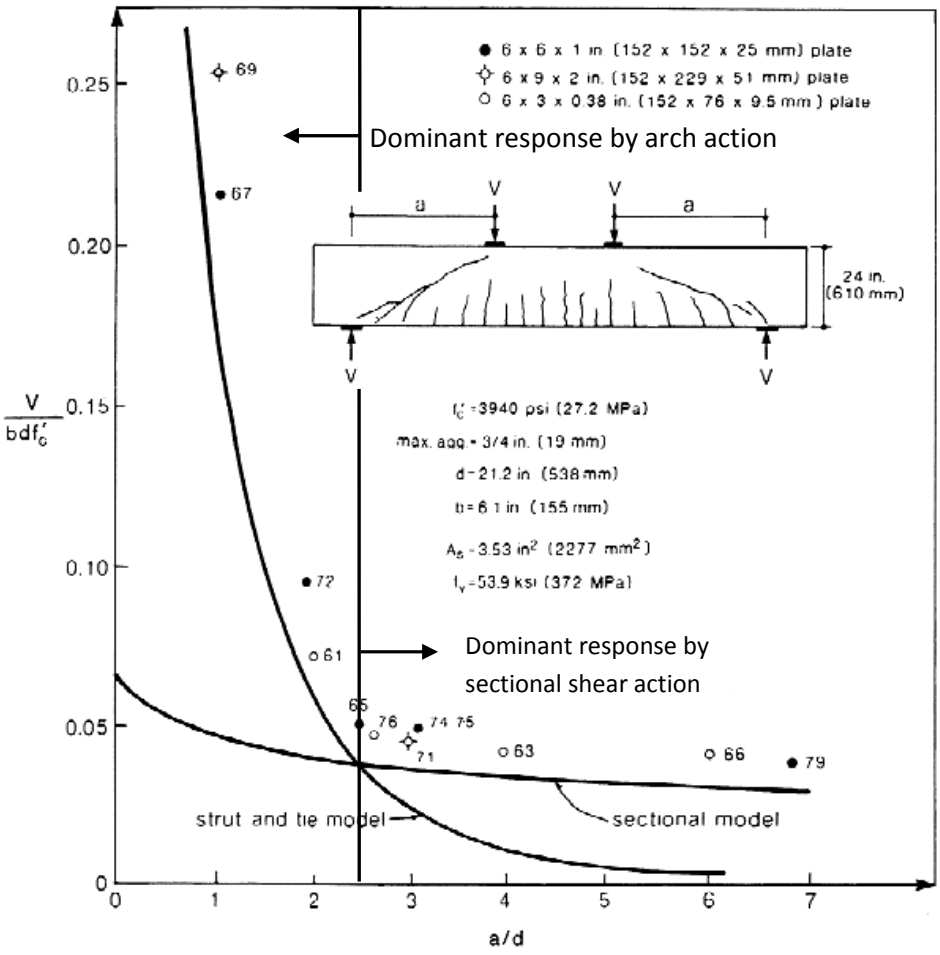

Figure 2-2: Relationship between the a/d ratio and the shear strength of steel reinforced concrete beams tested by Kani et al. (1979) (adapted from Collins and Mitchell 1997).

2.3.2.1 Slender Beams

The shear capacity of reinforced concrete slender members is governed by the breakdown of beam action. Shear failure of slender members occurs once the inclined cracks disrupt equilibrium. Sectional shear failures are characterized by an "S-shaped" failure crack (Collins et al. 2008). The shear strength, V_c, of slender members is

influenced by the aggregate size, a_g, compressive strength of the concrete, f_c', reinforcement ratio, ρ, and the member height, h, as documented in the state of the art report by ACI-ASCE Committee 445 (1999). As shown in Figure 2-3, the a/d ratio has a much smaller influence on the shear capacity of slender members than non-slender members.

The main assumption in flexural modelling of slender members is that *plane sections remain plane*; axial strains vary linearly over the member height at a section. Various empirical and theoretical flexural and shear models have been developed that are based on the assumption of linear strain variation and uniform shear stress distribution and are summarized elsewhere (i.e. ACI 445R-99).

Slender members reinforced with FRP containing no transverse reinforcement have been studied by numerous researchers. The shear behaviour of FRP reinforced members is similar to steel reinforced members with the exception that the shear capacity of GFRP reinforced members is lower than steel reinforced members having the same reinforcement ratio (i.e. Yost et al. 2001, Razaqpur et al. 2004, Tureyen and Frosch 2002). Sectional shear models for FRP reinforced concrete members are discussed in section 2.5.

2.3.2.2 Deep Beams

Work by Zsutty (1968), Kani et al. (1979), and others has shown that there is a substantial change in the shear transfer mechanism as the a/d ratio approaches 2.5 (Figure 2-2). At a/d ratios less than 2.5, arch action becomes the dominant force transfer mechanism in steel reinforced concrete members following diagonal cracking. It is also well known that the transition from deep members to slender members does not occur at a fixed a/d ratio, but occurs gradually between an a/d ratio of 2.0 to 2.5 depending on the specific member configuration (Birrcher et al. 2009, Wight and MacGregor 2009).

Prior to cracking of the concrete, an elastic stress distribution exists in deep members. Cracking disrupts the stress distribution and a major reorientation of the internal forces occurs such that forces tend to flow directly from the loading points to the supports. Arch action involves the formation of compression struts to directly transmit the load to the supports while the flexural reinforcement acts as a tie holding the base of the arch together. Unlike slender members with no web reinforcement, deep members have substantial reserve capacity after diagonal cracking as illustrated in Figure 2-3 (Wight and MacGregor 2009). Figure 2-3 also shows that in concrete members containing no web reinforcement, shear failures typically occur prior to flexural failure when the a/d ratio is less than about 6.5.

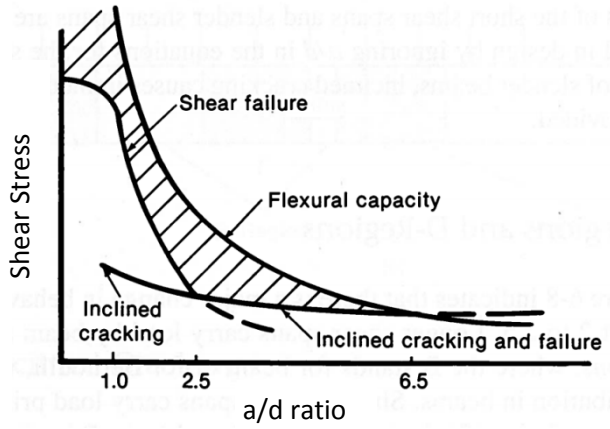

Figure 2-3: Shear stress at cracking and failure in a simply supported beam containing no web reinforcement and loaded on the top by two point loads (adapted from Wight and MacGregor 2009).

In deep members, the assumptions of *plane sections remain plane* and uniform shear stress distribution used in the design and analysis of slender members are not valid (ACI 445R-99). If sectional shear design approaches are used for deep members, the true shear capacity can be much higher as demonstrated in Figure 2-2. A nonlinear strain distribution dominates the deep member behaviour. Therefore, empirically derived design methods, truss models, or finite element analysis are some of the techniques used in analysis and design of non-slender members. One common method is the strut and tie model (STM) which is the method of interest in this research project and is described in section 2.5.3.

Unlike slender members, the shear capacity of deep members is highly dependent on the boundary conditions; namely the size of the loading and support areas (Collins and Mitchell 1997). The size of the boundary conditions is directly considered when using STMs for analysis.

According to Wight and MacGregor (2009), the behaviour and failure of deep beams without web reinforcement can be grouped into two categories according to a/d ratios. Very short members having an a/d ratio of 0 to 1.0 develop inclined cracks joining the loading point and support, which destroys the shear flow in the member while direct compression zones develop between the loads and supports (i.e. arch action). The failure modes of such beams are shown in Figure 2-4. Short beams having an a/d ratio of 1.0 to 2.5 are able to carry additional loads after inclined cracking due to a redistribution of internal forces into an arch mechanism. As the a/d ratio increases, the shear capacity rapidly drops as indicated in Figure 2-3. Shear tension failures, which involve the splitting of the concrete along the tension reinforcement, and shear compression failures, which occur when the concrete crushes in the flexural compression zone at the tip of the diagonal crack, are most common and illustrated in Figure 2-5(a) and Figure 2-5(b) respectively.

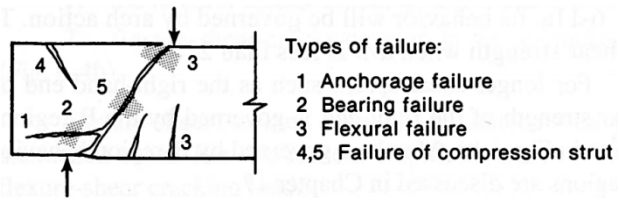

Figure 2-4: Failure modes of deep beams having an a/d ratio of 0 to 1.0 (Wight and MacGregor 2009).

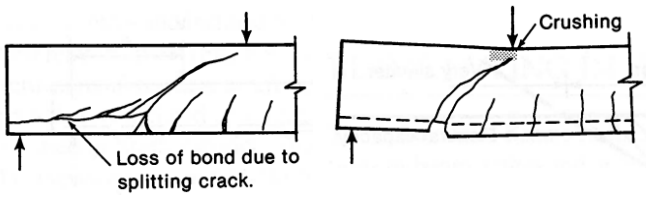

(a) (b)

Figure 2-5: Failure modes of deep beams having an a/d ratio of 1.0 to 2.5 where (a) is a shear-tension failure and (b) is a shear compression failure (Wight and MacGregor 2009).

Several factors have been identified that influence the shear capacity of deep members. The most influential parameter is the a/d ratio, investigated by Kani (1966) and demonstrated in Figure 2-2. In addition, Kani (1966 and 1967) determined that the reinforcement ratio and member height influenced the shear capacity. Increasing the reinforcement ratio resulted in an increase in shear strength while an increase in member height caused a decrease in shear stress at failure. Walraven and Lehwalter (1994) also found a significant size effect in the capacity of steel reinforced deep members containing no web reinforcement.

Additional information on the behaviour of deep members is given by Wight and MacGregor (2009), Collins and Mitchell (1997), Kani (1964) and others. Deep beam modelling techniques are discussed in section 2.5.

2.4 Previous Experimental Research on FRP Reinforced Concrete Deep Beams

Very few research programs have focused on the performance of concrete deep members reinforced with internal FRP reinforcement. This section summarizes the findings of the previous research on FRP reinforced concrete deep members.

2.4.1 El-Sayed (2006)

A test program consisting of 12 specimens (h = 400 mm) was conducted where the main variables were the reinforcement type (steel, CFRP, and GFRP), reinforcement ratio, and the a/d ratio ($0.9 < a/d < 1.7$). The specimens contained no distributed web

reinforcement. The specimens were loaded in a four-point bending configuration using stroke control. The main mode of failure was by diagonal splitting of the concrete between the support and loading point except for the specimens having an a/d ratio less than 1.0 which failed in flexural compression.

Both the FRP and steel reinforced specimens developed arching action after inclined cracking. Arch action was confirmed by the uniform strain distribution in the reinforcement along the length of the span. The specimens reinforced with CFRP had higher shear strengths than the equivalent specimens reinforced with steel while the GFRP reinforced specimens had slightly lower shear strengths than the steel reinforced specimens. The arch action was reported to be more efficient in the specimens reinforced with FRP than steel. The researcher suggested that more bond slippage could occur with FRP reinforcement when compared to steel since the FRP was sand coated, producing a more efficient arch mechanism.

For all reinforcement types, an increase in the a/d ratio produced a decrease in the shear strength. The specimens had a stiffer post cracking load deflection response at low a/d ratios than at higher a/d ratios. It was also reported that wider cracks occurred at failure in beams with smaller a/d ratios.

The shear strength of the specimens was found to be proportional to the reinforcement ratio regardless of the reinforcement type. As the reinforcement ratio increased or the modulus of elasticity of the reinforcement increased, the post cracking flexural stiffness of the specimens increased. In addition, larger crack widths were observed with a decrease in the reinforcement modulus of elasticity.

2.4.2 Nehdi et al. (2008)

Nehdi et al. (2008) presented the experimental results of eight CFRP reinforced, seven GFRP reinforced, and four steel reinforced concrete deep beams. The main variables in the test program were the *a/d* ratio, effective depth, axial stiffness of the reinforcement, and the concrete strength. The majority of the specimens had an effective depth, d, of 150 mm. Specimens having an effective depth of 250 mm and 350 mm were also tested. The a/d ratio ranged from 1.4 to 2.3 and the reinforcement ratio varied between 1.13 and 2.33%. Normal strength concrete (target f_c' = 35 MPa) and high strength concrete (target f_c' = 60 MPa) mixes were used but the final normal concrete strength varied from 35 MPa to 48 MPa and the high strength concrete achieved 63 MPa. The beams were tested in a four-point bending configuration using load control.

The shear capacity of the CFRP reinforced specimens was reported to be higher than the shear capacity of the steel reinforced specimens having the same effective depths, a/d ratios and similar reinforcement ratios and concrete strengths. GFRP reinforced

specimens with d = 150 mm failed at load levels between 6 and 35% lower than the corresponding steel and CFRP reinforced specimens and had more extensive and wider diagonal cracks. The CFRP reinforced specimens had crack widths that were comparable to the steel reinforced specimens. The majority of the CFRP and steel reinforced specimens failed in diagonal shear cracking (Omeman et al. 2008). The failure mode of the GFRP reinforced beams was not reported although the load deflection plots provided in Nehdi et al. (2008) indicate some failed in a ductile manner.

Increasing the a/d ratio resulted in a decrease in the shear capacity and corresponding mid-span deflection of the CFRP reinforced specimens. Increasing the reinforcement ratio and the concrete strength produced an increase in the shear capacity. Large strains were recorded in the GFRP and CFRP reinforcement at failure, with strain values ranging between 0.5% and 1.2%. Increasing the specimen height, h, resulted in a slight increase in the failure shear stress as shown in Figure 2-6. However, even though the reinforcement ratio, concrete strength, and the a/d ratio were similar, they were not constant. The a/d ratio was 4% smaller for the larger beams.

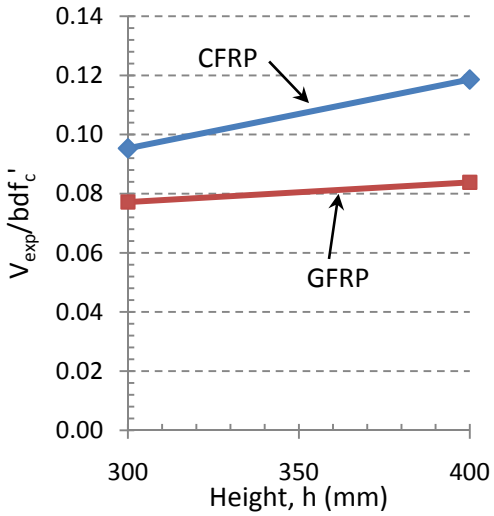

Figure 2-6: Comparison of similar beams from Nehdi et al. (2008) showing the influence of height on the failure shear stress.

2.4.3 Additional Research Work

Two other researchers have reported some experimental data on FRP reinforced concrete deep beams. Razaqpur et al. (2004) tested a CFRP reinforced beam having an a/d ratio of 1.83. However, no detailed description of the failure mechanism was given and the boundary conditions are unknown. Since no bearing plate dimensions were given, this specimen was not included in the analysis section (Chapter 5) of this study as plate sizes are an integral part in calculating the load carrying capacity using STMs (Collins and Mitchell 1997).

Guadagnini et al. (2003) described an experimental program where the shear strength of concrete beams reinforced with external FRP links was examined. The a/d ratio ranged from 1.1 to 3.3 which theoretically put the majority of the specimens in the deep beam category. Since these specimens contained shear reinforcement (external FRP links), they fall outside the scope of this study.

2.5 Existing Shear Models

There have been numerous models proposed for the shear behaviour of slender concrete members reinforced with FRP. Furthermore, there are additional shear models for steel reinforced concrete slender and deep members which could be applicable to FRP reinforced concrete members. This section describes some of the models that have either been proposed or are in use in codes for the shear design of both FRP and steel reinforced concrete members. Sectional shear models for steel reinforced members and FRP reinforced members are described in section 2.5.1 and section 2.5.2, respectively. A general overview of STMs is given in section 2.5.3 followed by the introduction of specific code models for steel reinforced concrete deep members.

The models are shown without the resistance factors and are provided in SI units.

2.5.1 Slender Steel Reinforced Members – CSA A23.3-04

The general method for calculating the shear capacity of concrete members containing no stirrups or distributed longitudinal reinforcement is shown below.

$$V_c = \lambda\beta\sqrt{f'_c}b_w d_v \quad \textbf{2.1}$$

$$\beta = \frac{0.40}{(1+1500\varepsilon_x)} \cdot \frac{1300}{(1000+s_{ze})} \quad \textbf{2.2}$$

$$\varepsilon_x = \frac{M_f/d_v + V_f}{2E_s A_s} \leq 0.003 \quad \textbf{2.3}$$

$$s_{ze} = \frac{35d_v}{15+a_g} \geq 0.85d_v \quad \textbf{2.4}$$

$$d_v = greater\ of\ 0.72h\ and\ 0.9d \quad \textbf{2.5}$$

The model used in CSA A23.3-04 (Bentz and Collins 2006) assumes that the shear capacity at failure can be predicted by the aggregate interlock mechanism for shear force transfer across a crack. The model is based on simplifications to the modified compression field theory (MCFT) (Vecchio and Collins 1986). The MCFT is a model that considers equilibrium, compatibility, stress-strain relationships, and tension stresses in cracked reinforced concrete.

The shear capacity, V_c, is determined from an average shear stress in the concrete acting over an area defined by the beam width, b_w, and effective shear depth, d_v. The value of V_c is assumed to be proportional to the tensile strength of the concrete. The aggregate interlock mechanism, which is represented by the β factor in Equation 2.1, is dependant on the axial strain and effective crack spacing. As the longitudinal strain at mid-depth (Equation 2.3) increases or as the effective crack spacing increases (Equation 2.4), the crack widths also increase and the stress that can be transmitted across the cracks by aggregate interlock decreases.

The β equation (Equation 2.2) was developed by approximating the nonlinear relationship between crack width and longitudinal strain with a linear equation and focusing the equation on strains less than 0.001. This strain corresponds to initial yielding of Grade 400 steel (f_y = 400 MPa) since ε_x is calculated at mid-depth (Bentz and Collins 2006). Hoult et al. (2008) demonstrated that the equation becomes increasingly conservative for large tensile strains as the linear crack width approximation deviates further from the nonlinear relationship derived from the MCFT (see section 2.5.2.2).

The effective crack spacing, s_{ze}, accounts for the so-called size effect in shear and is a function of the average crack spacing and the maximum aggregate size. The crack spacing increases as the effective depth increases, which decreases the aggregate interlock, reducing the shear capacity. The aggregate size ceases to have a significant mechanical influence on shear strength for concrete having a compressive strength above 70 MPa as the cracks tend to pass through the aggregate rather than around. According to the CSA A23.3-04 shear model, the aggregate size value, a_g, in Equation 2.4 is taken as zero if f_c' is greater than 70 MPa and is linearly reduced to zero as f_c' increases from 60 to 70 MPa.

At direct point loads, a fan shaped pattern of compressive stresses radiating away from the point load exists which reduces the tension component in the reinforcement caused by shear. As a result, the maximum design tension in the reinforcement does not need to exceed that due to the maximum moment alone (CSA A23.3-04 Explanatory Note N11.3.9.4). The longitudinal strain at mid-depth, ε_x, need not exceed $(M_{fmax}/d_v)/(2E_{FRP}A_{FRP})$ where M_{fmax} is the maximum moment at the location of a direct loading point.

For sections closer than d_v from the face of the support, Equation 2.3 is evaluated using the applied moment, M_f, and shear, V_f, determined at the section d_v from the face of the support. The moment and shear values in Equation 2.3 are always taken as positive and M_f shall not be taken less than $V_f d_v$.

CSA A23.3-04 indirectly limits crack widths at service loads to 0.4 mm and 0.33 mm for interior and exterior exposure, respectively (CSA A23.3-04 explanatory note N10.6.1)

Using a database of 30 steel reinforced concrete members, Hoult et al. (2008) reported an average test to predicted strength ratio of 1.16 with a 15% coefficient of variation (COV) for the CSA A23.3-04 shear model. Including 116 FRP reinforced concrete slender members produced an average test to predicted strength ratio of 1.38 with a COV of 17%.

2.5.2 Slender FRP Reinforced Beams

2.5.2.1 CSA S6-06 (Addendum 2009)

The method provided in CSA S6-06 (2009) for determining the shear capacity of FRP reinforced concrete beams is similar to the technique used in the shear design of slender steel reinforced concrete members (section 2.5.1) except that Equation 2.6 has a slightly different format. The CSA S6-06 shear model is also a mechanical model based on the MCFT as described in section 2.5.1. The nominal shear capacity of FRP reinforced slender beams without transverse reinforcement, V_c, is given as:

$$V_c = 2.5\frac{0.40}{(1+1500\varepsilon_x)}\cdot\frac{1300}{(1000+s_{ze})}f_{cr}b_w d_v \quad \textbf{2.6}$$

$$\varepsilon_x = \frac{M_f/d_v + V_f}{2E_{FRP}A_{FRP}} \leq 0.003 \quad \textbf{2.7}$$

$$s_{ze} = \frac{35d_v}{15+a_g} \geq 0.85d_v \quad \textbf{2.8}$$

$$d_v = greater\ of\ 0.72h\ and\ 0.9d \quad \textbf{2.9}$$

$$f_{cr} = 0.4\sqrt{f'_c} \leq 3.2\ MPa \quad \textbf{2.10}$$

In addition, the axial strain at mid-depth, ε_x (Equation 2.7), does not need to exceed $(M_{fmax}/d_v)/(2E_{FRP}A_{FRP})$ where M_{fmax} is the maximum moment at a direct point load. The region around a direct point load consists of a fan-shaped pattern of compressive stresses radiating from the point load and the tension in the reinforcement does not exceed that due to the maximum moment alone. However, this is not true at an indirect support where the tension in the reinforcement is greater than that due to the moment alone (CSA S6-06 Commentary C8.9.13).

For sections closer than d_v to the support, Equation 2.7 is evaluated using the applied moment and shear at d_v from the support. The value for the moment and shear in Equation 2.7 is always taken as positive and M_f shall not be taken as less than $V_f d_v$.

The design process involves checking that the shear capacity is greater than the applied shear force at all sections along the beam. CSA S6-06 requires that minimum stirrups be provided throughout the full length of beams longitudinally reinforced with FRP, even if

the concrete shear capacity (V_c) exceeds the shear demand. The minimum stirrup requirement is given in as:

$$A_{v,min} = 0.06\sqrt{f_c'}\frac{b_w s}{\sigma_v} \quad \textbf{2.11}$$

$$\sigma_v = smaller\ of\ \frac{(0.05r/d_s + 0.3)f_{FRPbend}}{1.5}\ and\ E_{vFRP}\varepsilon_v \quad \textbf{2.12}$$

$$\varepsilon_v = \left[f'_c \frac{\rho E_{FRP}}{\rho_{vFRP} E_{vFRP}}\right]^{0.5}\left[1 + 2\left[\frac{\sigma_n}{f_c'}\right]\right] \leq 0.0025 \quad \textbf{2.13}$$

The maximum stress in FRP bars at the serviceability limit state shall not exceed $0.25f_{FRPu}$ for glass FRP and $0.65f_{FRPu}$ for carbon FRP (i.e. to limit creep of the FRP reinforcement, see section 2.2). When the maximum tensile strain in the FRP reinforcement under full service load exceeds 0.0015, the crack widths are not to exceed 0.5 mm for members subjected to aggressive environments and 0.7 mm for other members.

El-Sayed and Benmokrane (2008) calculated the average experimental to calculated shear capacity to be 1.72 with a COV of 20.1% using a database of 69 concrete members and the CSA S6-06 (2009) shear model. The specimens were reinforced with longitudinal glass, carbon, or aramid FRP and contained no web reinforcement. The database covered a wide range of design parameters.

2.5.2.2 Hoult et al. (2008)

Hoult et al. (2008) developed an enhancement to the shear model for steel reinforced concrete beams from the Canadian concrete design code, CSA A23.3-04 (see section 2.5.1), to account for the typically higher axial strains occurring in members with FRP reinforcement. In the derivation of the CSA A23.3-04 model (Bentz and Collins 2006), a so-called first order (i.e. linear) approximation to the crack width versus the longitudinal strain relationship was developed for use with steel reinforced concrete members due to the limited range of axial strains occurring in steel reinforced concrete members. In contrast, the axial strains in FRP reinforced concrete beams at failure can be much higher due to the typically lower stiffness of the FRP when compared with steel. To better model the crack widths as predicted by the MCFT, Hoult et al. (2008) developed a so-called second order (i.e. nonlinear) approximation to the diagonal crack width relationship as shown in Figure 2-7. The Hoult et al. (2008) shear capacity model for members reinforced with only longitudinal FRP is given in Equation 2.14.

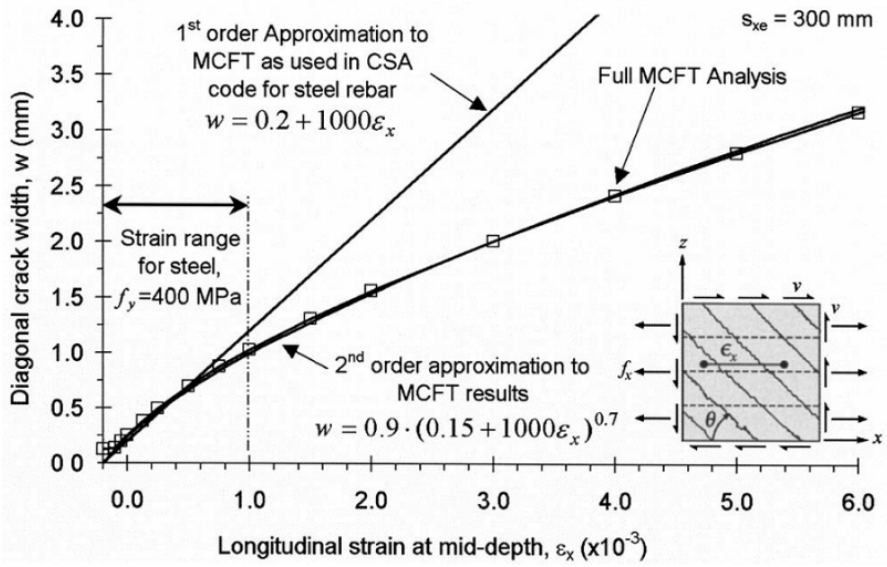

Figure 2-7: First and second order approximation to the MCFT crack width relationship (Hoult et al. 2008).

$$V_c = \frac{0.30}{0.5 + (1000\varepsilon_x + 0.15)^{0.7}} \cdot \frac{1300}{(1000 + s_{ze})} \sqrt{f'_c} b_w d_v \qquad \textbf{2.14}$$

$$\varepsilon_x = \frac{M_f / d_v + V_f}{2E_{FRP} A_{FRP}} \qquad \textbf{2.15}$$

$$s_{ze} = \frac{31.5d}{16 + a_g} \geq 0.77d \qquad \textbf{2.16}$$

The effective depth, d_v, is taken as $0.9d$. As is the case with the CSA A23.3-04 and CSA S6-06 shear models described in section 2.5.1 and 2.5.2.1, respectively, the shear capacity consists of strain and size terms both of which are influenced by the crack spacing and crack width. The aggregate size for high strength (f_c' > 70 MPa) and lightweight concrete is taken as zero since the cracks tend to pass through the aggregate.

Using a database containing 146 beams, Hoult et al. (2008) reported an average experimental to calculated shear capacity ratio of 1.15 with a COV of 14.9% using this model. The database contained specimens longitudinally reinforced with steel, aramid FRP, carbon FRP, and glass FRP but without transverse reinforcement. The 30 steel reinforced specimens had an average experimental to predicted strength ratio of 1.06 with a COV of 15.7%. In addition, no trends in the test to predicted ratios were observed with respect to f_c', a/d ratio, reinforcement ratio, width, or the reinforcement modulus of elasticity indicating that the model could properly account for these design

parameters. The effect of h on the shear capacity prediction ratio could not be established due to a lack of specimens with different heights in the assembled database.

2.5.2.3 CSA S806-02

CSA S806-02 is the Canadian code addressing the design and construction of reinforced concrete members containing FRP. The shear design provisions from this code are only valid for members not subjected to significant axial tension. For FRP reinforced concrete members having an effective depth not exceeding 300 mm, the shear capacity is calculated as:

$$V_c = 0.035\lambda \left(f'_c \rho E_{FRP} \frac{V_f}{M_f} d \right)^{1/3} b_w d \qquad \textbf{2.17}$$

$$0.1\lambda\sqrt{f'_c} b_w d < V_c < 0.2\lambda\sqrt{f'_c} b_w d \qquad \textbf{2.18}$$

The quantity $V_f d / M_f$ is not to be taken as greater than 1.0. $V_f d / M_f$ is the value of the factored shear, V_f, divided by the factored moment, M_f, at the section under consideration and is the inverse of the a/d ratio for a simply supported member. Equation 2.17 takes into account the beam slenderness and the rigidity of the longitudinal reinforcement. As the M_f / V_f ratio increases, the shear capacity predictions decrease. A decrease in the stiffness of the longitudinal reinforcement also reduces the shear capacity. In addition, CSA S806 defines an upper and lower limit on the shear capacity calculated using Equation 2.17 as given by Equation 2.18. These limits match the V_c and $½ V_c$ values determined from the simplified shear method of CSA A23.3-94 for steel reinforced concrete members having d < 300 mm.

The shear capacity of members having an effective depth exceeding 300 mm is calculated using Equation 2.19 which accounts for the size effect in shear. Equation 2.19 is equivalent to $½ V_c$ determined from the simplified shear method of CSA A23.3-94 for steel reinforced concrete members having d > 300 mm.

$$V_c = \left(\frac{130}{1000 + d} \right) \lambda\sqrt{f'_c} b_w d \geq 0.08\lambda\sqrt{f'_c} b_w d \qquad \textbf{2.19}$$

In members where the reaction force in the direction of the applied shear introduces compression into a support region, the sections located less than d from the face of the support may be designed for the same shear force that occurs at a distance of d from the support face.

CSA S806-02 limits the tensile stresses in the GFRP reinforcement under sustained loads to $0.3 f_{FRPu}$.

Using the CSA S806-02 shear model, El-Sayed and Benmokrane (2008) calculated the average experimental to calculated shear capacity to be 1.26 with a COV of 27.4% using a database of 69 simply supported FRP reinforced beams. The beams were longitudinally reinforced with glass, carbon, or aramid FRP and contained no web reinforcement. The database covered a wide range of design parameters.

2.5.2.4 ISIS Design Manual No. 3, Version 2 (2007)

Intelligent Sensing for Innovative Structures (ISIS) developed design guidelines for the use of FRP to reinforce and strengthen concrete structures. ISIS published a series of design manuals that address the production, testing, and use of FRP. Design manual 3 (ISIS 2007) provides guidance for design of concrete structures internally reinforced with FRP. The shear model given in the design manual is similar to the simplified method of determining the shear capacity in steel reinforced members as outlined in CSA A23.3-94.

The shear capacity of FRP reinforced concrete members containing no transverse web reinforcement and having an effective depth less than 300 mm is calculated using Equation 2.20.

$$V_c = 0.2\lambda\sqrt{f'_c}\,b_w d\sqrt{\frac{E_{frp}}{E_s}} \qquad \textbf{2.20}$$

For beams which have an effective depth greater than 300 mm, V_c is calculated using Equation 2.21. The difference between Equation 2.20 and Equation 2.21 is that a size effect term is included in the latter to account for the observed reduction in shear capacity as the member depth increases.

$$V_c = \left(\frac{260}{1000 + d}\right)\lambda\sqrt{f'_c}\,b_w d\sqrt{\frac{E_{frp}}{E_s}} \qquad \textbf{2.21}$$

Equation 2.20 and Equation 2.21 are the same equations given in CSA A23.3-94 for the design of steel reinforced members having d < 300 mm and d > 300 mm, respectively, except that in both cases a reduction factor based on the stiffness of the longitudinal FRP reinforcement is applied to account for the lower shear strength as E_{frp} decreases.

At the serviceability limit states, ISIS design manual No. 3 (2007) recommends limiting crack widths in FRP reinforced concrete members to 0.5 mm and 0.7 mm for exterior and interior exposure respectively. The allowable FRP stress limit under service loads is $0.65f_{FRPu}$ for CFRP, $0.35f_{FRPu}$ for AFRP, and $0.25f_{FRPu}$ for GFRP.

El-Sayed and Benmokrane (2008) calculated the shear capacity of 69 simply supported FRP reinforced concrete beams containing no transverse reinforcement using the 2001 version of the ISIS design manual. In the 2001 ISIS design manual No. 3, Equation 2.21

had a lower limit on the shear strength. However, all shear capacity predictions were greater than the lower limit for specimens having depths greater than 300 mm and the test to predicted shear capacity ratios are valid for the 2007 ISIS design manual. The average test to predicted shear capacity ratio for this model was 1.24 with a COV of 30.4%.

2.5.2.5 ACI 440.1R-06

According to ACI committee 440, the shear design of FRP reinforced concrete is similar to that of steel reinforced concrete as given in ACI 318-08. However, the mechanical properties of FRP affect the shear strength with the main factors being the low FRP modulus of elasticity and low transverse shear strength of FRP. Using a model developed by Tureyen and Frosch (2003), the shear capacity of flexural (i.e. slender) members is determined by Equation 2.22.

$$V_c = \frac{2}{5}\sqrt{f'_c}\, b_w c \qquad \textbf{2.22}$$

where c is the cracked transformed section neutral axis depth and is computed using Equation 2.23 for singly reinforced, rectangular cross-sections. The axial stiffness of the FRP reinforcement is accounted for in Equation 2.22 through the computation of the neutral axis depth which is dependent on the longitudinal reinforcement ratio and the ratio of the modulus of elasticity of the FRP bars to the concrete. ACI 440.1R-06 also states that a minimum amount of shear reinforcement must be provided when the factored shear load exceeds $\phi V_c/2$.

$$c = kd \qquad \textbf{2.23}$$

$$k = \sqrt{2\rho n_f + \left(\rho n_f\right)^2} - \rho n_f \qquad \textbf{2.24}$$

$$\rho = FRP\ reinforcement\ ratio = \frac{A_{FRP}}{b_w d} \qquad \textbf{2.25}$$

$$n_f = \frac{E_{FRP}}{E_c} \qquad \textbf{2.26}$$

According to ACI 440.1R-06, Equation 2.22 is equivalent to the equation that is used in evaluating the shear capacity of concrete members reinforced with steel (ACI 318-08) except that a factor of $12k/5$ ($k = d/c$) has been included in Equation 2.22 to account for the reduced axial stiffness of FRP reinforcement.

ACI 440.1R-06 limits the stress in the FRP under sustained load to $0.20f_{FRPu}$ for GFRP, $0.30f_{FRPu}$ for AFRP, and $0.55f_{FRPu}$ for CFRP to avoid creep rupture of the FRP reinforcement. The committee also recommended using crack width limitations

identical to CSA S806-02 at service loads. The maximum crack width for interior exposure is 0.7 mm and 0.5 mm for exterior exposure.

Tureyen and Frosch (2003) validated the shear model using a database of 370 reinforced concrete beams containing no transverse reinforcement and failing in shear. The database contained 326 steel reinforced concrete beams and 44 FRP reinforced concrete beams. The test to calculated shear strength ratio for the entire test database ranged from 0.99 to 2.07 with an average ratio of 1.36 and a standard deviation of 0.21. Using a database of 69 beams reinforced only with longitudinal FRP, El-Sayed and Benmokrane (2008) determined the average test to calculated shear strength ratio to be 1.80 with a COV of 14.3% using the ACI 440.1R-06 shear model.

2.5.2.6 Razaqpur and Isgor (2006)

Razaqpur and Isgor (2006) proposed a modified version of the shear model from CSA S806-02. The proposed method is applicable to FRP reinforced members with no transverse reinforcement and was intended to overcome deficiencies identified in CSA S806-02: shear transfer through arch action at a/d less than 2.5 was not considered, unconservative results could occur for beams having d > 300 mm, and a minimum concrete contribution that may be unconservative in some instances. The following equation was proposed by Razaqpur and Isgor (2006) to predict the shear capacity of FRP reinforced concrete members not subjected to axial forces and containing no transverse reinforcement:

$$V_c = V_{c1} + V_{c2} = 0.035 k_m k_s k_a [1 + k_r] \sqrt{f'_c} b_w d \leq 0.2 k_s \sqrt{f'_c} b_w d \quad \textbf{2.27}$$

The shear resistance of the member, V_c, is a combination of the contributions from the uncracked concrete, V_{c1}, and the aggregate interlock, V_{c2}. The factor k_m accounts for the interaction of the factored moment and shear on the shear capacity, k_r corresponds to the reinforcement stiffness, k_a accounts for the contribution of arch action, and k_s accounts for observed size effect in shear.

$$k_m = \left(\frac{V_f d}{M_f}\right)^{2/3} \quad \textbf{2.28}$$

$$k_r = (E_{FRP}\rho)^{1/3} \quad \textbf{2.29}$$

$$k_a = 1.0 \; for \left(\frac{M_f}{V_f d}\right) \geq 2.5 = \frac{2.5}{(M_f/V_f d)} \; for \left(\frac{M_f}{V_f d}\right) < 2.5 \quad \textbf{2.30}$$

$$k_s = 1.0 \; for \; beams \; with \; d \leq 300$$
$$= \frac{750}{450 + d} \; for \; beams \; with \; d > 300 \qquad \textbf{2.31}$$

In calculating k_a, M_f/V_fd shall not be taken as less than 1.0. The effect of the maximum aggregate size on shear capacity is not included in the model.

Razaqpur and Isgor (2006) found that the model provided good predictions for the shear strength of 62 FRP reinforced slender specimens and the one FRP reinforced deep specimen (a/d = 1.82) included in the database of test results. The average experimental shear capacity to the model capacity was 1.28 with a standard deviation of 0.27.

2.5.3 Strut and Tie Models

Strut and tie modelling is a technique used to analyze regions of nonlinear strain distributions and is described in detail by Schlaich et al. (1987), Marti (1985), ACI-ASCE Committee 445 (1999), and Wight and MacGregor (2009). Therefore, this section will only provide a brief description on the use of STMs before introducing the strut and tie modelling design provisions from the two design codes considered in this study.

Nonlinear strain distributions in concrete members are caused by changes in geometry or loading and are commonly referred to as disturbed regions or *D-regions*. The remaining portions of the member that are not subjected to disturbances are referred to as *B-regions*. St. Venant's principle suggests that the effect of a disturbance will be negligible at about one member depth away from the load or geometric discontinuity. Figure 2-8 shows the extent of D-regions and B-regions according to this principle. In B-regions, beam theory applies and the flexural and shear capacity can be determined using sectional flexural and shear approaches which are based on the assumption of plane sections remain plane and uniform shear stress distribution, respectively. Sectional approaches are not applicable in D-regions as the axial strain is nonlinear and the shear stress distribution is not uniform (ACI 445R-99). In deep members, the entire member consists of a D-region (i.e. a/h ratio is less than 2.0) as shown in Figure 2-9.

For the strut and tie modelling technique, the flow of forces in a simply supported deep member after cracking is idealized using a pin-jointed truss model consisting of compression struts and tension ties. The struts and ties intersect at nodes. Therefore, STMs consist of three main elements: struts, ties, and nodes. Struts are used to represent the assumed compressive stress fields in the concrete after cracking. Ties represent the primary tension reinforcement with the tie location made to correspond to the centroid of the reinforcement. The tie also consists of the surrounding concrete that is concentric with the axis of the reinforcement. The surrounding concrete is not considered in the design; however, the surrounding concrete will reduce the elongation of the tie (ACI 318-08). In strut and tie modelling, bond between the tie and concrete is

assumed not to exist and the tension in the tie is constant over its length between adjacent nodes.

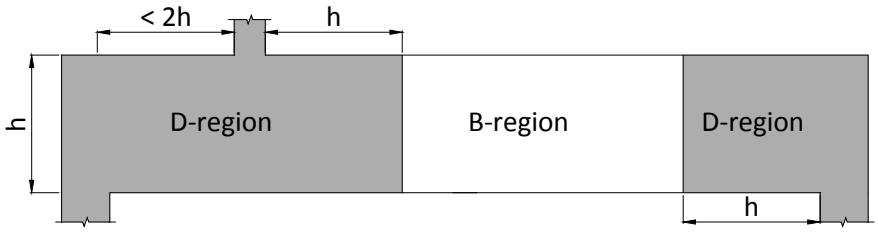

Figure 2-8: D-regions and B-regions in a simply supported beam.

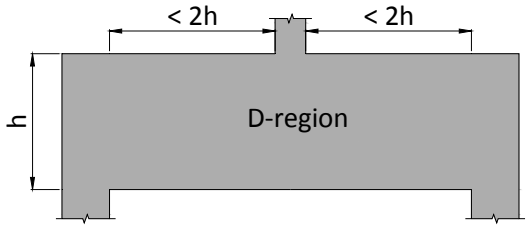

Figure 2-9: A deep simply supported member.

Struts, ties, and nodes must be properly proportioned to resist the applied forces. Strut and tie modelling is based on the lower bound theory of plasticity and the capacity of the model is always less than the true capacity if the truss is in equilibrium and has sufficient deformation capacity to allow redistribution of forces into the assumed truss elements (Schlaich et al, 1987). An example of a STM for a beam under four-point loading is shown in Figure 2-10.

Two types of struts are of interest in this research program, prismatic and bottle-shaped. The horizontal strut located between the two loading plates in Figure 2-10 can be assumed as prismatic. The compression zone is bounded by the beam face on the top and the neutral axis on the bottom, preventing the transverse spread of compressive stresses along the strut length. In design, the top strut is typically assumed to be uniformly stressed with a depth that is smaller than the distance to the neutral axis. Struts that are located such that the width can change along the length are bottle-shaped struts as illustrated in Figure 2-10 for the case of the diagonal struts. With the spreading of the compressive stresses in a bottle-shaped strut, transverse tensile stresses develop leading to cracking of the strut parallel to the strut axis. In members with no distributed web reinforcement, failure can occur due to splitting of the strut (Wight and MacGregor 2009). The dimensions of a strut are determined by the sizes of the nodal zones at either end of the strut. Based on the nodal zone dimensions, the bottle-shaped struts are often idealized as being prismatic or uniformly tapered, as shown in Figure 2-10, in order to simplify design, but the influence of the spreading action from the bottle-shape must be considered.

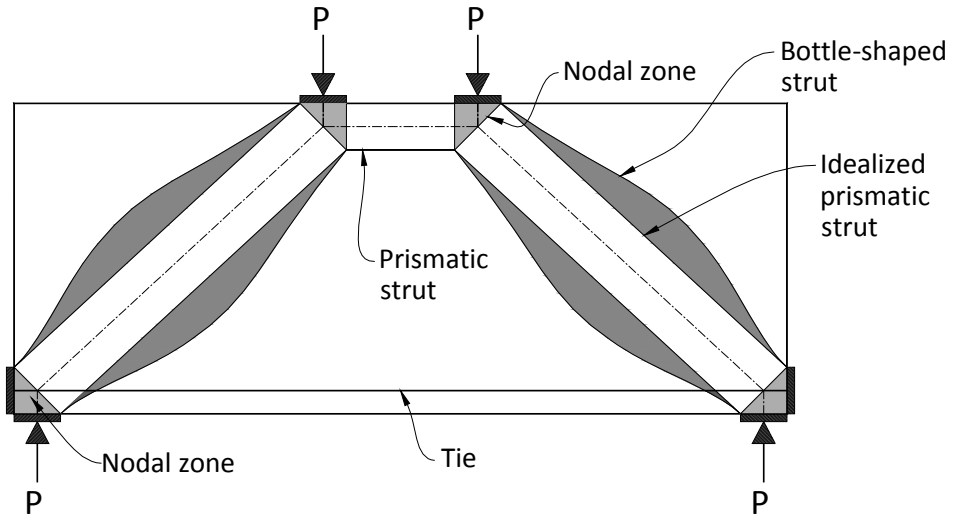

Figure 2-10: Strut and tie model of a simply supported deep beam containing no web reinforcement.

The size of each nodal zone is defined by the boundary conditions. The size of the bearing area (bearing plates in the case of Figure 2-10) defines one side. The depth of the compression zone or the height of the tension zone defines the second side. Four types of nodal zones can be identified and are shown schematically in Figure 2-11:

- CCC – bounded by compression on all sides (top nodes in Figure 2-10)
- CCT – bounded by two struts and a maximum of one tie (bottom nodes in Figure 2-10)
- CTT – bounded by one strut and two ties (not covered in this study)
- TTT – multiple ties (not covered in this study)

In nodes anchoring ties, the force from a properly anchored tie is applied on the back side of the node as a bearing stress as shown in Figure 2-12(a). The bearing area is assumed to have a height twice the distance from the centroid of the reinforcement (which coincides with the tie in the STM) to the beam surface. Nodes anchoring ties have a lower capacity as discussed further in sections 2.5.3.1 and 2.5.3.2.

In a STM, the ties must be properly anchored by bond, hook, or mechanically. Ties anchored by bond must be adequately developed at the edge of the extended nodal zone as shown in Figure 2-12(b). The force from a tie anchored by bond is assumed to be applied at the back side of the node by the force spreading action indicated in Figure 2-12(b).

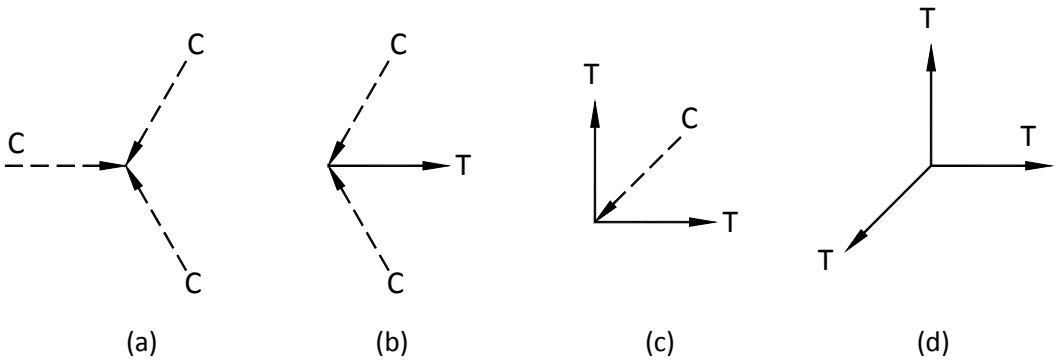

Figure 2-11: (a) CCC node, (b) CCT node, (c) CTT node, and (d) TTT node.

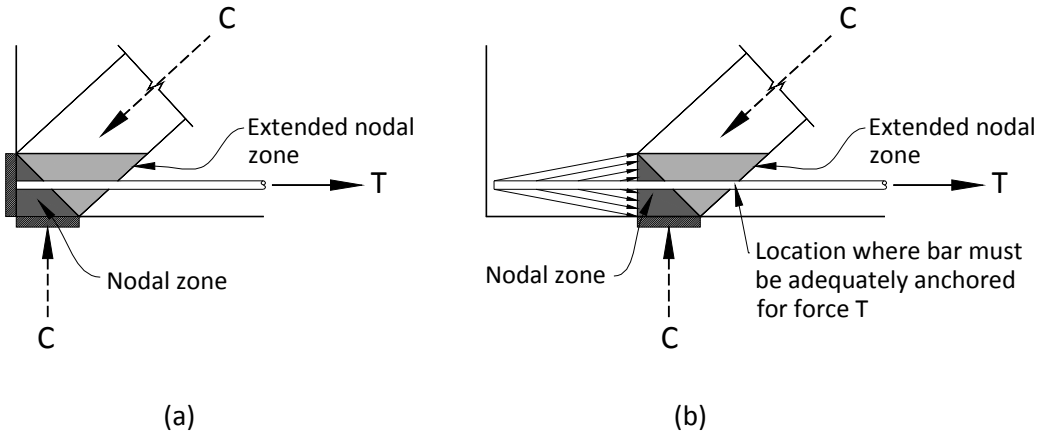

Figure 2-12: CCT nodes (a) tie force is anchored by a bearing plate and (b) tie force anchored by bond with compressive stresses acting on the node (Adapted from Wight and MacGregor 2009).

The use of STMs allows for easy visualization of the flow of forces. In addition, truss models account for shear and moments simultaneously (i.e. they do not require separate flexure and shear models as is the case for slender members).

Since no published STM provisions exist for use with FRP reinforced concrete deep members, STMs used in the analysis of steel reinforced concrete deep members are considered in this study. ACI 318-08 and CSA A23.3-04 have strut and tie modelling provisions for concrete members that have a non-linear strain distribution. For each code, the first step in strut and tie modelling involves the selection of a suitable truss model to transfer the loads to the supports. An example of a truss model for a deep beam under four-point bending is given in Figure 2-13. In design, the selection of an appropriate model typically involves some iteration or trial and error of the truss geometry to ensure that the stresses in all struts, ties, and nodal regions are within the permitted stress limits as defined in the sections below. For use in analysis, an iterative solution technique is typically required to solve the maximum capacity of a given truss model.

While the general procedure for strut and tie modelling is similar in both CSA A23.3-04 and ACI 318-08, the stress limits for the struts differ.

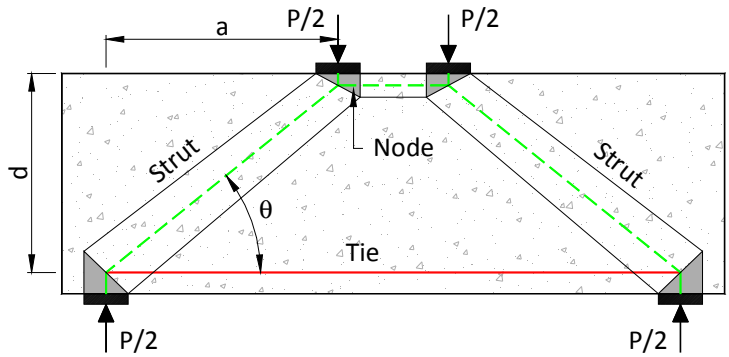

Figure 2-13: Simple truss model for a deep beam under four-point bending.

2.5.3.1 CSA A23.3-04

CSA A23.3-04 requires the use of the STM provisions for regions of members in which the *plane sections remain plane* assumption of beam theory is not applicable. These so-called disturbed regions occur at load or geometric discontinuities. The explanatory notes on CSA A23.3-04 (Cement Association of Canada, 2006) further define disturbed regions as extending by a distance of d from the discontinuity. According to this definition, the beam in Figure 2-13 is considered a deep beam if the a/d ratio is less than 2.0.

The maximum compressive stresses permitted in struts are defined using a MCFT-based approach to consider the influence of cracking caused by coexisting transverse tensile strains (Vecchio and Collins, 1986). Concrete not subjected to principal tension strains greater than 0.002 can resist a compressive stress of $0.85f_c'$ (CSA A23.3-04 explanatory note N11.4.2.3). In regions where reinforcement crosses a strut, the transverse tensile strain, ε_1, is typically much larger and the compressive load carrying capacity is decreased. The limiting compressive stress in a strut crossed by a tension tie is given by:

$$f_{cu} = \frac{f'_c}{0.8 + 170\varepsilon_1} \leq 0.85f_c' \qquad \textbf{2.32}$$

where ε_1 is the transverse tensile strain (Figure 2-14) calculated as:

$$\varepsilon_1 = \varepsilon_s + (\varepsilon_s + 0.002)cot^2\theta \qquad \textbf{2.33}$$

The parameter θ is the angle between the compressive strut and the adjoining tie as shown in Figure 2-13 and ε_s is the tensile strain in the tension tie crossing the strut (Figure 2-14). The CSA A23.3-04 explanatory note N11.4.2.3 states that if the strain in the reinforcement varies over the width of the strut (as would be the case in the bottom

nodes in Figure 2-13), it is appropriate to use the strain at the centerline of the strut in Equation 2.33. Normally in such instances, the strain at the outside edge of the node (location a in Figure 2-14) is assumed to be approximately zero. The strain in the reinforcement where the centroid of the reinforcement leaves the extended nodal zone and enters the span (location c in Figure 2-14) is equal to the full tension tie strain, ε_s. Note that the strain in the reinforcement is assumed constant for the entire span between the lower nodes of Figure 2-13. Therefore, the strain at the center of the strut (location b in Figure 2-14) would be one half of the full strain, ε_s, in the reinforcement at the location where the centroid of the reinforcement leaves the extended nodal zone (location c in Figure 2-14). From Equation 2.32 and 2.33, it is observed that as the tensile reinforcement strain increases or as the strut angle decreases, the compressive load carrying capacity of the strut is reduced.

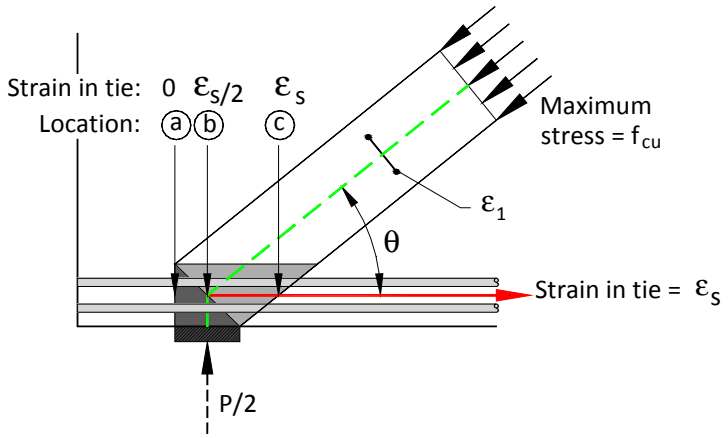

Figure 2-14: Nodal region showing the strain in the strut and tie.

The reinforcement area must be proportioned such that the calculated tensile force in the tie does not exceed $f_y A_s$. The tie must also be suitably anchored either by the appropriate development length, hook, or mechanical anchorage to ensure that the calculated tension in the reinforcement can be resisted at the location where the centroid of the reinforcement crosses the inside edge of the strut (i.e. refer to Figure 2-12(b)).

CSA A23.3-04 also requires that the stresses in the nodal zones not exceed $0.85f_c'$ for CCC nodes (i.e. top nodes in Figure 2-13), $0.75f_c'$ for CCT nodes (i.e. bottom nodes in Figure 2-13), and $0.65f_c'$ for CTT nodes. The reduced stress limits for nodal regions anchoring ties account for the detrimental effect of tensile strains on the compressive strength of concrete.

Crack control reinforcement is required in the form of an orthogonal grid of reinforcing bars near each face of the concrete member. The ratio of the reinforcement area to the

gross concrete area is to be at least 0.002 in each direction and the maximum bar spacing is not to exceed 300 mm. The distributed reinforcement controls the crack widths and spacing to ensure minimum member ductility such that significant redistribution of stresses is possible (CSA A23.3-04 explanatory note N11.4.4.2).

The strut and tie modelling provisions given in CSA S6-06 and AASHTO LRFD (2007) for the disturbed regions of steel reinforcement members are also based on the MCFT formulation and are very similar to the CSA A23.3-04 STM.

Using a database of 214 steel reinforced concrete deep beams containing varying amounts of distributed web reinforcement, Park and Kuchma (2007) reported an average measured to calculated strength ratio of 1.64 with a 35% coefficient of variation. Nehdi et al. (2008) used the CSA A23.3-04 STM to calculate the capacity of 16 FRP reinforced concrete deep beams without transverse reinforcement and reported an average measured to predicted strength ratio of 2.33 with a 16% coefficient of variation. In calculating the capacity of the FRP reinforced concrete deep beams, Nehdi et al. (2008) assumed a strain in the tie of 0.002 for all members and the influence of this assumption will be further discussed in Chapter 5.

2.5.3.2 ACI 318-08

ACI 318-08 defines deep beams as follows:

- Members which can develop direct compression struts between the loads and supports,
- Members with clear spans equal to or less than four times the overall member height, h, or
- Members with concentrated loads within twice the member height, h, from the face of the support.

Such members are to be designed using strut and tie modelling or by taking into account the nonlinear strain distribution. Appendix A of ACI 318-08 further defines disturbed regions based on the St. Venant's principle where the stresses due to axial load and bending approach a linear distribution at a distance h away from the load or geometric discontinuity. Therefore, disturbed regions are assumed to extend h away from the load or geometric discontinuity.

Unlike CSA A23.3-04, ACI 318-08 has a limit of 25 degrees for the minimum angle (θ) between the axis of any strut and tie entering a node. The limit is to avoid incompatibilities due to the shortening of the strut and lengthening of the ties.

The compressive strength of a strut without longitudinal reinforcement is evaluated at each end according to Equation 2.34.

$$F_{ns} = f_{ce}A_{cs} \quad \textbf{2.34}$$

In Equation 2.34, the effective compressive strength of the concrete is given by Equation 2.35.

$$f_{ce} = 0.85\beta_s f_c' \quad \textbf{2.35}$$

$\beta_s = 1.0$ for struts of uniform cross-sectional area over its length, 0.75 for bottle-shaped struts with distributed reinforcement, and 0.6λ for bottle-shaped struts without distributed reinforcement where λ = 1.0 for normal weight concrete.

The spread of the compression force in a bottle-shaped strut can lead to splitting of the concrete parallel to the axis of the strut; therefore, a lower factor is used in Equation 2.35 for bottle-shaped struts compared to prismatic struts. Contrary to the CSA A23.3-04 STM, the ACI 318-08 STM does not require distributed reinforcement if the appropriate β_s factor is used in Equation 2.35. If β_s = 0.75 is used in Equation 2.35, the axis of the strut must be crossed by reinforcement proportioned to resist the tensile forces caused by the spreading of the compression forces. The compression forces are assumed to spread at a slope of 2 longitudinal to 1 transverse to the axis of the strut. Alternatively, if f_c' does not exceed 41 MPa (6000 psi), the reinforcement quantity crossing the strut should satisfy Equation 2.36.

$$\sum \frac{A_{si}}{b_s s_i} \sin \alpha_i \geq 0.003 \quad \textbf{2.36}$$

In Equation 2.36, A_{si} is the area of the transverse reinforcement crossing the strut, b_s is the strut width, s_i is the spacing of the transverse reinforcement, and α_i is the agle between the axis of the strut and the reinforcement crossing the strut.

ACI 318-08 requires that the stresses in the nodal zones not exceed $0.85\beta_n f_c'$ where β_n is 1.0 for CCC nodes, 0.80 for CCT nodes, and 0.60 for CTT nodes. The nodal stresses are calculated using the area of the nodal zone face that is perpendicular to the force acting on the face.

The strength of a tie is not to exceed $f_y A_s$. The axis of the reinforcement in a tie shall coincide with the axis of the tie in the strut and tie model. The tie must also be suitably anchored by an appropriate development length, hook, or mechanical anchorage. The tie force must be developed at the point where the centroid of the reinforcement of the tie leaves the extended nodal zone and enters the span (i.e. refer to Figure 2-12(b)).

Using a database of 214 steel reinforced concrete deep beams containing varying amounts of distributed web reinforcement, Park and Kuchma (2007) reported an average measured to calculated strength ratio of 1.77 with a 32% coefficient of

variation. Nehdi et al. (2008) reported an average measured to calculated strength ratio of 1.05 with a 21% COV for 16 FRP reinforced concrete deep beams containing no transverse reinforcement. The average measured to calculated strength ratio of the eight FRP and two steel reinforced concrete deep beams tested by El-Sayed (2006) was reported to be 0.66 with a 16.7% COV. The STM predictions were greater than the experimental capacity for all specimens including the specimens reinforced with steel. El-Sayed (2006) attributed the poor predictions to the premature splitting failure of the struts due to a lack of distributed web reinforcement.

2.6 Summary

This chapter provided an overview of the shear behaviour of reinforced concrete members containing no web reinforcement. Sectional and deep member behaviour was introduced which has been well documented in many publications. The transition between a deep member and a slender member is generally accepted to occur at an a/d ratio of about 2.5 in steel reinforced concrete members. Slender steel reinforced concrete members are analyzed using sectional flexure and shear models. The CSA A23.3-04 shear model is based on simplified MCFT relationships. Similar sectional models have been developed for FRP reinforced slender members including some sectional shear models that also used simplified MCFT based relationships (Hoult et al. 2008 and CSA S6-06). Razaqpur and Isgor (2006) have proposed a sectional shear model which also accounts for the influence of the a/d ratio.

STMs are one technique used to model members having small a/d ratios. STM provisions have been incorporated into several of the design codes for steel reinforced concrete construction (i.e. CSA A23.3-04, CSA S6-06, ACI 318-08, AASHTO LRFD 2007). Currently, the use of STMs has not been extended to FRP reinforced deep beams. In fact, very little research has been conducted on the behaviour and analysis of FRP reinforced concrete deep beams.

The FRP reinforced deep beams from Nehdi et al. (2008) and El-Sayed (2006) are further considered in Chapter 5 where the shear capacity of these beams and new test data developed in this study are used to validate modelling approaches for FRP reinforced concrete deep beams.

3 Experimental Program

3.1 Introduction

An extensive experimental program was developed to investigate the shear capacity of fibre reinforced polymer (FRP) reinforced concrete deep members. The primary objective of the laboratory test program was to determine whether arch action forms in FRP reinforced deep beams. The new test data was used with other published results to develop and validate modelling techniques for such members in Chapter 5.

The specimen configurations in this study were selected to encompass a wide spectrum of design variables. The primary variables included the height, h, shear span-to-depth (a/d) ratio, reinforcement ratio, ρ, and concrete compressive strength, f_c'. To study the concrete contribution to the shear capacity, no transverse or distributed web reinforcement was included in the specimens. The longitudinal reinforcement consisted of glass FRP (GFRP) since GFRP is the most common type of FRP reinforcement used in the construction of concrete members. In addition, GFRP has a lower modulus of elasticity than carbon FRP which was expected to result in higher longitudinal strains in the reinforcement at failure when all other variables are kept constant. Large longitudinal strain levels were required to validate the shear models past the strain values generally used in steel reinforced deep beam design.

A total of 12 large-scale tests were conducted in the I. F. Morrison Structural Engineering Laboratory at the University of Alberta. This chapter contains information on the design, fabrication, and testing of the specimens. Details on the configuration of the specimens and the material properties of the GFRP and the concrete are also included. Additional information on the GFRP and concrete properties are contained in Appendices A and B, respectively. Detailed information on the instrumentation of the deep beam specimens is given in Appendix C.

3.2 Design and Configuration of the Specimens

The specimens were designed such that the a/d ratios would cover a wide range of the deep beam category. The a/d ratios of approximately 1.1, 1.5, and 2.1 were also chosen to fill gaps in the limited experimental data available on FRP reinforced concrete deep beams (i.e. El-Sayed 2006, and Nehdi et al. 2008). The specimens having a/d ratios of 2.1 are close to the value of 2.5 where the sectional capacity models are generally assumed to be valid. Varying the a/d ratio changes the strut inclination angle, θ, which is a variable affecting the maximum allowable diagonal strut stress in the CSA A23.3-04 strut and tie model (STM). Decreasing the strut angle will also increase the strain in the FRP reinforcement if all other variables are held constant. In the CSA A23.3-04 STM, the reinforcement strain will affect the maximum allowable stress in the diagonal strut.

Therefore, utilizing a wide range of specimen a/d ratios enabled the thorough investigation of the strain and angle parameters in the CSA A23.3-04 STM.

Three series of specimens were designed having nominal heights, h, of 300, 600, and 1000 mm respectively to determine the influence of size on the shear capacity. The nominal width, b_w, of all specimens was 300 mm. All of the specimens were designed to fail by crushing of the diagonal struts. The specimen configurations are shown in Figure 3-1.

The specimens were identified by three characters. The first character A, B, or C refers to the overall specimen height: h = 300, 600, and 1000 mm, respectively. The second character is a number which increments from 1 for each set of specimen sizes. The last character, N or H, indicates whether the concrete is normal or high strength respectively.

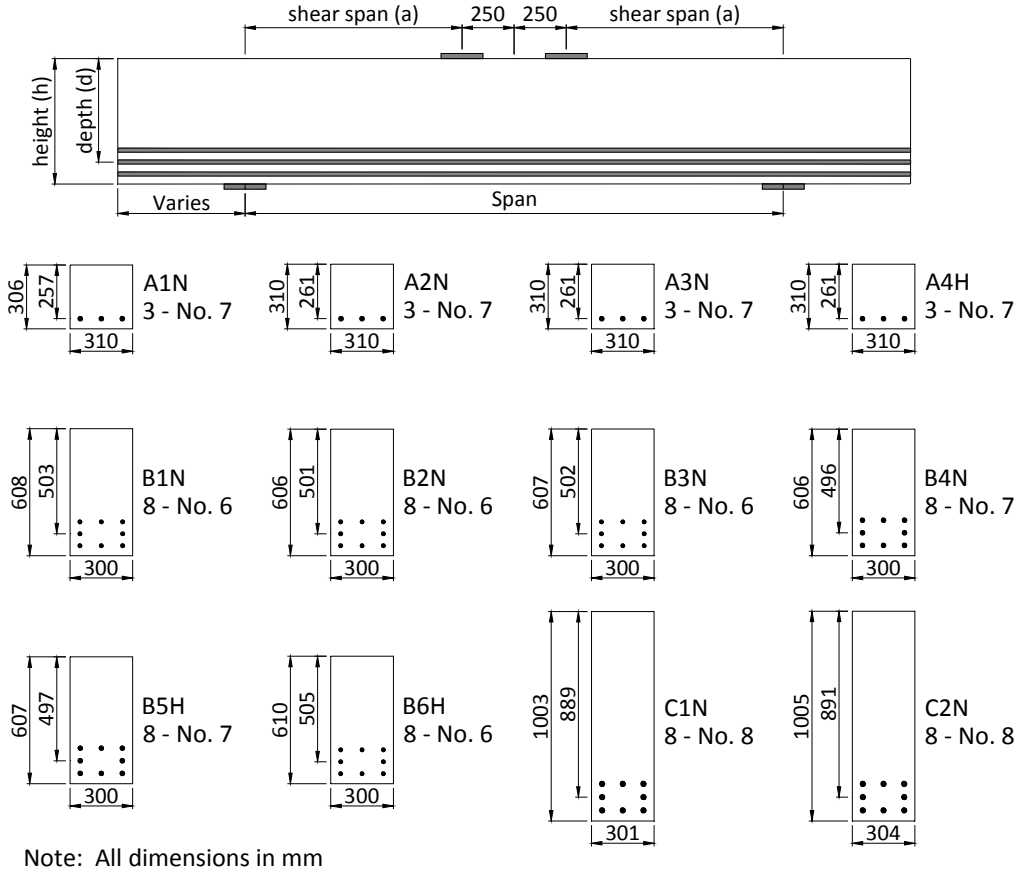

Note: All dimensions in mm
38 mm clear cover and 38 mm clear spacing between layers of reinforcement.

Figure 3-1: Specimen geometry.

A four-point bending configuration was chosen. With four-point bending, a constant moment region is present between the two loading plates which allows for the development of a well defined flexural compression zone as shown in Figure 3-2(a).

With a single point load, the top nodal zone where the load is applied and maximum flexural compression occurs at the same location as shown in Figure 3-2(b) making it difficult to determine the type of failure (i.e. bearing or flexural compression failure). The distance between the centerline of the loading plates was set to 500 mm for all specimens for ease of test setup.

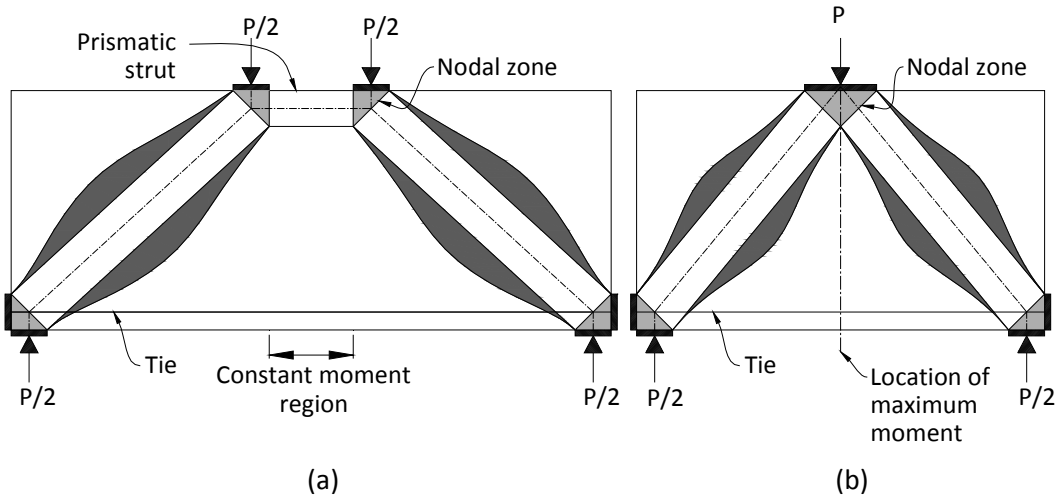

Figure 3-2: Four (a) and three (b) point bending configuration showing the location of the maximum moment.

Preliminary designs were developed using the CSA A23.3-04 STM (section 2.5.3.1) for steel reinforced concrete deep members with simple modifications to account for the mechanical properties of the GFRP reinforcement. In the strut and tie modelling of steel reinforced concrete members, the strain in the tie is assumed to be equal to the yield strain of the steel. The linear elastic nature of the FRP must be taken into account since both the strain and force in the FRP tension tie increase as the applied load increases. Therefore, an iterative approach is required to solve for the two unknowns: the failure load and corresponding strain in the tie. During each iteration the strain in the FRP was recalculated based on the applied load. The desired mode of failure with the STM was strut crushing although it was recognized that a lack of distributed web reinforcement may lead to a strut splitting failure. Therefore, the plate sizes and reinforcement ratio, ρ, were selected to prevent nodal and flexural failures. In addition, the reinforcement was selected such that under equivalent serviceability limit state loads the stress level in the FRP would not exceed the serviceability requirements given in CSA S6-06 clause 16.8.3. Under service load, the stress in the GFRP must not exceed 25% of the specified tensile strength of the GFRP bar. For each specimen, the equivalent service load was back-calculated from the predicted *factored* resistance by assuming a dead to live load ratio of 1.0 and load factors of 1.25 and 1.5 for dead and live load respectively. Note that all other design calculations were based on *nominal* strength predictions (i.e. all resistance factors were set to 1.0).

The plate lengths, L_b, where length refers to the plate dimension in the same direction as the span, were scaled linear proportional to the specimen height, h. A plate having length of L_b = 200 mm was chosen for specimens with h = 600 mm. For the h = 300 mm specimens, the plate length was reduced to L_b = 100 mm and for the h = 1000 mm specimens, the plate length was scaled to L_b = 330 mm. In all instances, the plate width was the same or greater than the beam width, b_w.

Since the validity of applying the STM to FRP reinforced deep beams was a hypothesis, the flexural capacity of each specimen was also calculated using a strain compatibility approach (Collins and Mitchell 1997). To prevent flexural failure, the specimens were designed such that the flexural capacity was at least 30% higher than the capacity prediction from the preliminary STM which predicted strut crushing.

To study the effect of concrete strength on the shear capacity, both normal and high strength concretes were used. The nominal strength (f_c') of these concretes were assumed as 35 and 70 MPa, respectively, during specimen design.

To determine the influence on capacity from the parameters a/d, ρ, h, and f_c', the specimens were designed such that at least two specimens had all variables approximately constant except for the one being studied. To determine the influence of size on the shear capacity, the a/d ratio, ρ, and f_c' were held approximately constant while h and L_b were varied. Note that the reinforcement configurations (size of bars, spacing, cover, and number of layers) were not scaled. The reinforcement ratio could not be held completely constant due to the practical bar sizes available. The relationships between the specimens are shown in Figure 3-3.

The final reinforcement configuration and as-built cross-sectional dimensions of the twelve specimens are shown in Figure 3-1. Table 3-1 shows additional as-built dimensions. The unconventional reinforcement layout where only two bars were present in the middle layer of specimens with h = 600 mm and 1000 mm resulted from design modifications completed after the material properties of the supplied GFRP bars were determined from testing. The bars had larger cross-sectional areas than originally specified on the manufacturer's datasheet. Therefore, the center bar was omitted to produce specimens that had similar characteristics as the original design, which had been based on FRP cross-sectional areas from the manufacturer's datasheet.

Overhangs of varying lengths were provided beyond both supports in all specimens to allow for adequate anchorage of the GFRP. The bars were extended approximately a development length past the centerline of the support plate. The development length was calculated according to CSA S6-06. Side and bottom clear cover was set to 38 mm. Vertical bar clear spacing was also 38 mm.

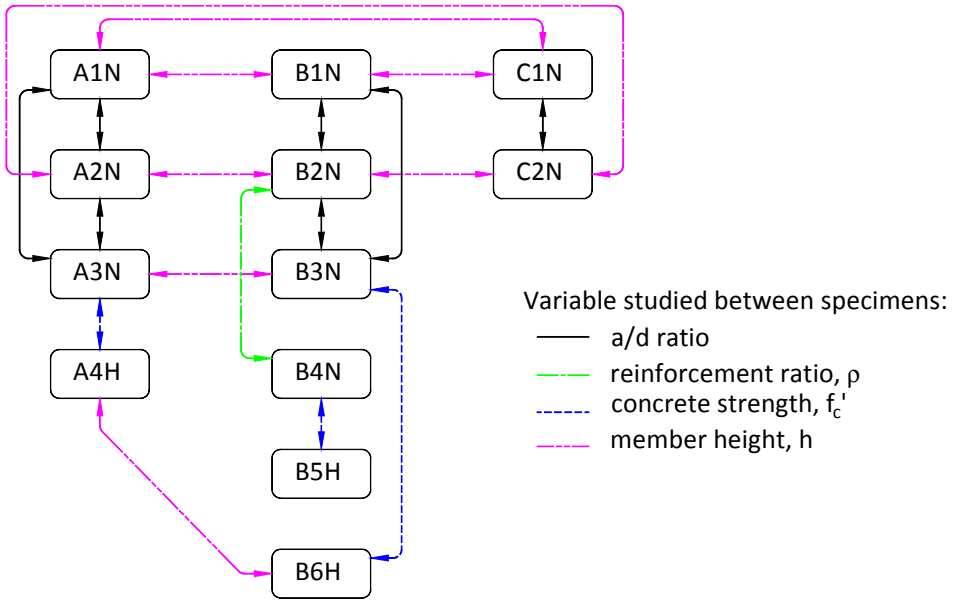

Figure 3-3: Relationship between the specimens.

Table 3-1: As-built specimen properties.

Specimen	a/d	ρ (%)	height, h (mm)	effective depth, d (mm)	shear span, a (mm)	span length, center of supports (mm)	width, b_w (mm)	plate length, L_b (mm)
A1N	1.07	1.49	306	257	276	1052	310	100
A2N	1.44	1.47	310	261	376	1252	310	100
A3N	2.02	1.47	310	261	527	1553	310	100
A4H	2.02	1.47	310	261	527	1553	310	100
B1N	1.08	1.70	608	503	545	1590	300	200
B2N	1.48	1.71	606	501	743	1986	300	200
B3N	2.07	1.71	607	502	1040	2580	300	200
B4N	1.48	2.13	606	496	736	1971	300	200
B5H	1.48	2.12	607	497	736	1971	300	200
B6H	2.06	1.70	610	505	1040	2580	300	200
C1N	1.10	1.58	1003	889	974	2448	301	330
C2N	1.49	1.56	1005	891	1329	3157	304	330

3.3 Fabrication of Test Specimens

Three sets of formwork were used to cast the specimens. A single 300 mm (Figure 3-4) high steel formwork consisting of three channel sections was used along with taller wooden forms. The 600 mm high formwork allowed two specimens to be cast next to each other. This form was made of 19 mm thick plywood with a built-up steel angle on

the outside to provide rigidity. The 600 mm high forms shown in Figure 3-4 were used three times to produce six specimens. Subsequently, the 600 mm high forms were converted to 1000 mm high forms (Figure 3-5) and two specimens were cast simultaneously in this form. In total there were four concrete casts and for each cast, three specimens were prepared, one specimen in the 300 mm form and two specimens in the taller double forms.

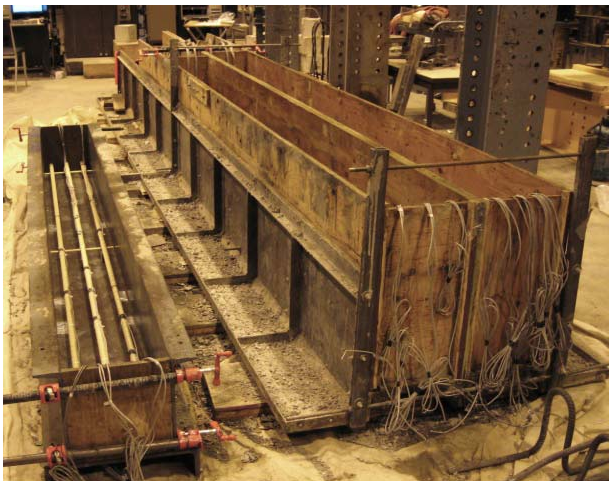

Figure 3-4: Formwork for h = 300 mm (left) and h = 600 mm (right) specimens.

Figure 3-5: Formwork for h = 1000 mm specimens.

Since no stirrups were included in the specimens, the fabrication of the rebar cages required the use of small GFRP framing bars near the ends of the specimens and at mid-span. The framing bars in the specimens with h = 600 mm and 1000 mm consisted of two short vertical bars to carry three transverse horizontal bars which supported the longitudinal bars as shown in Figure 3-6(a). For the specimens with h = 300 mm, only transverse horizontal framing bars were provided (Figure 3-6(b)). The framing bars were placed approximately 200 mm from the specimen ends; well away from the locations of

the supports to prevent the bars from disrupting the force flow in the direct struts and nodal regions. The bars were tied together using plastic ties and plastic chairs were placed along the bar length to obtain proper clear cover. In addition, chairs were used as vertical spacers between the layers of longitudinal bars. The horizontal framing bars had the same width as the formwork to prevent the reinforcement from moving laterally while casting. The longitudinal bars were also tied to the form with thin wire at mid-span and both ends to prevent floatation of the bars. No clear cover was provided at the ends of the specimens. The ends of the forms made contact with the reinforcement to facilitate in the tying down and positioning of the reinforcement. Steel lifting hooks were placed near the ends of the specimens such that in all cases the steel hooks were beyond the support location to ensure no interference in the internal load transfer mechanism during testing.

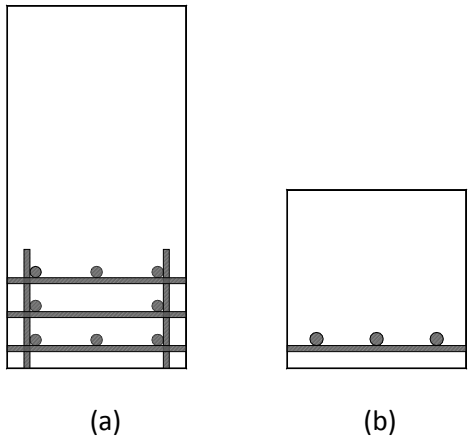

Figure 3-6: Cross-section showing the support bars for the longitudinal bars (a) h = 600 and 1000 mm and (b) h = 300 mm.

Three specimens were cast simultaneously from the same batch of concrete. Table 3-2 lists the specimens that were cast from the same batch of concrete. The concrete was placed in layers and was internally vibrated. Each set of specimens was finished by hand floating (Figure 3-7) and moist cured under plastic for seven days. After removal from the forms, the specimens were stored in the laboratory until the day of testing. With the exception of specimens B5H, B6H, C1N, and C2N, all the specimens were removed from the forms between 7 and 14 days. The four aforementioned specimens were stored in the forms for approximately 30 days due to space constraints.

Table 3-2: List of specimens cast from each concrete batch.

Batch No. 1	Batch No. 2	Batch No. 3	Batch No. 4
B3N	B1N	B5H	C1N
B4N	B2N	B6H	C2N
A3N	A1N	A4H	A2N

Figure 3-7: Finishing a set of specimens.

3.4 Material Properties

3.4.1 Glass FRP Reinforcement

The GFRP bars were manufactured by BP Composites Ltd. The bars contained surface deformations from wrapping groups of fibres diagonally in opposite directions to form a diamond shape on top of the main longitudinal core as shown in Figure 3-8. The bars were also sand coated although this coating was not uniform in all cases. Some bars had sides which were heavily sand coated while the opposite side had very little sand coating as can be seen with the top bar in Figure 3-8.

Figure 3-8: GFRP bars, No. 8 at the top and two No. 7.

GFRP bars having three different nominal diameters were required for the longitudinal reinforcement in the concrete specimens. Five tension coupons for each nominal bar diameter were tested to determine the failure stress and modulus of elasticity. The cross-sectional area of the different nominal bar sizes were determined using volumetric measurements. Additional information on the GFRP material testing procedures and results are provided in Appendix A. Table 3-3 summarizes the measured properties of

the GFRP bars. The properties listed in Table 3-3 were used in the analysis of the concrete test specimens in Chapter 5.

Table 3-3: Properties of the glass FRP bars.

Bar Size (U.S. Customary Sizes)	Nominal Diameter (mm)	Glass Content (% vol)*	Area (mm^2)	Failure Stress (MPa)	Modulus of Elasticity (MPa)
No. 6	19	72.0	322	765	37900
No. 7	22	64.8	396	709	41100
No. 8	25	64.1	528	938	42300

* provided by the manufacturer

3.4.2 Concrete

Two types of concrete were required. A normal strength concrete with specified nominal strength of 35 MPa at 28 days and a high strength concrete with specified nominal strength of 70 MPa at 28 days were delivered by ready-mix trucks. The maximum aggregate size in both mixes was 14 mm. During each concrete cast, 18 - 100 mm x 200 mm concrete cylinders were created for quality control purposes and for determining the compression strength on the day of the specimen tests. Three 150 x 150 x 500 mm prisms were also cast.

The quality control cylinders and prisms were removed from the moulds 24 hours after casting and cured in a moist curing facility until testing. The quality control tests consisted of testing cylinders at 7, 14, 21, and 28 days to observe the strength gain and to determine the 28 day concrete strength as is commonly done in industry. In addition, the three 150 x 150 x 500 mm prisms were also tested at 28 days in a four-point bending configuration (third point configuration, CSA A23.2-04) to determine the modulus of rupture. The testing of the quality control cylinders and prisms is shown in Figure 3-9.

Figure 3-9: Quality control testing of a cylinder (left) and a modulus of rupture test.

Three cylinders were used to determine the concrete strength of each deep beam specimen on the day of test (i.e. 9 cylinders total per cast). These cylinders were cured in the same location and under the same conditions as the beam specimens. The three cylinders were tested on or the day after the beam specimen was tested by using a MTS 2600 loading frame and a strain yoke equipped with three LVDTs (Figure 3-10) to allow the determination of the stress-strain response.

The strength of the concrete at 28 days and at the time of the deep beam specimen tests is given in Table 3-4. The age of the concrete at the time of the deep beam specimen test is given in the last column of Table 3-4. Additional information on concrete testing procedures and results are provided in Appendix B. The concrete strengths from the specimen cured cylinders (i.e. third column in Table 3-4) were used in subsequent calculations (Chapters 4 and 5).

Figure 3-10: Cylinder test with a strain yoke to determine the stress-strain response.

Table 3-4: Concrete properties.

Beam	f_c (28 days, moist cured [MPa])	**f_c'(strength of deep beam specimens [MPa])**	Age at testing (days)
A1N	41.1	**40.2**	171
A2N	41.9	**45.4**	36
A3N	37.1	**41.3**	173
A4H	64.2	**64.6**	160
B1N	41.1	**40.5**	129
B2N	41.1	**39.9**	108
B3N	37.1	**41.2**	105
B4N	37.1	**40.7**	111
B5H	64.2	**66.4**	96
B6H	64.2	**68.5**	106
C1N	41.9	**51.6**	104
C2N	41.9	**50.7**	97

3.5 Test Setup

The specimens were tested in a MTS testing frame having a load capacity of 6600 kN in compression. A stiff loading beam was used to apply two equal point loads on the specimen. Each specimen was supported on roller assemblies and knife edges to allow longitudinal motion and rotation. Both loading points also contained rollers and knife edges. The specimens were tested with all four roller assemblies free to rotate. At high loads, some of the specimens would gradually roll to one side. To prevent this, one roller assembly would be locked to avoid further movement. Bearing plates were 100 x 310 x 38 mm and 200 x 300 x 50 mm for the h = 300 and 600 mm specimens, respectively. For specimens with h = 1000 mm, load and reaction plates were 330 x 330 x 38 mm and 330 x 330 x 75 mm, respectively. A thin layer of plaster was used between the specimen and the bearing plates to ensure uniform contact. The test setup is shown in Figure 3-11.

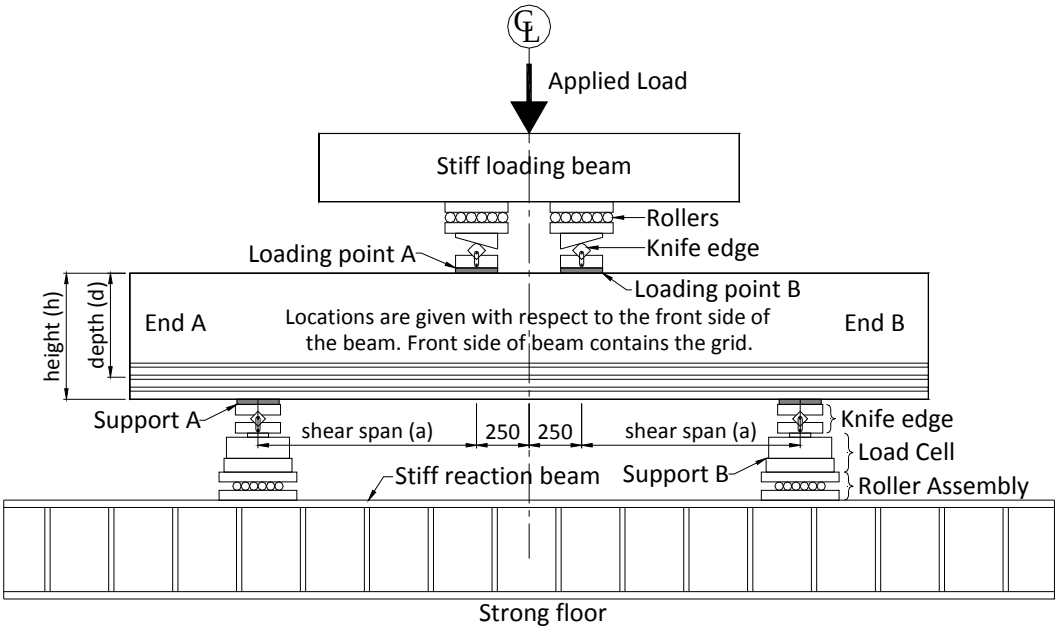

Figure 3-11: Test configuration.

Prior to testing, each of the specimens was painted on both sides with a thin coat of white latex paint to facilitate the observation of cracking during testing. A square orthogonal grid, shown in Figure 3-12, was drawn on the front (south) face of the specimen as a reference.

The specimen orientation as shown in Figure 3-11 was used throughout this document. The front side of the specimen contained the square grid markings while the back surface was speckled with black paint for strain measurement with a DIC system (section 3.6.5). End A is the left end (west) of the specimen when facing the front side of the specimen and end B is on the right end (east). The supports, loading points, and shear

spans are referenced with respect to end A or end B depending on which side of the specimen centerline they are located (Figure 3-11).

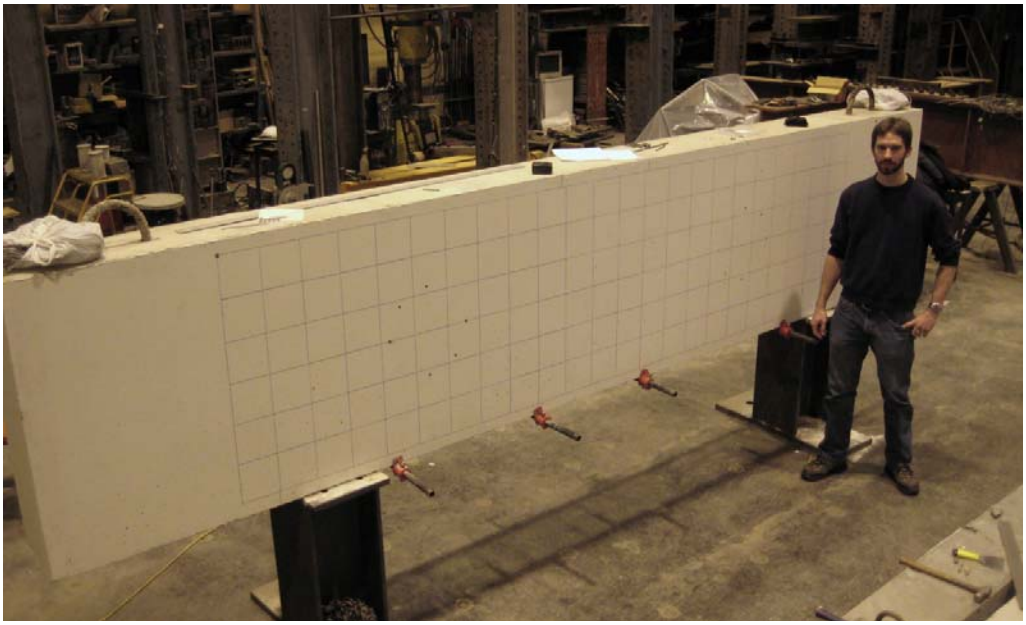

Figure 3-12: Painted specimen (h = 1000 mm) with the grid drawn on the front surface.

3.6 Instrumentation

3.6.1 Strain Gauges

Electrical resistance strain gauges were applied to the FRP bars to measure the strain during the tests. Between 12 and 28 strain gauges were applied for each specimen. In general, strain gauges were applied to the bars at the center of the supports and loading points, mid-span, and at a uniform spacing in the shear spans. The majority of the strain gauges were applied on the bottom bars except at the location of the supports, loading points, and mid-span where strain gauges were applied on all layers. The strain gauges were used to observe whether a tied arch mechanism had formed during the test. The strain in the GFRP bars at the supports was of interest as this is the location where the tie crosses the strut. The diagonal strut capacity when using the CSA A23.3-04 STM is dependent on the strain in the tie at the center of the strut.

The strain gauges had an electrical resistance of 120 ohms and were manufactured by Kyowa Electronic Instruments Co. Ltd. These 5 mm gauge length strain gauges were of type KFG-5-120-C1-11. The sand was removed from the GFRP bars with an electric rotary tool fitted with an abrasive point. Care was taken not to damage the bar although some resin was removed along with the sand. Subsequently, the area was prepared using 400 grit sandpaper and cleaned with a conditioner and neutralizer. The strain gauge was glued to the bar using M-Bond 200 adhesive. A waterproofing coating was

applied to protect the strain gauge against damage. Appendix C contains additional information on the strain gauges and the locations.

3.6.2 External Instrumentation

The external instrumentation is shown schematically in Figure 3-13. Figure 3-14 shows the instrumentation on specimen B1N which is typical of most specimens. Detailed instrumentation for each specimen is given in Appendix C. A series of five linear variable differential transformers (LVDT) were mounted along the bottom of the specimens to measure vertical deflection at the supports, quarter-span and mid-span. Deflection was measured at the supports to take into account the global vertical movement of the specimen caused by the compression of the roller assembly, load cell, and knife edge assembly. A horizontal LVDT was mounted near the bottom of end face A to measure global longitudinal movements.

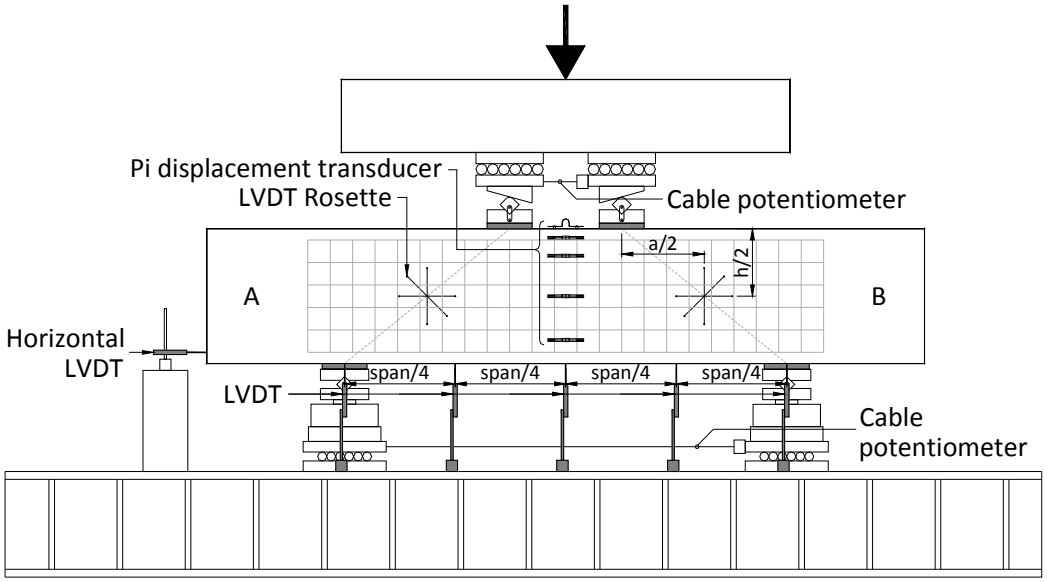

Figure 3-13: Location of the instrumentation.

A cable potentiometer was installed between the support assemblies to monitor the expansion of the overall span. Similarly, another cable potentiometer was installed between the two loading points to measure the relative movement.

A 45° LVDT rosette was installed at mid-height in each shear span centered on a line drawn from the centerlines of the loading and support plates to measure the average strains in the diagonal struts. Three LVDTs were used at each location as shown in Figure 3-13. The LVDTs were attached by drilling 20 mm deep holes into the concrete and installing 6.4 mm threaded rods using epoxy.

Electronic PI displacement transducers were installed at the center of the specimen in the constant moment region. In the first two specimens tested (B3N and B4N), only two

PI gauges were installed and in latter specimens, up to five PI gauges were used (B1N, B2N, B6N, C1N, and C2N). Typically there was a PI gauge installed on the top surface of the specimen between the loading plates and the remaining PI gauges were installed on the front face at mid-span with two near the top, one at mid-height, and one at the centroid location of the reinforcement. The PI gauges had 100 mm gauge lengths and were screw mounted to the fixing jig which was attached to the concrete with epoxy. Figure 3-15 shows the upper three PI gauges installed on specimen B2N. Although the PI gauge data was collected, it was not reported in this document as the analysis methods investigated in this study did not require the use of this data.

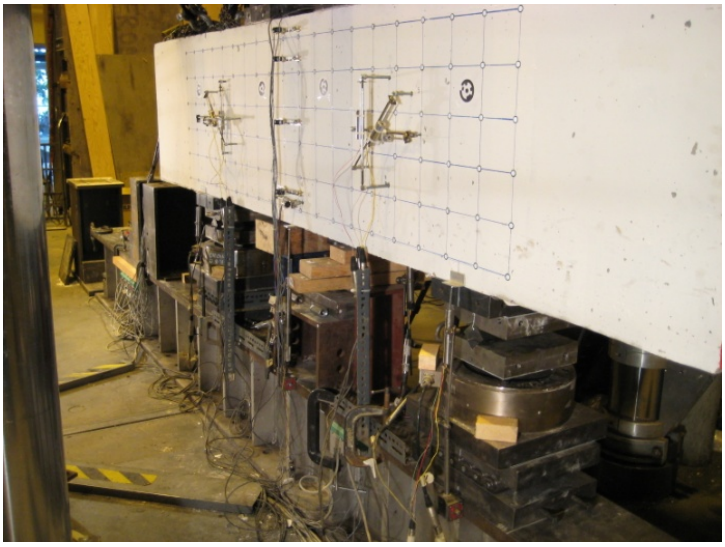

Figure 3-14: External sensors on specimen B1N.

Figure 3-15: Three PI gauges installed at mid-span of specimen B2N.

In addition to the built-in load cell on the MTS 6000 test frame, a 1338 kN load cell was used at each support as shown in Figure 3-11. The two load cells measured the applied

MTS load plus the self-weight of the specimen and loading assembly. These load cells were used to confirm that proper and symmetrical loading was taking place during the test. However, the two support load cells were omitted from the test setup for specimens C1N and C2N for two reasons: the predicted load for specimen C1N was in excess of the load cell capacity and the test setup would have been increasingly unstable if the load cells had been included.

3.6.3 Data Acquisition

Data from the instrumentation was captured using two data acquisition systems. The strain gauges, load cells, PI gauges, rosette LVDTs and the center deflection LVDT were connected to a HBM MGCplus data acquisition system. The measurement software was Catman Professional 6.0. The remaining deflection LVDTs, horizontal LVDT, and cable potentiometers were connected to a National Instrument system and LabVeiw 2009 was used as the measurement software. Data was collected every 5 seconds for the duration of the test.

3.6.4 Photogrammetry

Prior to testing the specimens, retro-reflective targets, 2FR-1410 manufactured by WNBC in LA Inc, were adhered to the front surface of the specimens. The targets were placed at the intersection of the gridlines that were marked on the front surface of the specimens (Figure 3-16). Coded targets were applied at four locations near the mid-height of the specimen at the support and loading locations (Figure 3-16). Each coded target was unique and used to automatically reference the same location in different images.

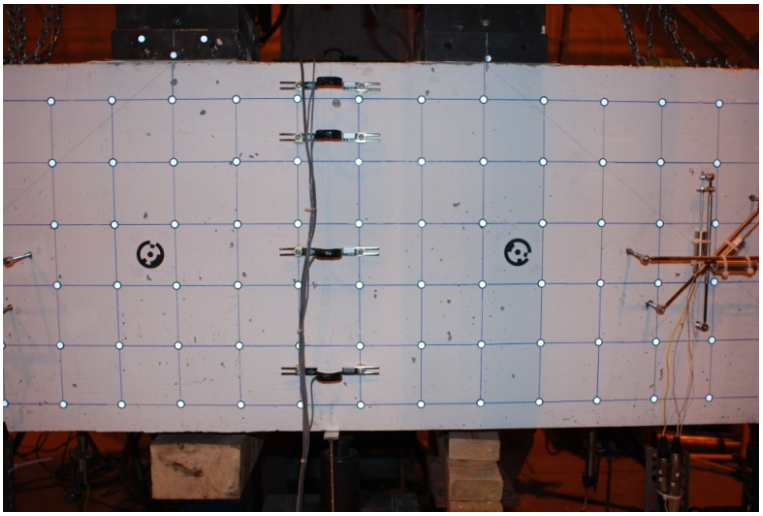

Figure 3-16: Photogrammetry photograph of specimen B2N with retro-reflective targets at the intersection of the gridlines and two larger coded targets.

A DSLR camera having a fixed focal length was used to take approximately 30 pictures of the specimen from different locations and angles prior to loading and after each load increment.

The photogrammetry results are not discussed in this document as this project did not have time allocated for the processing and analyzing of the images.

3.6.5 Optical Strain Measuring System

A three dimensional optical strain measuring system from Correlated Solutions Inc., based on the digital image correlation (DIC) technique was used to measure the strain fields on the back surface of the specimens. Three camera pairs were set up for each specimen. The areas of interest were the two shear spans and the constant moment region. The surface of each specimen was speckled with black paint using an air spray gun to produce small circular black dots covering approximately 50% of the specimen's surface as seen in Figure 3-17. This enabled the optical system to track the gray value pattern in subsets during successive frames as the test progressed and to calculate the strain fields. The system took images every 15 seconds during loading of the specimen. Reference lines were drawn on the back surface of the specimen to assist in the analysis of the strain maps. The majority of the results from the DIC system have not been included in this document due to the time required to analyze and interpret the results.

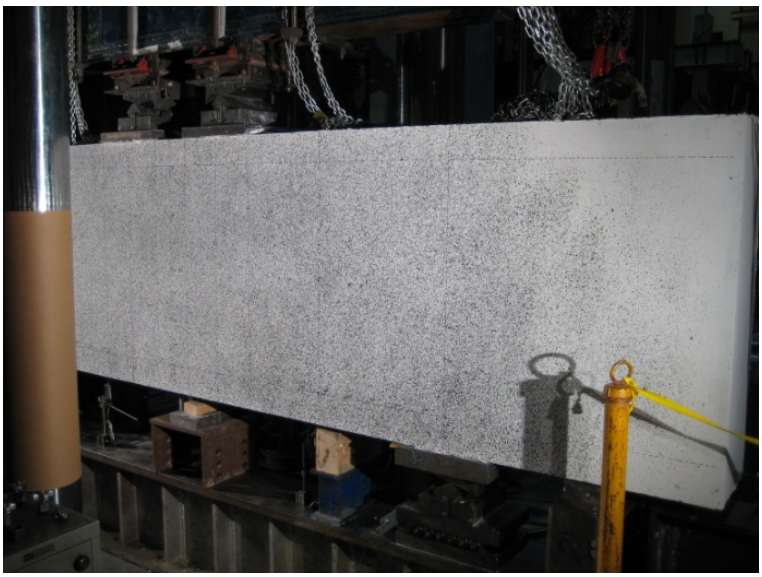

Figure 3-17: Black speckling on the back surface of a beam (h = 1000 mm) for use with the DIC system.

Two types of Fujinon CCTV lenses, HF12.5SA-1 and HF35SA-1, were used depending on the size of the area of interest. The 5.0 megapixel cameras, model GRAS-50S5M/C from Point Grey Research, had a maximum resolution of 2448 (vertical) x 2048 (horizontal) pixels.

3.7 Test Procedure

The specimens were tested in displacement control. A displacement rate of 0.1 to 0.25 mm per minute of machine stroke was used depending on the stiffness of the specimen. Each specimen was loaded in 5-10 increments. After each increment, the deflection was held while manual observations were made. Cracks were marked and their width measured using a crack comparator gauge. Photographs were taken at each load increment to document the crack propagation and crack widths.

Prior to the start of loading, all strain and displacement readings on the data acquisition systems were set to zero. Data was recorded for the entire duration of the test including while loading was paused for manual observations. Duration of the tests ranged between 3-6 hours.

4 Test Results

4.1 General

All twelve specimens were loaded to failure in displacement control, which allowed for the observation of the post peak behaviour. The majority of the specimens failed suddenly with no warning and a significant drop in load occurred. These tests were stopped after the sudden drop in force resistance. Specimens A1N and B1N did not experience a sudden drop in load. The load carrying ability of these two specimens decreased gradually and the tests were halted once the load dropped by approximately 15% and 10% of the peak load, respectively. At approximately 90% of the peak load, specimens A1N and B1N had deteriorated to such an extent that continued loading was unsafe.

A summary of the key experimental results for the specimens is given in Table 4-1. The applied load (P) is the applied load measured by the load cell in the MTS 6000 load frame plus the self-weight of the loading apparatus (i.e. loading beam, loading plates, rollers, and knife edge assembly). The self-weight of the specimen is not included in P. Since the specimens were tested using two point loads where each point load was $P/2$, the peak shear capacity of the specimen is $P_{max}/2$.

Table 4-1: Experimental results.

				Ultimate Load				Equivalent Service Load		
Specimen	a/d ratio	ρ (%)	f_c' (MPa)	Failure Type[1]	Failure End	P_{max} (kN)	Δ_{max} (mm)[2]	P_s (kN)	Δ_s (mm)	f_{FRPs}/f_{FRPu} (%)[3]
A1N	1.07	1.5	40.2	FC	-	814	12.4	407	4.0	37
A2N	1.44	1.5	45.4	SC	A	471	11.3	235	3.7	22
A3N	2.02	1.5	41.3	SC	A	243	10.9	121	2.6	14
A4H	2.02	1.5	64.6	DT	B	192	9.5	96	0.9	5
B1N	1.08	1.7	40.5	FC	-	1273	9.1	637	3.5	25
B2N	1.48	1.7	39.9	SC	A	799	13.1	400	4.6	16
B3N	2.07	1.7	41.2	SC	A	431	15.3	215	2.7	14
B4N	1.48	2.1	40.7	SC	B	830	11.5	415	3.4	21
B5H	1.48	2.1	66.4	S	B	1062	14.2	531	5.1	21
B6H	2.06	1.7	68.5	DT	A	376	12.9	188	1.3	4
C1N	1.10	1.6	51.6	SC	B	2269	15.9	1135	6.1	22
C2N	1.49	1.6	50.7	S	A	1324	18.3	662	6.7	15

[1]DT – diagonal concrete tension failure, FC – flexural compression failure, SC – shear compression failure, S – compression strut failure. [2]Mid-span deflection occurring at the peak load. [3]Stress level in the bottom layer of GFRP reinforcement as a percentage of the GFRP tensile capacity.

The loads from the load cells at the supports are not reported here but the values were compared against the MTS load cell and were in good agreement. Similar load values were observed from each support load cell indicating that the specimens were loaded symmetrically. Near the end of the tests, the load difference between the two support reactions was less than 3%.

For each specimen, the mid-span deflection (Δ_{max}) at the time of maximum load (P_{max}) is reported in Table 4-1. The deflection values were adjusted to account for average support settlement.

Equivalent service loads were calculated using the basic limit state equation, $\phi R \geq \alpha_n S_n$ where ϕ is the resistance factor, R is the nominal resistance of a structural element, α_n is the load factor, and S_n is the load effect under specified loads. The nominal resistance was assumed to be equal to the experimental capacity. The equivalent service loads were calculated by assuming a 3:1 dead to live load ratio. Load factors of 1.25 and 1.5 were assumed for the dead and live load, respectively, consistent with CSA A23.3-04. Since all specimens experienced concrete failure as opposed to reinforcement failure, the concrete resistance factor, ϕ_c = 0.65, was used (CSA A23.3-04). Therefore, the equivalent service load, P_s, corresponded to 50% of the peak load, P_{max}, and is reported in Table 4-1 along with the corresponding measured mid-span deflection, Δ_s. The service load mid-span deflection was also adjusted for vertical support movement.

The stress in the GFRP at the service load is an important factor in the design of FRP reinforced members and must be kept below $0.25 f_{FRPu}$ (CSA S6-06) to prevent creep rupture of the reinforcement. The stress level in the GFRP at the service load was between 4% and 37% of the GFRP tensile capacity, f_{FRPu}, with only specimen A1N exceeding the $0.25 f_{FRPu}$ limit.

4.2 Failure Mechanisms

Amongst the specimens, four types of failure mechanism were observed. The failure mechanism for each specimen is given in Table 4-1. Shear compression was the most common failure mode, occurring in six of the specimens. Shear compression failure was characterized by the crushing of the concrete in the flexural compression zone at the tip of the main diagonal crack. The main diagonal crack extended from the inside edge of the support plate towards the inside edge of the loading plate, into the flexural compression zone. At failure, the crack penetrated through the top of the specimen. The specimens would fail suddenly with almost no warning and movement would occur along the diagonal crack. Figure 4-1 shows a typical shear compression failure.

Flexural compression failures occurred in specimens A1N and B1N. This type of failure was characterized by the crushing of the concrete in the flexural compression zone between the two loading plates as shown in Figure 4-2. At failure, there was also

movement along the main diagonal cracks; however, this sliding action along the main diagonal cracks occurred after deterioration of the compression zone. The main diagonal cracks in each shear span propagated from the inside edge of the reaction plates towards the inside edge of the loading plates. Near the loading plates, the cracks became horizontal and eventually joined. The region above the horizontal crack between the loading plates would then slowly deteriorate through crushing of the concrete.

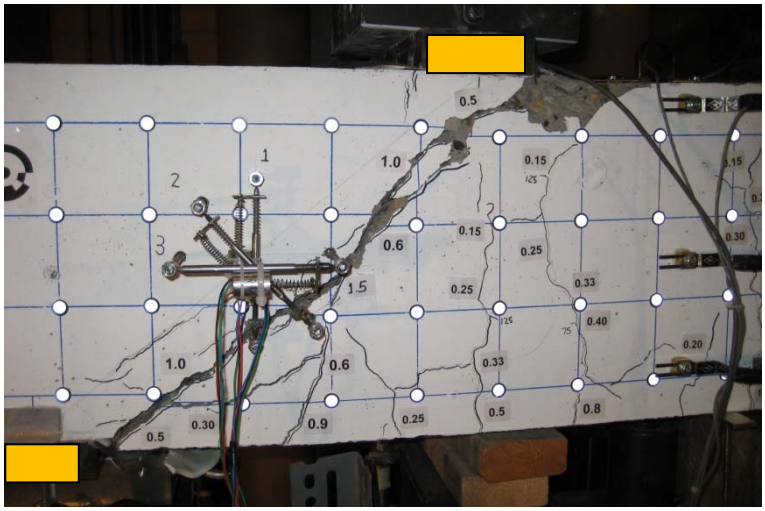

Figure 4-1: Shear compression failure in specimen A2N. Only shear span A is shown and the center of the beam is at the right edge of the image. Loading and reaction plates are shown in yellow.

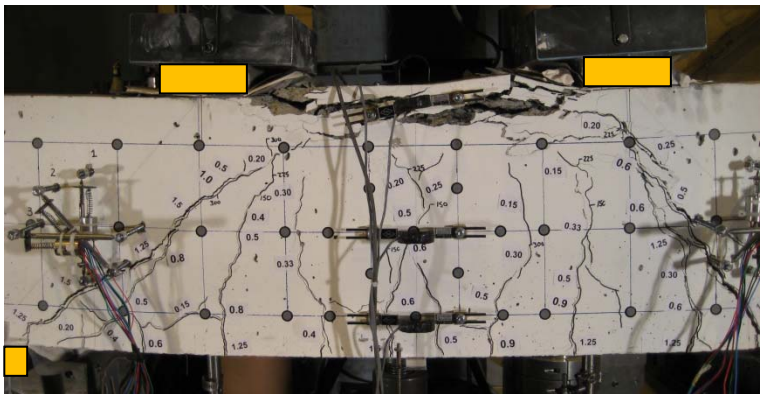

Figure 4-2: Flexural compression failure in specimen A1N. Loading and reaction plates are shown in yellow.

Failure of the diagonal compression struts occurred in specimens B5H and C2N. In both specimens, one of the diagonal compression struts would fail in a very brittle and noisy manner. Concrete pieces were ejected from the diagonal strut at failure. The load carrying capacity of the specimens at failure dropped more than 60 percent. Figure 4-3 shows the diagonal compression strut failure in specimen B5H.

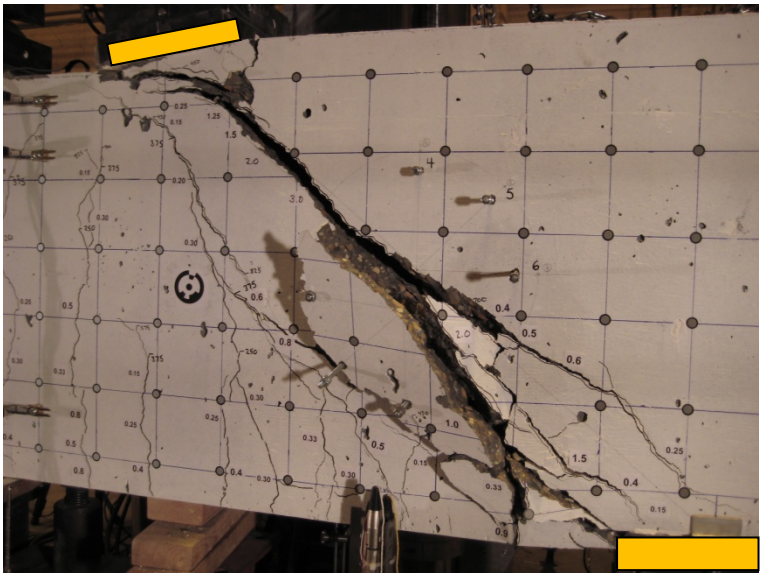

Figure 4-3: Failure of the compression strut in specimen B5H (shear span B). Loading and reaction plate are shown in yellow.

A concrete diagonal tension failure or splitting failure occurred in specimens A4H and B6H. A major curved diagonal cracked formed in each shear span from the inside edge of the reaction plate towards the inside edge of the loading plate. The diagonal crack extended above the diagonal line between the center of the reaction and support plate. As the crack opening became large, a vertical crack formed from the top surface of the concrete in the shear span and intersected the diagonal crack leading to an immediate drop in load carrying capacity (more detail on the crack formation is given in section 4.3). The concrete above the diagonal crack was forced upwards after the vertical crack formed as shown in Figure 4-4.

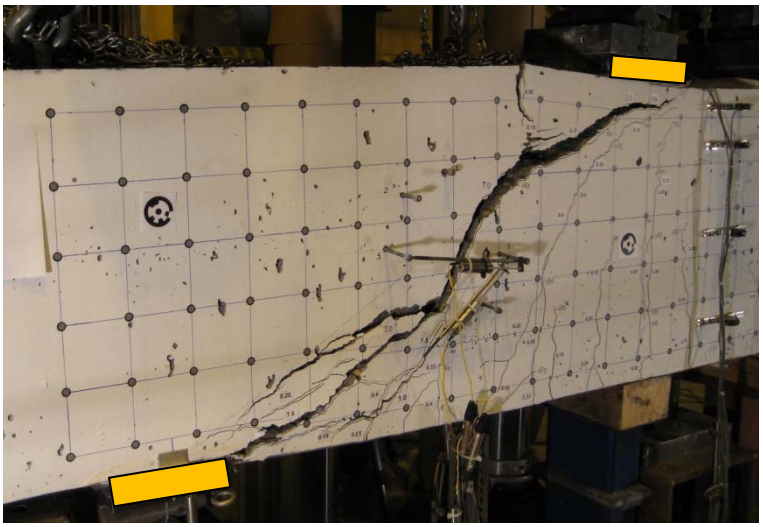

Figure 4-4: Concrete tension failure of specimen B6H. Loading and reaction plate are shown in yellow.

4.3 Crack Patterns and Crack Widths

For all specimens, the first cracks appeared at the bottom near mid-span. The cracks were visually noticed during pauses in loading but the cracks would have formed prior to that particular load stage. The cracking load for each specimen was therefore determined from the load-deflection response. After cracking, the effective concrete area was reduced, decreasing the moment of inertia and consequently reducing the stiffness of the beam. Therefore, the load where the bilinear load deflection curve began to deviate from the initial linear segment was reported as the flexural cracking load in Table 4-2. Flexural cracking occurred between 14 and 35% of P_{max}. The flexural cracking load to peak load ratio did not depend on the a/d ratio, ρ, or h when considered individually. The average flexural cracking load was 18% of P_{max} with a COV of 15% for the normal strength specimens (f_c' ≈ 40 MPa). For specimens A4H, B5H, and B6H with high strength concrete (f_c' ≈ 66 MPa), the cracking load was 31%, 20%, and 35% of P_{max}, respectively, indicating that the flexural cracking load was dependent on the concrete strength.

Table 4-2: Cracking load and maximum crack widths at the last load stage and at the equivalent service load.

Specimen	Flexural cracking load [kN] (% of P_{max})	Load when first inclined crack formed, P_c [kN] (% of P_{max})	Maximum crack width at last load stage			Maximum crack width at the service load	
			Width (mm)	Load (kN)	% of P_{max}	Width (mm)	Load (kN)*
A1N	115 (14)	312 (38%)	1.5	762	94	0.9	387
A2N	65 (14)	187 (40%)	1.5	387	82	0.5	237
A3N	55 (23)	143 (59%)	1.5	223	92	0.33	143
A4H	60 (31)	163 (85%)	2.5	184	96	0.3	113
B1N	230 (18)	387 (30%)	1.25	1012	76	0.9	637
B2N	140 (18)	287 (36%)	3.0	737	92	0.8	437
B3N	75 (17)	237 (55%)	2.75	362	84	0.33	237
B4N	160 (19)	412 (50%)	4.0	812	98	0.5	412
B5H	210 (20)	387 (36%)	4.0	962	91	1.25	587
B6H	130 (35)	212 (56%)	7.0	362	96	0.3	212
C1N	380 (17)	613 (27%)	2.5	1813	80	1.5	1213
C2N	250 (19)	413 (31%)	4.5	1163	88	1.5	713

* The maximum crack width from the load stage nearest to the service load value (Table 4-1) is reported.

The flexural cracks in the constant moment region rapidly propagated to approximately 80% of the overall specimen height, h, in all specimens. Subsequently, additional flexural cracks formed progressively closer to the supports in the shear spans. These cracks almost immediately became inclined (diagonal) cracks and grew towards the loading

plates. The load (P_c) at which the first inclined crack appeared (visually during pauses in loading) is given in Table 4-2. An inclined crack is defined as any crack in the shear span that deviates significantly from the vertical. The inclined cracks in all specimens appeared between 27% and 59% of the peak load except for specimen A4H where the inclined crack formed at 85% of the peak load. Since the equivalent service load was determined to be 50% of P_{max} (section 4.1), most of the members had diagonal cracks at the service condition.

The P_c/P_{max} ratio serves as a measure of the reserve load capacity after the formation of the first inclined crack. Specimens with larger a/d ratios had a smaller reserve capacity after formation of the first inclined crack when compared to specimens with small a/d ratios (Figure 4-5(a)). Increasing h caused a decrease in the P_c/P_{max} ratio (Figure 4-5(a)). The inclined cracking shear stress, normalized with the square root of f_c', decreased as the a/d ratio or h increased as shown in Figure 4-5(b). The influence of the concrete strength and reinforcement ratio on the P_c/P_{max} ratio was inconclusive due to the large scatter shown in Figure 4-6. In all instances, the low P_c/P_{max} ratio or high reserve load capacity was indicative of the formation of arch action after inclined cracking occurred.

The maximum crack widths for the specimens at the equivalent service load varied between 0.3 and 1.5 mm (Table 4-2). Only half of the specimens met the CSA S6-06 crack width criterion for structures not subjected to aggressive environments where the maximum allowable crack width is 0.7 mm. Specimens which satisfied the CSA S6-06 crack width requirement typically had larger a/d ratios, larger ρ, or smaller h.

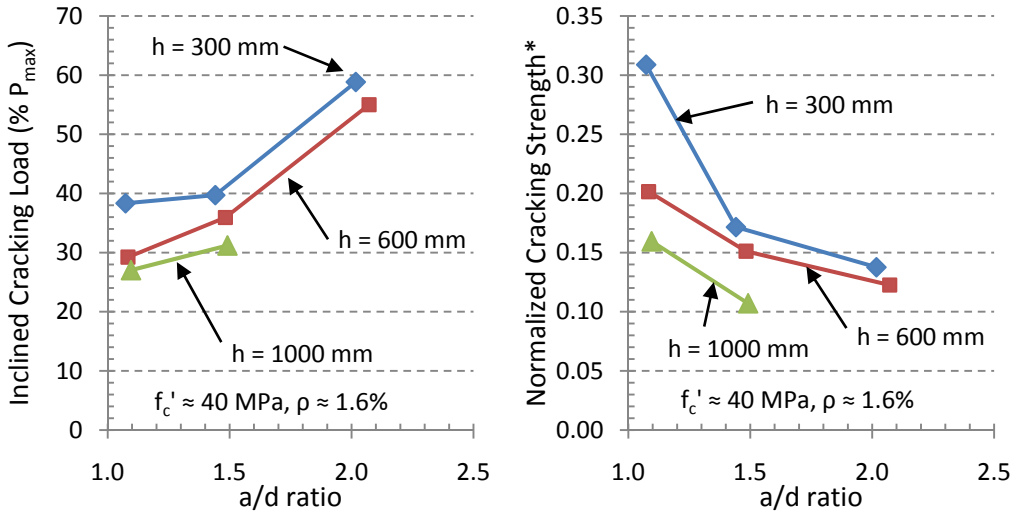

Figure 4-5: (a) influence of the a/d ratio and h on the inclined cracking load and (b) the normalized inclined cracking shear stress.

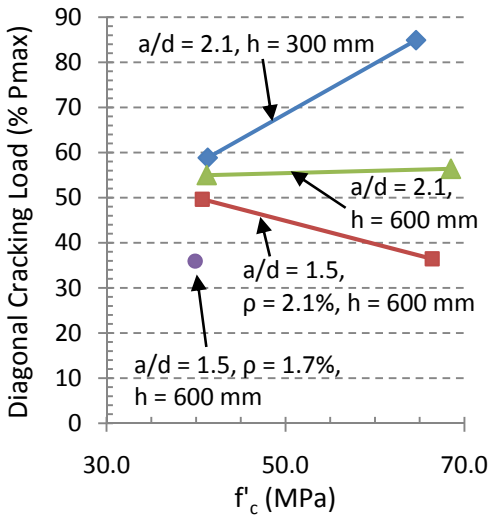

Figure 4-6: Influence of f_c' and ρ on the P_c/P_{max} ratio.

Prior to reaching P_{max}, all specimens had at least one main inclined crack in both shear spans. The main inclined crack would extend from the inside edge of the reaction plate towards the loading plate. Usually the crack trajectory was towards the inside edge of the loading plate and the crack would become increasingly horizontal near the flexural compression zone. Smaller secondary inclined cracks were observed parallel to the main inclined crack close to the support region in the majority of the specimens. These cracks would often initiate near the centroid of the reinforcement overtop of the support location and expand diagonally away in both the up and down directions. In specimens A1N, A2N, B1N, B2N, and C1N a second diagonal crack formed parallel to the main diagonal crack and extended from the support to the loading point. The formation of the inclined cracks indicated that redistribution of internal forces was occurring.

Crack diagrams showing the condition of the specimens after failure are given in Figure 4-7, Figure 4-8, and Figure 4-9 for specimens having h = 300, 600, and 1000 mm respectively. In all diagrams, the inclined crack that led to failure is indicated in a heavier line-weight. Crushing and spalling of concrete is indicated by shading.

Note that although some specimens had localized crushing near one of the loading plates in the flexural compression region, this was due to shear compression failure and not due to flexural crushing. For example, specimen A2N (Figure 4-7) had slight crushing of the concrete at the inside edge of the loading plate which occurred due to the shear crack emerging. The strain in the top of the concrete at mid-span just prior to P_{max} was approximately 2400 με (as determined by the DIC system), below the concrete crushing strain of 2800 με as measured by the companion cylinder tests (Appendix B).

After formation of the main inclined cracks in both shear spans of specimen A1N, the top end of the two inclined cracks became horizontal and progressed towards mid-span, delineating the inside boundary of an arch mechanism. Sliding occurred along the main

inclined crack at end B although this was initiated by the crushing of the concrete between the loading plates.

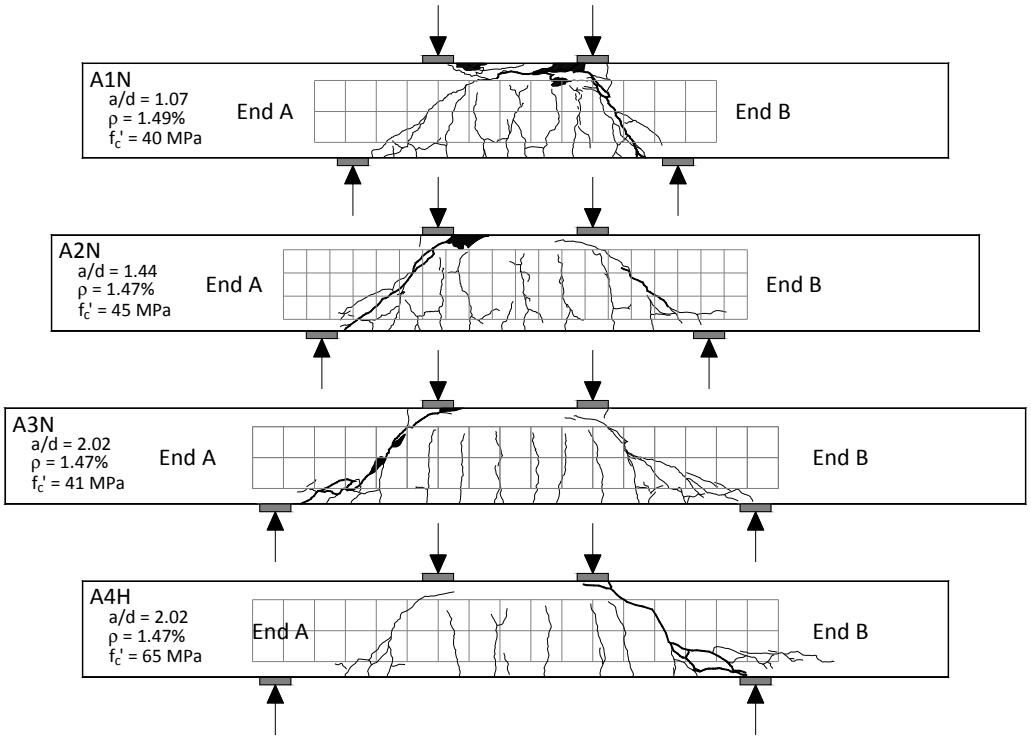

Figure 4-7: Crack diagram after failure of specimens with h = 300 mm.

The main inclined crack in shear span B of specimen A4H initiated as a flexural crack approximately 200 mm to the inside of support B. The flexural crack extended above the diagonal line between the centerlines of the loading and support plate. Figure 4-10 shows the original diagonal line between the center of the loading and support plates of specimen A4H at the conclusion of test. The crack then grew more horizontal and extended towards the loading plate. Near the bottom of this crack, at approximately 1/3 of the specimen height, a new crack formed that extended towards the inside edge of the reaction plate which completed the formation of the critical crack. Once the crack had formed, very little additional load could be carried before failure. Large deflections resulted (section 4.4.1) and the inclined crack width became increasingly larger. The specimen continued to hold load past the peak load with the crack width growing to approximately 10 mm. Splitting cracks formed along the reinforcement as shown in Figure 4-7. The splitting cracks formed as a result of the visible downwards movement of the center section of the specimen (dowel action) and the clockwise rotation of end B which produced a prying action as the diagonal crack width increased (see Figure 4-10). The large crack opening indicated that arch action formed as aggregate interlock was no longer possible. However, the arch action was insufficient to support additional load due to the curvilinear nature of the crack which prevented the efficient transfer of load to the support.

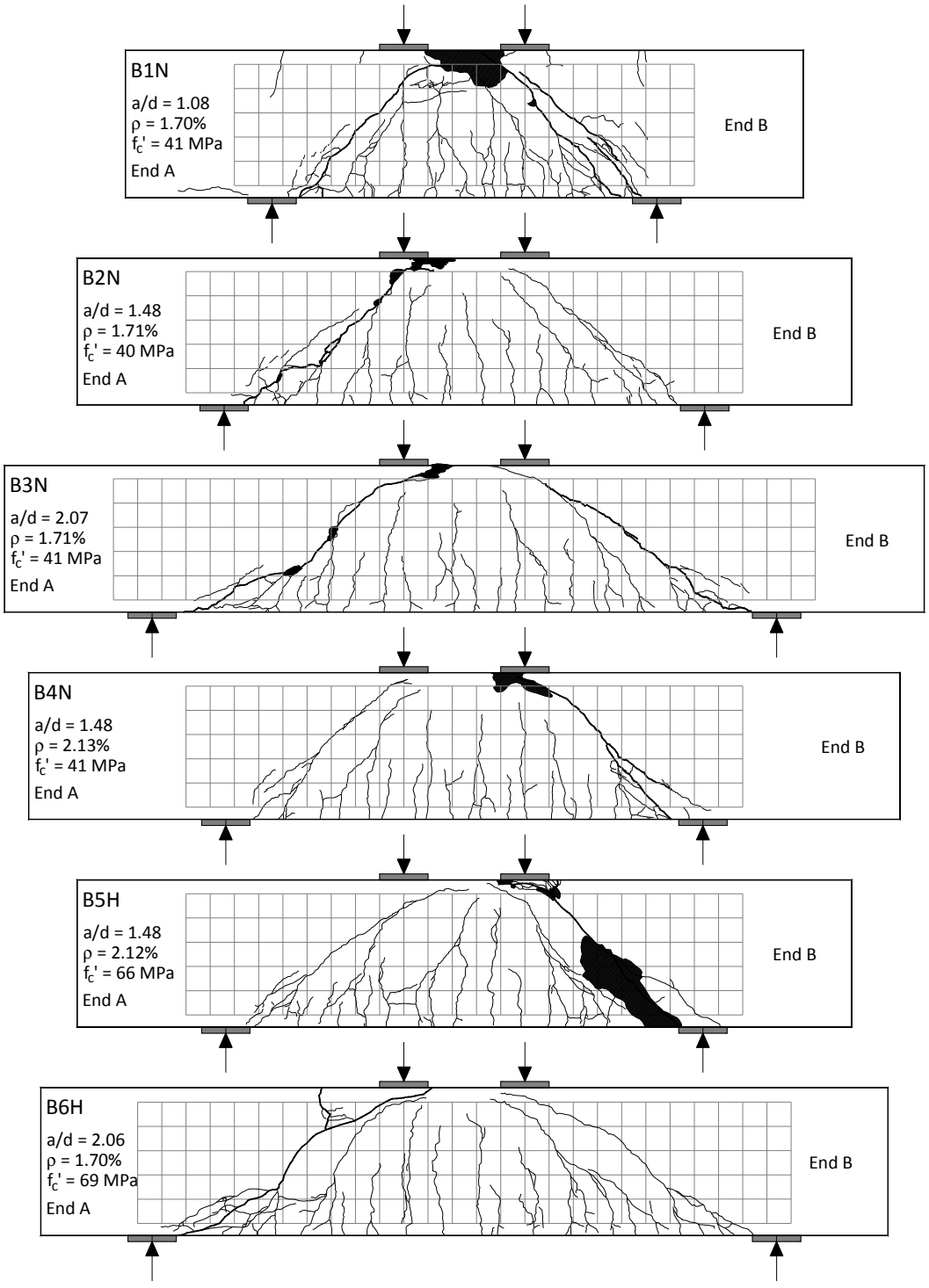

Figure 4-8: Crack diagram after failure of specimens with h = 600 mm.

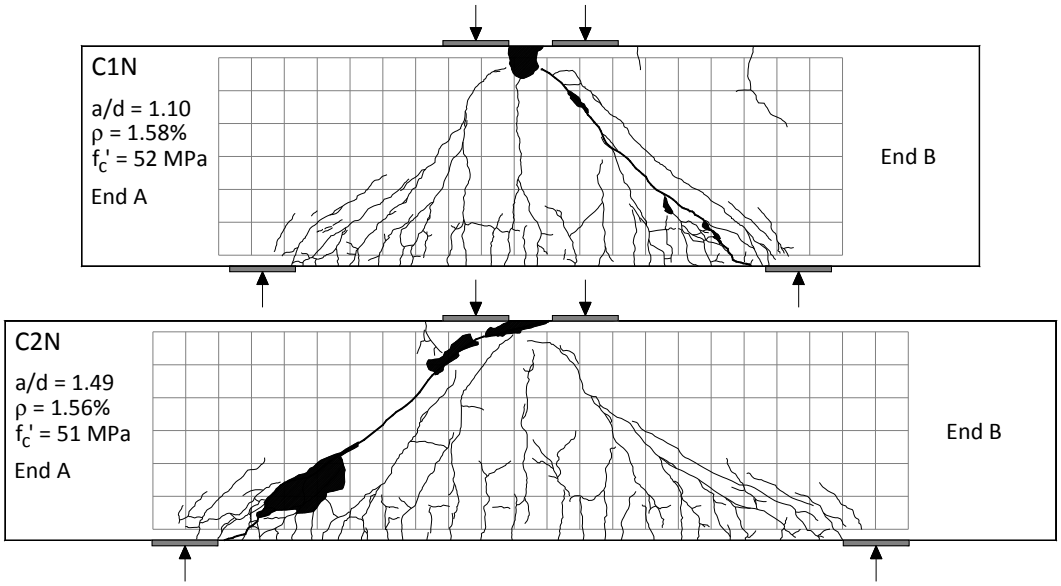

Figure 4-9: Crack diagram after failure of specimens with h = 1000 mm.

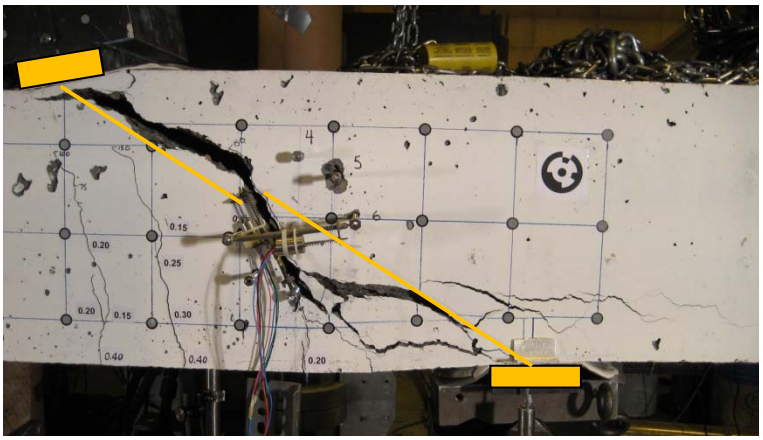

Figure 4-10: End B of specimen A4H at the conclusion of the test. Loading and reaction plates are shown in yellow.

The main inclined cracks in specimen B1N propagated from the inside edges of the support plates towards the inside edges of the loading plates. Approximately 60 mm from the top of the beam, the cracks joined horizontally through or slightly below the flexural compression zone. Crushing of the concrete in the flexural compression zone to a depth of greater than 150 mm from the top had occurred when the peak load was finally attained. In addition, the main inclined crack width in each shear span grew in size and a horizontal splitting crack was observed to the right of support A near the location of the bottom reinforcement layer. This indicated possible slippage of the bottom layer of reinforcement due to the high strain present in the bars at the support.

Specimen B6H had a cracking behaviour that was similar to specimen A4H. The main inclined crack in shear span A of specimen B6H initiated as a flexural crack at the bottom

of the specimen near the middle of the shear span and propagated above the diagonal line drawn from the centerline of the support and loading plates. Subsequently, an inclined crack extended from the existing inclined crack at a dimension of about h/3 from the soffit towards the inside edge of the reaction plate forming the critical crack. Since the aggregate interlock ceased to exist once the crack grew in width, the load had to be transmitted by arch action. The lack of top reinforcement limited the load carrying ability of the curved arch and a tensile splitting crack formed at the top of the shear span as shown in Figure 4-8.

The crack patterns in all of the specimens indicated the formation of an arch mechanism. Crack widths measured at the last loading stage prior to P_{max} are shown in Table 4-2 and ranged from 1.25 to 7.0 mm. At failure, the cracks were even wider but exact measurements could not be taken. The cracks were large enough in some cases to easily see through the full specimen width indicating the complete breakdown of the aggregate interlock shear transfer mechanism.

Appendix C contains crack diagrams that show the progression of the cracks and the corresponding crack widths for each specimen.

4.4 Load Deflection Behaviour

4.4.1 Specimens with h = 300 mm

The relationship between the applied load, P, and the adjusted mid-span deflection (Δ) is shown in Figure 4-11 for specimens having h = 300 mm. Specimens A2N and A3N both exhibited a sudden drop in load carrying capacity after the peak load was attained. The failure of specimen A1N was gradual with crushing occurring in the main flexural compression zone. The test was halted once the load had dropped 15% from the peak value. Although specimen A2N failed in shear compression, the post peak load carrying capacity remained largely intact as the mid-span deflection increased by approximately 1 mm after which the load dropped suddenly. The load carrying capacity of specimen A4H showed little change at the peak load as the mid-span deflection and inclined crack widths grew larger. A gradual decrease in load carrying capacity occurred after the peak load was attained.

As the a/d ratio increased, the post cracking stiffness of the specimens decreased. The post cracking stiffnesses of specimens A3N and A4H, both with a/d ratios of 2.1 but different concrete strengths, were similar. For the specimens with normal strength concrete (f_c' = 40 MPa) the mid-span deflection at failure increased slightly as the a/d ratio decreased. Specimen A4H (f_c' = 65 MPa) had a smaller deflection at the peak load than corresponding specimen A3N (f_c' = 41 MPa).

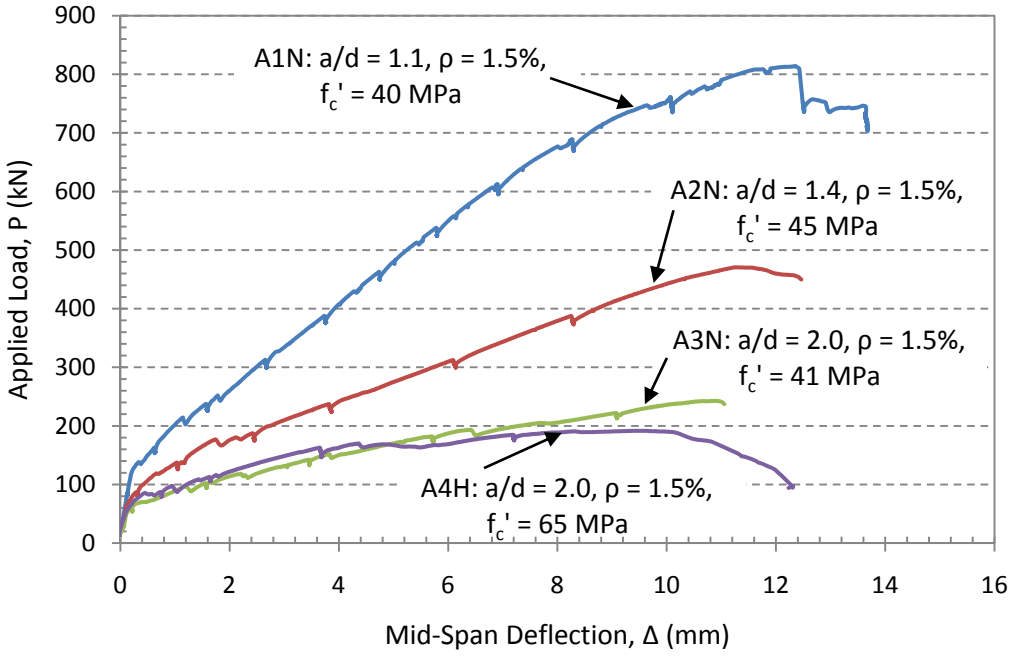

Figure 4-11: Load-deflection response of specimens with h = 300 mm.

4.4.2 Specimens with h = 600 mm

Figure 4-12 shows the load-deflection response of specimens having h = 600 mm and f_c' ≈ 40 MPa. Specimens B2N and B3N experienced brittle failures while specimen B4N experienced a more ductile failure. Specimen B1N reached a load of 1273 kN at which point there was a 3% loss of load. The specimen continued to gain load but the behaviour was characterized by a reduced stiffness as crushing of the flexural compression region initiated. At 1286 kN, a sudden 8% drop in load was recorded. As the flexural region continued to crush, load carrying ability was slowly regained and reached a new maximum of 1324 kN. Extreme deterioration of the flexural compression zone was observed. After reaching the peak load, the load carrying capacity decreased at an increasing rate and the test was halted due to safety concerns. The final peak load of 1324 kN was considered unrepresentative for modelling purposes as the drop in load carrying capacity from the prior local peak of 1273 kN and subsequent regain in strength was thought to be an unreliable mechanism. For subsequent discussions and analysis in this study, the failure load of specimen B1N was taken as 1273 kN. Nevertheless, specimen B1N demonstrated that a large amount of ductility can be provided by the concrete.

The initial flexural stiffnesses of specimens B1N, B2N, B3N, and B4N were the same. The post cracking flexural stiffnesses of the specimens decreased and the mid-span deflections at the peak loads increased (peak load for specimen B1N now considered as 1273 kN) as the a/d ratio increased from 1.1 to 2.1 as seen in Figure 4-12. Figure 4-12 also indicates that specimen B4N which had a reinforcement ratio 24% larger than

specimen B2N had a stiffer loading response and a capacity that was 4% greater than specimen B2N. The mid-span deflection of specimen B4N at the peak load was 12% less than B2N.

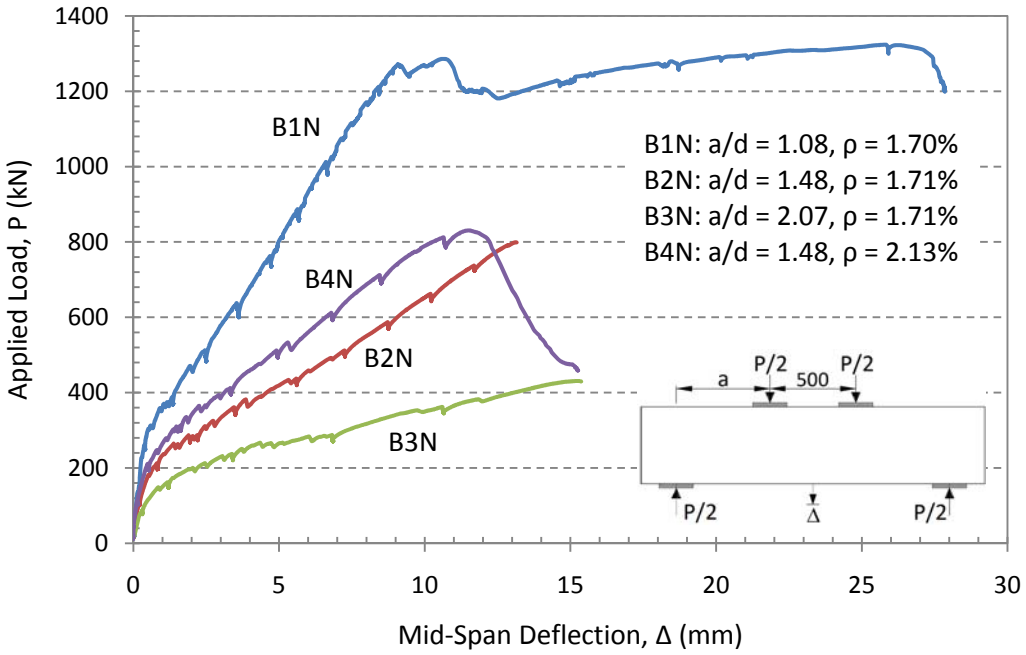

Figure 4-12: Load-deflection response of specimens with h = 600 mm and f_c' ≈ 40 MPa.

Specimens B5H and B6H had the same initial flexural stiffness. Specimen B5H, which had a smaller a/d ratio than specimen B6H, displayed a stiffer post cracking loading response than specimen B6H (Figure 4-13). Failure of specimen B5H was extremely brittle with significant damage along the main inclined crack including concrete pieces falling off the specimen. The load carrying capacity immediately dropped by approximately 80%. Specimen B6H also failed suddenly and the load carrying capacity dropped by about 60%.

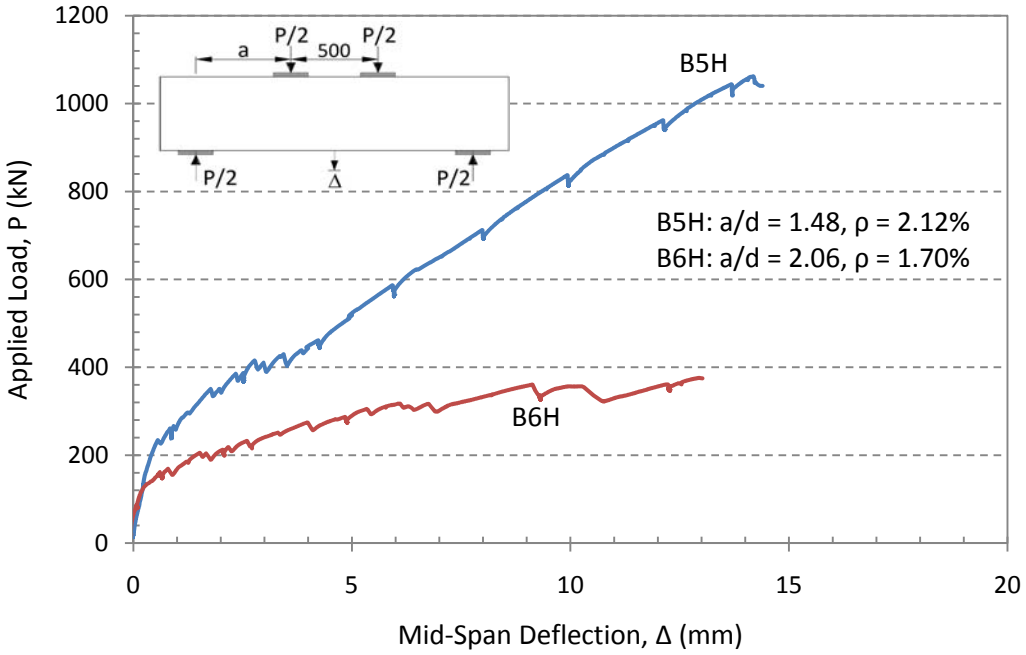

Figure 4-13: Load-deflection response of specimens with h = 600 mm and f_c' ≈ 67 MPa.

4.4.3 Specimens with h = 1000 mm

Both specimens having h = 1000 mm failed abruptly with a loss in load carrying capacity of 30% and 60% in specimens C1N and C2N, respectively. Although crushing of concrete was observed between the two loading plates, the failure of specimen C1N resembled more of a brittle shear failure than a flexural compression failure. Crushing of the concrete appears to have resulted from the shear crack propagating towards the inside edge of the loading plates. The linear nature of the loading response in Figure 4-14 also indicated a shear failure rather than a more gradual flexural compression failure.

Specimen C2N, which had a greater a/d ratio than specimen C1N, had a less stiff post cracking loading behaviour. Specimen C2N had a 15% greater mid-span deflection at the peak load than specimen C1N.

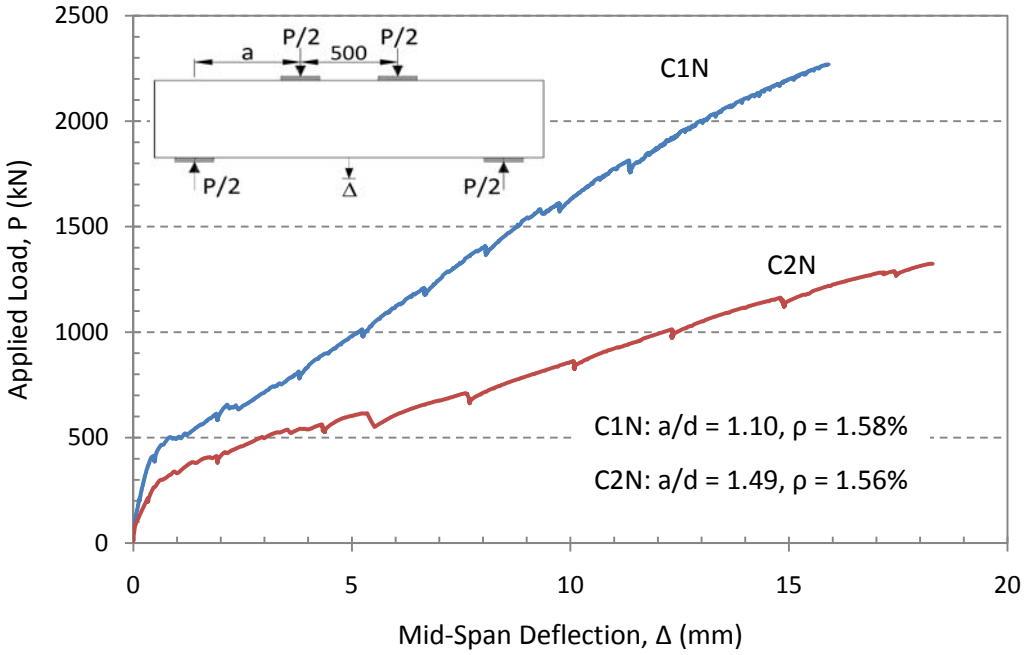

Figure 4-14: Load-deflection response of specimens with h = 1000 mm and f_c' ≈ 51 MPa.

4.4.4 Comparison of the Specimen Load-Deflection Responses

Specimens B4N and B5H, which were identical except for the concrete strength, had similar load deflection response up to approximately 90% of specimen B4N failure load as shown in Figure 4-15. Similarly, specimens B3N and B6H, which were also identical except for the concrete strength, exhibited the same load deflection response. As seen from Figure 4-15 and from Figure 4-7 for specimens A3N and A4H, the concrete strength had no discernable effect on the post cracking stiffness of the specimens.

Specimen B5H had a concrete strength 63% greater than specimen B4N and a 28% larger peak load. Specimen B6H had concrete that was 66% stronger than specimen B3N and the peak load was 87% of the specimen B3N peak load. Similarly, specimen A4H had a concrete strength 56% greater than specimen A3N and the peak load was 79% of the specimen A4H peak load. As discussed previously (section 4.3), the crack pattern prevented an efficient arch mechanism from forming in specimens A4H and B6H.

No trend was observed in the mid-span deflection at peak load in the sets of specimens where concrete strength was the only variable. While specimen B5H had a larger mid-span deflection at the peak load than specimen B4N, both specimens A4H and B6H had smaller mid-span peak load deflections than specimens A3N and B3N, respectively.

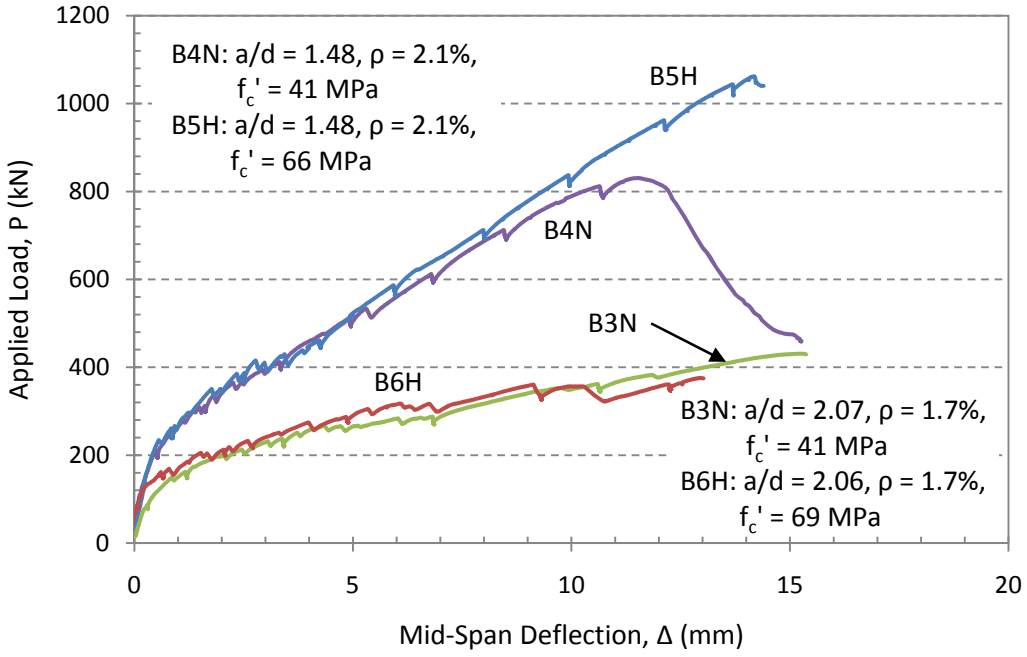

Figure 4-15: Comparison of the load-deflection response of similar specimens with different concrete strengths.

Specimens A1N, B1N, and C1N had similar reinforcement ratios, concrete strengths, and a/d ratios but different heights. From Figure 4-16, the post cracking stiffness of the loading response was similar between specimens B1N and C1N. Specimen A1N, however, had a less stiff response; the slope of the linear portion of the post cracking load deflection response prior to flexural crushing was approximately 60% of the post cracking stiffness of specimen B1N and C1N. Comparing specimens A2N, B2N, and C2N which have similar properties but different heights shows that they all had very similar post cracking stiffness (Figure 4-17). Specimens A3N and B3N, both having similar properties except for height, also had a very similar post cracking stiffness and are shown in Figure 4-18.

As the specimen height increased, the deflection at peak load also increased as shown in Figure 4-17 and Figure 4-18. However, in Figure 4-16 specimen B1N did not follow this trend. The deflection at P_{max} = 1273 kN was less than the peak load deflection in specimen A1N.

The experimental results showed that the post cracking stiffness of the specimens tested increased as the a/d ratio decreased or as the reinforcement ratio increased. From the comparisons of the loading responses, the post cracking stiffness of the specimen did not depend on h or f_c'. Higher peak loads and corresponding mid-span deflections were attained with specimens having a larger h.

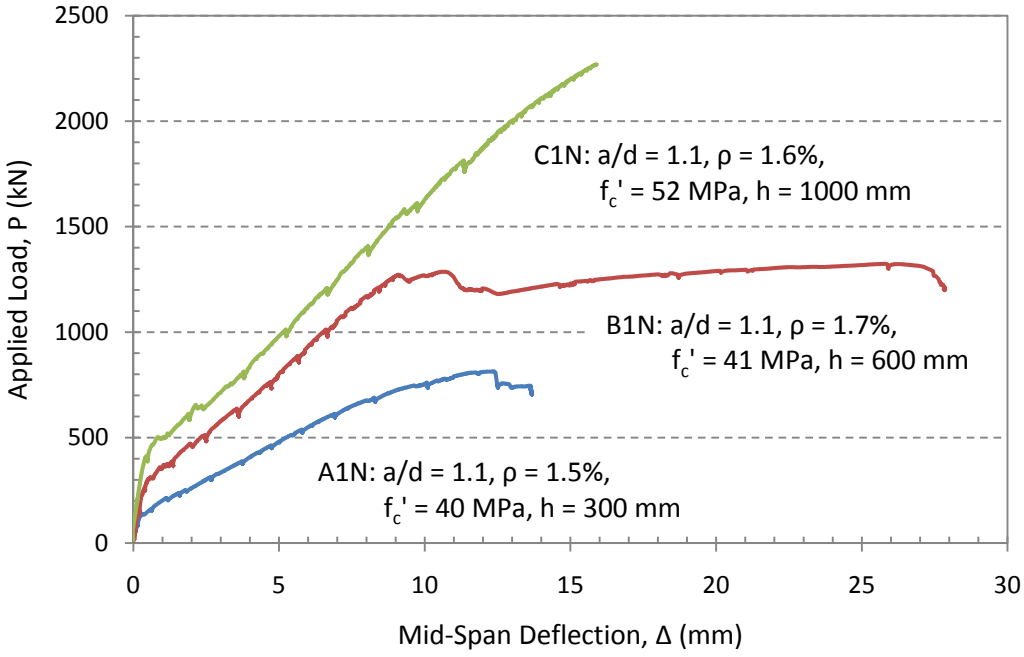

Figure 4-16: Load-deflection response of specimens with *a/d* = 1.1.

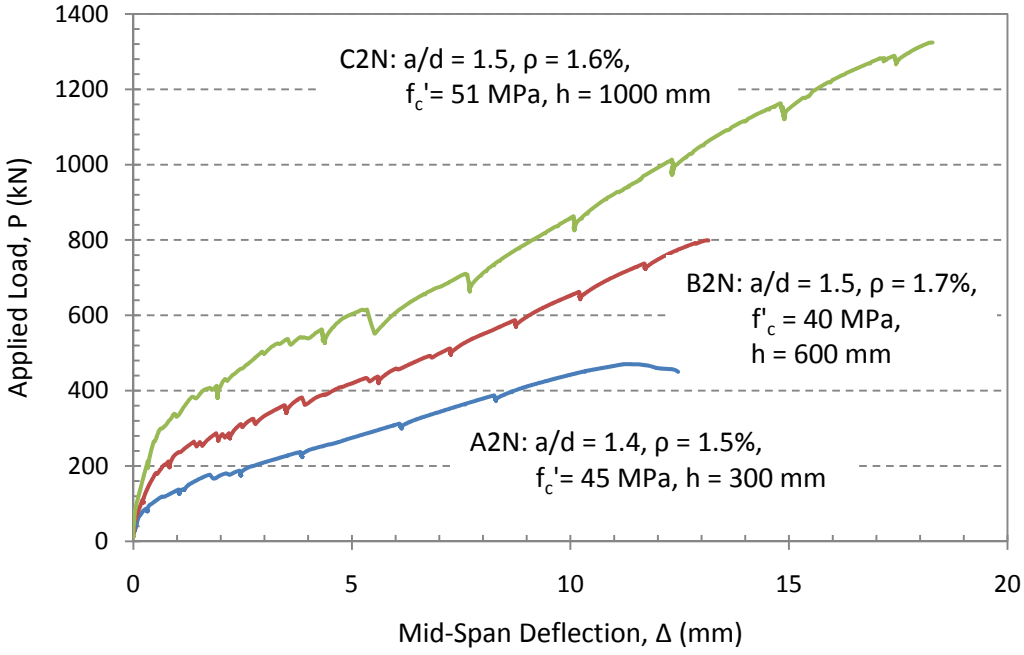

Figure 4-17: Load-deflection response of specimens with *a/d* = 1.5.

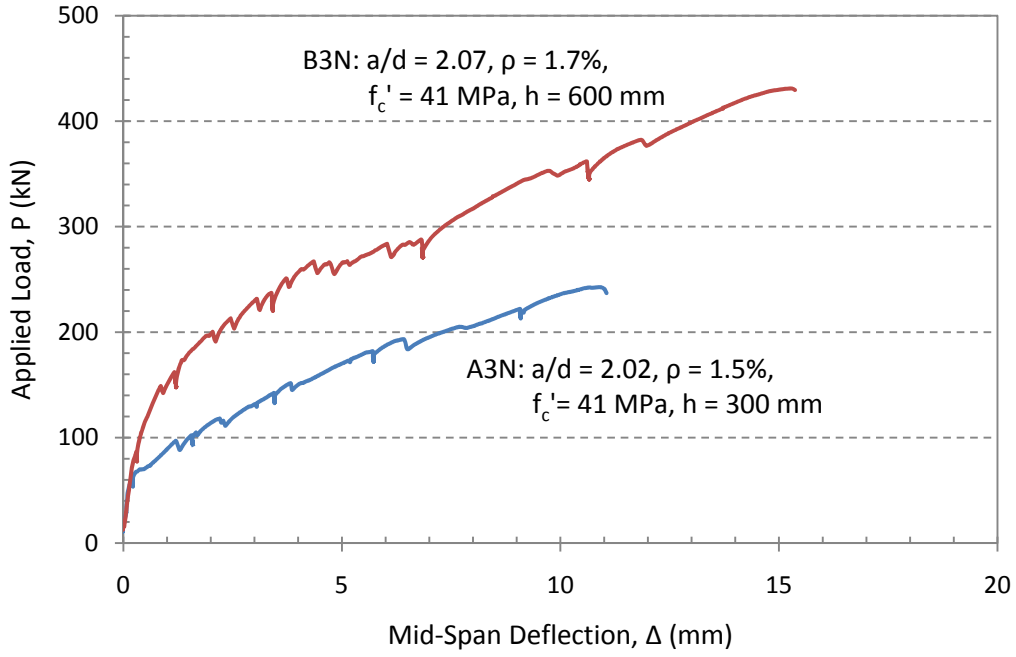

Figure 4-18: Load-deflection response of specimens with a/d = 2.1.

4.5 Reinforcement Strains

For all specimens there was minimal change in the GFRP reinforcement strain until the formation of the first flexural crack. The strain readings of the bottom bar increased rapidly in the vicinity of the first crack, usually in the constant moment region. As more cracks formed closer to the supports, the measured strains in the GFRP reinforcement would also increase closer to the support. In the un-cracked regions, strain readings showed minimal strain changes in the GFRP. As loading progressed, the strains in the reinforcement became similar between the supports indicating the formation of a tied arch mechanism. The strain distribution in the bottom reinforcement layer of B1N as the load increased is shown in Figure 4-19 and is typical of all specimens. In the majority of the specimens, the strain in the GFRP at the center of the support was significantly lower than the strain reading at mid-span. With the exception of specimens A4H and B1N, no strain increase was registered in the GFRP past the supports with the first strain gauge typically located 100-250 mm past the edge of the support. In addition, a strain gradient between the bottom, middle and top reinforcement layer was present (Table 4-3). The bottom reinforcement layer, being the furthest from the neutral axis had the largest strains.

The strain level in the bottom reinforcement layer outside of the span in end A of specimen B1N increased to about 50% of the mid-span strain level at the final failure load of 1324 kN. The splitting crack that had formed near the location of the bottom

reinforcement (section 4.3) was caused by increase in the GFRP reinforcement strain level and possible slippage of the reinforcement.

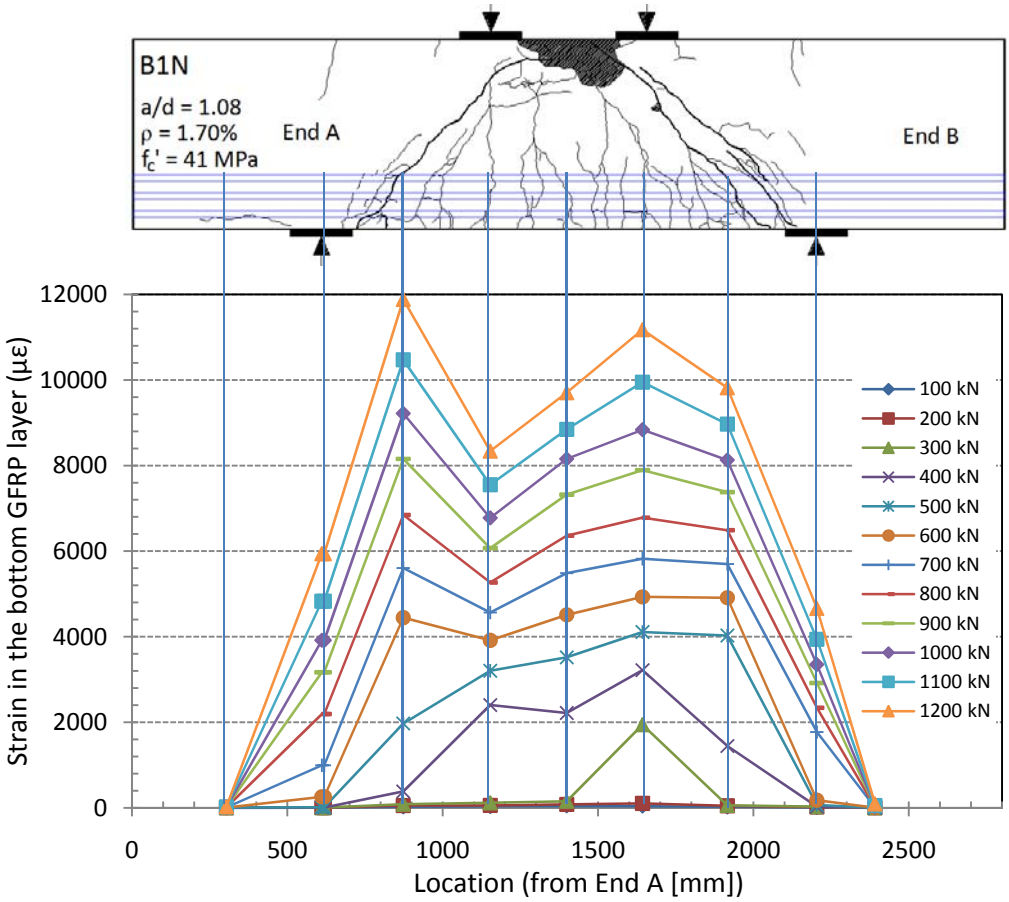

Figure 4-19: Typical reinforcement strain distribution along the bottom layer of reinforcement as the load increased (specimen B1N shown).

Specimen A4H experienced longitudinal splitting cracks near support B as shown in Figure 4-7. There was an increase in reinforcement strain in the end region past support B prior to failure which corresponds to the visual observation of the splitting cracks. At the peak load, the strain in the GFRP past support B was approximately the same as the mid-span strain (Figure 4-20).

The reinforcement strain distribution is an indicator of whether and to what extent a tied arch mechanism formed in the specimens. In a fully developed tied arch mechanism, the strain level in the reinforcement is expected to be approximately uniform from support to support. In all specimens, the strain distribution between the supports at peak load was approximately constant indicating an arch mechanism had developed. Specimen A4H had a strain distribution where the strain in the center of

shear span B was 75% of the strain at mid-span. However, high strains were recorded in shear span A and past support B at failure.

Table 4-3 shows the mid-span strains in the reinforcement layers at the peak load and equivalent service load conditions. The average strain at the centroid of the reinforcement at the center of the support plate is also provided in Table 4-3. Detailed information on the reinforcement strain distribution during loading and at the peak load is given in Appendix C for all the specimens.

Table 4-3: Strain in the GFRP at the peak load and at service load.

	Total Load - GFRP Strain						Service Load
Specimen	Bottom Layer Mid-span (με)	Middle Layer Mid-span (με)	Top Layer Mid-span (με)	Average Mid-span (με)	Average Strain (με) Support A	Average Strain (με) Support B	Strain Bottom Layer at Mid-span (με)
A1N	17437			17437	11389	7255	6456
A2N	8930			8930	5811	4675	3737
A3N	5968			5968	2057	2528	2477
A4H	4776			4776	50	5491	899
B1N	10387	8526	6188	8367	5207	4062	4967
B2N	8560	6366	5692	6873	2728	1496	3326
B3N	5439	5212	5081	5244	259	800	2775
B4N	7918	5350	5275	6182	2511	2397	3605
B5H	8247	6593	5847	6896	3757	2531	3616
B6H	5581	4209	3702	4497	756	66	851
C1N	10633	8571	-	9602	5084	4084	4777
C2N	7171	6242	6630	6841	2876	967	3262

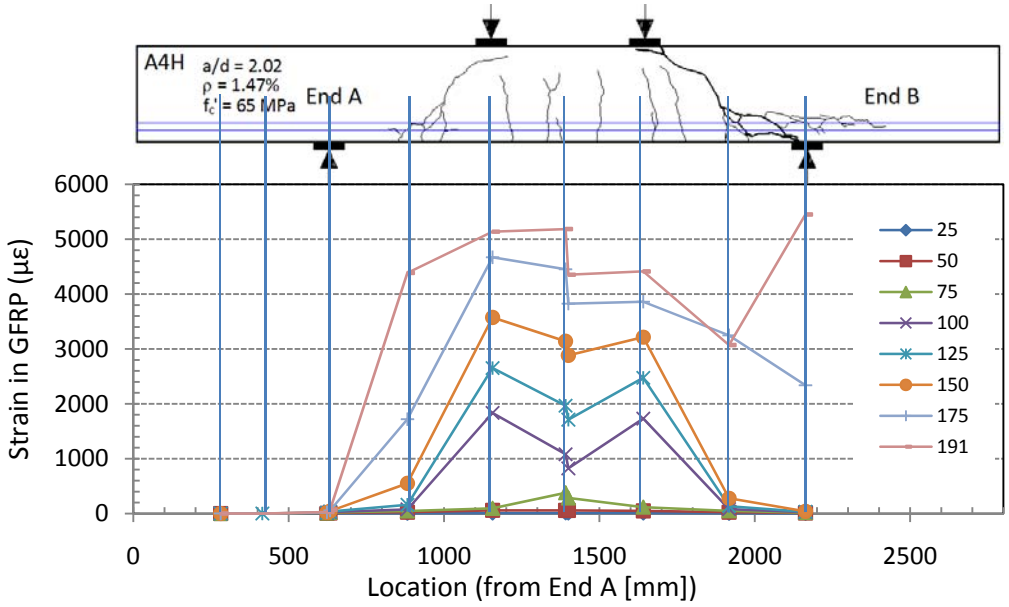

Figure 4-20: Reinforcement strain distribution in specimen A4H as loading progressed.

4.6 Shear Capacity Trends

Several trends were observed from the peak loads. The main variables that influenced specimen capacity are introduced in this section and further analysis is provided in Chapter 5.

Shear capacity trends are discussed in terms of a/d ratio, height, h, reinforcement ratio, ρ, and concrete strength, f_c', which were the main variables in the test program. The peak shear stress was normalized by f_c' as shown in Equation 4.1.

$$\frac{P_{max}}{2f'_c b_w d} \qquad \textbf{4.1}$$

Figure 4-21(a) shows that as the a/d ratio decreased, there was a significant increase in the normalized shear capacity regardless of the member height, reinforcement ratio or concrete strength.

Specimens having different heights were tested to determine if there was a size effect on the shear carrying capacity of GFRP reinforced deep beams. The dimensions of loading and support plates in the direction of the span were scaled in proportion to the specimen height, h, to eliminate the bearing plates as a variable (i.e. proportionally scaled nodal size in the strut and tie model) as was also done by Tan et al. (2008). Figure 4-21(b) shows the influence of size on the normalized shear capacity. The specimens included in Figure 4-21(b) were grouped by similar a/d ratios and have similar ρ (≈ 1.6%) and f_c' (≈ 40 MPa). For the three a/d ratios, 1.1, 1.5, and 2.1, the normalized shear capacity decreased as the specimen height increased with the exception of specimen

A2N. The effect was most pronounced in the specimens having an a/d ratio of 1.1. In addition, specimen height had minimal influence on the normalized shear capacity for a/d = 1.5 and 2.1 when h was less than 600 mm. However, this trend could be due in part to the difference in reinforcement ratio between the 300 mm and 600 mm deep beams. The reinforcement ratio of the h = 300, 600, and 1000 mm specimens were 1.5, 1.7, and 1.6%, respectively. A higher reinforcement ratio is known to produce a higher shear capacity (i.e. Kani 1966 and 1967, El-Sayed 2006). Also, it is noted that specimens A1N and B1N, with a/d = 1.1, experienced flexural compression failures in the constant moment region. Therefore, the load which would have resulted in a shear failure is not known for specimens A1N and B1N, but the shear capacity must be higher than the shear present at flexural failure.

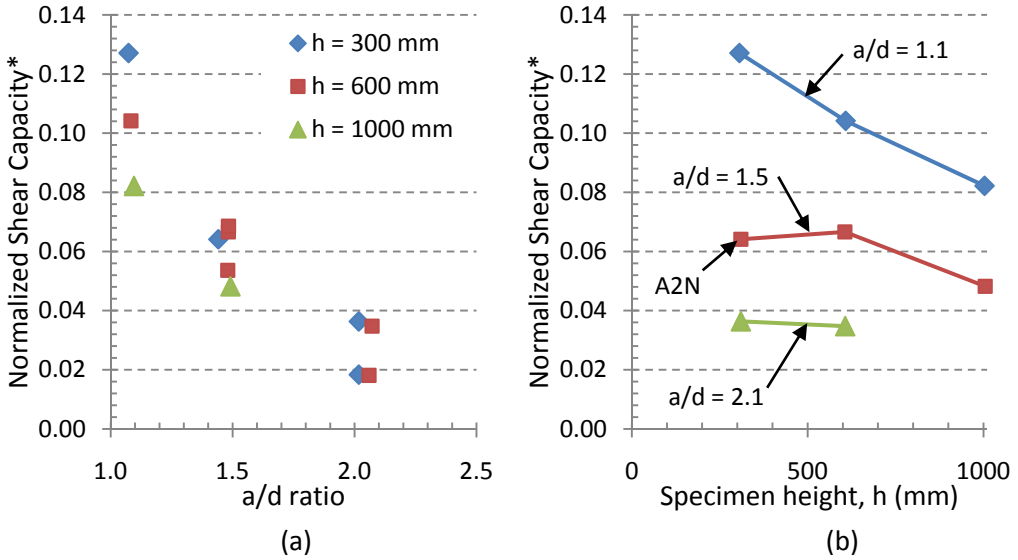

Figure 4-21: Influence of: (a) a/d ratio on shear capacity, and (b) member height on shear capacity. *Equation 4.1

Increasing the reinforcement ratio by 24% resulted in a 3% increase in the normalized shear capacity (Figure 422(a)) of specimen B4N compared to specimen B2N. Increasing the concrete strength by 63% while maintaining ρ = 2.13% resulted in a 22% decrease in the normalized shear capacity (Figure 4-22(a) and top curve in (Figure 4-22b)).

As the concrete strength of the specimens increased, the normalized shear capacity decreased (Figure 4-22 (b)) regardless of the a/d ratio, ρ, or h. For the specimens with a/d = 2.0 and 2.1, increasing the concrete strength approximately 64% resulted in a 50% decrease in the normalized shear capacity.

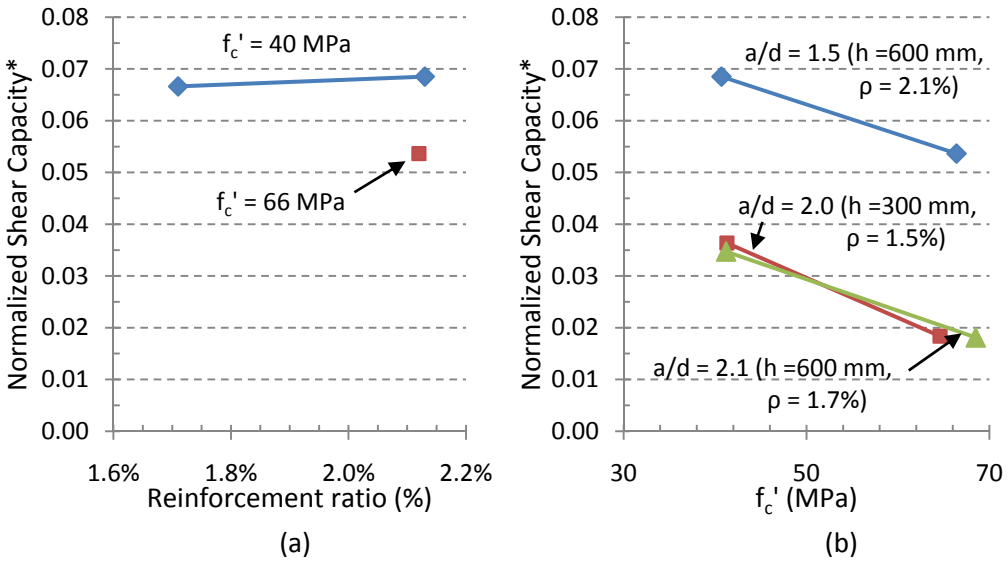

Figure 4-22: Influence of: (a) reinforcement ratio on shear capacity and (b) concrete strength on shear capacity. *Equation 4.1

Figure 4-23(a) shows that as the strain in the bottom layer of reinforcement at mid-span increased, the normalized shear capacity also increased regardless of specimen configuration. Lower a/d values resulted in higher mid-span strain in the reinforcement and higher normalized shear capacities when compared to larger a/d values as shown in Figure 4-23(b).

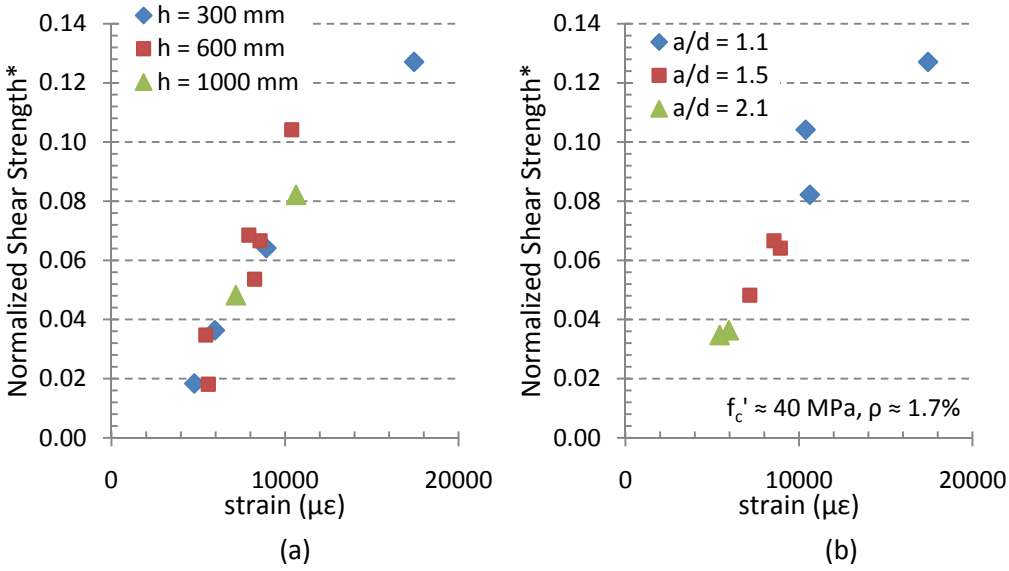

Figure 4-23: Mid-span strain in the bottom layer of reinforcement at the peak load (a) for all specimens and (b) for specimens grouped by a/d ratio. *Equation 4.1

4.7 Summary

The following are the key observations from the experiments:

- Half of the specimens failed suddenly in shear compression. Specimens A1N and B1N failed in flexural compression with a gradual loss in load carrying capacity. Diagonal strut failures occurred in specimens B5H and C2N. The diagonal strut failure was extremely brittle and resulted in a large loss of load carrying capacity. Specimens A4H and B6H experienced a diagonal tension failure.
- Well defined crack patterns and constant strain distribution along the longitudinal reinforcement indicated an arch mechanism was able to develop in all specimens.
- Large inclined crack widths of 1.5 to 7.0 mm were noted at the last load stage prior to failure of the specimens. Many of the diagonal cracks were observed to be wider at failure, and in some instances the cracks were wide enough to easily see through the specimen.
- The maximum crack widths at the equivalent service load condition varied between 0.3 and 1.5 mm.
- The stress level in the bottom GFRP reinforcement layer at the equivalent service load condition varied between 4 and 37% of f_{FRPu} with only one specimen exceeding the CSA S6-06 stress limit of $0.25 f_{FRPu}$. The stress in the GFRP is limited at the equivalent service load by CSA S6-06 to prevent creep rupture.
- After the initial appearance of inclined cracks originating from the bottom of the specimens, the majority of the specimens had significant post cracking reserve capacities varying between 70% and 270% of the inclined cracking load. The abundant reserve capacity indicated the specimens were able to redistribute the internal forces and develop an arch mechanism. Only beam B4H had a low reserve capacity of 18% due to the unfavourable crack pattern where one inclined crack extended above the diagonal line drawn between the centers of the loading and support plates. Failure occurred shortly after this crack formed.
- As loading progressed, the strain distribution in the longitudinal GFRP reinforcement became approximately constant between the supports indicating the formation of a tied arch mechanism.
- The post cracking stiffness of the specimens was dependent on the reinforcement ratio and the a/d ratio but not the specimen height or concrete strength. Increasing the reinforcement ratio or decreasing the a/d ratio increased the post cracking stiffness.
- The shear capacity was strongly influenced by the a/d ratio. Decreasing the a/d ratio increased the normalized shear capacity and the strains in the bottom reinforcement layer.

- The normalized shear capacity increased by 3% when the reinforcement ratio increased by 24% for the specimen with h = 600 mm.
- The results indicated a size effect in the specimens having a/d = 1.1 where increased member height resulted in reduced normalized shear stress at the peak load. Specimens having a/d = 1.5 and 2.1 had no significant size effect in shear when h increased from 300 to 600 mm. However, since there was some variation in the specimen parameters, a detailed relationship for size effect could not be established.
- Increasing the concrete strength resulted in a decreased normalized shear capacity.

5 Analysis and Discussion

5.1 Shear Capacity Predictions

The shear capacities of the test specimens were calculated using the arch and sectional models described in Chapter 2. These strength predictions were compared to the measured peak loads. Due to a lack of specific shear provisions for FRP reinforced concrete deep beams, the arching mechanism was modelled using the strut and tie modelling technique used for steel reinforced concrete beams. The resistance factors in all models considered were taken as 1.0. As-built dimensions and measured material properties were used in all calculations.

5.1.1 Strut and Tie Models

The behaviour of the specimens indicated that an arch mechanism was able to form. All specimens had substantial reserve capacity after formation of inclined cracks. The large crack openings prior to failure, large enough in some instances to see through the full specimen width, indicated that aggregate interlock was not the predominate shear transfer mechanism at failure. The primary load transmission was directly from the loading points to the supports through diagonal compression struts. Measured strain distribution in the reinforcement was consistent with a tied arch mechanism.

Strut and tie models (STM) were used to represent the arch mechanism that formed in the specimens. As discussed previously (section 2.5.3), STMs are based on the theory of plasticity. Plastic deformation is required to enable the redistribution of stresses into the stress flow assumed in the truss model. In steel reinforced concrete deep beams, the plasticity is typically provided by yielding of the steel reinforcement. However, FRP is an elastic material and will not provide the required plasticity. Therefore, the concrete must provide the plastic deformation required by the strut and tie modelling approach. The beams tested in this study required very little redistribution of stresses as the loading configuration was relatively simple and the corresponding truss model selected (Figure 5-1) was close to the elastic stress trajectories. In addition, the truss model was statically determinate. Concrete has limited plasticity unless confined; however, specimen B1N showed extremely ductile behaviour after crushing of the flexural compression zone was detected. The reserve deformation capability demonstrates the ductility of the overall system while the stress level in the GFRP continued to increase with increasing load.

A simple truss model with direct diagonal compression struts as shown in Figure 5-1 was adopted for the calculation of the shear capacities. The centerline location of the tie coincided with the centroid of the FRP reinforcement. The bottom node dimensions were defined by the bearing plate size and by the height of the tension tie which was taken as twice the distance from the specimen soffit to the reinforcement centroid. The

height of the top nodes/compression zone and the corresponding inclination angle, θ, of the diagonal struts were defined during the calculations. Dimensions for the shear span length, a, and effective depth, d, were known from the as-built dimensions. In all instances, the shear capacity was determined iteratively by incrementing the total applied load, P.

Three different STMs were evaluated. Two of the models were based on the CSA A23.3-04 provisions while the third model was based on the STM provisions given in ACI 318-08 Appendix A.

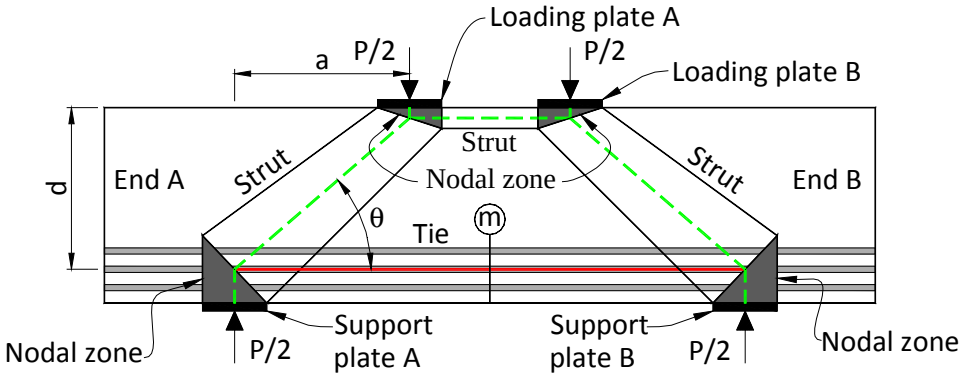

Figure 5-1: Truss model configuration for calculating the shear capacity of the FRP reinforced deep beam specimens.

5.1.1.1 CSA A23.3-04

The strut and tie modelling approach from CSA A23.3-04 for steel reinforced deep beams was adopted with minor modifications. When using the STM to predict the capacity of steel reinforced members, the steel is typically assumed to yield such that the stress in the tie is the yield stress, f_y, and the reinforcement strain is taken as the yield strain. GFRP is linear elastic and hence, an increase in strain will increase the stress and force in the GFRP until rupture at a stress of f_{FRPu}. Therefore, the actual strain in the GFRP must be calculated and taken into account when applying the STM.

The crushing strength of the diagonal struts in the CSA A23.3-04 STM (Equation 2.32) is dependent on the principal tensile strain, ε_1, which is calculated using Equation 2.33. The principal tensile strain is dependent on the tie strain, ε_s. In steel reinforced members where the tensile strain in the tie changes as the tie crosses the strut, ε_s is the strain in the reinforcement at the center of the strut, location c in Figure 5-2 (location c is the node or intersection of the centerlines of the strut and tie). According to CSA A23.3-04 explanatory note N11.4.2.3, the strain in the tie at the center of the strut is usually assumed to be half of the mid-span strain, (location m in Figure 5-1) if the steel reinforcement is being developed in the nodal/extended nodal region, between locations b and d in Figure 5-2 (i.e. half of the yield strain since the steel is assumed to

yield). Refer to section 2.5.3.1 for more detail on CSA A23.3-04 methodology to consider the strain in the reinforcement crossing a strut.

In applying the STM to FRP reinforced beams, the strain term, ε_s, in Equation 2.33 was replaced with ε_{frp}, the longitudinal strain in the FRP at mid-span. Since the bars were being developed past the support plates, in some cases the FRP strain at location b in Figure 5-2 was greater than zero. Therefore, the FRP strain at the center of the strut may be greater than half of the mid-span strain. The experimental results indicated that the strain at the centroid of the reinforcement at the centerline of the support plate varied between 15 and 115% of the mid-span strain. The average strain in the GFRP bars at the center of the nodal zone considering all specimens was 54% of the mid-span strain. Therefore, two approaches to calculating the traverse tensile strain, ε_1, were employed. The first approach considered the full mid-span strain which assumes that the reinforcement was mostly developed to the outside of the node (i.e. beyond location b in Figure 5-2) and Equation 2.33 was rewritten as:

$$\varepsilon_1 = \varepsilon_{frp} + (\varepsilon_{frp} + 0.002)cot^2\theta \qquad \textbf{5.1}$$

where ε_{frp} is the same as the centroidal mid-span FRP strain (i.e. at location m in Figure 5-1 or to the right of location d in Figure 5-2).

In the second approach, the limiting compressive strut strength was calculated by assuming the FRP strain at the center of the strut (location c in Figure 5-2), $\varepsilon_{frp,c}$, was half the mid-span strain. In this instance, Equation 2.33 was rewritten as:

$$\varepsilon_1 = \varepsilon_{frp,c} + (\varepsilon_{frp,c} + 0.002)cot^2\theta \qquad \textbf{5.2}$$

$$\varepsilon_{frp,c} = \frac{\varepsilon_{frp}}{2} \qquad \textbf{5.3}$$

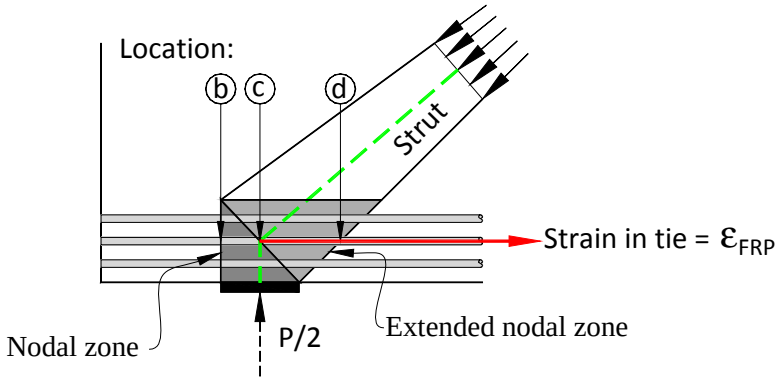

Figure 5-2: Nodal region of the STM shown in Figure 5-1.

Note that in both variations of the CSA A23.3-04 STM, Equations 5.1 and 5.2 are only required when calculating the strut capacity at the lower end of the diagonal strut in the

STM shown in Figure 5-1 since this is the location where the reinforcement crosses the strut. At the upper end of the diagonal strut, the strut capacity is limited by the nodal zone.

In both approaches, the capacity was calculated using an iterative process. The applied load was incremented until the stress in the diagonal strut at the face of the bottom nodal zone reached the limiting stress, f_{cu}, calculated using Equation 2.32. In each load increment, the moment at mid-span was calculated. By assuming the stress in the top horizontal strut to be $0.85f_c'$, the top strut height and the force in the FRP tie were calculated simultaneously. Once the dimension of the top strut was known, the truss configuration was complete. The diagonal strut angle, θ, was calculated based on the centerline of the strut and the forces in the diagonal struts were determined from equilibrium. The FRP strain at mid-span, ε_{frp}, was calculated by dividing the previously determined FRP tensile force by the axial stiffness ($E_{FRP}A_{FRP}$). Equation 5.1 and Equation 5.2 were used to calculate the transverse tensile strain across the diagonal strut for approach 1 and 2 respectively. Subsequently, the limiting compressive strut stress, f_{cu}, was calculated using Equation 2.32 and compared to the previously determined strut stress. These steps were repeated as the load was incremented. The maximum load was reached once the stress in the diagonal strut equalled the limiting compressive stress. The nodal stresses were calculated in each iteration. In all instances the maximum predicted load capacity was limited by diagonal strut crushing and not by tie or nodal failure. A flowchart defining the calculation procedure is shown in Figure 5-3. Note that in each iteration, the strain in the FRP was recalculated.

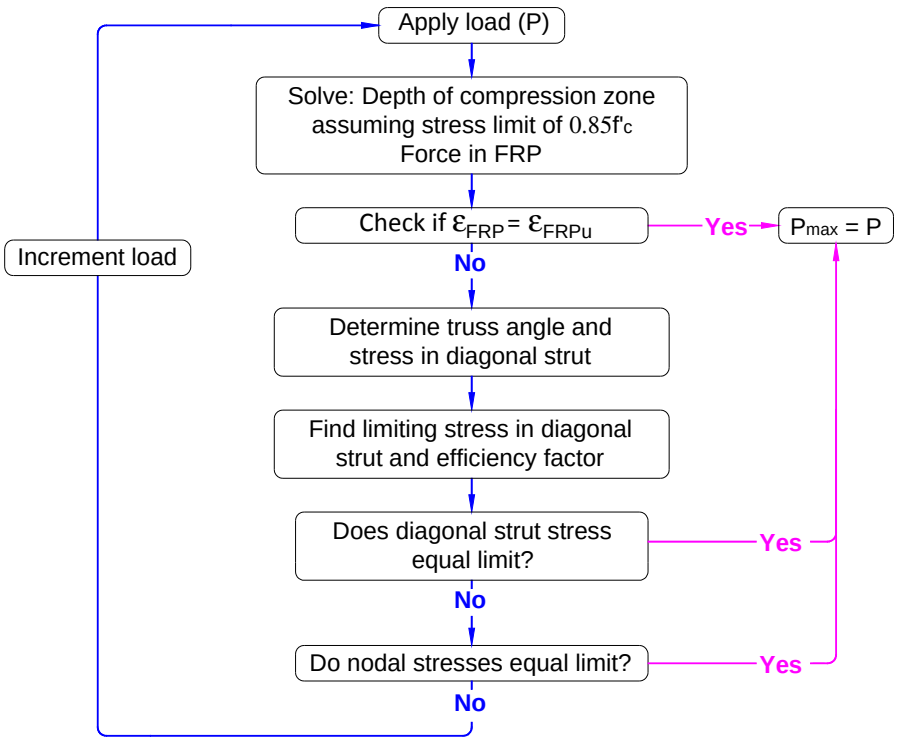

Figure 5-3: Iteration procedure to determine the load capacity of a FRP reinforced deep beam using STM.

Use of the CSA A23.3-04 STM for new construction requires that minimum distributed reinforcement be provided for crack control. Although no distributed reinforcement was provided in the specimens in this study, the STM model was applied regardless with the expectation that the predicted capacities may be higher than the experimental capacities in some cases due to the potential early failure of the struts from splitting action. However, it is noted that in some members it may be possible to have no distributed reinforcement spanning the disturbed region while still satisfying CSA A23.3-04 provisions. CSA A23.3-04 requires the ratio of the distributed reinforcement area to gross area to be at least 0.002 in each direction and the maximum spacing of this reinforcement to not exceed 300 mm. Therefore, in the specimens with h = 300 mm, it would be possible to have no distributed reinforcement in the shear span and still meet the code requirements (i.e. specimen A1N). Therefore, it was expected that the STM may become unconservative as h increases when no distributed reinforcement is present.

Table 5-1 shows the capacity predictions of the specimens using the two variations of the STM described above (i.e. Equation 5.1 and Equation 5.2). The predicted capacities, V_{cs1} and V_{cs2} for the capacity predictions using Equation 5.1 and Equation 5.2, respectively, were compared with the experimental results, V_{exp}. Figure 5-4 shows the relationship between a/d and the V_{exp}/V_{cs1} and V_{exp}/V_{cs2} ratios for the specimens.

Table 5-1: Capacity predictions using two variations of the CSA A23.3-04 STM.

Specimen	a/d	ρ (%)	f_c' (MPa)	h (mm)	Using Equation 5.1 (i.e. ε_{frp})				Using Equation 5.2 (i.e. $\varepsilon_{frp,c}$)			
					V_{c1} (kN)	V_{exp}/V_{c1}	$\varepsilon_{exp}/\varepsilon_{FRP}$*	ν_1**	V_{c2} (kN)	V_{exp}/V_{c2}	$\varepsilon_{exp}/\varepsilon_{FRP}$*	ν_2**
A1N	1.07	1.49	40.2	306	292	1.39	2.55	0.25	372	1.09	1.96	0.33
A2N	1.44	1.47	45.4	310	205	1.15	1.40	0.19	263	0.90	1.08	0.25
A3N	2.02	1.47	41.3	310	109	1.11	1.27	0.15	138	0.88	0.99	0.19
A4H	2.02	1.47	64.6	310	144	0.67	0.77	0.13	186	0.52	0.59	0.16
B1N	1.08	1.70	40.5	608	578	1.10	1.22	0.25	735	0.87	0.94	0.32
B2N	1.48	1.71	39.9	606	361	1.11	1.18	0.20	459	0.87	0.92	0.25
B3N	2.07	1.71	41.2	607	208	1.04	1.14	0.15	263	0.82	0.89	0.19
B4N	1.48	2.13	40.7	606	412	1.01	1.24	0.22	516	0.80	0.97	0.27
B5H	1.48	2.12	66.4	607	564	0.94	1.02	0.18	723	0.73	0.78	0.23
B6H	2.06	1.70	68.5	610	289	0.65	0.71	0.12	373	0.50	0.54	0.16
C1N	1.1	1.58	51.6	1003	1022	1.11	1.45	0.26	1305	0.87	1.12	0.33
C2N	1.49	1.56	50.7	1005	636	1.04	1.21	0.21	810	0.82	0.93	0.27
Mean – all specimens						1.03	1.26	0.19		0.81	0.98	0.25
Standard Deviation						0.20	0.46	0.05		0.16	0.36	0.06
Coefficient of Variation						0.20	0.36	0.25		0.20	0.36	0.25
Mean – specimens with $f_c' \approx 40$ MPa						1.12	1.41	0.21		0.88	1.09	0.27
Standard Deviation						0.11	0.44	0.04		0.09	0.34	0.05
Coefficient of Variation						0.10	0.31	0.20		0.10	0.31	0.20

*Strain at the centroid of the GFRP at mid-span where ε_{exp} is the average measured tensile strain at the centroid of the reinforcement at the peak load and ε_{FRP} is the strain corresponding to V_{c1} or V_{c2} as calculated by the STM, **the efficiency factor, ν, is discussed in section 5.1.1.4.

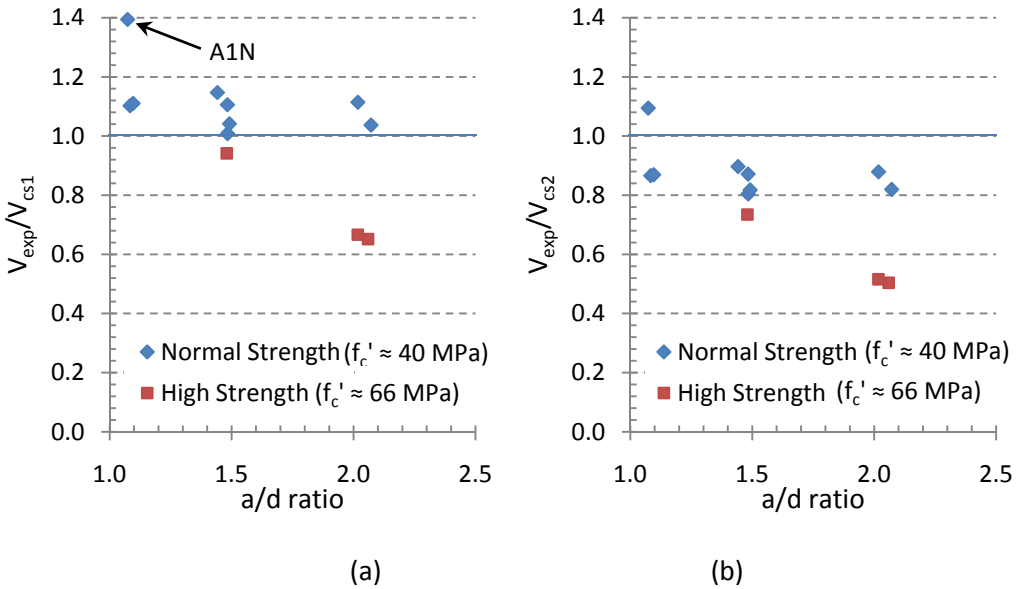

(a) (b)

Figure 5-4: Comparison of experimental shear capacity to predicted capacity from the CSA A23.3-04 STM using (a) ε_{frp} and (b) using $\varepsilon_{frp,c}$

The mean test to predicted capacity ratio, V_{exp}/V_{cs1}, when Equation 5.1 was used in the STM calculations was 1.03 with a 20% coefficient of variation (COV). All specimens with normal strength concrete ($f_c' \approx 40$ MPa) had a V_{exp}/V_{cs1} ratio greater than 1.0. The mean V_{exp}/V_{cs1} was 1.12 with a 10% COV for the subset of specimens with normal strength concrete. The specimens with high strength concrete ($f_c' \approx 66$ MPa) were over-predicted (i.e. $V_{exp}/V_{cs1} < 1.0$), especially specimens A4H and B6H which had an a/d ratio of 2.1 (Figure 5-4(a)). These two specimens exhibited crack patterns which prevented full direct compression struts from forming as discussed further in section 5.2. Specimen B5H was slightly over-predicted with $V_{exp}/V_{cs1} = 0.94$, but unlike specimens A4H and B6H, this beam developed a complete arching mechanism. With the exception of specimen A1N and the specimens with the high strength concrete, no discernable trend in V_{exp}/V_{cs1} was noticed in Figure 5-4(a) indicating the STM properly accounts for the influence of the a/d ratio on capacity.

Table 5-1 also shows the ratio of the experimental strain (ε_{frp}) at peak load to the STM predicted strain at the centroid of the FRP at mid-span. With the exception of specimens A4H and A6H, the experimental to predicted strain ratios were greater than 1.0 with a mean of 1.26 and a COV of 36%. Specimen A1N has an experimental to predicted strain ratio of 2.55. Specimen A1N failed in flexure and at a load 39% higher than predicted which corresponds to a higher FRP strain at failure. As the horizontal compression zone between the loading plates crushed, the neutral axis was forced downwards and the internal moment arm was reduced. A reduction in the internal moment arm resulted in higher forces in the horizontal compression zone and in the FRP reinforcement leading to substantially higher FRP strains.

When Equation 5.2 was used in calculating the capacities of the specimens, the mean test to predicted ratio V_{exp}/V_{cs2} was 0.81 with a 20% COV. No discernable trend in V_{exp}/V_{cs2} with respect to the a/d ratio was observed for the specimens with normal strength concrete (Figure 5-4(b)). However, as the a/d ratio increased 40% from 1.5 to 2.1 for the high strength concrete specimens, V_{exp}/V_{cs2} decreased by 32%, from 0.73 to 0.50. With the exception of specimen A1N, all specimens had V_{exp}/V_{cs2} ratios of less than 1.0. In addition, the predicted mid-span FRP strain was slightly greater than the measured peak load strain with a mean experimental to predicted strain ratio of 0.98 (Table 5-1).

5.1.1.2 ACI 318-08

Shear capacity predictions were made using the ACI 318-08 Appendix A strut and tie modelling provisions. Since the specimens did not contain distributed reinforcement, the stress limit in the bottle-shaped diagonal struts was defined by Equation 2-35 with β_s taken as 0.6. Using an iterative procedure, the shear capacity, V_{cs3}, of each specimen was determined. In each iteration the load was incremented until the model predicted failure through strut crushing. Nodal crushing and FRP rupture did not govern the load

capacity of any specimens in this study. The depth of the top horizontal strut and the force in the reinforcement were calculated simultaneously by assuming a stress in the top strut of $0.85f_c'$ to resist the applied moment at mid-span. The diagonal strut angle was determined and the diagonal forces calculated. The strut stress was critical at the upper end of the bottle-shaped strut which had a smaller cross-sectional area. A flowchart of the calculation procedure is given in Figure 5-3. Contrary to the CSA A23.3-04 STM, the ACI 318-08 diagonal strut stress factor is constant, simplifying the calculation of the limiting strut stress. The calculated shear capacities according to the ACI 318-08 STM are given in Table 5-2.

Table 5-2 shows that the ACI 318-08 STM gave capacity predictions that were greater than the experimental capacities (i.e. $V_{exp}/V_{cs3} < 1.0$) for all specimens except specimen A1N. Specimen A1N had $V_{exp}/V_{cs3} = 1.0$. The mean experimental to predicted shear capacity (V_{exp}/V_{cs3}) ratio was 0.60 with a 34% COV. As the a/d ratio increased, the ACI model gave increasingly smaller V_{exp}/V_{cs3} ratios as shown in Figure 5-5 indicating poor modelling correlation with the a/d ratio. In addition, the specimens with high concrete strength ($f'_c \approx 66$ MPa) and $a/d = 2.1$ had very poor shear capacity predictions ($V_{exp}/V_{cs3} \approx 0.28$) compared to the specimens with normal strength concrete ($f'_c \approx 40$ MPa). El-Sayed et al. (2006), using a similar strut and tie modelling procedure, also reported that the V_{exp}/V_{cs3} ratio was less than 1.0 for all FRP reinforced deep beams with an average $V_{exp}/V_{cs3} = 0.63$.

For the majority of specimens tested in this study, the predicted mid-span strain in the reinforcement, ε_{FRP}, as calculated by the ACI 318-08 STM was higher than the measured strain at the peak load, ε_{exp}. The mean $\varepsilon_{exp}/\varepsilon_{FRP}$ ratio was 0.72 with a 53% COV.

Table 5-2: Capacity predictions using the ACI 318-08 STM.

Specimen	a/d	ρ (%)	f_c' (MPa)	h (mm)	V_{cs3} (kN)	V_{exp}/V_{cs3}	$\varepsilon_{exp}/\varepsilon_{FRP}$*
A1N	1.07	1.49	40.2	306	409	1.00	1.77
A2N	1.44	1.47	45.4	310	358	0.66	0.77
A3N	2.02	1.47	41.3	310	221	0.55	0.60
A4H	2.02	1.47	64.6	310	346	0.28	0.31
B1N	1.08	1.70	40.5	608	791	0.80	0.87
B2N	1.48	1.71	39.9	606	589	0.68	0.69
B3N	2.07	1.71	41.2	607	411	0.52	0.55
B4N	1.48	2.13	40.7	606	601	0.69	0.82
B5H	1.48	2.12	66.4	607	982	0.54	0.56
B6H	2.06	1.70	68.5	610	690	0.27	0.28
C1N	1.1	1.58	51.6	1003	1661	0.68	0.86
C2N	1.49	1.56	50.7	1005	1253	0.53	0.58
Mean						0.60	0.72
Standard Deviation						0.20	0.38
Coefficient of Variation						0.34	0.53
Mean – specimens with $f_c' \approx 40$ MPa						0.68	0.83
Standard Deviation						0.15	0.37
Coefficient of Variation						0.22	0.44

*Strain at the centroid of the GFRP at mid-span where ε_{exp} is the average measured tensile strain at the centroid of the reinforcement at the peak load and ε_{FRP} is the strain corresponding to V_{c3} as calculated by the STM.

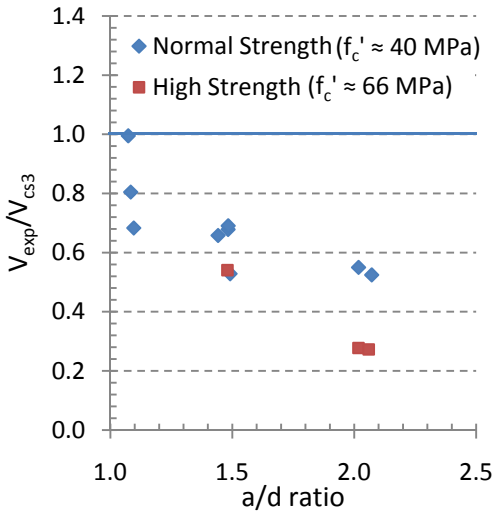

Figure 5-5: Comparison of experimental shear capacity to predicted capacity from the ACI 318-08 STM.

5.1.1.3 Additional Specimens from Previous Studies

The three STMs described in sections 5.1.1.1 and 5.1.1.2 were also used to predict the shear capacities of the 24 FRP reinforced deep beam specimens from the El-Sayed (2006) and Nehdi et al. (2008) experimental research programs. In these two previous research programs, 12 of the specimens were reinforced with carbon FRP and 12 with glass FRP. The majority of the specimens had overall heights smaller than in the current study with member heights ranging from h = 200 mm to 400 mm. Specimen II-C-1.2/0.9 tested by El-Sayed (2006) was removed from the database as the failure capacity of this specimen was not determined due to the specimen strength exceeding the testing frame capacity.

The experimental shear capacity to the STM prediction ratios are given in Table 5-3 for the three different STM models. The average experimental capacities to predicted ratios were V_{exp}/V_{cs1} = 1.29, V_{exp}/V_{cs2} = 1.04, and V_{exp}/V_{cs3} = 1.24 for the STMs using the CSA A23.3-04 model with Equation 5.1 and Equation 5.2, and the ACI 318-08 model, respectively.

Table 5-3 also shows the average experimental to predicated shear capacity ratio for the specimens when grouped according to carbon and glass FRP reinforcement. The two CSA A23.3-04 STMs have comparable average V_{exp}/V_{cs} ratios for the specimens reinforced with carbon and glass FRP. The ACI 318-08 STM has V_{exp}/V_{cs3} = 1.40 (COV = 39%) and 1.07 (COV = 36%) for the specimens with carbon and glass FRP reinforcement, respectively. The low V_{exp}/V_{cs3} ratio for GFRP reinforced specimens when compared with the CFRP reinforced specimens and the high COV in both cases indicated that the ACI 318-08 STM was not able to provide similar prediction quality as the reinforcement stiffness changed.

Contrary to what was found for the specimens in the current experimental program, the ACI 318-08 model had a mean V_{exp}/V_{cs3} ratio slightly greater than 1.0 for both the carbon and glass reinforced beams when taken in aggregate. However, a closer examination of Table 5-3 indicates that only 1/3 of the El-Sayed (2006) specimens had $V_{exp}/V_{cs3} \geq 1.0$ while 13/15 specimens had $V_{exp}/V_{cs3} \geq 1.0$ in the Nehdi et al. (2008) test program. Some of the specimens from Nehdi et al. (2008) had experimental capacities that were greater than the predicted capacity by a factor of almost three. The reason for the large discrepancy is not known as neither Nehdi et al. (2008) nor Omeman et al. (2008) provided crack diagrams or detailed explanations of the beam behaviour. However, the boundary conditions in the test setup may have provided some longitudinal restraint thereby increasing the load carrying capacity of the specimens. One of the two loading points and a support were pinned (Omeman et al. 2008).

Table 5-3: Shear capacity predictions of specimens from previous studies using the CSA A23.3-04 and ACI 318-08 STM.

Reference	Specimen	d (mm)	f_c' (MPa)	a/d ratio	ρ (%)	FRP type	E_{frp} (GPa)	V_{exp} (kN)	CSA A23.3-04		ACI 318-08
									V_{exp}/V_{cs1}	V_{exp}/V_{cs2}	V_{exp}/V_{cs3}
El-Sayed (2006)*	II-C-0.7/1.6	326	40	1.69	0.78	carbon	134	179.5	0.98	0.79	0.82
	II-C-1.2/1.3	326	40	1.3	1.24	carbon	134	372	1.16	0.95	1.30
	II-C-1.2/1.6	326	40	1.69	1.24	carbon	134	195	0.92	0.76	0.89
	II-C-1.7/1.6	326	40	1.69	1.71	carbon	134	233.5	1.00	0.84	1.07
	II-G-0.8/1.6	326	40	1.69	0.78	glass	42	164.5	1.37	1.05	0.75
	II-G-1.2/0.9	326	40	0.92	1.24	glass	42	450.5	1.33	1.04	1.22
	II-G-1.2/1.3	326	40	1.3	1.24	glass	42	269	1.25	0.97	0.94
	II-G-1.2/1.6	326	40	1.69	1.24	glass	42	175	1.22	0.95	0.80
	II-G-1.7/1.6	326	40	1.69	1.71	glass	42	196	1.21	0.96	0.89
Nehdi et al. (2008)**	CF-B-1	150	34.7	1.55	1.13	carbon	134	92.6	1.31	1.08	1.49
	CF-B-1.5	150	38.9	1.83	1.13	carbon	134	77.5	1.32	1.08	1.34
	CF-B-2	150	40.6	2.33	1.13	carbon	134	45.8	1.16	0.96	1.04
	CF-pl-1.5	150	37.4	1.83	1.69	carbon	134	81.2	1.26	1.06	1.46
	CF-pl-2.0	150	39.6	1.83	2.26	carbon	134	92.8	1.28	1.10	1.57
	CF-d-250	250	41.7	1.41	1.35	carbon	134	149.1	1.21	1.01	1.75
	CF-d-350	350	37.6	1.36	1.21	carbon	134	234.1	1.77	1.49	2.92
	CF-f'c-60	150	63.1	1.83	1.13	carbon	134	113. 5	1.40	1.12	1.21
	F-B-1	150	35.5	1.55	1.29	glass	40.8	67.8	1.36	1.06	1.06
	F-B-1.5	150	48	1.83	1.29	glass	40.8	64.3	1.39	1.08	0.90
	F-B-2	150	48	2.33	1.29	glass	40.8	28.9	0.96	0.74	0.55
	F-pl-1.5	150	48	1.83	1.72	glass	40.8	73.6	1.43	1.12	1.03
	F-pl-2.0	150	35.2	1.83	2.31	glass	40.8	61.0	1.30	1.04	1.17
	F-d-250	250	42	1.41	1.39	glass	40.8	121.6	1.46	1.14	1.42
	F-d-350	350	48	1.36	1.25	glass	40.8	211.3	1.99	1.55	2.06
All Specimens											
Mean									1.29	1.04	1.24
Standard Deviation									0.24	0.19	0.50
Coefficient of Variation									0.18	0.18	0.40
El-Sayed Specimens											
Mean									1.16	0.92	0.97
Coefficient of Variation									0.14	0.11	0.20
Nehdi Specimens											
Mean									1.37	1.11	1.40
Coefficient of Variation									0.18	0.17	0.40
Carbon Reinforced Specimens											
Mean									1.23	1.02	1.40
Coefficient of Variation									0.18	0.19	0.39
Glass Reinforced Specimens											
Mean									1.35	1.06	1.07
Coefficient of Variation									0.18	0.18	0.36

*specimens from El-Sayed (2006) had b_w = 250 mm

**specimens from Nehdi et al. (2008) had b_w = 150 mm

The results from the El-Sayed research program were consistent with the results obtained from the current study. In the current study, the CSA A23.3-04 model utilizing

Equation 5.1 gave average experimental to predicted capacity ratios that were greater than 1.0 while the CSA A23.3-04 model using Equation 5.2 and the ACI 318-08 model gave experimental to predicted capacity ratios that were less than 1.0. For all three models, the COV was lower for the specimens in the current study when compared to the specimens from Nehdi et al. (2008).

In general, the ACI 318-08 model produced a large amount of scatter regardless of the specimen configurations; the coefficient of variation was double that of the two CSA A23.3-04 STMs.

5.1.1.4 Comparison of the Strut and Tie Models

Based on Table 5-1, Table 5-2, Table 5-3, Figure 5-4, and Figure 5-5, the CSA A23.3-04 STM where the diagonal strut capacity is calculated using the full mid-span tie strain (i.e. Equation 5.1) gave the best predictions for all specimens analyzed. The results from the large-scale specimens tested in the current study were combined with the results from previous researchers (Table 5-3) to form a database of 36 specimens. The CSA A23.3-04 STM using ε_{frp} (i.e. Equation 5.1) to calculate the shear capacity had a mean V_{exp}/V_{cs1} ratio of 1.20 with a COV of 21%. The CSA A23.3-04 STM based on $\varepsilon_{frp,c}$ (i.e. Equation 5.2) had a mean V_{exp}/V_{cs2} ratio of 0.96 with a COV of 22%. The ACI 318-08 STM had a mean V_{exp}/V_{cs3} ratio of 1.02 with a COV of 51%. Figure 5-6 and Figure 5-7(a) show the experimental to predicted ratio versus the a/d ratio for each specimen for the three different STMs. The CSA A23.3-04 model using Equation 5.1 gave the safest predictions with only 17% of the specimens having $V_{exp}/V_{cs1} < 1.0$. The majority (56%) of the specimens had $V_{exp}/V_{cs2} < 1.0$ when Equation 5.2 was used as shown in Figure 5-6(b). Poor predictions were given by the ACI 318-08 model even though it had a mean V_{exp}/V_{cs3} of almost 1.0. Using the ACI 318-08 model resulted in predictions where 53% of the specimens had $V_{exp}/V_{cs3} < 1.0$. Figure 5-7(a) demonstrates the variability in the predictions as a/d changed indicating that the ACI 318-08 STM was incapable of accurately modelling FRP reinforced concrete members for all practical a/d ratios.

Nehdi et al. (2008) found that the ACI 318-08 model became very conservative as the effective depth, d, of the beams increased beyond 300 mm. However, Nehdi et al. (2008) conducted the experimental study using specimens with typically very small effective depths, d, of 150 mm with only two specimens that had d slightly greater than 300 mm. Figure 5-7(b) shows the experimental to predicted shear capacity ratios with respect to the effective depth of the specimens using the ACI 318-08 STM. The large-scale specimens from the current experimental program indicated that the ACI 318-08 STM predictions were significantly greater than the experimental capacities and that the two experimental results from Nehdi et al. (2008) having effective depths greater than 300 mm appear to be outliers.

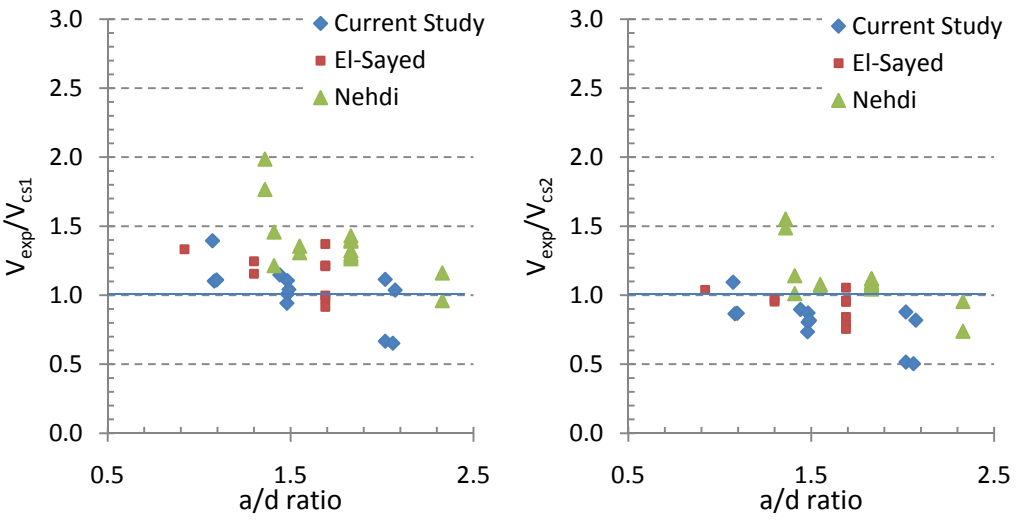

Figure 5-6: Comparison of the experimental shear capacity to the predicted capacity from the CSA A23.3-04 STM using (a) ε_{frp} and (b) using $\varepsilon_{frp,c}$.

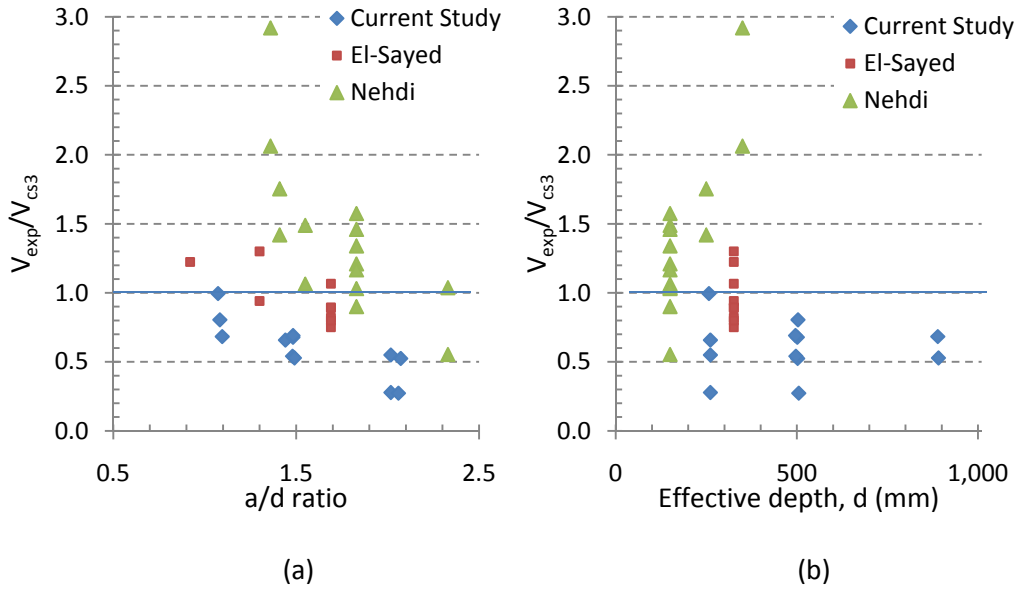

Figure 5-7: Comparison of the experimental shear capacity to the predicted capacity from ACI 318-08 STM with respect to (a) a/d ratio and (b) effective depth.

Contrary to the ACI 318-08 STM, the two models adopted from CSA A23.3-04 were able to account for the influence of the a/d ratio and effective depth, d. No overall trend was identified in the V_{exp}/V_{cs} ratios as the a/d ratio and d increased as seen in Figure 5-6 and Figure 5-8. The ACI 318-08 STM showed a decreasing V_{exp}/V_{cs3} ratio as the a/d ratio and d increased (Figure 5-7).

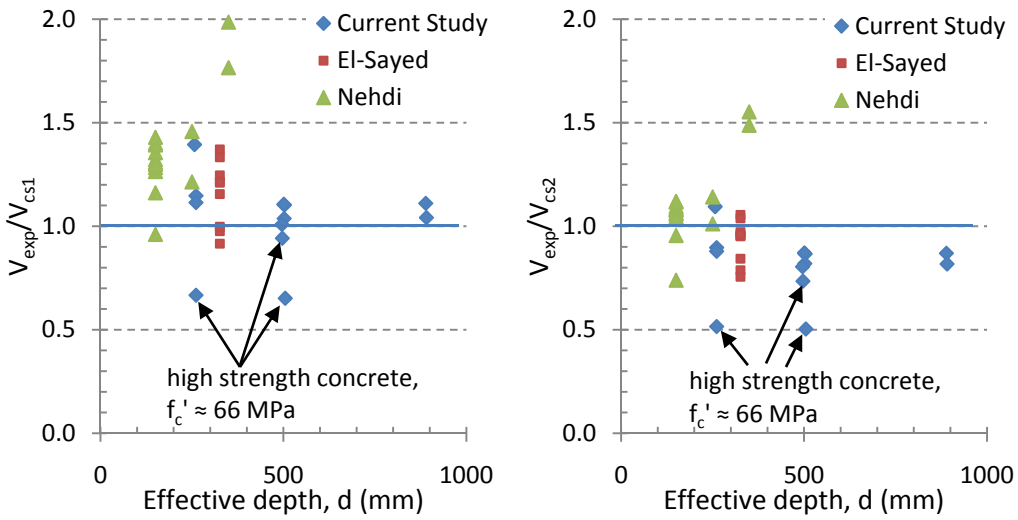

Figure 5-8: Comparison of experimental shear capacity to predicted capacity from the CSA A23.3-04 STM with respect to d using (a) ε_{frp} and (b) using $\varepsilon_{frp,c}$.

The CSA A23.3-04 STM indirectly incorporates the a/d ratio, ρ, and reinforcement stiffness, $A_{FRP}E_{FRP}$, and directly incorporates b_w and f_c'. The three variables, a/d, ρ, and $A_{FRP}E_{FRP}$ all influence the strength of the diagonal strut and are collectively accounted for in the efficiency factor, ν, used to calculate the strut compressive capacity. The strut capacity equation (i.e. Equation 2.32 or 2.35) can be written as:

$$f_{cu} = \nu f_c' \qquad \textbf{5.4}$$

where the efficiency factor for the CSA A23.3-04 STM is given as:

$$\nu = \frac{1}{0.8 + 170\varepsilon_1} \leq 0.85 \qquad \textbf{5.5}$$

Efficiency factors for the tested specimens were calculated using Equation 5.5 during the iterative process to solve the predicted shear capacity (see Figure 5-3) and are shown in Table 5-1 for the two CSA A23.3-04 STMs. The efficiency factors, ν_1 and ν_2 correspond to V_{cs1} and V_{cs2}, respectively. The efficiency factors decreased as the a/d ratio increased as shown in Figure 5-9 and ranged from 0.12 to 0.26 and 0.16 to 0.33 for ν_1 and ν_2, respectively.

In ACI 318-08, the efficiency factor is given as:

$$\nu_{ACI} = 0.85\beta_s \qquad \textbf{5.6}$$

and β_s is 0.6 for bottle-shaped struts containing no distributed reinforcement as was the case in this study. Therefore, the efficiency factor when using the ACI 318-08 STM was a

constant value of ν_{ACI} = 0.51 regardless of the specimen geometry or the configuration of the STM.

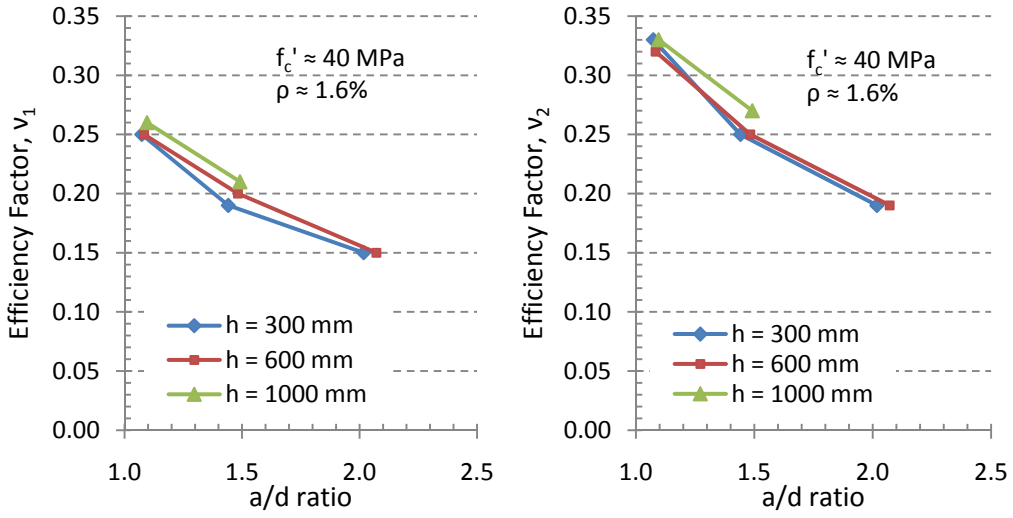

(a) (b)

Figure 5-9: Efficiency factors for the diagonal struts calculated from the CSA A23.3-04 STM using (a) ε_{frp} (Equation 5.1) and (b) $\varepsilon_{frp,c}$ (Equation 5.2).

The ACI 318-08 STM is an empirically derived model and the efficiency factor, ν_{ACI}, was established for use with steel reinforced members and does not necessarily apply to other reinforcement types. The ACI 318-08 efficiency factor is also independent of the a/d ratio. As the a/d ratio increases, the CSA A23.3-04 model predicts a lower maximum strut stress due to a smaller θ (Equation 5.1 and 5.2) while the ACI 318-08 maximum strut stress remains constant. The a/d ratio is taken into account through the strut angle, θ, when calculating the ε_1 term in Equation 5.5. As a result, the V_{exp}/V_{cs3} ratio from the ACI 318-08 STM model decreases with increasing a/d ratio as indicated in Figure 5-5. In contrast, Figure 5-4 shows no a/d dependence as observed from the experimental to predicted capacity ratios for the CSA A23.3-04 STMs, indicating the CSA A23.3-04 STM was capable of properly considering the effects of the a/d ratio.

The CSA A23.3-04 efficiency factor also accounts for the strain in the reinforcement. Higher reinforcement strains result in more or wider cracks leading to a degradation of the strut capacity. Since GFRP has a lower Young's modulus than steel, it is expected that wider cracks occur in GFRP reinforced deep beams when compared to steel reinforced beams with identical capacity. The experimental programs conducted by Nehdi et al. (2008) and El-Sayed (2006) confirmed that wider cracks occur in GFRP reinforced deep beams when compared to steel reinforced deep beams. Wider cracks result in less strut confinement which lowers the compressive capacity of the strut. The CSA A23.3-04 efficiency factor, which is based on the MCFT, decreases as the reinforcement strain increases (CSA A23.3-04 explanatory note N11.4.2.3). In the STM

shown in Figure 5-1, the strut capacity is calculated at the bottom using Equation 5.5 since this is the location where the tension tie crosses the strut. At the top end of the strut, the strut capacity is calculated based on the node capacity which is a compression only node and has an efficiency factor of 0.85. In contrast, ACI 318-08 calculates the strength of the bottle-shaped strut at either end using the same efficiency factor of 0.51. The ACI 318-08 model assumes that the spreading of the force in the bottle-shaped strut will cause cracking but neglects to account for additional cracking at the lower end of the strut due to the tension tie. Figure 5-9 together with Figure 5-4 and Figure 5-5 demonstrates that the efficiency factor cannot remain constant if the prediction ratios are to remain consistent and hence, the ACI 318-08 STM constant efficiency factor approach is not suitable to FRP reinforced deep beams.

Both the CSA A23.3-04 and the ACI 318-08 STM directly account for the compressive strength of the concrete in the strut capacity and node capacity calculations. However, only CSA A23.3-04 has lower and upper limits of 20 MPa and 80 MPa, respectively, on the compressive strength of concrete. No limitation on the compressive strength of the concrete was found in ACI 318-08 Appendix A. Bahen and Sanders (2009) identified that both the ACI 318-08 and AASHTO (2007) STMs can give unconservative predictions of member strength when the concrete strength exceeds 41 MPa and 48 MPa in steel reinforced beams, respectively. The AASHTO 2007 STM is similar to the model in CSA A23.3-04 and Bahen and Sanders' (2009) findings also apply. The ACI 318-08 model was found to give unconservative predictions of member strength for all concrete strengths regardless of whether crack control reinforcement was used, which is similar to the findings in this study with FRP reinforced deep beams. Brown et al. (2005) also reported that the ACI 318-08 and AASHTO (2007) STMs gave an "unacceptable" number of unconservative strength predictions for specimens containing no web reinforcement. The AASHTO 2007 STM design provisions, similar to the CSA A23.3-04 STM provisions, require installation of minimum quantities of distributed steel reinforcement. Similar results as reported by Brown et al. (2005) and Bahen and Sanders (2009) were obtained with the high strength concrete specimens in this study. Specimens A4H and B6H had a compressive strength of 65 MPa and 69 MPa, respectively, and had V_{exp}/V_{cs} ratios less than 1.0 when calculated using the CSA A23.3-04 and the ACI 318-08 STMs. However, since no distributed reinforcement was present in the specimens, no conclusion can be drawn about whether the CSA A23.3-04 STM model is valid for high strength concrete specimens.

Regardless of whether high strength concrete is used, the ACI 318-08 STM is not well adapted for use with FRP reinforced deep beams since it does not consider the influence of the reinforcement mechanical properties.

5.1.2 Sectional Shear Models

Numerous models are available in the codes and literature that have been developed to model the shear capacity of slender members containing internal FRP reinforcement. Since no design guidelines are available specifically for deep members containing FRP reinforcement, designers may also use sectional design methods for deep members. This section examines whether the shear capacities of the FRP reinforced deep members can be accurately predicted using the seven sectional models described in section 2.5. The experimental to predicted shear capacity ratios, V_{exp}/V_c, are given in Table 5-4 for the specimens from the current study. The critical section used in analysis was taken at d_v (d for the CSA S806-02 and Razaqpur and Isgor (2006) models) from the loading point towards the support if a/d > 2.0. For specimens which had a/d ≤ 2.0, the critical section was assumed to be at a/2, at the mid-point of the shear span. Note that the CSA S6-06 (2009) and CSA A23.3-04 sectional shear models are the same and only the ratios from CSA A23.3-04 are discussed in this section.

Table 5-4: Experimental to predicted sectional shear capacity ratios of the deep beam specimens.

Beam	a/d	ρ (%)	f_c' (MPa)	h (mm)	V_{exp} (kN)	V_{exp}/V_c					
						ACI 440.1R-06	ISIS 2007	CSA S806-02	CSA A23.3-04*	Hoult et al. (2008)	Razaqpur and Isgor (2006)
A1N	1.07	1.49	40.2	306	407	11.1	8.9	5.0	6.1	5.2	4.0
A2N	1.44	1.47	45.4	310	236	6.1	4.8	2.8	3.4	3.0	2.2
A3N	2.02	1.47	41.3	310	122	3.2	2.6	1.5	1.9	1.7	1.2
A4H	2.02	1.47	64.6	310	96	2.3	1.6	1.0	1.4	1.2	0.7
B1N	1.08	1.70	40.5	608	637	8.9	8.8	7.7	5.5	4.8	4.2
B2N	1.48	1.71	39.9	606	400	5.6	5.6	4.9	3.5	3.2	2.7
B3N	2.07	1.71	41.2	607	216	3.0	3.0	2.6	2.0	1.8	1.4
B4N	1.48	2.13	40.7	606	415	5.1	5.5	5.0	3.2	3.0	2.7
B5H	1.48	2.12	66.4	607	531	5.7	5.5	5.0	3.9	3.6	2.8
B6H	2.06	1.70	68.5	610	188	2.3	2.0	1.7	1.7	1.5	1.0
C1N	1.1	1.58	51.6	1003	1135	8.2	9.3	7.4	5.8	5.3	5.3
C2N	1.49	1.56	50.7	1005	662	4.8	5.4	4.3	3.4	3.2	3.1
Mean						5.53	5.25	4.07	3.47	3.12	2.60
Standard Deviation						2.75	2.68	2.19	1.63	1.41	1.41
Coefficient of Variation						0.50	0.51	0.54	0.47	0.45	0.54

*CSA A23.3-04 and CSA S6-06 (2009) are the same model and have the same ratios.

The ACI 440.1R-06 sectional shear model was extremely conservative especially in the case of specimen A1N which had a test to predicted capacity ratio of 11.1. The ACI 440.1R-06 model does not account for arch action or the influence of the a/d ratio on member strength. From Figure 5-10 it is apparent that the ACI 440.1R-06 sectional shear model gave better predictions as the a/d ratio approached 2.5. Similar to the ACI

440.1R-06 model, the ISIS (2007) sectional shear model gave highly conservative shear capacity predictions at low a/d values as shown in Figure 5-11. At a/d = 1.1, the average V_{exp}/V_c ratio was 9.0 and decreased to an average V_{exp}/V_c = 2.3 at a/d = 2.1.

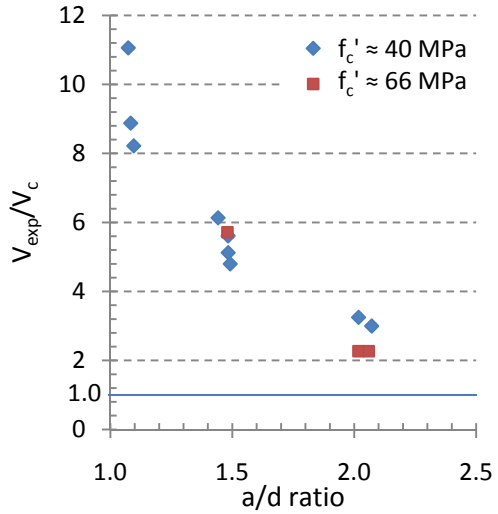

Figure 5-10: Shear capacity predictions using the ACI 440.1R-06 sectional shear model.

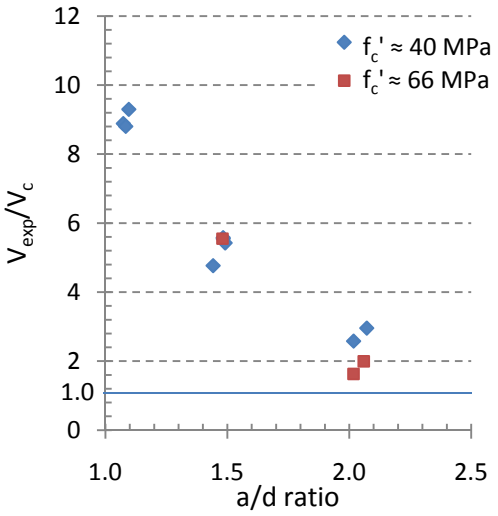

Figure 5-11: Shear capacity predictions using the ISIS (2007) sectional shear model.

The CSA S806-02 sectional shear model has two separate sets of equations depending on whether the effective depth, d, is greater than 300 mm. From Figure 5-12 it is apparent that the equation for members having d < 300 mm produces better predictions than the equation for taller members when compared against the members tested in this study. The equation for taller members incorporates a size effect for sectional shear, however, arch action is unaccounted for and the predictions for the taller specimens were even more conservative than the h = 300 mm specimens.

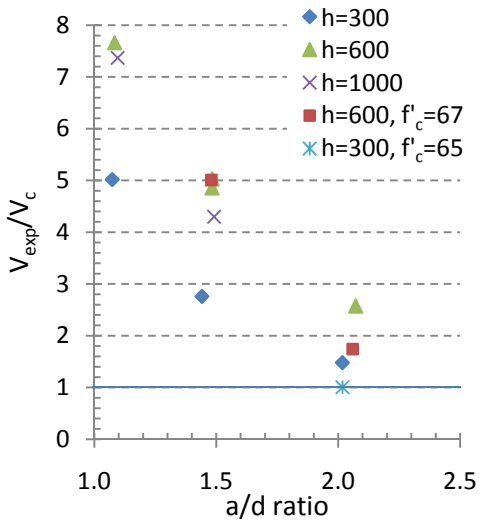

Figure 5-12: Shear capacity predictions using the CSA S806-02 sectional shear model.

An iterative technique was required to calculate the shear capacities of specimens using the CSA S6-06/CSA A23.3 and Hoult et al. (2008) sectional shear models. In calculating the shear capacity, the moment and shear at the critical section was used in the calculation of the longitudinal strain, ε_x, at mid-depth of the member as described in section 2.5. The shear capacity was calculated by increasing the load until the applied shear equalled the shear capacity at the critical section. The relationship between the experimental to predicted shear capacities and a/d ratio for the CSA S6-06/CSA A23.3 and Hoult et al. (2008) models are plotted in Figure 5-13 and Figure 5-14, respectively.

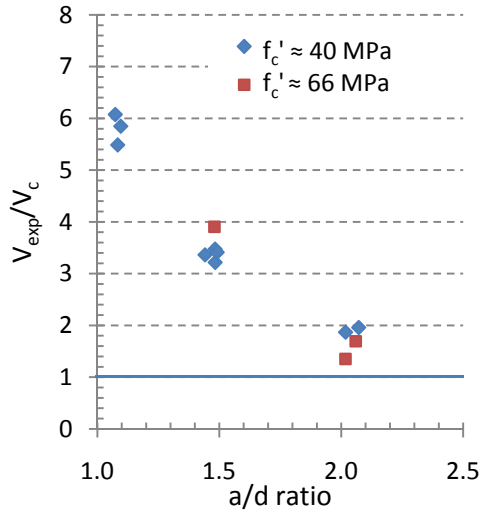

Figure 5-13: Shear capacity predictions using the CSA A23.3-04 sectional shear model.

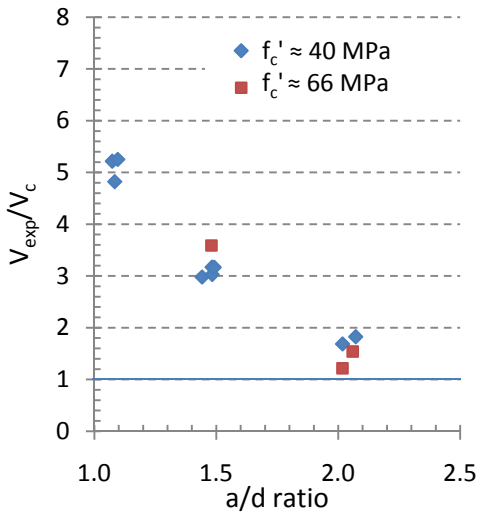

Figure 5-14: Shear capacity predictions using the Hoult et al. (2008) sectional shear model.

Unlike the CSA S806-02 model (Figure 5-12), all three sectional shear models, CSA S6-06, CSA A23.3-04, and Hoult et al. (2008), gave consistent results for member having the same a/d ratio but different heights, h. This indicated that these models were able to consistently account for the influence of member height on shear capacity. However, these models were not capable of accurately predicting the shear capacity of deep beams for all specimen configurations. Better predictions were obtained as the a/d ratio increased. Of the three models, the Hoult et al. (2008) model gave the best predictions at all a/d ratios. As discussed in section 2.5.2.2, Hoult et al. (2008) showed that the model was better than the CSA A23.3-04 sectional shear model for the range of ε_x values expected in slender members reinforced with FRP.

The Razaqpur and Isgor (2006) sectional shear model, which was specifically formulated for beams containing no transverse reinforcement, including those with small a/d ratios, increasingly under-predicted the shear capacity as the a/d ratio decreased as shown in Figure 5-15. Even though the model was intended to also be used on members having small a/d ratios, the model was incapable of properly accounting for the a/d ratio. Although better than the CSA S806-02 sectional shear model, the Razaqpur and Isgor (2006) model displayed a similar trend in which the size effect in shear was poorly modelled as indicated in Figure 5-15. For any given a/d ratio, specimens with a smaller d have V_{exp}/V_c ratios closer to 1.0 than specimens with larger d. In the case of the specimens having an a/d ratio of 2.1 and high strength concrete (A4H and B6H), the V_{exp}/V_c ratios were less than or equal to 1.0. It is possible that the Razaqpur and Isgor (2006) shear model may be even more unconservative at larger a/d ratio, but this issue was outside the scope of the current research project.

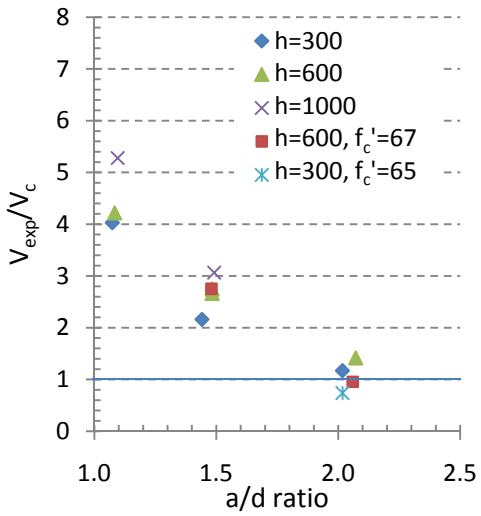

Figure 5-15: Shear capacity predictions using the Razaqpur and Isgor (2006) sectional shear model.

In general, all of the sectional shear models examined were incapable of properly modelling the capacity exhibited through arch action at small a/d ratios. The models became increasingly conservative as the a/d ratio decreased. The ACI 440.1R-06 sectional shear model had the worst predictions of the shear models studied for the members tested. Even at an a/d ratio of 2.1 the ACI 440.1R-06 shear model had V_{exp}/V_c ratios that were greater than 2.0. Of the three sectional shear models based on the modified compression field theory (CSA S6-06, CSA A23.3-04, and Hoult et al. 2008), the Hoult et al. (2008) model gave the best predictions. This was expected as the Hoult et al. (2008) model is an enhanced version of the steel reinforced shear model (CSA A23.3-04) and takes into consideration the typically higher reinforcement strains when FRP is used instead of steel. The Razaqpur and Isgor (2006) sectional shear model gave the best overall predictions (Table 5-4). However, this model resulted in an average V_{exp}/V_c ratio of 0.9 for the two specimens with $f_c' \approx 66$ MPa and an a/d ratio of 2.1. As indicated earlier, the Razaqpur and Isgor (2006) sectional shear model had some scatter at any particular a/d ratio due to changes in h while the Hoult et al. (2008) sectional shear model did not exhibit as much scatter.

The shear capacity predictions for the specimens tested by Nehdi et al. (2008) and El-Sayed (2006) are given in Table 5-5. The average experimental to predicted shear capacity ratios were similar to the values obtained for the specimens in the current study and ranged from 2.60 to 5.77 for the Razaqpur and Isgor (2006) and ACI 440.1R-06 sectional shear models, respectively. While large V_{exp}/V_c ratios were generated by the sectional shear models, large values of COV were also obtained that ranged from 32% to 47%. The standard deviation ranged from 0.84 for the Razaqpur and Isgor (2008) model to 2.16 for the ACI 440.1R-06 sectional shear model.

Table 5-5: Shear capacity predictions of specimens from previous research programs using sectional shear models.

Reference	Specimen	a/d ratio	FRP type	V_{exp}/V_c					
				ACI 440.1R-06	ISIS Canada	CSA S806-02	CSA A23.3-04*	Hoult et al. 2008	Razaqpur and Isgor (2006)
El-Sayed	II-C-0.7/1.6	1.69	carbon	3.76	2.17	3.55	2.14	2.05	1.80
	II-C-1.2/1.3	1.3	carbon	6.38	4.50	7.37	3.75	3.61	3.73
	II-C-1.2/1.6	1.69	carbon	3.35	2.36	3.86	1.97	1.95	1.96
	II-C-1.7/1.6	1.69	carbon	3.52	2.82	4.62	2.12	2.14	2.34
	II-G-0.8/1.6	1.69	glass	5.81	3.55	3.26	3.13	2.72	1.65
	II-G-1.2/0.9	0.92	glass	12.83	9.73	8.92	7.05	5.90	4.52
	II-G-1.2/1.3	1.3	glass	7.66	5.81	5.33	4.21	3.67	2.70
	II-G-1.2/1.6	1.69	glass	4.99	3.78	3.47	2.74	2.48	1.76
	II-G-1.7/1.6	1.69	glass	4.84	4.23	3.88	2.70	2.51	1.97
Nehdi et al.	CF-B-1	1.55	carbon	6.26	4.27	3.49	3.39	3.12	3.49
	CF-B-1.5	1.83	carbon	5.06	3.37	2.76	2.74	3.82	2.76
	CF-B-2	2.33	carbon	2.95	1.95	1.62	1.71	1.59	1.59
	CF-pl-1.5	1.83	carbon	4.53	3.61	2.95	2.53	2.44	2.95
	CF-pl-2.0	1.83	carbon	4.55	4.00	3.28	2.59	2.53	3.28
	CF-d-250	1.41	carbon	5.30	3.76	3.08	3.04	2.95	3.08
	CF-d-350	1.36	carbon	6.34	4.61	7.55	3.84	3.72	3.88
	CF-f'c-60	1.83	carbon	6.45	3.87	3.18	3.50	3.22	3.17
	F-B-1	1.55	glass	7.21	5.60	3.24	3.70	3.12	2.53
	F-B-1.5	1.83	glass	6.30	4.56	3.78	3.22	2.72	2.06
	F-B-2	2.33	glass	2.83	2.05	1.38	1.57	1.33	0.96
	F-pl-1.5	1.83	glass	6.34	5.22	2.90	3.27	2.86	2.36
	F-pl-2.0	1.83	glass	5.04	5.04	2.41	2.65	2.40	2.28
	F-d-250	1.41	glass	7.19	5.53	3.22	3.83	3.38	2.50
	F-d-350	1.36	glass	9.03	6.69	6.04	4.99	4.34	3.10
Mean				5.77	4.29	3.92	3.18	2.94	2.60
Standard Deviation				2.16	1.69	1.86	1.16	0.96	0.84
Coefficient of Variation				0.37	0.39	0.47	0.37	0.33	0.32

*CSA A23.3-04 and CSA S6-06 (2009) are the same model and have the same ratios.

5.1.3 Recommended Shear Model

As shown in section 5.1.2, all the sectional shear models analyzed in this study gave poor predictions of capacity for specimens having a/d ratios less than 2.5. The sectional shear models increasingly under-predicted the shear capacity as the a/d ratio decreased. This was expected as none of the models are capable of properly accounting for the arching mechanism which was observed in the specimens tested.

As is the case with steel reinforced members, the shear capacity of deep members must be computed using an alternative method. STMs have been developed and refined to give good predictions of capacity for steel reinforced members. This study has shown that the ACI 318-08 STM provisions cannot be adapted to FRP reinforced deep beams without major changes. The ACI 318-08 model was not capable of accounting for the

influence on capacity from the higher reinforcement strains resulting from the use of FRP instead of steel reinforcement. The ACI 318-08 STM over-predicted the shear capacity of the specimens tested in this study by up to 75%.

The CSA A23.3-04 STM was capable of overcoming the deficiencies associated with the ACI 318-08 STM. The model was able to directly account for the influences of the reinforcement strain and the a/d ratio (through the strut angle); two parameters which have a large impact on the shear capacity of deep members. Nehdi et al. (2008) reported that the CSA A23.3-04 model was very conservative in predicting the shear capacity of FRP reinforced deep beams and was not suitable for use with FRP reinforced beams. However, Nehdi et al. (2008) assumed a fixed tie strain of 0.002 when calculating the diagonal strut efficiency factor. The strain value of 0.002 can only be assumed in steel reinforced concrete beams where Grade 400 steel is at the yield point. To properly apply the CSA A23.3-04 STM, the elastic nature of the FRP must be accounted for, which was done in this study through the use of the FRP strain directly calculated from the applied loading and equilibrium of the internal forces at mid-span.

Two methods for calculating the CSA A23.3-04 efficiency factors were discussed in this study. The efficiency factor can either be calculated using the full or half the mid-span FRP strain (i.e. Equation 5.1 or Equation 5.2, respectively). Using the full mid-span FRP strain gave experimental to predicted shear capacity (V_{exp}/V_{cs1}) ratios greater than 1.0 for the majority of the specimens tested. Using only half the mid-span FRP strain resulted in the majority of the specimens having $V_{exp}/V_{cs2} < 1.0$. Using the full mid-span FRP strain (ε_{frp}) when determining the diagonal strut strength was also supported based on the reinforcement strain gauge readings located in the support regions. In the specimens tested, the strain readings at the centerline of the supports were between 15 and 115% of the measured mid-span strains which indicated that in some specimens the average strain in the FRP passing through the strut was closer to the full strain value. The test results from El-Sayed (2006) and Nehdi et al. (2008) showed similar strain readings at the supports.

Since the intent of the current study was to provide a method for predicting the shear capacity of full scale members, the experimental data from the large-scale specimens should be given greater consideration. Therefore, this study considered members with $h > 300$ mm and up to 1000 mm to be more representative of the beam sizes used in industry. The best STM predictions for the large-scale specimens tested in this study were obtained by using the CSA A23.3-04 STM with the full FRP strain (Equation 5.1).

Therefore, the CSA A23.3-04 STM where the strut capacity is calculated by assuming the strain in the FRP passing through the strut is the same as the mid-span FRP strain (Equation 5.1) is the recommended model for calculating the shear capacity of deep beams reinforced with FRP and having no distributed reinforcement. Using sectional models to determine the shear capacity of FRP reinforced deep beams is a safe

alternative but can have adverse effects on the member economy as the a/d ratio decreases.

The accuracy of the MCFT based CSA A23.3-04 STM in predicting the strut capacity of the FRP reinforced specimens also validated the underlying MCFT theory as applied to strut capacity. This study showed that the MCFT based formulation for strut capacity is applicable to reinforced concrete members having tensile reinforcement strains up to 8 times the typical values for steel reinforced members. The yield strain for commonly used Grade 400 steel is normally assumed to be 0.002.

5.2 Discussion of the Experimental Results

5.2.1 Comparison of the Crack Diagrams with the STM

As discussed in section 5.1.3, the CSA A23.3-04 STM using Equation 5.1 where the mid-span FRP strain is used in the strut capacity determination was recommended for calculating the shear capacity of deep beams reinforced with FRP. The STM configurations at the predicted loads corresponding to strut crushing were superimposed on the failure crack diagrams for each specimen as shown in Figure 5-16 to Figure 5-18 for specimens having h = 300 mm, 600 mm, and 1000 mm, respectively. Although the STMs indicated failure by strut crushing, the most common failure in the tests was shear compression. In deep beams with no distributed reinforcement and with geometric properties proportioned to prevent a flexural failure, the strut is expected to develop splitting cracks which can lead to failure (Wight and MacGregor 2009). With the exception of Specimens A1N, A3N, A4H, C1N, C2N, the specimens tested developed a primary diagonal crack that was near the centerline of the strut at mid-depth of the specimen and parallel to the strut axis.

The majority of the specimens had diagonal cracks that were parallel to the strut orientation, which indicated that the assumed STM was appropriate. In most instances, the diagonal cracks became parallel to the horizontal compression struts near the tops of the specimens. The crack tips, which usually extended past the loading plates into the compression zones, were located at the lower edges of the assumed horizontal struts. Specimen A1N shown in Figure 5-16 developed splitting cracks at the lower edge of the assumed horizontal strut. This horizontal splitting action was a continuation of the crack delineating the inside edge of the diagonal strut and provided a good fit with the STM. With the exception of specimens B1N, C1N, and C2N, the flexural cracks did not reach the assumed lower edge of the horizontal strut indicating that the neutral axis was lower than the bottom edge of the strut. In establishing the STM geometry, the top prismatic strut was assumed to be stressed to the strut's stress limit of $0.85f_c'$. In actuality, the top strut extends to the neutral axis which is located at the top of the flexural crack tips. The strut is not uniformly stressed as assumed in the idealized STM; the stress varies across the strut and becomes nonexistent at the neutral axis.

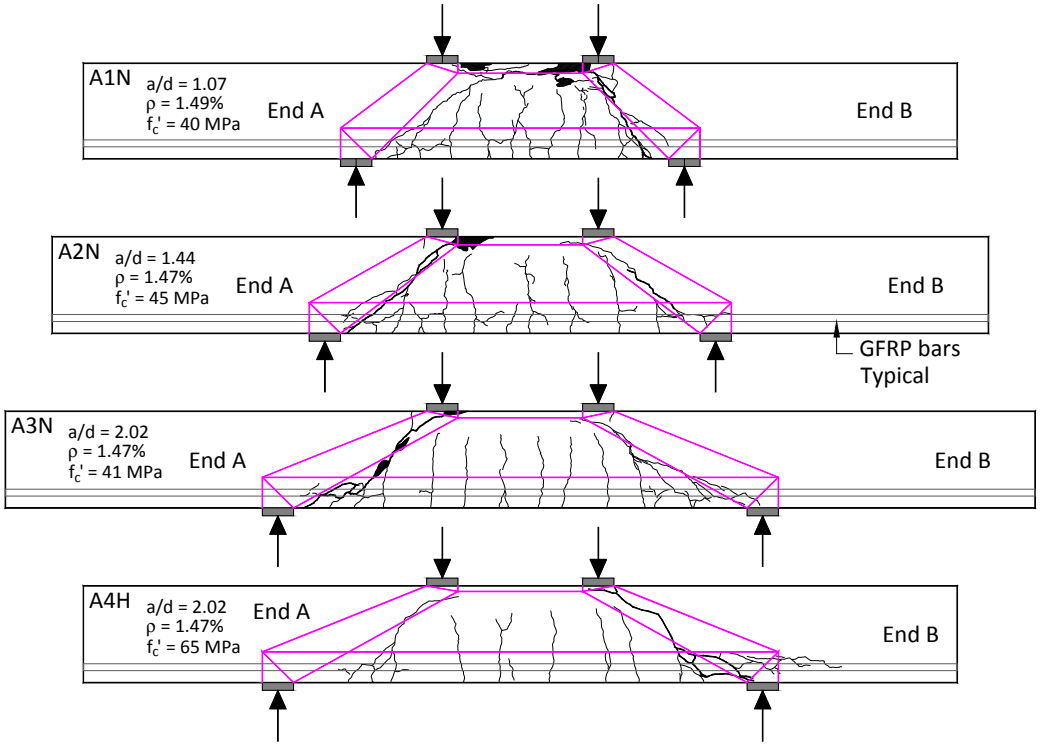

Figure 5-16: STM superimposed on the crack diagrams of specimens having h = 300 mm.

The trusses superimposed on the crack diagrams demonstrate why specimens A4H and B6H failed prematurely compared to the prediction from the STM. Specimens A4H and B6H had V_{exp}/V_{cs1} = 0.67 and 0.65, respectively. Specimen A4H (Figure 5-16) developed a diagonal crack in shear span B that initiated 200 mm inside of the edge of the bearing plate. The diagonal crack in shear span B extended to the same height with a similar angle as the adjacent cracks, penetrating part way into the idealized diagonal strut location. Subsequently, the crack propagated towards the support at an orientation consistent with the strut inclination. However, the diagonal crack split the upper part of the diagonal strut in half and prevented load from being directly transmitted from the loading point to the support in the lower half of the strut, especially after the crack grew in width and aggregate interlock along the crack was reduced. Since a fully intact strut was not able to form, the specimen carried less load than predicted by the STM. The brittle nature of the high strength concrete and the higher location of the neutral axis when compared to the equivalent lower strength concrete specimen at the same load (A3N) are reasons for the high initial penetration of the diagonal crack.

Specimen B6H as shown in Figure 5-17 had a diagonal shear crack similar to the one in specimen A4H. The main diagonal shear crack which originated inside shear span A, 400 mm from the inside edge of the bearing plate, extended into the middle of the idealized diagonal strut before rotating and propagating parallel to the strut axis. As a result, the upper portion of the strut was bisected by the crack which prevented the

transfer of load in the inner half of the strut as the cracks grew in width. The reduced effective strut cross-section and the curved force flow once the crack opened wide enough to destroy aggregate interlock prevented the specimen from reaching the full predicted load from the STM.

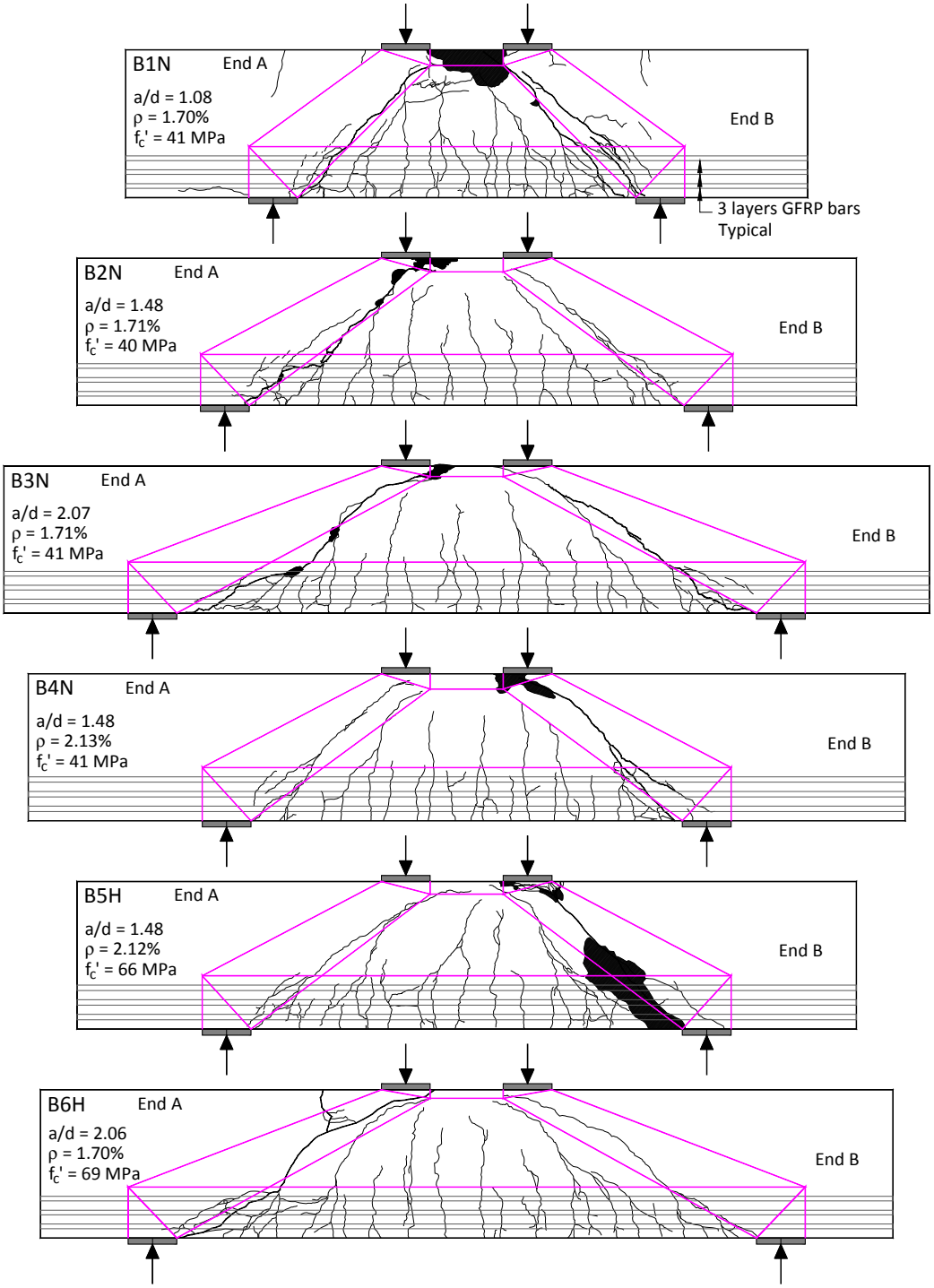

Figure 5-17: STM superimposed on the crack diagrams of specimens having h = 600 mm.

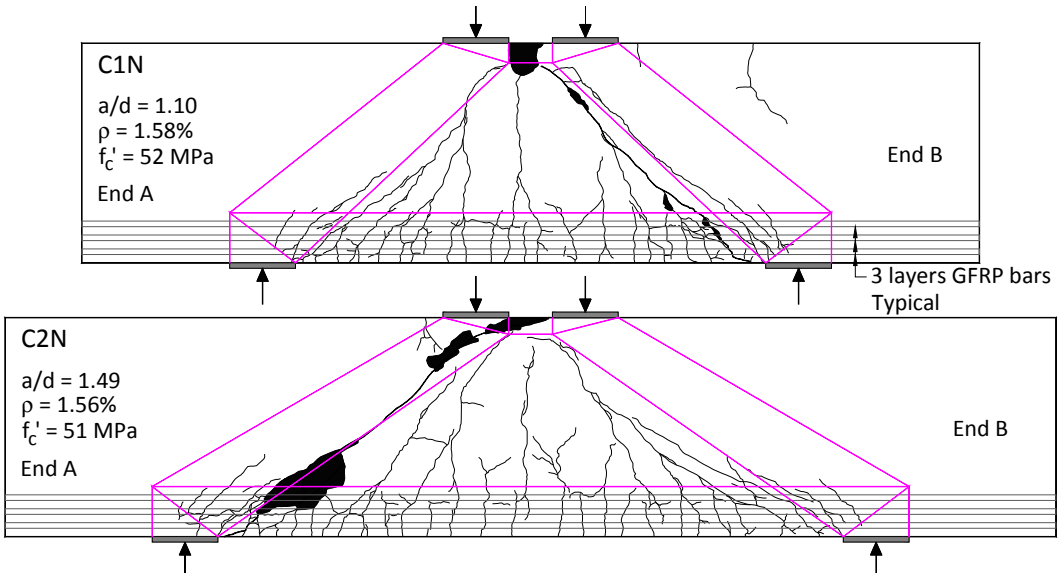

Figure 5-18: STM superimposed on the crack diagrams of specimens having h = 1000 mm.

Specimens A4H and B6H both demonstrated that the transition between arch action and sectional shear behaviour does not occur at a distinct a/d ratio, but rather gradually. Both specimens exhibited arch action albeit to a lesser extent than predicted by the STM. The main diagonal cracks had a curved nature that approached the "S-shaped" crack characteristic of sectional shear failure (Collins et al. 2008). Specimens A4H and B6H both had an a/d ratio of 2.1 which is considered to be in the transition zone between sectional shear behaviour and arch action for steel reinforced concrete beams (Wight and MacGregor 2009). Therefore, a gradual a/d transition zone between arch action and beam action is also present in FRP reinforced beams.

Specimen B5H developed a diagonal crack that was parallel to and in the center of the right diagonal strut as shown in Figure 5-17. This splitting crack, which is expected in steel reinforced deep beams containing no web reinforcement, resulted in an abrupt failure with substantial crushing and splitting of the concrete near the lower end of the strut. Specimen B5H failed at 94% of the predicted load which may have been due in part to a lack of distributed web reinforcement. Web reinforcement is required according to CSA A23.3-04 STM design provisions which were adopted for FRP reinforced deep beam modelling in this study. However, the geometry of the STM is compatible with the crack diagram.

Whereas the majority of the specimens developed major diagonal cracks inside the theoretical strut boundaries, specimens C1N and C2N did not. The major diagonal cracks developed parallel to the inside edges of the struts and became horizontal at the bottom edges of the top horizontal struts. In effect, the cracks delineated the inside

edges of the concrete arches as shown in Figure 5-18. The crack diagrams for specimens C1N and C2N agree with the outline of the strut and tie model.

In the majority of the specimens, most noticeably in specimens B1N, B2N, B3N, B4N, B5N, C1N, and C2N, secondary smaller cracks parallel to the strut direction formed near the bottom of the diagonal struts. These cracks, which were located closer to the ends of the specimen than the primary diagonal cracks, formed near the centroid of the reinforcement and extended slightly past the location of the upper reinforcement layer. The width of these secondary cracks ranged between 0.2 and 0.6 mm at the last load stage prior to specimen failure. These cracks were expected since the strain in the reinforcement was high and the reinforcement prevented any one crack from opening excessively. The cracks disappeared at a short distance above the reinforcement and the main crack was observed to become wider towards mid-height of the specimens.

5.2.2 Comparison of the Specimens to Steel Reinforced Deep Beams

In general, the specimens displayed similar characteristics, as reported in the literature, to steel reinforced deep beams during failure. The predominant shear compression failure observed in the specimens is one of the failure mechanisms which occur in steel reinforced deep members as identified by ACI Committee 326 (1974). The failure of steel reinforced beams containing no web reinforcement as reported by Mathey and Watstein (1963) was similar to the failure of the current specimens. Mathey and Watstein (1963) observed that the majority of the beams having an a/d ratio of 1.51 failed in shear compression. The diagonal tension crack became parallel to the top surface of the beam near the load point and extended into the constant moment region. Crushing of the concrete occurred in the region of constant moment. The majority of the FRP reinforced deep beams also had the diagonal crack become horizontal near the loading point and penetrate into the constant moment region. Failure also occurred with concrete crushing inside the constant moment region.

In steel reinforced deep beams with distributed reinforcement, cracks tend to be smaller in width and more uniform (Smith and Vantsiotis 1982). Distributed reinforcement also helps prevent strut splitting failure (Wight and MacGregor 2009). Beams containing no web reinforcement have larger crack widths than beams containing web reinforcement. In addition, the failure load of beams containing distributed web reinforcement compared to beams without distributed reinforcement is higher (Tan et al. 2008, Smith and Vantsiotis 1982). Researchers have also reported that beams without distributed web reinforcement are brittle and have variable failure loads. Beam with web reinforcement are ductile and can have substantially higher failure loads than beams without web reinforcement (Rogowsky and MacGregor 1986, Shin et al. 1999, Garay Moran 2008). Since the FRP reinforced deep beams displayed similar behaviour to steel reinforced deep beams, it is expected that distributed reinforcement will have similar beneficial effects on FRP reinforced deep beams as it does with steel

reinforced deep beams. Although FRP web reinforcement is elastic, the reinforcement should prevent crack widths from opening excessively, producing smaller but more numerous cracks. The ductility and load capacity is also expected to increase. However, the effect of web reinforcement in FRP reinforced deep beams is inconclusive due to a lack of experimental data.

5.3 Parametric Study

A parametric study was conducted to determine the influence of various parameters on the shear capacity of FRP reinforced beams and the transition point between predominantly sectional and arch action. Three variables were considered: the longitudinal reinforcement ratio, ρ, beam height, h, and the axial stiffness of the reinforcement, $E_{FRP}A_{FRP}$. In all cases, hypothetical beams were examined that had similar properties to the test series from this study and from the literature to allow for comparisons between the modelled and experimental results.

Two shear capacity models were considered, a STM and a sectional model. The STM based on the CSA A23.3-04 STM incorporating the full FRP strain at mid-span in the limiting strut stress calculation (using Equation 5.1) was found to give predictions in good agreement with test results for deep beams as discussed in section 5.1.3. This STM was adopted for use in the parametric study. The truss model configuration shown in Figure 5-1 was used in modelling the hypothetical beams, all of which were loaded in a four-point bending configuration.

The Hoult et al. (2008) model was implemented as the sectional shear model in the parametric study. Although the Hoult et al. (2008) model gave poor predictions of capacity for deep beams, it was considered the best sectional shear model for use in this study. Both the selected STM model and the Hoult et al. (2008) sectional shear model were developed from the same underlying theory, the MCFT (sections 2.5.2.2 and 2.5.3.1). The use of different models based on a common theoretical approach as opposed to empirically derived models was considered important for this study. The Hoult et al. (2008) model is an enhanced version of the CSA A23.3-04 sectional shear model for steel reinforced beams derived to specifically model FRP reinforced slender beams. The Hoult et al. (2008) sectional shear model for slender beams was found to accurately predict the shear strength of FRP and steel reinforced concrete beams as described elsewhere (Hoult et al. 2008, Bentz et al. 2010).

In all scenarios investigated, the beams modelled had $0.4 \leq a/d \leq 7.0$ and the predicted shear strengths (V_{pre}) were normalized by the product of the effective depth, d, width, b_w, and compressive strength of concrete, f_c'. The shear strength (V_{pre}) was calculated with the resistance factors set to 1.0 (i.e. nominal capacity). The critical section in the analysis using Hoult et al. (2008) sectional shear model was taken at d_v from the loading point when $a/d > 2.0$ and at $a/2$ when $a/d \leq 2.0$. The predicted shear capacity was

always taken as the greater of the STM or the sectional shear model result since the STM is a lower bound solution.

5.3.1 Influence of the Longitudinal Reinforcement Ratio

To study the effect of the longitudinal reinforcement ratio, ρ, on the shear capacity of FRP reinforced beams, beams having the properties given in Figure 5-19 were investigated. All beam properties were kept constant while ρ was varied from 0.8% to 2.0%. The beam height, h, effective depth, d, width, b_w, bearing plate sizes, and concrete strength, f_c', were consistent with the "B – series" specimens from the current experimental research program with normal strength concrete (f_c' = 40 MPa). This was done to facilitate direct comparison to the results given in Chapter 4. Each beam configuration was examined over a range of a/d ratios.

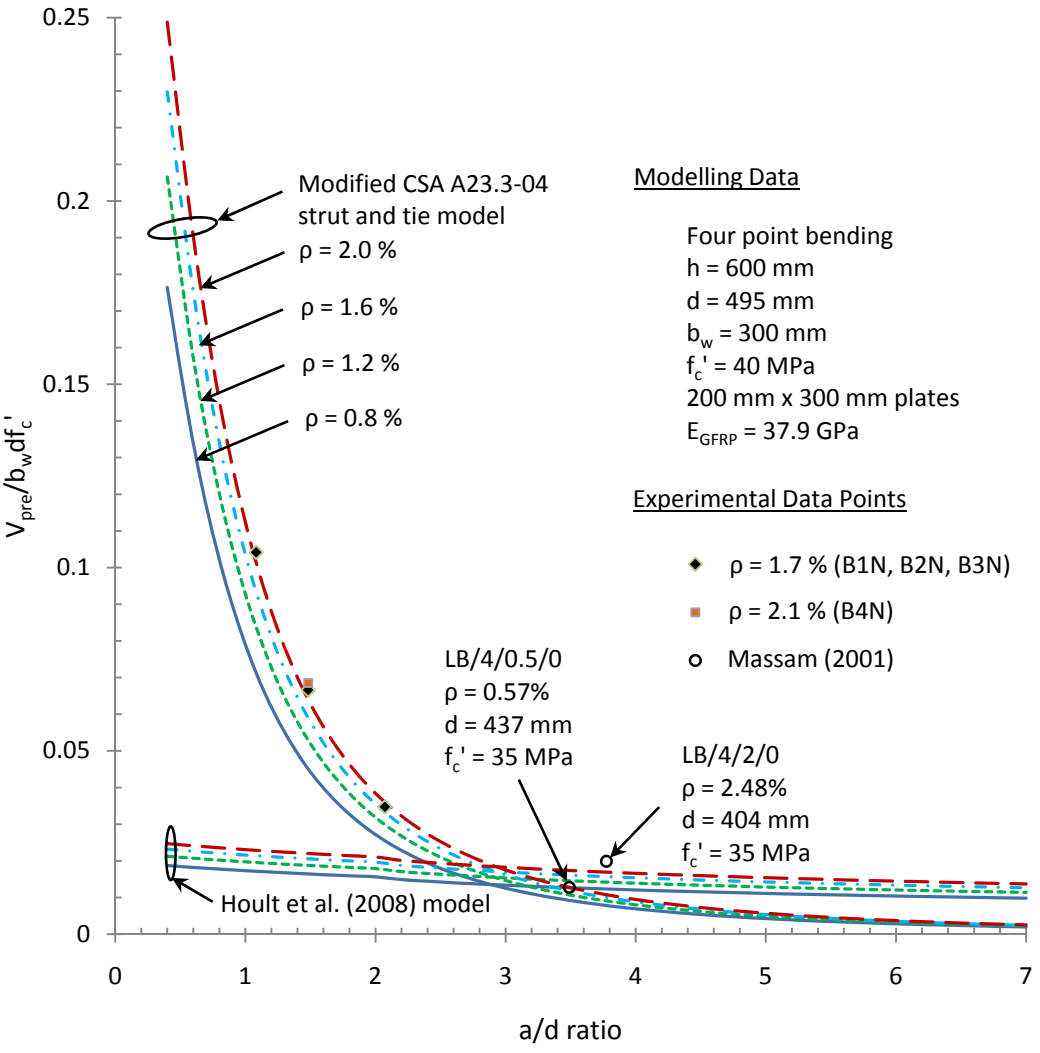

Figure 5-19: Influence of the longitudinal reinforcement ratio on the shear capacity.

The normalized shear strength of identical beams having different reinforcement ratios was plotted against the a/d ratio in Figure 5-19. As expected, the shear capacity increased as the a/d ratio decreased for both the sectional and STM models. An increase in the reinforcement ratio resulted in an increase in the normalized shear capacity for both models.

Since the STM is a lower bound solution, the predicted capacity is the greater of the STM or sectional shear model result. The a/d transition point where either the sectional model or the STM gives better predictions is determined by the location where the respective curves in Figure 5-19 intersect. Therefore, the normalized shear capacity given by the STM, which deviates rapidly from the normalized sectional shear capacity at low a/d ratios is used to predict the shear strength of beams at a/d less than the transition point. At a/d values higher than the transition point, the sectional shear model gives better predictions and the STM gives very low predictions. The intersection point for the beams having a reinforcement ratio of ρ = 1.6% occurred at a/d = 2.9. As the reinforcement ratio increased, the transition a/d increased. At a reinforcement ratio of ρ = 2.0%, the intersection point of the two models occurred at a/d = 3.0.

Experimental data points from the current test program have been superimposed on the curves shown in Figure 5-19 and show good agreement with the STM. Two specimens from Massam (2001) had similar properties to the modelled beams and both show good agreement with the sectional shear model prediction (Figure 5-19).

5.3.2 Size Effect in Shear

The overall height, h, of steel reinforced beams has been well documented as having a significant influence on the shear capacity for members without web reinforcement (Wight and MacGregor 2009, ACI-ASCE Committee 445 1999). As the member height increases, the shear stress at failure decreases in the case of slender beams. There is, however, debate as to whether a similar size effect on the failure shear stress also occurs for deep beams. Researchers have reported that when the strengths of deep beam specimens without web reinforcement are normalized by effective depth, d, width, b_w, and concrete compressive strength, f_c', there is a size effect where beams with larger h have lower shear stress at failure (Kani 1967, Walraven and Lehwalter 1994, Birrcher et al. 2009). The predicted STM capacity is in part a function of the size of the nodal zones and not a direct function of the member height. The STM indicates that the effective depth of a deep member has no influence on the shear capacity (Sneed 2007). Birrcher et al. (2009) found that normalizing the experimental shear capacity by the predicted shear capacity from the STM indicated no size dependence and that the size effect reported in the literature is the result of "incorrectly assuming" that the shear strength is a function of member height.

To further investigate the influence of member height on the failure shear stress of FRP reinforced beams, two scenarios were considered. In the first scenario, the beam height was varied from h = 300 mm to 1000 mm while all other variables were held constant, including the bearing plate sizes. The d/h ratio was also kept constant. The resulting normalized shear capacity curves are shown in Figure 5-20 for both the STM and the sectional shear model.

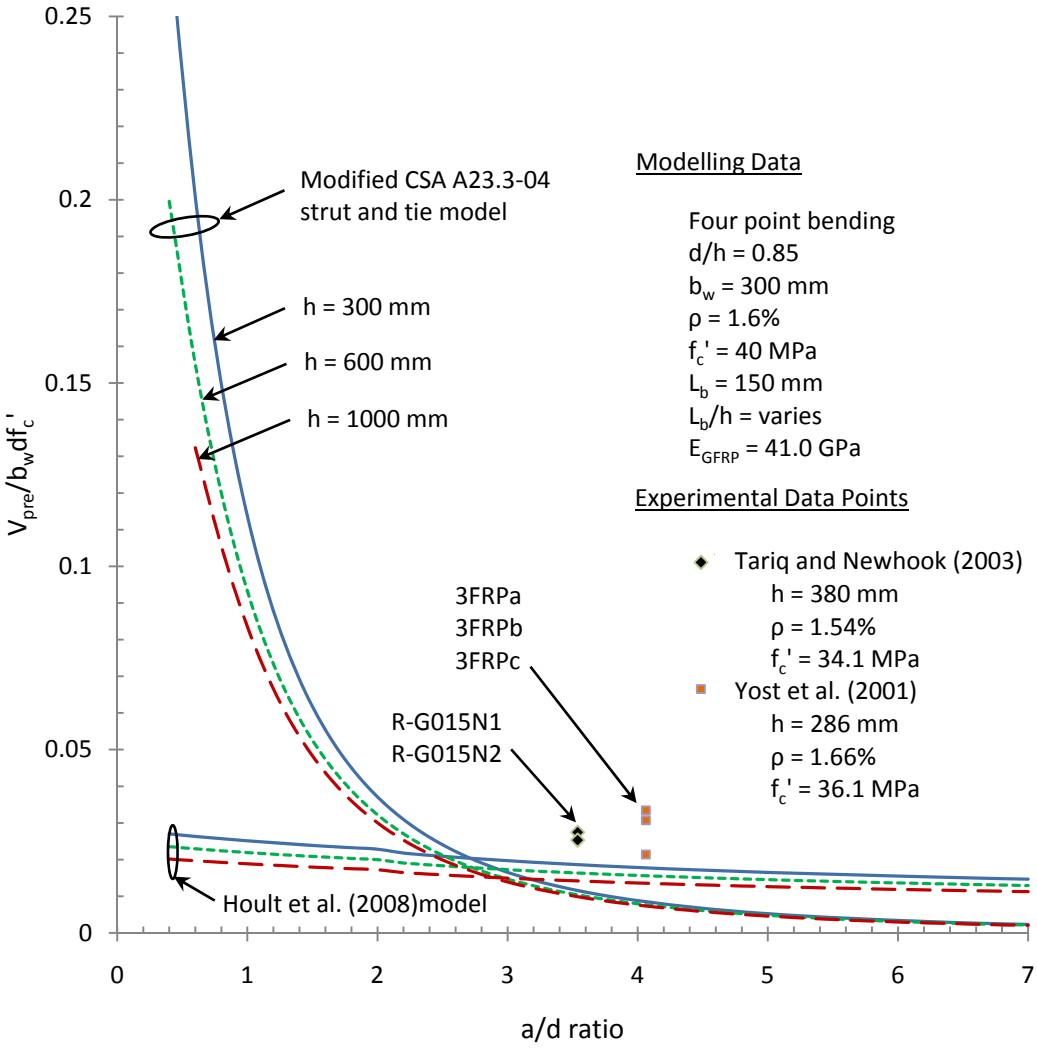

Figure 5-20: Influence of size effect on the shear capacity when the bearing plate sizes are held constant (150 mm x 300 mm).

A well defined size effect in shear was predicted by the STM for FRP reinforced deep beams having constant bearing plate sizes (Figure 5-20). Beams having large h had a lower predicted normalized shear capacity than beams with small h. The size effect became more pronounced as the a/d ratio decreased. At a/d ratios greater than 4.0, the STM showed very little size dependence while the sectional model still predicted greater normalized shear capacity for beams having smaller h. The transition a/d ratio

where the STM and sectional model shear capacity curves intersect also varies with depth. For the beams with h = 1000, the transition point occurred at an a/d ratio of 2.9 and this a/d value decreased as the height decreased. At a beam height of 300 mm, the transition point occurred at an a/d ratio of 2.7. Although the modelling data was based on the test specimens from the current experimental program, they were not included in Figure 5-20 as the bearing plate sizes were not held constant for the specimens. Several data points taken from the literature for FRP reinforced concrete slender beams having similar properties to the model beams were included in Figure 5-20. These beams had shear capacities that were in excess of the sectional shear model predictions.

In the second scenario, the beams were scaled geometrically with the exception of the beam width. The beam width is not considered an important parameter in understanding size effect influence on shear (Kani 1967, Sherwood et al. 2006). As in the specimens tested, the bearing plate length to beam height ratio (L_b/h) was kept constant at 0.333. All other variables including the d/h ratio were kept constant. This was similar to the approach recommended by Sneed (2007) to determine the influence of effective depth on the shear strength of concrete beams. The size effect influence on normalized shear capacity when the specimens were geometrically scaled is shown in Figure 5-21.

The normalized shear capacity curve for the STM is dramatically different in Figure 5-21 when compared with Figure 5-20. The STM predicted no size effect in the normalized shear capacity when the bearing plate sizes were scaled geometrically in proportion to member height. This confirms that the strut and tie model is not a function of the specimen height, h, but rather, a function of the nodal zone dimensions. Scaling both the beams and the bearing plates geometrically results in geometrically scaled nodal zones.

The sectional shear model is independent of the bearing plate sizes since the critical section occurs away from the bearing plates (Collins and Mitchell, 1997). Therefore, the size effect in shear is present for slender members regardless of the bearing plate sizes and the Hoult et al. (2008) model curves shown in Figure 5-21 are identical to those in Figure 5-20. The transition range of a/d values where the shear capacity curves cross the STM curves has increased since the three STM curves have merged into one when compared to Figure 5-20. The a/d transition point ranged from 2.6 to 3.1 for beams having h = 300 mm and 1000 mm, respectively. The specimens from the test program and from Gross et al. (2003) having similar properties to those modelled show good agreement with the parametric study results in Figure 5-21.

This parametric study has shown that the shear capacity decreases in beams with constant bearing plate sizes as the member height is increased while all other parameters remain constant. This is the apparent size effect in shear for deep beams. However, if plate sizes are also scaled, no size effect in shear will result.

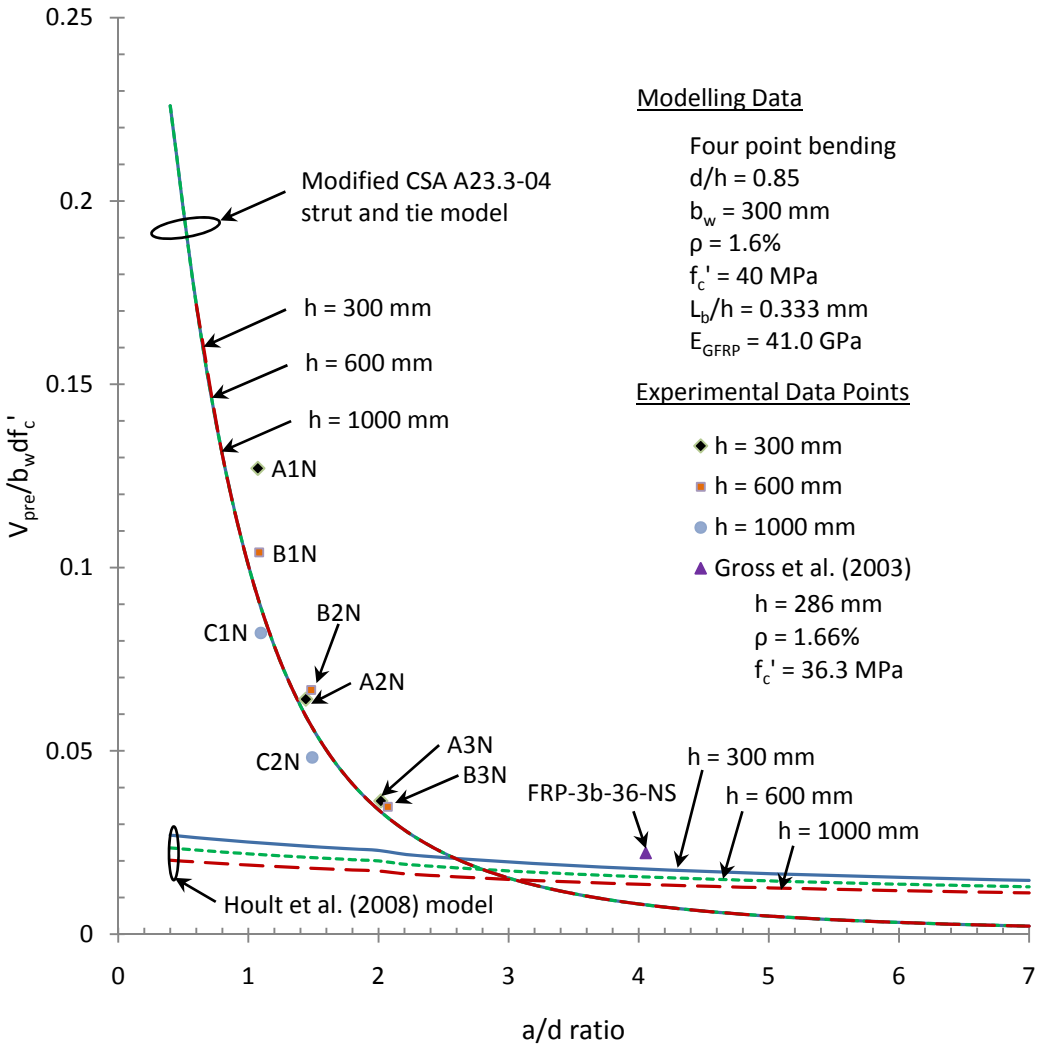

Figure 5-21: Influence of size effect on shear capacity of geometrically scaled FRP reinforced beams.

5.3.3 Influence of the Reinforcement Axial Stiffness

Since there is more than one type of FRP available, the influence of FRP stiffness on the shear capacity of FRP reinforced beams was investigated. Carbon FRP (CFRP) has a higher stiffness than glass FRP (GFRP). Two beam configurations were modelled and both had geometric properties consistent with the specimens from El-Sayed (2006). One beam configuration was reinforced with CFRP and the other with GFRP. In both cases, the modulus of elasticity was the same as in the El-Sayed (2006) specimens. Each beam configuration was examined with a range of a/d ratios. The plate sizes were held constant for all beams.

The shear capacity curves for both the STM and the sectional model (Figure 5-22) show an increase in normalized shear capacity when the reinforcement stiffness is increased.

The experimental data points from El-Sayed (2006) included in Figure 5-22 correlate well with the normalized shear capacity curves. The a/d transition point where the curves from the different models coincide is similar for the CFRP and GFRP reinforced beams. In both sets of beams, the transition point occurs at an a/d ratio of approximately 2.7.

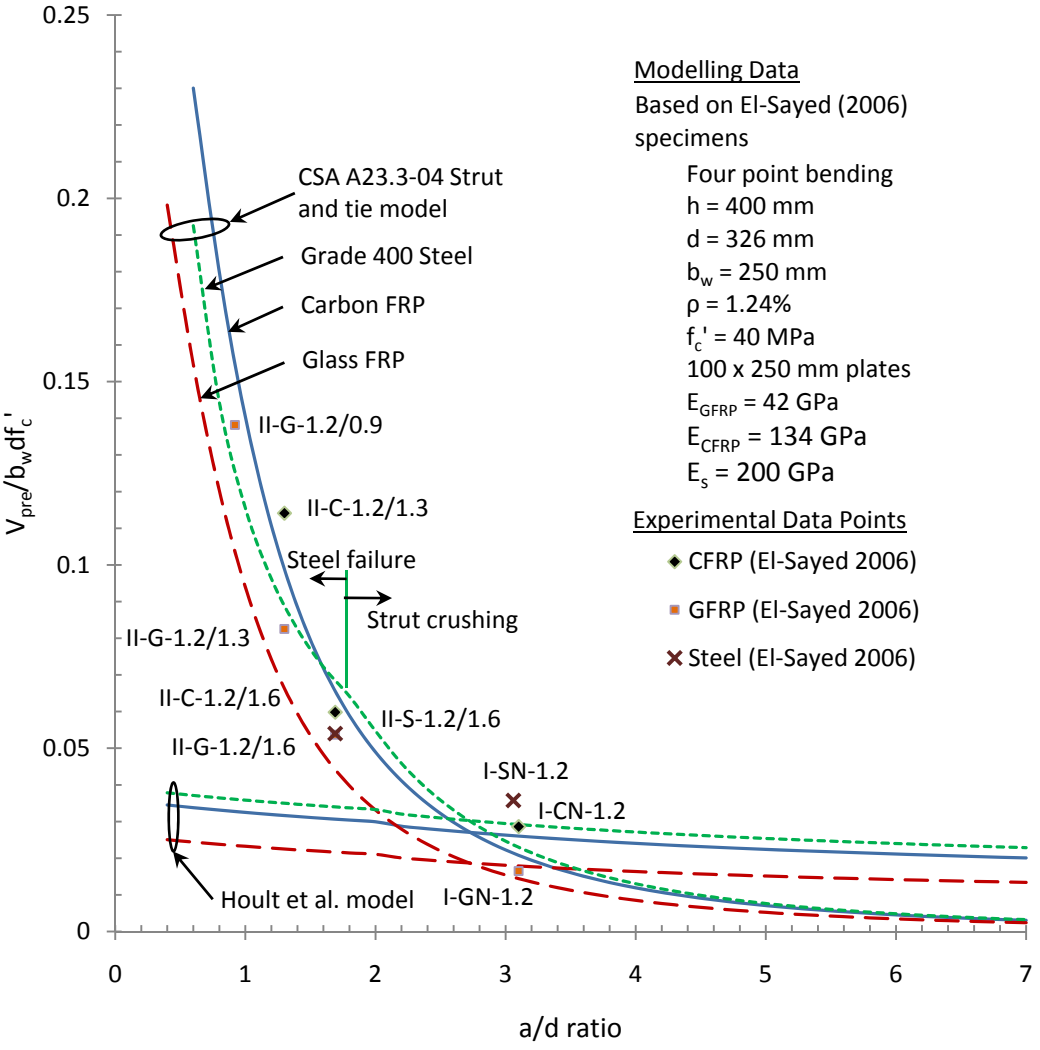

Figure 5-22: Influence of reinforcement axial stiffness on the shear capacity of FRP reinforced beams.

The normalized shear capacity curves for steel reinforced beams with similar geometry have also been included in Figure 5-22. The Grade 400 steel was modelled as elastic to a yield strength of f_y = 400 MPa using identical STM and sectional shear models as for the FRP reinforced members. The sectional normalized shear capacity curve for the steel reinforced beams show an increase in capacity compared to the CFRP curve since the steel has a higher stiffness than CFRP. The STM curve for the beams with steel reinforcement has higher normalized shear capacities than the CFRP reinforced beams at $a/d > 1.7$. At $a/d < 1.7$, the normalized shear capacity of the steel reinforced beams is

between the capacities of the GFRP and CFRP reinforced beams. The discrepancy is due to a change in the predicted failure mechanism of the steel reinforced beam. At a/d > 1.8, the predicted failure mechanism was by strut crushing in the STM model. When a/d < 1.8, the STM model predicted that the steel reinforcement stress reaches f_y. Therefore, from Figure 5-22, yielding of the reinforcement limits the load carrying capacity when compared to CFRP. El-Sayed (2006) and Nehdi et al. (2008) reported that the steel reinforced deep beams failed at a higher load than the GFRP reinforced concrete beams but at loads lower than the equivalent CFRP reinforced concrete beams. The a/d transition point where the sectional and STM normalized shear capacity curves intersect is similar to the GFRP and CFRP curves.

5.3.4 Transition from STM to Sectional Model

To determine whether the STM or sectional shear model should be used in predicting the shear capacity of any particular beam, two curves can be developed. The STM and sectional shear model are used to predict the shear capacity of the selected beam configuration over a range of a/d values. The shear capacity from both models is plotted against the a/d ratio. The STM model is used for the a/d ratios where it predicts higher shear capacities than the sectional models. Likewise, the sectional shear model is used for the a/d ratios where the sectional model gives higher predictions than the STM. Therefore, shear capacity curves can be generated for any beam configuration to determine where the transition a/d ratio occurs.

The a/d ratio where the STM or sectional model gives better predictions depends on several variables. The longitudinal reinforcement ratio and beam height regardless of whether or not the beams were geometrically scaled are two variables that produced a change in the a/d transition ratio. Changing the stiffness of the reinforcement while keeping all other parameters constant had no noticeable effect on the transition a/d ratio.

In steel reinforced concrete beams, a common assumption is that strut and tie modelling should be used when the a/d ratio is less than 2.5 with sectional shear models being used at higher a/d ratios (ACI 445R-99). The parametric study demonstrated that in FRP reinforced beams, the transition point does not occur at a fixed a/d ratio. For the beams modelled, the a/d value where the STM and sectional shear model gave the same result varied from 2.6 to 3.1. However, it is possible that the range could be even greater if a wider range of beam configurations were modelled. Therefore, the assumption that STM should not be used at a/d values greater than 2.5 in steel reinforced beams also serves as a conservative limit on the use of the STM for FRP reinforced beams. Since the higher shear capacity from either the STM or sectional model is used as the predicted capacity, errors in the transition a/d value typically do not have a significant affect on safety. Note that the above a/d ratios were determined based on nominal capacity (i.e. resistance factor = 1.0). Similar curves could be produced

for the factored resistances and it is expected that transition points for the models may shift slightly.

5.4 Summary and Conclusions

The shear capacities of FRP reinforced deep beams were calculated using various STMs and sectional models. Since no STMs have been previously developed for use with FRP reinforced deep beams, the CSA A23.3-04 and ACI 318-08 STM were used to predict the load capacity of the FRP reinforced deep beams. The ACI 318-08 STM is an empirically derived model developed for steel reinforced deep members. The CSA A23.3-04 STM is based on the MCFT which was expected to be applicable to any type of reinforcement due to the direct consideration of the reinforcement strains. Two variations of the CSA A23.3-04 STM were used. In the first, the transverse tensile strain across the strut was calculated using the full mid-span FRP strain, ε_{frp}, and in the second version, half the mid-span FRP strain was used, $\varepsilon_{frp,c}$. Due to the elastic nature of the FRP reinforcement, an iterative procedure was used to calculate the load capacity with the STMs.

The CSA A23.3-04 model considering the full FRP strain at mid-span, ε_{frp}, in the diagonal strut capacity calculations gave the best results with only 17% of the predictions being unconservative when including all the specimens from the current study and literature. The average V_{exp}/V_{cs1} ratio for a database of 36 specimens was 1.20 with a 21% COV. The ACI 318-08 model was determined to be unsuitable for predicting the load capacity of concrete deep members reinforced with FRP. The average V_{exp}/V_{cs3} ratio for the ACI 318-08 STM was 1.02 with a 51% COV when all specimens were included. The 12 large-scale specimens from the current study had an average V_{exp}/V_{cs3} ratio of 0.60 with a 34% COV. The diagonal strut efficiency factor in ACI 318-08 STM was derived for steel reinforced beams and is not applicable to FRP reinforced beams. The ACI 318-08 STM is incapable of accounting for the influence of high strains in the nodal zone on capacity and does not provide consistent results at different a/d ratios. The STM geometry from the CSA A23.3-04 STM was consistent with the observed crack patterns at failure. The majority of the specimens had the main diagonal crack split the strut along the centerline axis.

Comparisons with the failure mechanisms reported in the literature for steel reinforced beams indicated that FRP and steel reinforced beams have similar behaviour. As a result, it is expected that adding distributed web reinforcement in FRP reinforced deep beams will produce a more desirable response. Cracks are expected to be more numerous but narrower in width while the load capacity and ductility are expected to increase as is the case in steel reinforced deep beams. Nevertheless, the CSA A23.3-04 STM utilizing the full mid-span strain in the diagonal strut calculation was still found to be applicable to the specimens containing no distributed web reinforcement tested in the current study.

The sectional shear models predicted increasingly conservative shear capacities as the a/d ratio decreased. None of the sectional shear models were capable of accounting for the arch action observed in this study. Therefore, sectional shear models should not be used in the analysis or design of FRP reinforced deep beams. Although safe capacity predictions are generated by the sectional models, the resulting beams may be uneconomical.

A parametric study was undertaken to establish the influence of various parameters on the shear capacity of FRP reinforced beams. The a/d transition ratio where sectional shear models or STMs gave better predictions was established by plotting normalized shear capacity curves. The CSA A23.3-04 STM with the strut capacity based on the full mid-span FRP strain, ε_{frp}, and the Hoult et al. (2008) sectional shear model were used to develop the curves. The parametric study revealed that the normalized shear capacity increased when the reinforcement ratio, ρ, increased, the axial stiffness of the reinforcement, $E_{FRP}A_{FRP}$, increased, and when the a/d ratio decreased. The sectional model predicted decreased shear stress at failure as h increased which is the so-called size effect in shear. However, deep beams were found not to be size dependant if the specimens and boundary conditions were both geometrically scaled. If the specimens were geometrically scaled but the bearing plate sizes were kept constant, a size effect was introduced. Therefore, the shear strength of deep beams is dependant on the nodal zone geometry and not directly on the beam height.

The parametric study established that the transition a/d ratio where either the STM or the sectional model gives better predictions is dependant on several variables such as the reinforcement ratio, member height, and the reinforcement axial stiffness. The transition a/d ratio ranged from 2.6 to 3.1 depending on which variable was adjusted. The a/d ratio of 2.5, which is commonly used as the transition point between strut and tie and sectional modelling for steel reinforced members, can also be conservatively applied to FRP reinforced beams. At a/d ratios less than 2.5, the CSA A23.3-04 STM with the strut capacity based on the full FRP strain at mid-span can be used to model FRP reinforced beams containing no distributed web reinforcement. At a/d ratios greater than 2.5, the Hoult et al. (2008) sectional model can be used to predict the shear capacity.

6 Summary and Conclusions

6.1 Summary

The overall objectives of this study were to develop a better understanding of the shear behaviour of large-scale concrete deep beams with internal FRP reinforcement and to develop a modelling technique that accurately predicts the shear capacity of such beams. Shear behaviour and design methods have been examined over the last century for steel reinforced members (ACI-ASCE Committee 445 1999). At shear span-to-depth (a/d) ratios less than 2.5, steel reinforced members experience a rapid increase in shear capacity relative to members having a/d > 2.5 due to the breakdown of aggregate interlock and the formation of an arch mechanism. At a/d ratios greater than 2.5, sectional shear models are generally accepted to apply for calculating the shear capacities of steel reinforced concrete members.

Prior experimental and analytical work on FRP reinforced members has mainly focused on slender beams having a/d ratios greater than 2.5. Only two sets of published data exist for systematic study of FRP reinforced concrete deep beam behaviour (Nehdi et al. 2008 and El-Sayed 2006). Whereas strut and tie models (STM) have been developed for analyzing the capacity of steel reinforced concrete deep members, no such models are available in design codes for use with members reinforced with FRP. In fact, CSA S806-02 specifically states STM shall not be used in the design of FRP reinforced concrete deep beams. Design documents for FRP reinforced concrete such as ACI 440.1R-06, CSA S6-06, and ISIS 2007 only give provisions for sectional shear and provide no guidance with respect to deep beams. Therefore, the current study investigated whether the strut and tie modelling procedure is applicable to FRP reinforced concrete deep beams.

To fulfill the objectives of this study, experimental and analytical work was conducted. The experimental portion of the project consisted of testing to failure 12 large-scale GFRP reinforced concrete beams containing no distributed web reinforcement. Of these beams, four had nominal heights of h = 300 mm, six had h = 600 mm, and two had h = 1000 mm to study the influence of member height on the shear behaviour. The other variables included the a/d ratio which varied from 1.1 to 2.1, the reinforcement ratio which varied from 1.5 to 2.1%, and the concrete strength, f_c'. Two concrete strengths were used, a normal strength concrete mix having $f_c' \approx$ 40 MPa and a high strength mix with $f_c' \approx$ 66 MPa. The specimens were loaded to failure using displacement control in a four-point bending configuration.

The analytical investigation involved calculating the maximum shear loads of the specimens using several sectional shear models and STMs. The sectional models were existing models from various design codes, design guidelines, and publications (ACI 440.1R-06, CSA A23.3-04, CSA S6-06, CSA S806-02, Hoult et al. 2006, ISIS 2007, and

Razaqpur et al. 2006). Since no STM provisions were available specifically for use with FRP reinforced concrete deep beams, existing STMs (CSA A23.3-04 and ACI 318-08) for steel reinforced concrete members were adopted. The calculated shear capacities from each model were compared to the experimental results. Additional FRP reinforced concrete deep beam specimens from the literature were also analyzed. Based on the comparison of the predicted shear capacities and experimental results a recommended analysis model was developed for FRP reinforced concrete deep beams.

Using the validated analytical models, a parametric study was undertaken to investigate the influence of the reinforcement ratio, a/d ratio, member height, and axial FRP stiffness on the shear capacity of FRP reinforced concrete deep beams. Normalized shear curves were created to determine the transition a/d ratio where either sectional shear or the strut and tie model are appropriate.

6.2 Conclusions

The conclusions provided in this section are based on the laboratory test results for deep beam specimens and the analysis of these specimens and others reported in the literature.

6.2.1 Behaviour of the FRP Reinforced Deep Beam Specimens

- With the exception of two specimens, failure of the specimens was brittle. The majority of the specimens failed by shear compression after the formation of a major diagonal shear crack from the inside edge of the support plate to the inside edge of the loading plate. At an a/d ratio of 1.1, two out of the three specimens failed by flexural crushing of the concrete in the region between the loading plates. Only two specimens, both having an a/d ratio of 1.5, had diagonal compression strut failure.
- The failure mode was observed to be extremely ductile in specimen B1N. After initial crushing of the flexural region, the specimen continued to resist increasingly more load while undergoing substantial deformation.
- An arch mechanism was observed to form in all specimens. This was confirmed by the crack orientation, crack widths, and measured strains in the longitudinal reinforcement. Significant reserve capacity was available after the formation of the main diagonal cracks indicating internal redistribution of forces and the formation of an arch mechanism. Prior to failure, the measured crack widths were typically between 1.25 to 7.0 mm with cracks wide enough to see completely through some specimens indicating the complete breakdown of aggregate interlock. Uniform strain readings were obtained along the longitudinal reinforcement after the major diagonal cracks formed indicating a tied arch mechanism developed.

- The inclined cracking load (P_c) decreased with respect to the peak load (P_{max}) as the a/d ratio decreased. The average P_c/P_{max} ratio for specimens with concrete strength of $f_c' \approx 40$ MPa was 56% for $a/d = 2.1$ and 32% for $a/d = 1.1$. These P_c/P_{max} ratios showed that the reserve load capacity after diagonal cracking decreased as the a/d ratio increased indicating that the arch mechanism became less efficient at higher a/d ratios. The reserve capacity was found to be lower in the specimens having $a/d = 2.1$ and high concrete compressive strength ($f_c' \approx 66$ MPa) where the average P_c/P_{max} was 71% compared to the specimens with normal strength concrete ($f_c' \approx 40$ MPa).
- The post cracking stiffness of the FRP reinforced deep beam specimens was only dependant on the a/d ratio and reinforcement ratio. A decrease in a/d ratio or an increase in reinforcement ratio increased the post cracking stiffness of the specimens. The specimen height and concrete compressive strength had negligible effect on the post cracking stiffness of the FRP reinforced concrete specimens.
- The shear strength of the specimens was highly dependant on the a/d ratio where the shear strength increased as the a/d ratio decreased while all other variables were held constant.
- Increasing the reinforcement ratio increased the normalized shear strength. In this study, increasing the reinforcement ratio by 24% resulted in a 3% increase in the normalized shear strength.
- The results indicated a size effect in the specimens having $a/d = 1.1$ where increased member height resulted in reduced normalized shear stress at the peak load. Specimens having $a/d = 1.5$ and 2.1 had no significant size effect in shear when h increased from 300 to 600 mm. However, since there was some variation in the specimen parameters, a detailed relationship for size effect could not be established.
- The behaviour of the FRP reinforced concrete deep beam specimens was compared to the documented behaviour of steel reinforced deep beams. FRP reinforced concrete deep beams displayed similar behaviour to steel reinforced concrete deep beams.

6.2.2 Analysis

- STMs that directly consider the influence of the strain in the tie crossing the diagonal strut gave better strut capacity predictions than STMs that do not consider the strain in the tie.
- The CSA A23.3-04 STM provided good predictions of capacity for FRP reinforced concrete deep beams containing no distributed web reinforcement. Using the full mid-span strain in the FRP reinforcement to predict the diagonal strut capacity was in good agreement with the test results. The average experimental to predicted capacity ratio was 1.03 with a 20% coefficient of variation for the

12 specimens tested in this study. The average experimental to predicted capacity ratio was 1.20 with a 21% coefficient of variation for a database of 36 FRP reinforced concrete specimens. The STM prediction quality was consistent regardless of the a/d ratio, h, reinforcement ratio, or FRP reinforcement type. However, the capacity predictions for the specimens with high strength concrete ($f_c' \approx 66$ MPa) were unconservative especially for the specimens having $a/d = 2.1$.

- Using half the mid-span strain in calculating the diagonal strut capacity when using the CSA A23.3-04 STM was typically unconservative with an average experimental to predicted capacity ratio of 0.81 for the 12 specimens tested in this study. The average experimental to predicted capacity ratio was 0.96 with a 22% coefficient of variation for a database of 36 FRP reinforced concrete specimens.
- The ACI 318-08 STM was incapable of accurately modelling the capacity of FRP reinforced concrete beams containing no web reinforcement. The average experimental to predicted capacity ratio was 0.60 with a 34% coefficient of variation and 1.02 with a 51% coefficient of variation for the 12 specimens tested in this study and for the 36 member database, respectively.
- The sectional shear models (ACI 440.1R-06, CSA A23.3-04, CSA S6-06 (2009), CSA S806-02, Hoult et al. 2006, ISIS Canada 2007, and Razaqpur et al. 2006) had average experimental to predicted capacity ratios significantly greater than 1.0 for FRP reinforced concrete deep beams containing no web reinforcement. The predictions were increasingly conservative as the a/d ratio decreased with experimental to predicted capacity ratios being a high as 11.1 at an a/d ratio of 1.1. All of these models were incapable of considering the arching action. The sectional models gave poor but safe predictions for FRP reinforced concrete deep beams containing no web reinforcement.
- The CSA A23.3-04 STM indicated that there is no size effect on shear capacity in FRP reinforced concrete deep beams when the beams and the bearing plates are scaled geometrically. Keeping the plate sizes constant while changing h resulted in a size effect in shear.
- A parametric study using the CSA A23.3-04 STM model using the full mid-span FRP strain in calculating the diagonal strut capacity and the Hoult et al. (2008) sectional shear model indicated that the shear capacity increases when the reinforcement ratio increases, a/d ratio decreases, or the FRP axial stiffness increases.
- The transition a/d ratio where either the CSA A23.3-04 STM using the full mid-span strain in the strut capacity calculation or the Hoult et al. (2008) sectional shear model gives better predictions of capacity is dependent on the reinforcement ratio, member height, and FRP axial stiffness. Based on nominal capacities, the transition a/d ratio can conservatively be assumed to be 2.5.

When $a/d \leq 2.5$ and $a/d \geq 2.5$, the shear capacity can be accurately predicted using the STM and the sectional shear model, respectively.

6.2.3 Cautions and Limitations

Unlike steel, FRP is a linear elastic material that does not yield and does not provide ductility to a structure. The linear nature of the FRP must be taken into account when using the strut and tie modelling technique. In steel reinforced concrete members, the steel provides the required plastic deformation to allow redistribution of internal stresses into the adopted truss model. In FRP reinforced concrete members, the concrete can only provide limited ductility which may not be enough in truss models more complex than discussed in this study. The simple truss model used in this study was determinant and closely followed the internal forces as indicated by the theory of elasticity. Limited ductility was required in this instance which may not be the case in more complex STMs. Additional research is required to ensure the STM can be adopted for more complex members (see section 6.3).

6.3 Recommendations for Future Work

Based on the work conducted in the current study, several questions remain to be answered. Additional research is required to allow the adoption of the strut and tie modelling technique to FRP reinforced concrete members. The following recommendations for future work are suggested:

- The behaviour of FRP reinforced concrete deep beams containing distributed FRP web reinforcement should be examined through laboratory testing of large-scale specimens. The behaviour of specimens containing distributed FRP web reinforcement can then be compared to the behaviour of beams containing no web reinforcement. Varying configurations of distributed FRP should be used to determine the required quantity to produce cracks that have acceptable spacing and width. Strut and tie modelling of such beams should also be studied.
- Further examination of FRP reinforced concrete deep beams constructed with high strength concrete ($f_c' \geq 60$ MPa) is required to determine the suitability of the STM to such beams.
- In the current study, the beams having an a/d ratio of 1.1 experienced flexural crushing of the concrete even though the recommended version of the CSA A23.3-04 strut and tie model predicted failure by diagonal strut crushing. Laboratory tests of additional beams with smaller a/d ratios are required for further validation of the strut and tie model at low a/d ratios.
- Laboratory testing of FRP reinforced concrete beams having a range of a/d ratios is required to determine the transition a/d ratio where breakdown of the arch mechanism occurs. All variables must be kept constant for each series of specimens including the bearing plate sizes. It is expected that modelling can be

conducted to account for a large range of variables once the transition a/d ratio is verified by laboratory testing.

- Laboratory testing of FRP reinforced beams having different types of FRP needs to be conducted to determine the effect of bond on the member capacity. Since the arch mechanism development is influenced by the amount of reinforcement bond, different surface properties of FRP bars may influence the arch mechanism. In addition, different crack patterns may result depending on the surface characteristics of the reinforcement. Therefore, tests are required to quantify the effects of the reinforcement surface properties on the beam behaviour.
- Additional experiments are required to validate the use of STMs for FRP reinforced concrete members. Current and previously published research has only considered beams loaded in a four-point bending configuration with STMs that have direct struts from the load to the support. Such members do not require significant ductility to enable stress redistribution. Since FRP is an elastic material, it is not known whether more complex disturbed regions will develop sufficient plasticity to allow for the use of STMs. Therefore, laboratory experiments need to be conducted on FRP reinforced concrete members that have more complex disturbed regions including dapped end beam connections, corbels, walls with openings, and continuous deep beams.
- Finite elements analysis of the specimens is required to further study the behaviour of FRP reinforced concrete deep beams. Validated finite element models would allow for further parametric study of the variables that influence member strengths.
- Modelling techniques are required for FRP reinforced concrete deep beams to calculate the deflection, crack widths, and FRP stresses at the serviceability limit state.

References

ACI-ASCE Committee 426. 1974. Shear Strength of Reinforced Concrete Members, *Proceedings ASCE, Journal of the Structural Division*, 99 (ST6): 1091-1187.

ACI-ASCE Committee 445. 1999. *Recent Approaches to Shear Design of Structural Concrete (ACI 445R-99)*, American Concrete Institute, Farmington Hills, Michigan, United States.

ACI Committee 318. 2008. *ACI 318-08 Building Code Requirements For Structural Concrete and Commentary*, American Concrete Institute, Farmington Hills, Michigan, United States.

ACI Committee 440. 2006. *ACI 440.1R-06 Guide for the Design and Construction of Structural Concrete Reinforced with FRP Bars*, American Concrete Institute, Farmington Hills, Michigan, United States.

AASHTO. 2007. *AASHTO LRFD Bridge Design Specifications: SI units, 4th ed.,* American Association of State Highway and Transportation Officials, Washington, D.C., United States.

Bahen, N. and Sanders, D. H. 2009. Investigation of Strut Strength Using a Deep-Beam Database, *ACI Special Publication*, SP-265: 385-404.

Bentz, E. C. and Collins, M. P. 2006. Development of the 2004 Canadian Standards Association (CSA) A23.3 shear provisions for reinforced concrete, *Canadian Journal of Civil Engineering*, 33 (5): 508-520.

Bentz, E. C., Massam, L., and Collins, M. P. 2010. The Shear Strength of Large Concrete Members with FRP Reinforcement, *Journal of Composites for Construction*, Posted ahead of print Feb 4, 2010. Doi: 10.1061/(ASCE)CC.1943-5612-0000108.

Birrcher, D., Tuchscherer, R., Huizinga, M., Bayrak. O., Wood, S., and Jirsa, J. 2009. *Strength and Serviceability Design of Reinforced Concrete Deep Beams*, CTR Technical Report 0-5253-1, University of Texas, Austin, United States.

Brown, M. D., Sankovick, C. L., Bayrak, O., Jirsa, J. O., Breen, J. E., and Wood, S. L. 2005. *Design for Shear in Reinforced Concrete Using Strut-and-Tie Models*, Center for Transportation Research Report 0-4371-2, University of Texas, Austin, United States.

Canadian Standards Association. 1994. *A23.3-94 Design of concrete structures*, Canadian Standards Association, Rexdale (Toronto), Ontario, Canada.

Canadian Standards Association. 2002. *CAN/CSA-S806-02 Design and Construction of Building Components with Fibre-Reinforced Polymers*, Canadian Standards Association, Mississauga, Ontario, Canada.

Canadian Standards Association. 2004. *A23.1-04/A23.2-04 Concrete materials and methods of concrete construction/Test methods and standard practices for concrete*, Canadian Standards Association, Mississauga, Ontario, Canada.

Canadian Standards Association. 2004. *A23.3-04 Design of concrete structures*, Canadian Standards Association, Mississauga, Ontario, Canada.

Canadian Standards Association. 2009. *CAN/CSA-S6-06 Canadian Highway Bridge Design Code, Addendum*, Canadian Standards Association, Mississauga, Ontario, Canada.

Canadian Standards Association. 2006. *CAN/CSA-S6-06 Canadian Highway Bridge Design Code*, Canadian Standards Association, Mississauga, Ontario, Canada.

Canadian Standards Association. 2006. *Commentary on CAN/CSA-S6-06 Canadian Highway Bridge Design Code*, Canadian Standards Association, Mississauga, Ontario, Canada.

Cement Association of Canada. 2006. *Concrete Design Handbook, third edition*, Cement Association of Canada, Ottawa, Ontario, Canada.

Collins, M. P., Bentz, E. C., and Sherwood, E. G. 2008. Where is Shear Reinforcement Required? Review of Research Results and Design Procedures, *ACI Structural Journal*, 105 (5): 590-600.

Collins, M. P. and Mitchell, D. 1997. *Prestressed Concrete Structures,* Response Publications, Toronto, Ontario, Canada.

El-Sayed, A. K. 2006. *Concrete Contribution to the Shear Resistance of FRP-reinforced Concrete Beams*, PhD Dissertation, Universite de Sherbrooke, Quebec, Canada.

El-Sayed, A. K. and Benmokrane, B. 2008. Evaluation of the new Canadian highway bridge design code shear provisions for concrete beams with fiber-reinforced polymer reinforcement, *Canadian Journal of Civil Engineering*, 35 (6): 609-623.

Garay Moran, J. 2008. *Behaviour of concrete deep beams with high strength reinforcement*, MSc Dissertation, University of Alberta, Edmonton, Canada.

Gross, S. P., Yost, J. R., Dinehart, D. W., Svensen, E., and Liu, N. 2003. Shear Strength of Normal and High Strength Concrete Beams Reinforced with GFRP Bars, *High*

Performance Materials in Bridges: Proceedings of the International Conference, American Society of Civil Engineers, Kona, Hawaii, United States.

Guadagnini, M., Pilakoutas, K., and Waldron, P. 2003. Shear Performance of FRP Reinforced Concrete Beams, *Journal of Reinforced Plastics and Composites*, 22 (12): 1389-1407.

Hoult, N. A., Sherwood, E. G., Bentz, E. C., and Collins, M. P. 2008. Does the Use of FRP Reinforcement Change the One-Way Shear Behavior of Reinforced Concrete Slabs? *Journal of Composites for Construction*, 12 (2): 125-133.

ISIS Canada. 2001. *Reinforcing Concrete Structures with Fibre Reinforced Polymers – Design Manual 3*, ISIS Canada Corporation, Winnipeg, Manitoba, Canada.

ISIS Canada Research Network. 2006. *Durability of Fibre Reinforced Polymers in Civil Infrastructure – Durability Monograph*, ISIS Canada Corporation, Winnipeg, Manitoba, Canada.

ISIS Canada Research Network. 2007. *Reinforcing Concrete Structures with Fibre Reinforced Polymers – Design Manual 3, Version 2*, ISIS Canada Corporation, Winnipeg, Manitoba, Canada.

Kani, G. N. J. 1964. The riddle of shear failure and its solution, *ACI Journal Proceedings*, 61 (4): 441-467.

Kani, G. N. J. 1966. Basic Facts Concerning Shear Failure, *ACI Journal Proceedings*, 63 (6): 675-692.

Kani, G. N. J. 1967. How Safe Are Our Large Reinforced Concrete Beams? *ACI Journal Proceedings*, 64 (3): 128-141.

Kani, M. W., Huggins, M. W., and Wittkopp, R. R. 1979. *Kani on Shear in Reinforced Concrete*, Department of Civil Engineering, University of Toronto, Canada.

Marti, P. 1985. Basic Tools of Reinforced Concrete Beam Design, *ACI Journal Proceedings*, 82 (1): 46-56.

Marti, P. 1985b. Truss Models in Detailing, *Concrete International*, 7 (12): 66-73

Massam, L. N. 2001. *The behaviour of GFRP-reinforced concrete beams in shear,* M.A.Sc. Dissertation, University of Toronto, Ontario, Canada.

Mathey, R. G. and Watstein, D. 1963. Shear Strength of Beams Without Web Reinforcement Containing Deformed Bars of Different Yield Strengths, *ACI Journal Proceedings*, 60 (2): 183-208.

Nehdi, M., Omeman, Z., and El-Chabib, H. 2008. Optimal efficiency factor in strut-and-tie model for FRP-reinforced concrete short beams with (1.5<a/d<2.5), *Materials and Structures*, 41 (10): 1713-1727.

Omeman, Z., Nehdi, M., and El-Chabib, H. 2008. Experimental study on shear behavior of carbon-fiber-reinforced polymer reinforced concrete short beams without web reinforcement, *Canadian Journal of Civil Engineering*, 35: 1-10.

Park, J. and Kuchma, D. 2007. Strut-and-Tie Model Analysis for Strength Prediction of Deep Beams, *ACI Structural Journal*, 104 (6): 657-666.

Razaqpur, A. G. and Isgor, O. B. 2006. Proposed Shear Design Method for FRP-Reinforced Concrete Members without Stirrups, *ACI Structural Journal*, 103 (1): 93-102.

Razaqpur, A. G., Isgor, O. B., Greenaway, S., and Selley, A. 2004. Concrete Contribution to the Shear Resistance of Fiber Reinforced Polymer Reinforced Concrete Members, *Journal of Composites for Construction*, 8 (5): 452-460.

Rogowsky, D. M. and MacGregor, J. G. 1986. Design of Reinforced Concrete Deep Beams, *Concrete International*, 8 (8): 49-58.

Schlaich, J., Schäfer, K., and Jennewein, M. 1987. Towards a Consistent Design of Reinforced Concrete Structures, *PCI Journal*, 32 (3): 74-150.

Sherwood, E. G., Lubell, A. S., Bentz, E. C., and Collins, M. P. 2006. One-Way Shear Strength of Thick Slabs and Wide Beams, *ACI Structural Journal*, 103 (6): 794-802.

Shin, S., Lee, K., Moon, J., and Ghosh, S. K. 1999. Shear Strength of Reinforced High-Strength Concrete Beams with Shear Span-to-Depth Ratios between 1.5 and 2.5, *ACI Structural Journal*, 96 (4): 549-557.

Smith, K. N. and Vantsiotis, A. S. 1982. Shear Strength of Deep Beams, *ACI Journal Proceedings*, 79 (3): 201-213.

Sneed, L. H. 2007. *Influence of Member Depth on the Shear Strength of Concrete Beams*, PhD Dissertation, Purdue University, West Lafayette, Indiana, United States.

Tan, K.-H., Cheng, G.-H., and Zhang, N. 2008. Experiment to mitigate size effect on deep beams, *Magazine of Concrete Research*, 60 (10): 709-723.

Tariq, M. and Newhook, J. P. 2003. Shear Testing of FRP Reinforced Concrete Without Transverse Reinforcement, *Annual Conference of the Canadian Society for Civil Engineering*, Moncton, New Brunswick, Canada.

Tureyen, A. K. and Frosch, R. J. 2002. Shear Tests of FRP-Reinforced Concrete Beams without Stirrups, *ACI Structural Journal*, 99 (4): 427-434.

Tureyen, A. K. and Frosch, R. J. 2003. Concrete Shear Strength: Another Perspective, *ACI Structural Journal*, 100 (5): 609-615.

Vecchio, F. J. and Collins, M. P. 1986. The Modified Compression-Field Theory for Reinforced Concrete Elements Subjected to Shear, *ACI Journal Proceedings*, 83 (2): 219-231.

Walraven, J. and Lehwalter, N. 1994. Size Effects in Short Beams Loaded in Shear, *ACI Structural Journal*, 91 (5): 585-593.

Wight, J. K. and MacGregor, J. G. 2009. *Reinforced Concrete: Mechanics and Design (5th edition)*, Pearson Prentice Hall, Upper Saddle River, New Jersey.

Yost, J. R., Gross, S. P., and Dinehart, D. W. 2001. Shear Strength of Normal Strength Concrete Beams Reinforced with Deformed GFRP Bars, *Journal of Composites for Construction*, 5 (4): 268-275.

Zsutty, T. 1968. Beam Shear Strength Prediction by Analysis of Existing Data, *ACI Journal Proceedings*, 65 (11): 943-951.

Appendix A: Glass Fibre Reinforced Polymer Bars

This appendix describes the mechanical properties of the GFRP bars used in the deep beam specimens. The testing procedures and instrumentation used to determine the mechanical properties of the GFRP bars are documented in this appendix.

A.1 GFRP Bar Characteristics

The GFRP bars were manufactured by BP Composites (Edmonton, Alberta) in the fall of 2008. All bars were delivered cut to the required length. The fibres consisted of E-CR-glass while the matrix was vinylester resin. The bars had external fibres wrapped in two directions overtop of the longitudinal fibres in the core and were sand coated as seen in Figure A-1. The bar properties as specified by the manufacturer are given in Table A-1. Note that the cross-sectional area, tensile strength, and modulus of elasticity listed in Table A-1 were not used in any analysis reported in this document. The measured properties as described in the subsequent sections were used in the analysis.

Figure A-1: GFRP bars.

Table A-1: Bar specifications as provided by the manufacturer.

Properties	No. 6	No. 7	No. 8
Nominal diameter (mm)	19	22	25
Cross-sectional area (mm^2)	301	399	526
Weight (kg/m)	0.584	0.770	1.014
Glass content (% Vol)	72.0	64.8	64.1
Guaranteed Design Tensile Strength (MPa)	892	845	737
Modulus of Elasticity (GPa)	43.1	43.6	43.8
Average shear strength (MPa)	290	300	245
Nominal bond strength (MPa)	12.1	12.4	11.1
Transverse thermal expansion coefficient (10^{-6}/°C)	19.8	25.6	26.2
Longitudinal thermal expansion coefficient (10^{-6}/°C)	8.6	10.8	8.3

A.2 Cross-sectional Area

Test method B.1 from ACI 440.3R-04 was used to determine the cross-sectional area and equivalent diameter of the GFRP bars. A 250 mL Pyrex graduated cylinder with 2 mL gradients and partially filled with water was used in determining the volume of the bars. For each bar size, one specimen was tested and compared to the data on the manufacturer's datasheet as summarized in Table A-1. The calculated cross-sectional area of the No. 7 and No. 8 bars closely matched the values reported on the datasheets while the cross-sectional area of the No. 6 bar was 7% larger than the value on the datasheet. An additional No. 6 bar was tested with similar results. The results are given in Table A-2.

Table A-2: Cross-sectional properties of the GFRP bars measured in accordance with ACI 440.3R-04.

Bar Size (U.S. Customary)	Measured Cross-sectional Area (mm^2)	Equivalent Diameter (mm)
No. 6	322	20.2
No. 7	396	22.5
No. 8	528	25.9

A.3 Uniaxial Tensile Properties

Tensile coupon tests were carried out in accordance to the procedures in CSA S806-02 Annex C. The specimens were tested in a MTS 6000 testing frame equipped with wedge shaped hydraulic tension grips. The tensile specimens were prepared by the bar manufacturer in accordance with their procedure. The anchoring mechanism on each end of the specimen consisted of a steel cylinder filled with a non-explosive demolition agent which provided the expansive stresses necessary to anchor the FRP bar. The geometry of the specimens is given in Table A-3. The nomenclature for the identification of each specimen consisted of two numbers separated with a dash with the first number indicating the bar size in US customary units.

Table A-3: Specimen and anchor dimensions.

Specimen No.	Anchor Length (mm)	Anchor Outer Diameter (mm)	Specimen Gauge Length (mm)
6-1	574	34	649
6-2	574	34	648
6-3	575	34	652
6-4	575	34	652
6-5	575	34	651
7-1	582	42	1140
7-2	580	42	1136
7-3	578	42	1145
7-4	582	42	1134
7-5	580	42	1136
8-1	680	42	1246
8-2	680	42	1240
8-3	680	42	1244
8-4	680	42	1248
8-5	680	42	1241

Prior to testing, several electrical resistance strain gauges were applied to each specimen. Different strain gauges and application procedures were used. The most reliable method was later used in the instrumentation of the reinforcement in the concrete deep beam specimens. In all instances, the sand was removed in the vicinity of the gauge location prior to applying the strain gauge. Figure A-2(a) and (b) show strain gauges applied on the surface of a No. 6 and No. 8 bar, respectively.

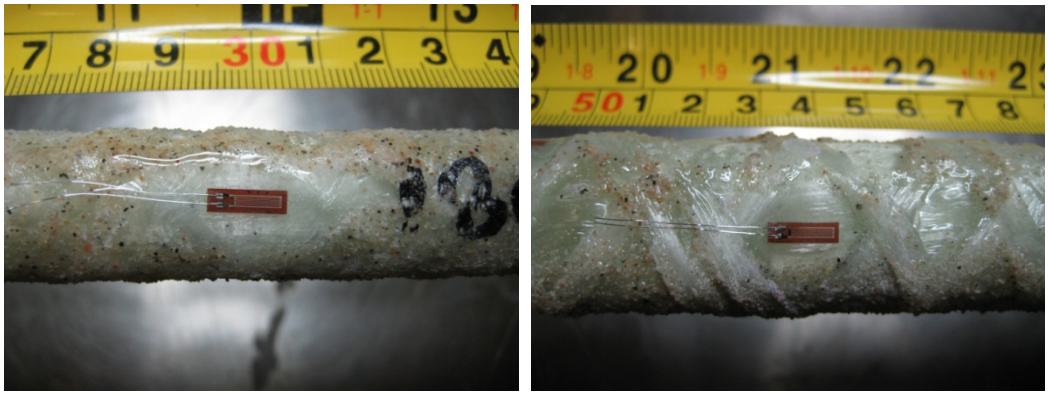

(a) (b)

Figure A-2: Strain gauge applied on (a) specimen 6-3 and (b) specimen 8-3.

The specimens were loaded into the test frame and an axial tension load of 5-10 kN was initially applied to set the grips. A cable potentiometer was attached to the bottom anchor with the cable attached to the top anchor to measure the full elongation of the specimen between the anchors as shown in Figure A-3. The cable potentiometer

remained attached for the full duration of the test. Since the cable potentiometer was attached to the anchors, incorrect elongation readings could be obtained if there was any slippage or elongation of the bar inside the anchor. Therefore, bar elongation was also measured over a localized region (≈ 115 mm) using a linear variable displacement transducer (LVDT) mounted on brackets (Figure A-4) that were attached near the middle of the bar gauge length. The LVDT was removed at approximately 75% of the manufacturer's predicted failure load of the bar to prevent possible instrument damage at specimen failure. The tension specimens were tested under displacement control with the applied force measured by the internal MTS 6000 load cell. The loading rate was 3.8, 6.5, and 7.3 mm/min for the No. 6, No. 7, and No. 8 specimens, respectively. All data was recorded on a HBM MGCplus data acquisition system at a frequency of 10 hertz using the measurement software Catman Professional 6.0. In addition, each test was videotaped since close visual observation was not possible due to safety concerns.

The results and a short description of the tests are given below. Although different types of strain gauges were used on most of the bars tested, only the results of the 5 mm gauge length type KFG-5-120-C1-11 strain gauges manufactured by Kyowa Electronic Instruments Co. Ltd. are shown in the figures. Typically only the data from one representative strain gauge is shown. The elongation readings from the cable potentiometer were converted to strain values by dividing the elongation by the initial bar gauge length (bar length between anchors).

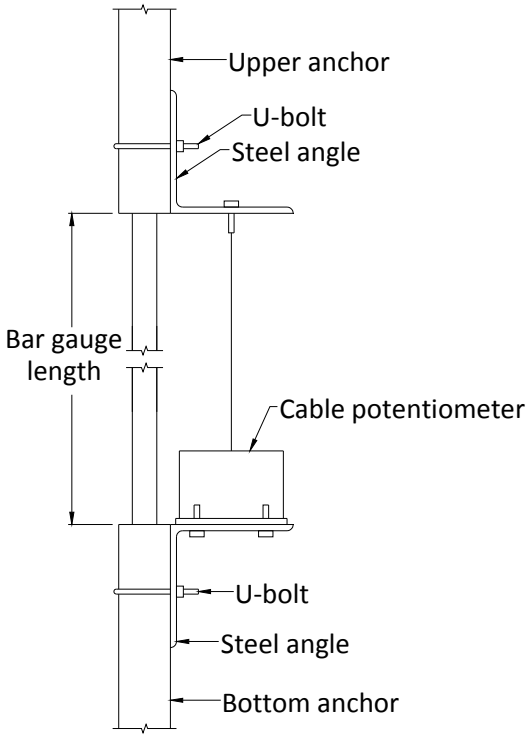

Figure A-3: Cable potentiometer configuration.

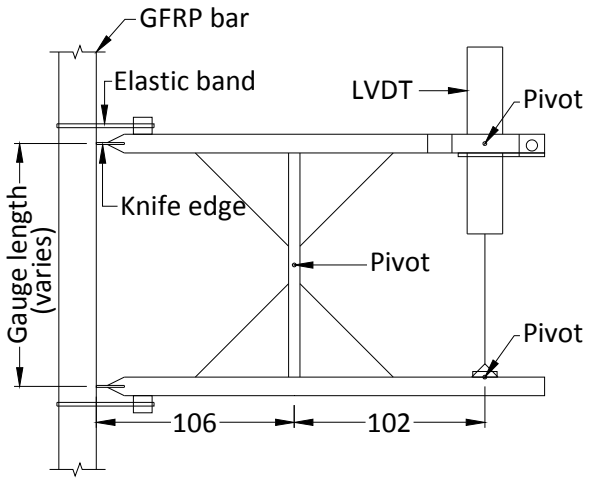

Figure A-4: LVDT and mounting bracket to measure strain in the GFRP bar.

Figure A-5: Typical tension test setup with strain gauges, LVDT, and cable potentiometer.

A.3.1 Specimen 6-1

During installation in the testing frame, the pressure setting for the hydraulic grips was too high which resulted in deformation of the top anchor. The deformation caused the specimen to be out of plumb by approximately 25 mm at the bottom anchor. However, the FRP bar had enough flexibility to easily force the bottom anchor into the hydraulic grip. At 234 kN, the upper steel anchor experienced tensile failure at the location where it entered the hydraulic grips. The FRP bar released all the elastic energy and the elastic rebound caused the bar to break into numerous pieces under compression failure. The load versus strain behaviour is shown in Figure A-6.

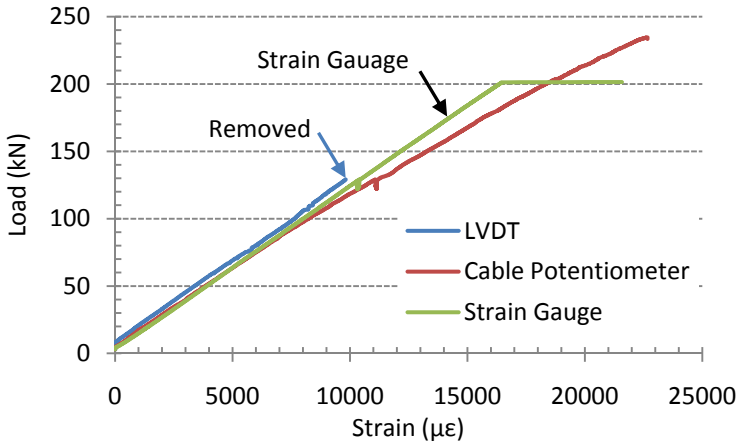

Figure A-6: Load-strain response of specimen 6-1.

A.3.2 Specimen 6-2

After testing of specimen 6-1, the hydraulic pressure setting for the grips was reduced to prevent deformation of the anchors. Specimen 6-2 failed in tension where the bar entered the top anchor. The overall bar behaviour is shown in Figure A-7. The discrepancy in the stiffness between the data measured by the LVDT and the cable potentiometer indicated that the tension coupon was experiencing elongation in the anchor region which was being measured by the cable potentiometer. Since the strain was computed based on the initial bar gauge length between the anchors, deformation/slippage of the bar inside the anchors was in effect increasing the gauge length which was unaccounted for in the calculation. Therefore, the bar stiffness as measured by the cable potentiometer appeared to decrease as loading progressed.

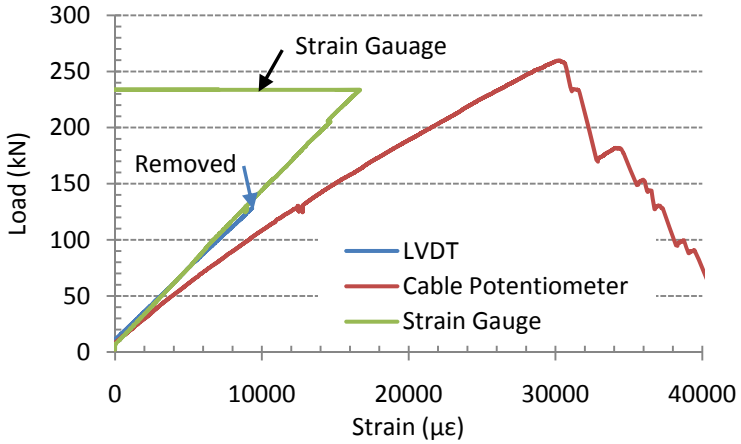

Figure A-7: Load-strain response of specimen 6-2.

A.3.3 Specimen 6-3

The specimen exhibited tension failure near the bottom anchor. Video analysis indicated that the failure initiated at the bottom anchor transition point. The overall bar behaviour is shown in Figure A-8. The LVDT had an initial lag in response but reported a similar stiffness in load-strain response as the strain gauges and the initial portion of the cable potentiometer.

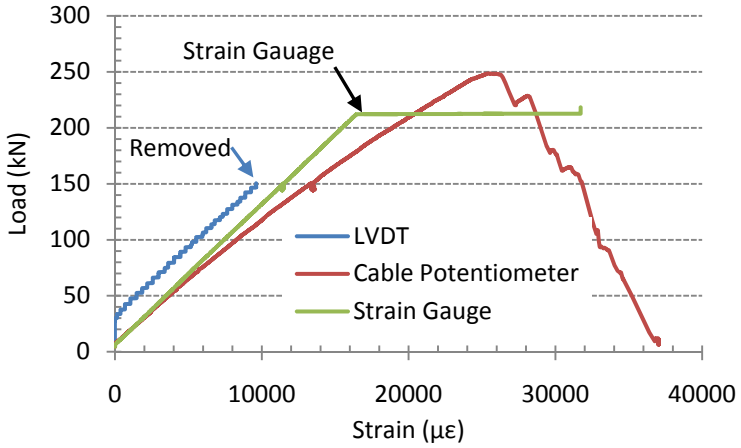

Figure A-8: Load-strain response of specimen 6-3.

A.3.4 Specimen 6-4

Specimen 6-4 had poor surface properties with very heavy diagonal strands producing deep depressions. Applying strain gauges on the longitudinal fibres was very difficult without causing damage to the diagonal fibres. Considerable cracking noise was heard very early in the loading process. At approximately 30% of the ultimate load, the strain gauge readings became unreliable. The early failure of the strain gauges may have resulted from the poor bar surface. The bar failed in a localized manner at the bottom

anchor transition point. After failure, the bar was slightly curved with the center deviating by about half a bar diameter from straight. The overall bar behaviour is shown in Figure A-9.

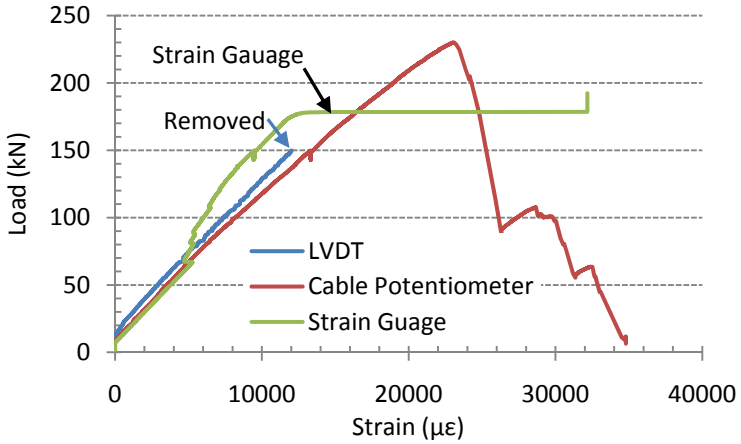

Figure A-9: Load-strain response of specimen 6-4.

A.3.5 Specimen 6-5

Specimen 6-5 had a very rough surface which made it difficult to apply strain gauges. Cracking noise was observed to start at a tensile load of 80 kN. At the same time, the strain gauges began to give erratic readings. The stress-strain response as measured by the LVDT was determined to be slightly bi-linear with the transition point to less stiff occurring at approximately 80 kN. Figure A-10 shows the load-strain behaviour of the bar.

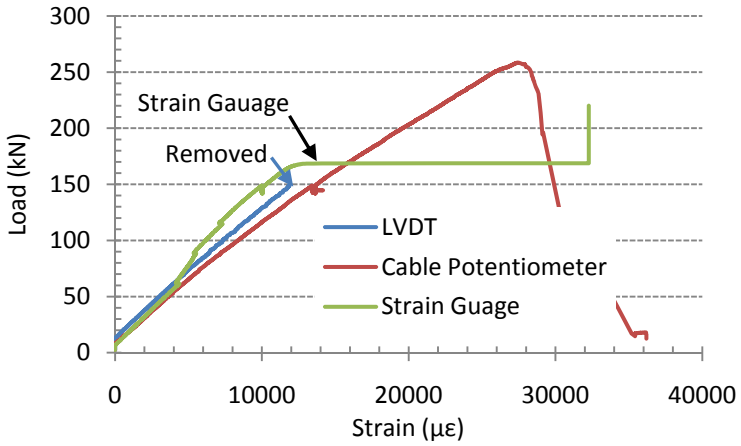

Figure A-10: Load-strain response of specimen 6-5.

A.3.6 Specimen 7-1

Localized failure occurred at the top anchor where the bar entered into the anchor. The overall bar behaviour is shown in Figure A-11. The majority of the strain gauges began to

give inconsistent results at a load of approximately 100 kN. The strain gauge shown in Figure A-11 gave good results almost to the peak load. The stepped response of the LVDT was due to friction in the pivot point of the LVDT bracket.

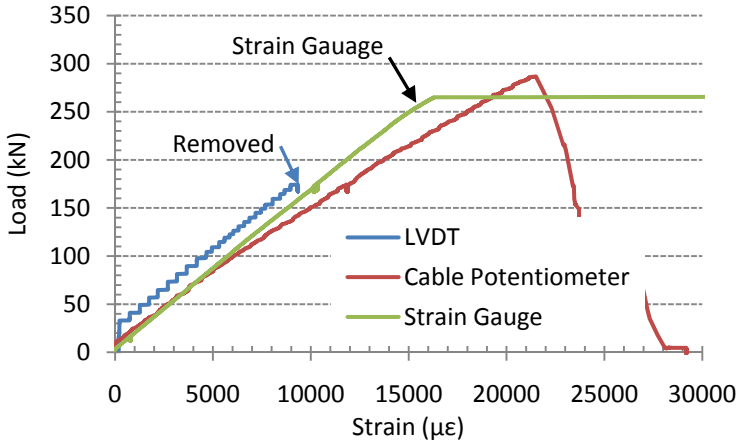

Figure A-11: Load-strain response of specimen 7-1.

A.3.7 Specimen 7-2

Failure occurred in the lower 100 mm of the bar length between the anchors. Figure A-12 shows the overall load behaviour. The strain readings from the strain gauges indicated a stiffer response when compared with the LVDT. At a load of approximately 80 kN, the slope of the strain gauge readings became even steeper as seen in Figure A-12. About half of the strain gauges recorded a small loss in strain at 80 kN after which a decreased strain rate was recorded.

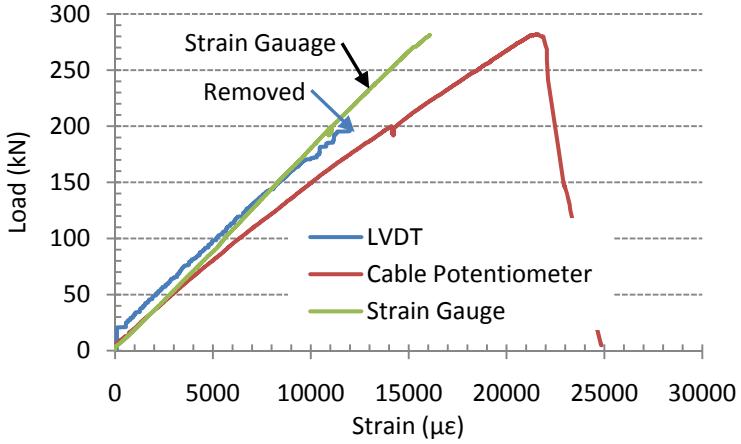

Figure A-12: Load-strain response of specimen 7-2.

A.3.8 Specimen 7-3

Tensile failure of specimen 7-3 occurred at the location where the bar entered the upper anchor. The overall bar behaviour is shown in Figure A-13. A 5 mm type KFG-5-

120-C1-11 strain gauge manufactured by Kyowa Electronic Instruments Co. Ltd. was applied in the transverse direction of loading to measure the circumferential strain. During loading, negative linear strain was recorded indicating the bar diameter was decreasing.

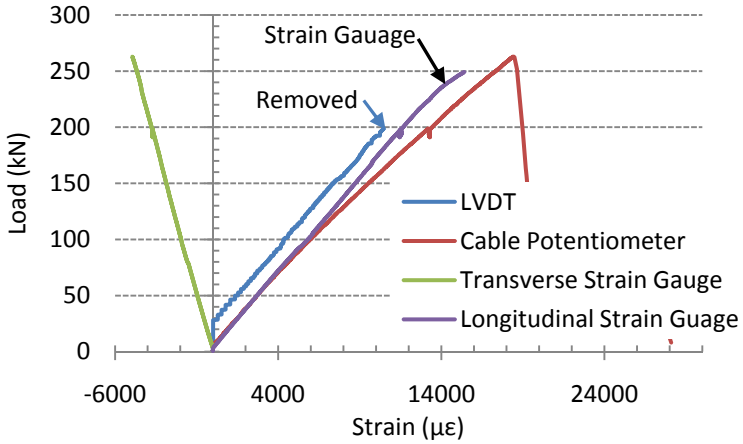

Figure A-13: Load-strain response of specimen 7-3.

A.3.9 Specimen 7-4

Specimen 7-4 failed where the bar entered the top anchor. The overall bar behaviour is shown in Figure A-14. Similar to specimen 7-3, some of the strain gauges recorded a decrease in strain rate (i.e. stiffer bar response) after reaching a load of 80-120 kN. The load where the change in recorded strain rate occurred was not consistent along the length of the bar. Near the bottom anchor, the change occurred at approximately 80 kN and near the top anchor at approximately 120 kN.

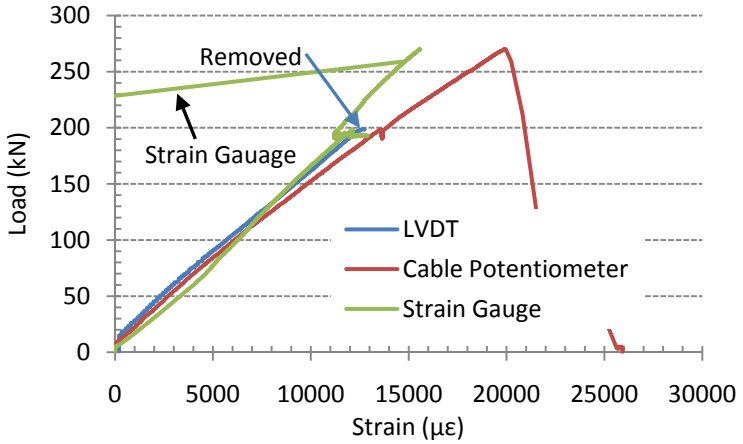

Figure A-14: Load-strain response of specimen 7-4.

A.3.10 Specimen 7-5

Specimen 7-5 failed at the location where the bar entered the upper anchor. The overall bar behaviour is given in Figure A-15. Similar to the other No. 7 specimens, all strain

gauges recorded a change in stiffness at 80 kN. Between 0 – 80 kN, the bar stiffness was greater than recorded by the LVDT and became even stiffer after 80 kN.

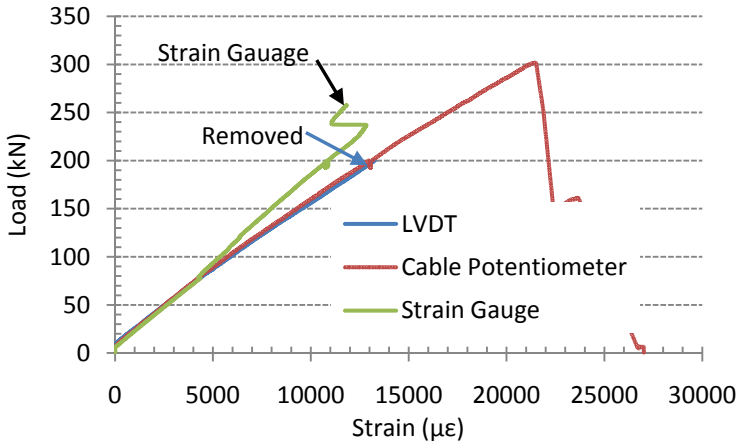

Figure A-15: Load-strain response of specimen 7-5.

A.3.11 Specimen 8-1

Due to uncertainty in the ultimate load capacity of the bar, the LVDT was removed at approximately 50% of the true bar capacity. The entire specimen failed in a brittle manner, producing a broom like effect over the entire bar length as shown in Figure A-16(a). The steel anchors were also observed to have elongated slightly. The overall bar behaviour is shown in Figure A-16(b). The LVDT experienced a lag in recording data due to friction in the pivot point of the LVDT bracket.

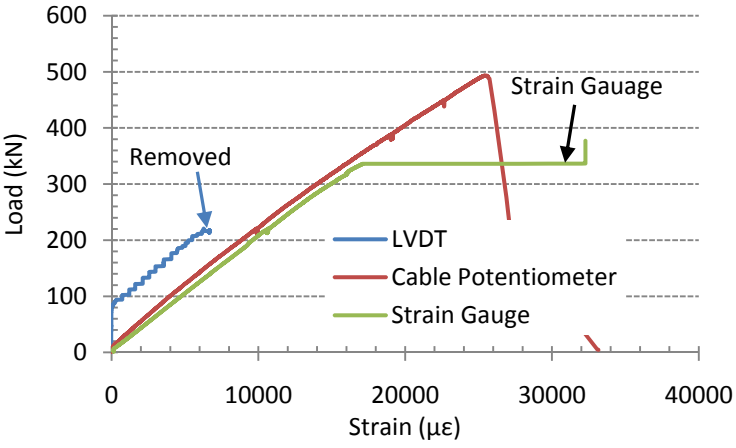

(a) **(b)**

Figure A-16: (a) tension failure of the FRP bar and (b) load-strain response of specimen 8-1.

A.3.12 Specimen 8-2

The bottom steel anchor yielded and ruptured in tension at the top end of the hydraulic grip. The elastic rebound caused a secondary compression failure in the FRP bar near the middle of the specimen length. The overall bar behaviour is shown in Figure A-17.

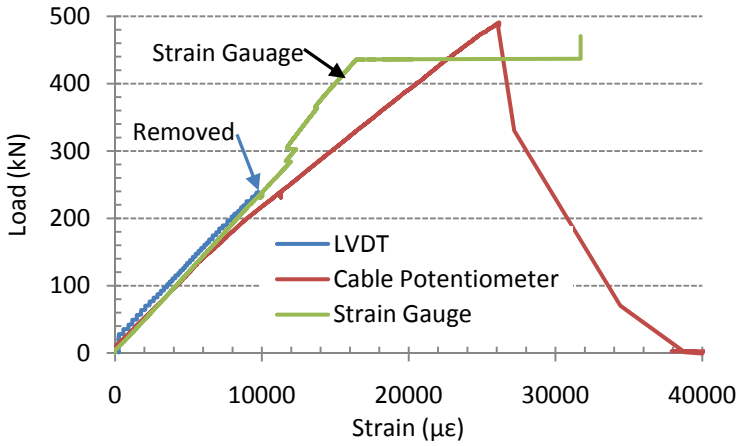

Figure A-17: Load-strain response of specimen 8-2.

A.3.13 Specimen 8-3

Specimen 8-3 failed in a similar manner to specimen 8-2 where the bottom anchor yielded and ruptured in tension. Figure A-18 shows the behaviour of the bar.

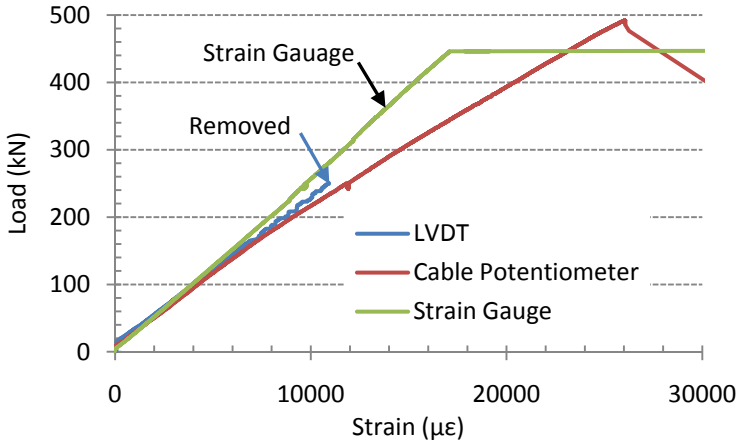

Figure A-18: Load-strain response of specimen 8-3.

A.3.14 Specimen 8-4

The entire length of specimen 8-4 experienced tension failure with the bar expanding into individual strands of fibre. The overall bar behaviour is shown in Figure A-19.

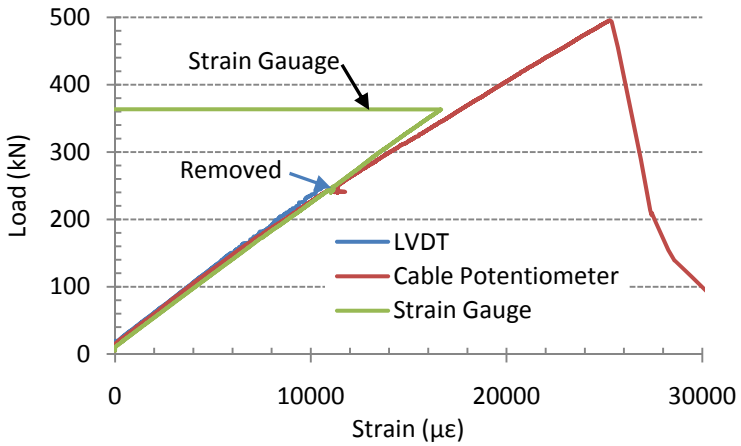

Figure A-19: Load-strain response of specimen 8-4.

A.3.15 Specimen 8-5

Specimen 8-5 exhibited sudden and brittle failure of the entire bar length. Figure A-20(a) shows the failed bar and Figure A-20(b) shows the overall bar behaviour.

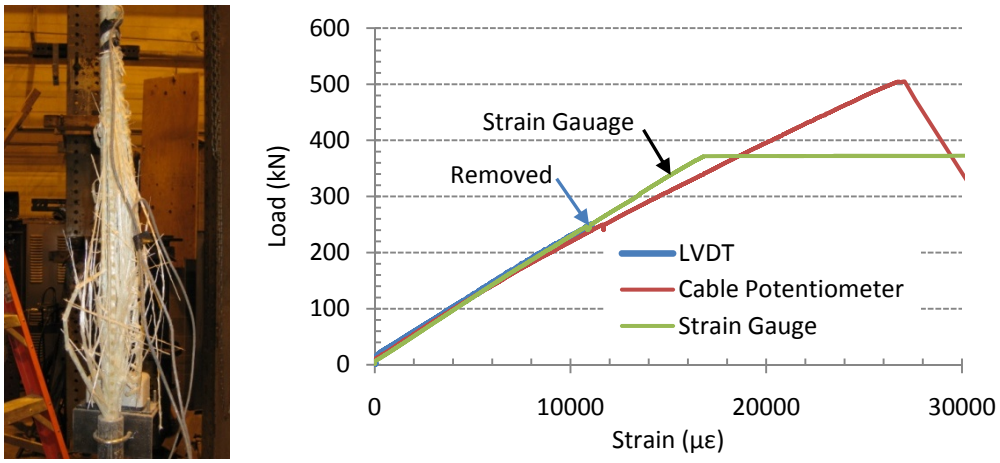

(a) (b)

Figure A-20: (a) failure and (b) load-strain response of specimen 8-5.

A.4 Discussion and Summary

The failure load, equivalent failure stress, and modulus of elasticity for all the bars are reported in Table A-4. The failure stress was calculated using the measured cross-sectional area. Note that the failure loads and stresses do not necessarily represent the true capacities of the GFRP bars. Failure in or near the anchors indicates a possible local stress concentration that could have caused the bar to fail prematurely. In the instances where the steel anchor yielded and ruptured, the actual failure load of the GFRP bar is higher than reported. Due to a limited number of tensile test specimens, no additional tests could be performed and none of the results were discarded. The values can be viewed as lower bound quantities.

The modulus of elasticity was calculated based on the LVDT data using a linear regression line. Unless otherwise noted in Table A-4, the modulus of elasticity was calculated over the region between 10% and 40% of the peak load. Some of the specimens exhibited a change in the slope of the load-strain relationship at approximately 30% of the failure load as indicated in Table A-4. In these cases, the modulus of elasticity was taken from the initial linear portion of the stress-strain response. From the preliminary design of the deep beam specimens, the stresses in the GFRP bars were not expected to exceed 40-50% of the ultimate capacity. From the experimental results, the stress level in the bottom layer of GFRP bars in the deep beam specimens varied between 27 and 69% (average = 47%) of the ultimate tensile capacity at the peak load with the exception of specimen A1N which had a stress level close to rupture. Hence, the modulus of elasticity between 10-40% of the maximum load was deemed appropriate.

The stiffness of the No. 8 bars as determined by the LVDT was consistent with the readings obtained from the electrical resistance strain gauges. However, this was not the case with the No. 7 specimens. The slope of the load versus strain response indicated that the average stiffness of the bar as measured by the LVDT was less than the localized measurements taken by the electrical resistance strain gauges. Generally, the strain gauges indicated slightly stiffer response than the LVDT at low loads with a sudden increase in stiffness at around 80 kN. At this load level, some of the strain gauges started producing erratic readings. There are two possible explanations. The first was that the strain gauges partially debonded. However, the majority of the strain gauges experienced the same effect at the same time indicating another event must have occurred. In some specimens, cracking was heard when the strain gauge readings began detecting different stiffnesses. Micro-cracks may have occurred in the resin with subsequent readings giving greater discrepancy between the localized and average strain. Micro-cracks could also have led to partial debonding of the strain gauges.

The majority of the strain gauges were adhered to the longitudinal section of the bar between the diagonal wrapped fibres as shown in Figure A-2. The bar was observed to bulge in-between the cross-over points of the wrapped fibres. During manufacturing, the wrapping process could have resulted in resin being forced away from the cross-over point creating the bulge between the wrapped fibres. More resin may locally influence the apparent stiffness of the bar and may have resulted in the higher stiffness report by some of the strain gauges. In addition, the behaviour of the strain gauges was related to the quality of the bar's surface. Some of the No. 6 bars (specimens 6-4 and 6-5) and the majority of the No. 7 bars had poor surface quality which may have contributed in poor strain gauge performance. Inconsistently spaced diagonal fibres, diagonal fibres that were not completely in contact with the main bar and inconsistent sand and resin coating were some of the surface defects identified.

Each specimen was instrumented with multiple strain gauges to assess the installation procedure and suitability of different types of strain gauges and adhesives. On any particular bar, the majority of the strain gauges provided consistent results. The type of strain gauge was determined to have a negligible effect on the strain readings. The type of adhesive used also had little effect on the results. Therefore, the most efficient procedure was chosen for use in applying strain gauges on the FRP bars in the deep beam specimens. Strain gauges manufactured by Kyowa Electronic Instruments Co. Ltd. having a gauge length of 5 mm and M-bond 200 adhesive were selected for use in the deep beam specimens.

The tensile test program exposed some problems with determining the tensile capacity of FRP bars. The steel anchors must be large enough to prevent excessive deformation or yielding of the steel. The size of the anchors provided by the GFRP supplier was not adequate for the No. 8 bars and did not meet the CSA S806-02 recommended size. Although not all No. 8 bars experienced anchor failures, all of the anchors yielded and a larger anchor should be used. The majority of the No. 6 and No. 7 bars failed near or partially within the anchors. This indicates a problem with the force transfer between the bar and the non-explosive demolition agent used as the bonding material which may have caused localized stresses to develop. Additional tests should be conducted to identify an improved anchor installation method.

The average experimental values reported in Table A-4 were used in the analysis of the deep beam specimens.

Table A-4: Summary of the tension test results.

Specimen No.	Area (mm^2)	Failure Load (kN)	Failure Stress (MPa)	Slope (kN/με)	Modulus of Elasticity (MPa)	Comments
No. 6 Bars						
6-1	322	234	728	0.0122	37950	Steel anchor tensile failure, FRP failure load unknown.
6-2	322	260	809	0.0126	39190	Failed at the anchor.
6-3	322	248	771	0.0121	37640	Failed at the anchor.
6-4	322	230	715	0.012	37330	Modulus of elasticity changes at about 75 kN. Value shown is for 15-60 kN. For 100-150 kN, slope is 0.0108. Failed at the anchor.
6-5	322	258	802	0.0121	37640	Modulus of elasticity changes at about 80 kN. Value shown is for 10-70 kN. For 100-150 kN, slope is 0.0106. Failed at the anchor.
Average		**246**	**765**	**0.0122**	**37900**	
No. 7 Bars						
7-1	396	287	725	0.0164	41410	
7-2	396	282	712	0.0164	41410	Modulus of elasticity changes at about 80 kN. Value shown is for 20-70 kN. For 100-200 kN, slope is 0.0144. Failed at the anchor.
7-3	396	263	664	0.0166	41920	Failed at the anchor.
7-4	396	270	682	0.0163	41160	Modulus of elasticity changes at about 80 kN. Value shown is for 20-70 kN. For 100-195 kN, slope is 0.0145 . Failed at the anchor.
7-5	396	302	763	0.0157	39650	Modulus of elasticity changes at about 80 kN. Value shown is for 10-80 kN. For 100-200, slope is 0.0134. Failed at the anchor.
Average		**281**	**709**	**0.01628**	**41100**	
No. 8 Bars						
8-1	528	494	936	0.0222	42050	
8-2	528	491	930	0.0229	43370	Steel anchor tensile failure, FRP failure load unknown.
8-3	528	492	932	0.0222	42050	Steel anchor tensile failure, FRP failure load unknown.
8-4	528	495	938	0.0225	42610	
8-5	528	505	956	0.0218	41290	
Average		**495**	**938**	**0.02232**	**42300**	

Appendix B: Concrete Properties

This appendix describes the properties of the concrete used in the deep beam specimens. Testing procedures and results are discussed.

B.1 Mix Design Specifications

The concrete was obtained from a local ready-mix supplier with the nominal specifications listed in Table B-1. A normal strength and a high strength concrete mix were required.

Table B-1: Concrete specifications.

Mix Type	Normal Strength	High Strength
28 day strength	35 MPa	70 MPa
Slump	80-120 mm	80-120 mm
Air content	Natural	Natural
Maximum aggregate size	14 mm	14 mm

B.2 Quality Control Tests and Results

For each concrete cast, quality control tests were conducted. A slump test was performed prior to casting the concrete in the forms. Numerous 100 x 200 mm and 150 x 300 mm cylinders were cast to determine the concrete strength at 7, 14, 21, and 28 days. To establish the modulus of rupture at 28 days, three 150 x 150 x 500 mm prisms were cast. The modulus of elasticity was not determined for the quality control cylinders. All of the concrete quality control specimens were stored in a 100% humidity room. All of the tests were conducted in accordance with CSA A23.2 (2002). Specifically, the following test methods were used:

- A23.2-3C Making and curing concrete compression and flexural test specimens
- A23.2-5C Slump of concrete
- A23.2-8C Flexural strength of concrete
- A23.9-9C Compressive strength of cylindrical concrete specimens

The test results for the four concrete batches are shown in Figure B-1 to Figure B-4. The concrete cast in batch No. 3 consisted of the high strength mix. The normal strength cylinders were sulphur capped while the ends of the high strength cylinders were prepared by grinding. All of the quality control specimens were tested in a FX700 Forney frame.

The average strength at 7 days for the normal strength concrete was 71% of the 28 day strength. The high strength concrete gained no strength between 21 and 28 days. However, at day 7, 87% of the 28 day strength had been attained.

Concrete Strength Test Results (Batch No. 1)

Specimen No.: **B3N, B4N, A3N**
Date: **May 27, 2009**

Load Amount: 3.0 m^3
Slump: **95 mm**

Cylinder Number	Age Days	Cylinder Diameter (mm)	Load (kN)	Compressive Strength (MPa)	Type of Failure	Comments
1	7	100	223	28.4	Cone	
2	14	100	259.9	33.1	Cone	
3	21	100	281.5	35.8	Shear	
4	28	100	293.5	37.4	Cone	**Average: 37.1 MPa**
5	28	100	275	35.0	Shear	
6	28	100	306.5	39.0	Cone	
7	28	150	602	34.1	Cone	**Average: 35.5 MPa**
8	28	150	672	38.0	Cone/Shear	
9	28	150	609	34.5	Cone	

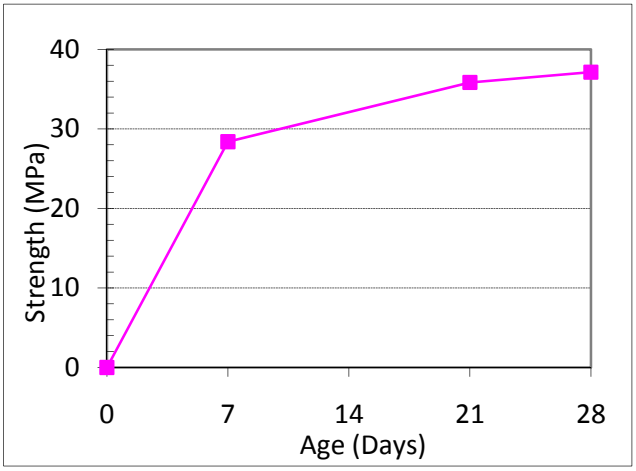

Flexural Test by third point loading	
Prism	Modulus of Rupture (MPa)
No. 1	3.9
No. 2	3.9
No. 3	3.8
Average	**3.9**

Figure B-1: Concrete quality control results for batch No. 1

Concrete Strength Test Results (Batch No. 2)

Specimen No.: **B1N, B2N, A1N**

Date: **June 9, 2009**

Load Amount: 3.0 m^3

Slump: **80 mm**

Cylinder Number	Age Days	Cylinder Diameter (mm)	Load (kN)	Compressive Strength (MPa)	Type of Failure	Comments
1	3	100	170	21.6	Cone	
2	7	100	232.5	29.6	Cone	
3	14	100	269.5	34.3	Cone	
4	21	100	301.5	38.4	Cone	
5	28	100	322	41.0	Cone	**Average: 41.1 MPa**
6	28	100	320.5	40.8	Cone	
7	28	100	325.5	41.4	Cone	
8	28	150	712	40.3	Cone	**Average: 39.5 MPa**
9	28	150	679.5	38.5	Cone	
10	28	150	700	39.6	Cone	

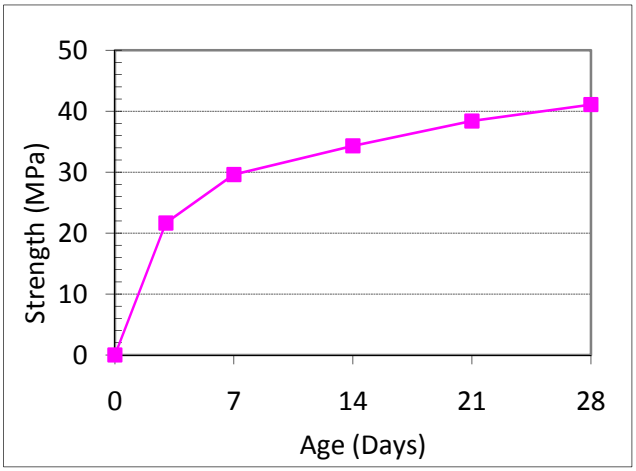

Flexural Test by third point loading	
Prism	Modulus of Rupture (MPa)
No. 1	4.3
No. 2	3.9
No. 3	3.9
Average	**4.0**

Figure B-2: Concrete quality control results for batch No. 2

Concrete Strength Test Results (Batch No. 3)

Specimen No.: **B5H, B6H, A4H**
Date: **June 17, 2009**

Load Amount: 3.0 m^3
Slump: **105 mm**

Cylinder Number	Age Days	Cylinder Diameter (mm)	Load (kN)	Compressive Strength (MPa)	Type of Failure	Comments
1	7	100	386.5	49.2	Cone	
2	14	100	436.5	55.6	Cone	
3	21	100	514.5	65.5	Cone	
4	28	100	490.5	62.5	Cone	**Average: 64.2 MPa**
5	28	100	498.5	63.6	Cone/shear	
6	28	100	523.5	66.7	Shear	
7	28	150	1182	66.9	Shear	**Average: 64.6 MPa**
8	28	150	1064	60.2	Cone/shear	
9	28	150	1177	66.6	Cone/shear	

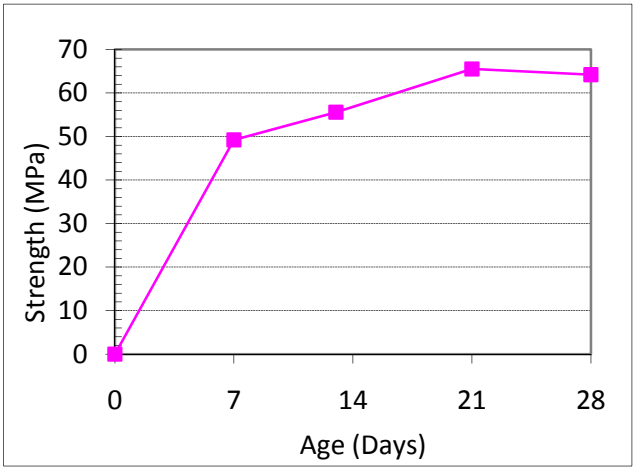

Flexural Test by third point loading	
Prism	Modulus of Rupture (MPa)
No. 1	5.9
No. 2	6.4
No. 3	6.5
Average	**6.3**

Figure B-3: Concrete quality control results for batch No. 3

Concrete Strength Test Results (Pour No. 4)

Specimen No.: **C1N, C2N, A2N**
Date: **October 7, 2009**

Load Amount: 3.5 m^3
Slump: **150 mm**

Cylinder Number	Age Days	Cylinder Diameter (mm)	Load (kN)	Compressive Strength (MPa)	Type of Failure	Comments
1	7	100	207	26.4	Cone	
2	14	100	282	35.9	Cone	
3	21	100	314	39.9	Cone	
4	28	100	329	41.8	Cone	**Average: 41.9 MPa**
5	28	100	346	44.0	Cone	
6	28	100	314	39.9	Cone	
7	28	150	720	40.7	Cone	**Average: 40.2 MPa**
8	28	150	703	39.8	Cone	

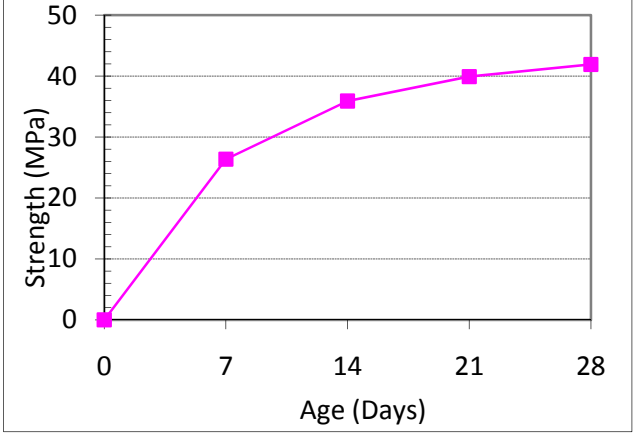

Flexural Test by third point loading	
Prism	Modulus of Rupture (MPa)
No. 1	4.1
No. 2	3.8
No. 3	3.6
Average	**3.9**

Figure B-4: Concrete quality control results for batch No. 4

B.3 Concrete Strength of the Beam Specimen

Additional 100 mm x 200 mm diameter concrete cylinders were made during the specimen casting for determining the concrete strength of each specimen. “Specimen” in this section refers to any of the 12 large-scale reinforced concrete beams. A total of three cylinders were cast for each specimen. These cylinders were cured and stored

under the same conditions as the corresponding specimens. The concrete strength of the specimens was determined by testing the three cylinders either on the same or following day as the specimen test. The test methods used to determine the compressive strength and the stress-strain response are:

- A23.9-9C Compressive strength of cylindrical concrete specimens
- ASTM C 469-02 Standard test method for static modulus of elasticity and poisson's ratio of concrete in compression

All the cylinders were tested in a MTS 2600 frame equipped with a spherical loading head. Loading was conducted using displacement control in order to allow for observation of the post-peak response of the concrete cylinders. A strain yoke shown in Figure B-5 having a gauge length of 100 mm was used to measure the strain response during loading. The strain was measured using three LVDTs inserted into the yoke at the third points circumferentially. The upper and lower portions of the yoke were held together by spacer bars during installation to ensure proper positioning. Three screws having pointed ends were tightened against the concrete in both the top and bottom portion of the yoke. The spacer bars were then removed and testing commenced. The load and strain readings were logged using a HBM MGCplus data acquisition with the Catman Professional 6.0 measurement software. The sampling rate was 1 Hz.

Figure B-5: Cylinder test using a yoke to determine the stress-strain response of the concrete. Two LVDTs are visible and the third is hidden behind the cylinder.

In all instances, the cylinders where loaded past the peak load with the yoke attached. This enabled the determination of deformation at the peak load and the post-peak response. The stress-strain response for each cylinder was calculated using the average

of the three LVDT readings and the force reading from the testing machine's internal load cell. The chord modulus of elasticity (i.e. between 0-40% of ultimate concrete strength) was determined according to ASTM C 469-02. Results for the cylinders of each specimen are given in the sections below. The average peak compressive strength was used in the analysis of the specimens (Chapter 5).

Note that initially the cylinders were tested using neoprene pads as the size of sulphur caps prevented installation of the yokes. However, poor cylinder performance was observed with the neoprene pads. Subsequently, use of sulphur caps that had smaller edges enabled the installation of the yokes. The high strength cylinders were end ground.

The stress-strain response typically became unreliable after approximately 20% drop in load from the maximum load. This was due to the yokes moving as a result of the concrete cracking.

B.3.1 Specimen A1N

Loading Rate: 0.2 mm/min
Cylinder Ends: Sulphur capped

	f_c'(MPa)	ε_c'(με)	E_c(MPa)	Comments
Cylinder 1	38.8	2682	23740	Cone failure
Cylinder 2	40.8	2769	22340	cone failure
Cylinder 3	41.0	2648	22970	cone failure
Average	**40.2**	**2700**	**23020**	

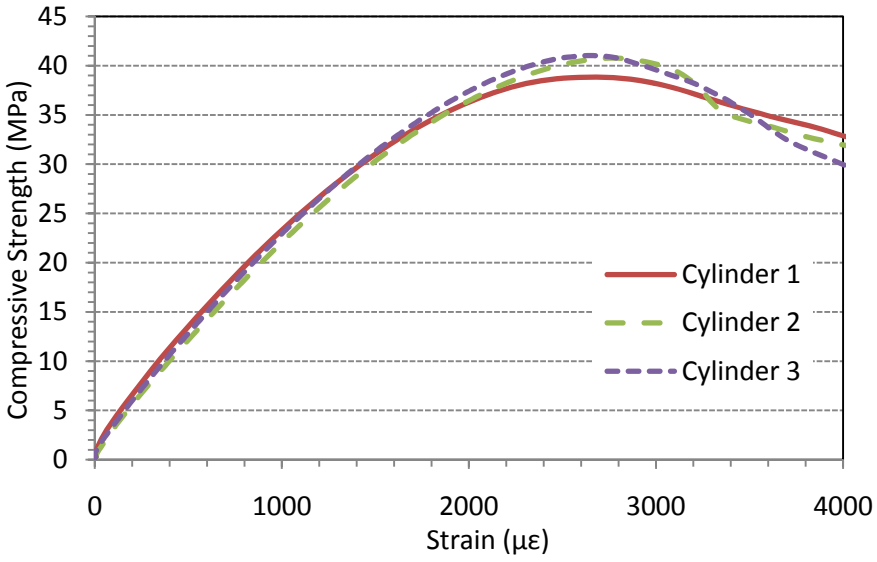

B.3.2 Specimen A2N

Loading Rate: 0.2 mm/min
Cylinder Ends: Sulphur capped

	f_c'(MPa)	ε_c'(με)	E_c(MPa)	Comments
Cylinder 1	47.2	2852	23960	Cone Failure
Cylinder 2	43.3	2866	22160	Cone Failure
Cylinder 3	45.6	2753	22440	Cone Failure
Average	**45.4**	**2824**	**22850**	

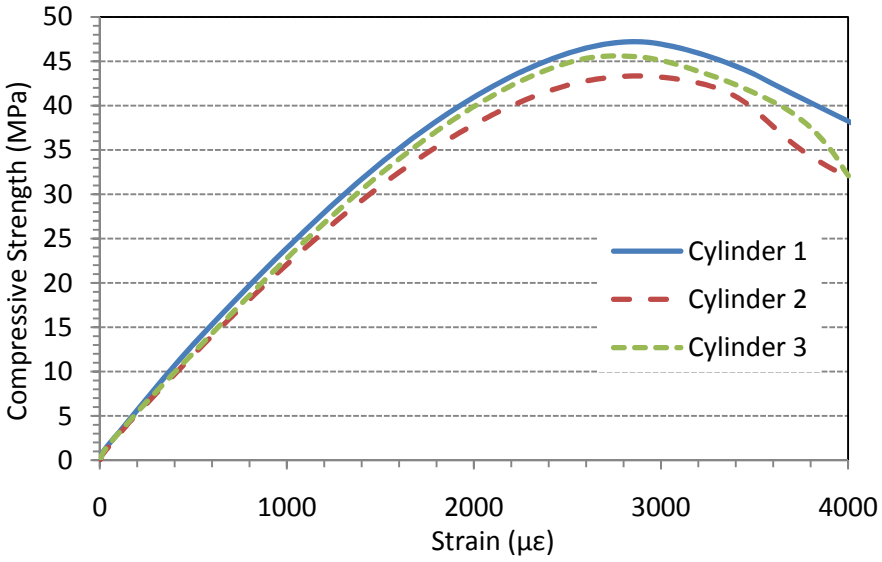

B.3.3 Specimen A3N

Loading Rate: 0.2 mm/min
Cylinder Ends: Sulphur capped

	f_c'(MPa)	ε_c'(με)	E_c(MPa)	Comments
Cylinder 1	42.3	2697	24280	Cone Failure
Cylinder 2	40.5	2439	24640	Cone Failure
Cylinder 3	41.1	2624	23540	Cone Failure
Average	**41.3**	**2587**	**24150**	

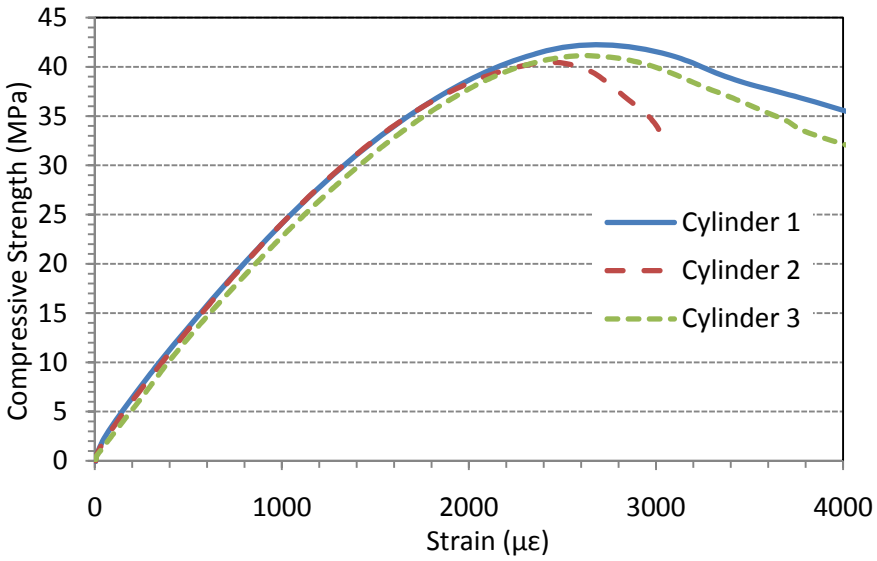

B.3.4 Specimen A4H

Loading Rate: 0.2 mm/min
Cylinder Ends: End Ground

	f_c'(MPa)	ε_c'(με)	E_c(MPa)	Comments
Cylinder 1	63.7	3021	22890	Cone Failure
Cylinder 2	66.7	2216	31470	Cone Failure
Cylinder 3	64.0	3442	22090	Cone Failure
Cylinder 4	64.0	3230	22370	Shear Failure
Average	**64.6**	**3231***	**22450***	

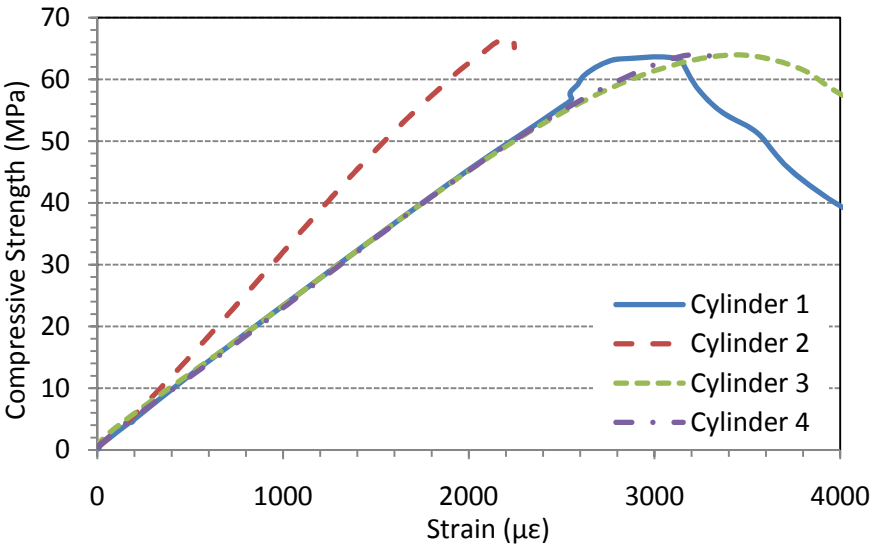

*Cylinder 2 results were discarded for these averages due to the stress-strain curve significantly deviating from the results of the other cylinders at 10 MPa indicating a problem with the yoke installation.
Post-peak response was not accurately recorded due to the yokes moving as a result of the concrete cracking.

B.3.5 Specimen B1N

Loading Rate: 0.4 mm/min
Cylinder Ends: Neoprene Caps

	f_c'(MPa)	ε_c'(με)	E_c(MPa)	Comments
Cylinder 1	40.0	2077	24180	Abrupt failure with one side blowing out
Cylinder 2	41.2	2547	22980	Side/end failure
Cylinder 3	40.2	2633	22800	Side/end failure
Average	**40.5**	**2419**	**23320**	

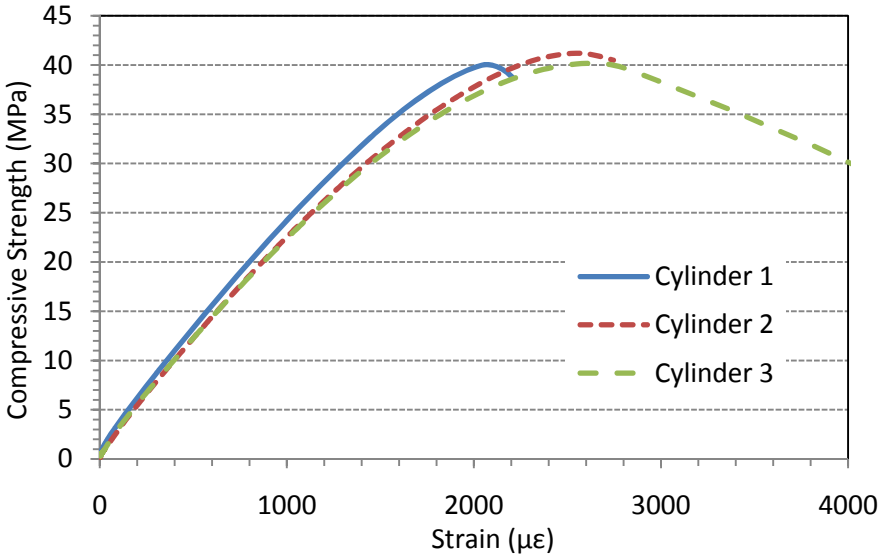

B.3.6 Specimen B2N

Loading Rate: 0.4 mm/min
Cylinder Ends: Neoprene Caps

	f_c'(MPa)	ε_c'(με)	E_c(MPa)	Comments
Cylinder 1	38.9	2402	23860	End Failure
Cylinder 2	41.2	2460	23260	End Failure
Cylinder 3	39.6	2576	22530	Shear Failure
Average	**39.9**	**2479**	**23210**	

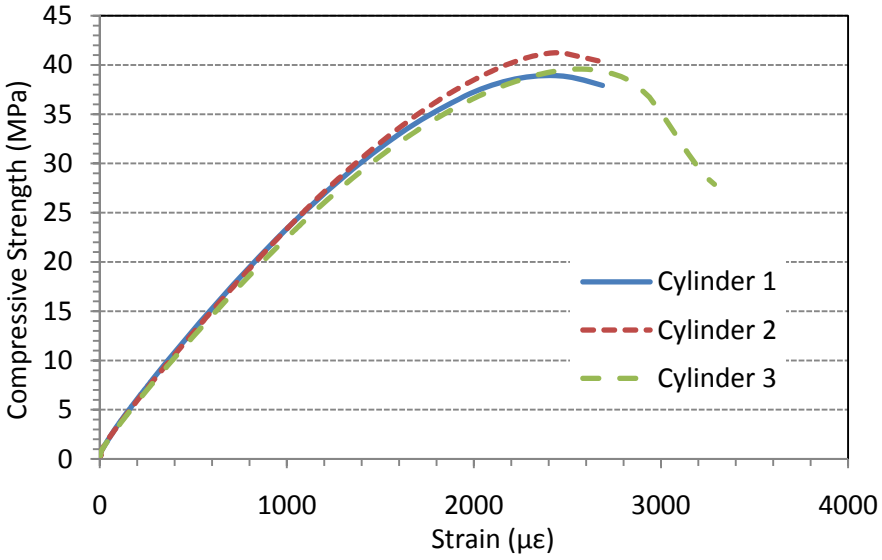

B.3.7 Specimen B3N

Loading Rate: 0.4 mm/min
Cylinder Ends: Neoprene Caps

	f_c'(MPa)	ε_c'(με)	E_c (MPa)	Comments
Cylinder 1	38.9	2578	23160	End Failure
Cylinder 2	41.2	2722	23810	End Failure
Cylinder 3	40.7	2380	24080	End Failure
Average	**41.2***	**2722***	**23680**	*** Cylinder 1 & 3 omitted**

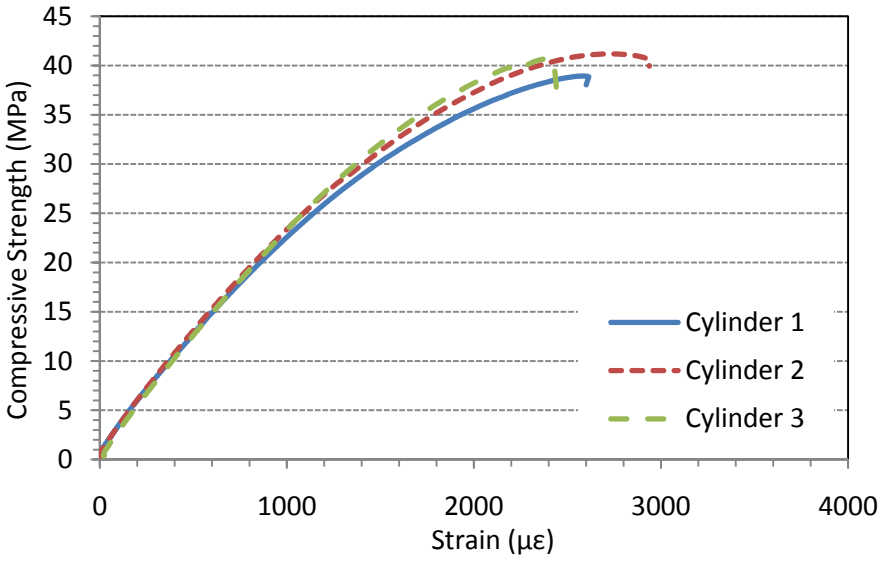

Cylinder 1 and 3 appeared to fail prematurely and were omitted in the calculations of f_c' and ε_c'. All cylinders failed abruptly with side fracture occurring at either the top or bottom end. Post-peak response could not be captured.

B.3.8 Specimen B4N

Loading Rate: 0.4 mm/min
Cylinder Ends: Neoprene Caps

	f_c'(MPa)	ε_c'(με)	E_c(MPa)	Comments
Cylinder 1	40.4	2430	24460	Top corner failed abruptly
Cylinder 2	40.9	2562	24120	Cone Failure
Average	**40.7**	**2496**	**24290**	

Cylinder 3 was discarded due to poor geometric properties as one end was not cylindrical.

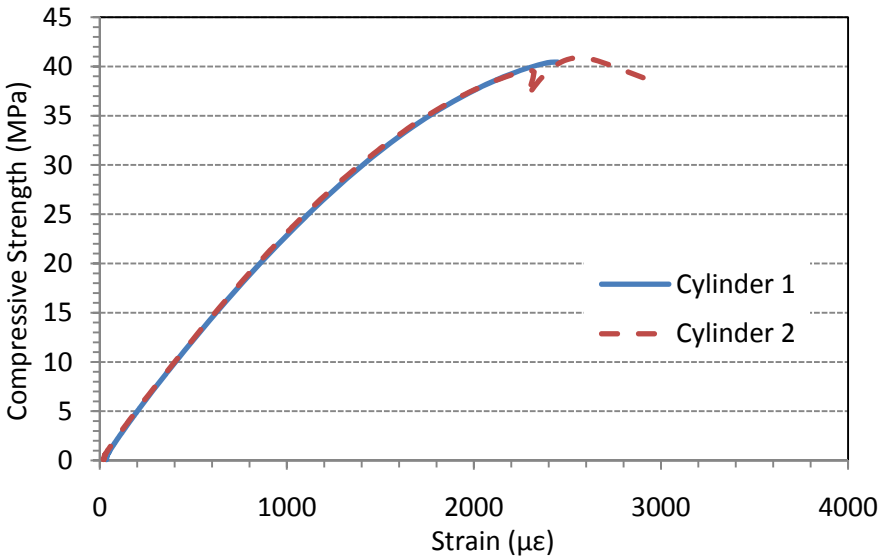

B.3.9 Specimen B5H

Loading Rate: 0.2 mm/min (0.1 mm/min for cylinder 1)
Cylinder Ends: End Ground

	f_c'(MPa)	ε_c'(με)	E_c(MPa)	Comments
Cylinder 1	64.3	3372	23690	Cone Failure
Cylinder 2	68.0	3462	24600	Cone Failure
Cylinder 3	66.9	3349	24120	Cone Failure
Average	**66.4**	**3394**	**24140**	

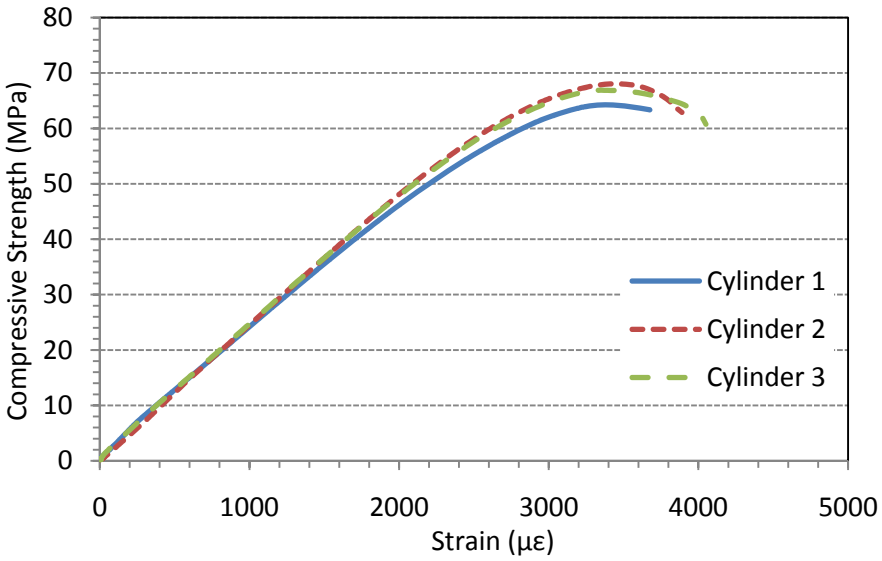

B.3.10 Specimen B6H

Loading Rate: 0.2 mm/min
Cylinder Ends: End Ground

	f_c'(MPa)	ε_c'(με)	E_c(MPa)	Comments
Cylinder 1	67.5	3366	23580	Cone Failure
Cylinder 2	70.9	3357	24610	Cone Failure
Cylinder 3	67.2	3348	23830	Cone Failure
Average	**68.5**	**3357**	**24010**	

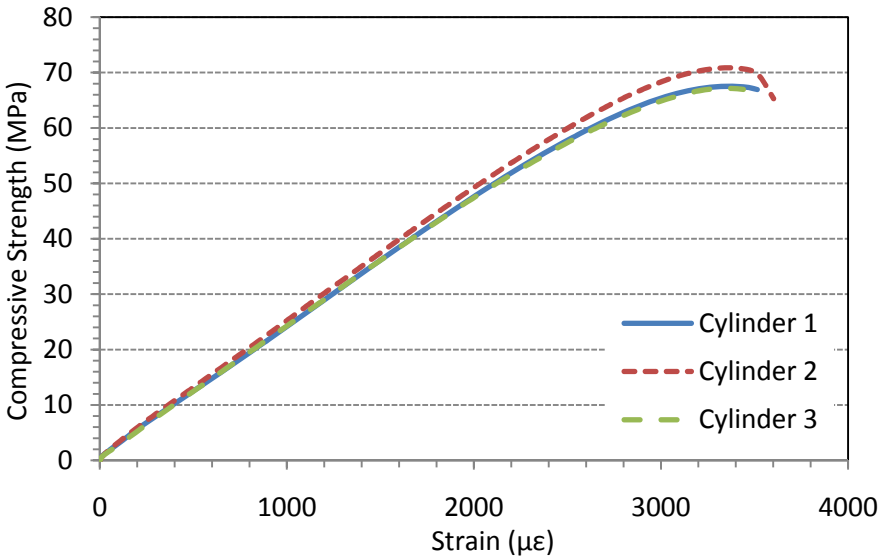

B.3.11 Specimen C1N

Loading Rate: 0.2 mm/min
Cylinder Ends: Sulphur Capped

	f_c'(MPa)	ε_c'(με)	E_c(MPa)	Comments
Cylinder 1	54.8	2653	27510	Cone Failure
Cylinder 2	51.5	2530	27470	Cone Failure
Cylinder 3	47.7	2493	26540	Cone Failure
Cylinder 4	52.3	2690	25950	Cone/Shear Failure
Average	**51.6**	**2592**	**26870**	

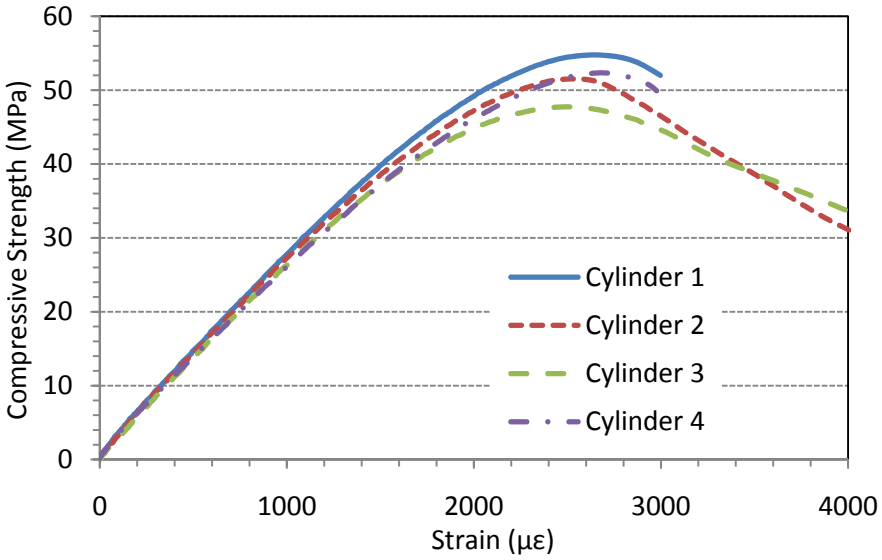

B.3.12 Specimen C2N

Loading Rate: 0.2 mm/min
Cylinder Ends: Sulphur capped

	f_c'(MPa)	ε_c'(με)	E_c(MPa)	Comments
Cylinder 1	49.4	2673	25120	Cone Failure
Cylinder 2	51.7	2847	24800	Cone Failure
Cylinder 3	50.9	2677	25850	Cone Failure
Average	**50.7**	**2732**	**25260**	

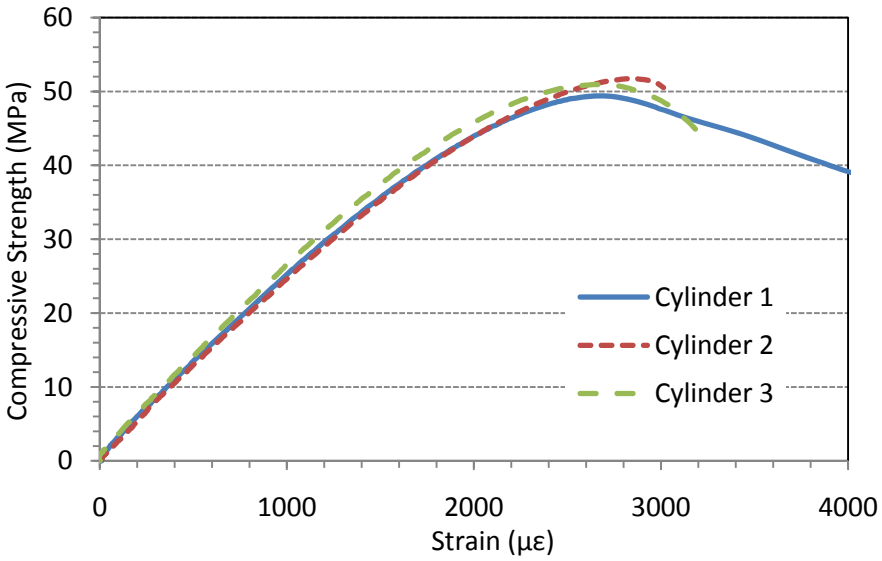

B.3.13 Summary

Consistent results were obtained for the concrete strength of the specimens cast from the same batch. Overall, the concrete from batch 1 and batch 2 had similar strengths. The concrete from batch 4 had strengths that were 25% greater than from batch 1 and 2 even though it was the same mix design.

The concrete strength of the specimens cast from batch 1, 3, and 4 was approximately 3%, 7%, and 23% greater than the 28 day concrete strength obtained from the quality control tests. This is not surprising considering that the majority of the specimens were tested between 36 and 173 days, well past the 28 days for the quality control tests. The concrete strength of the specimens from batch 2 was similar to the 28 day quality control strength.

Appendix C: Detailed Experimental Results for the Deep Beam Specimens

This appendix describes the testing of all GFRP reinforced concrete deep beam specimens considered during this study. Information on the test setup, instrumentation, and results are given in this appendix.

C.1 Test Setup and Instrumentation

The specimen orientation as indicated in Figure C-1 was used throughout the thesis including this appendix. The specimen was oriented east-west in the MTS 6000 test frame with the south face considered as the front side. The front side of the specimen contained the grid and the back side had a speckled black paint pattern for the DIC strain measurement system. When facing the front side of the beam, end A was on the left (i.e. west) and end B was on the right (i.e. east) as shown in Figure C-1.

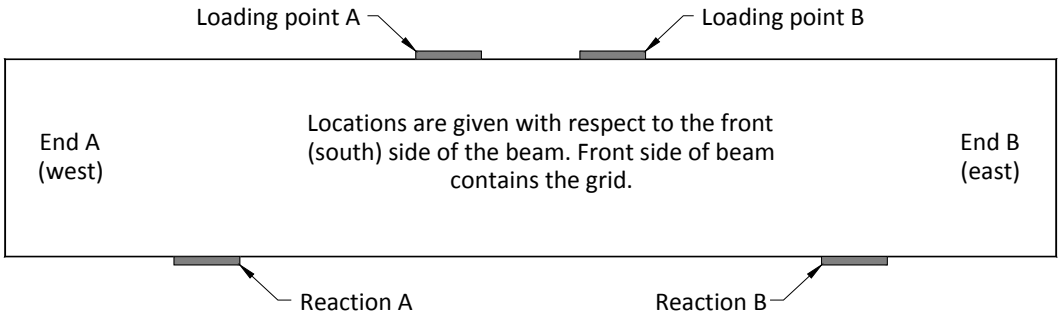

Figure C-1: Designation of test specimen orientation.

With the exception of specimens C1N and C2N, the support reaction assembly consisted of (from top to bottom) the bearing plate, knife edge, load cell, and rollers as shown in Figure C-2(a). Due to limited capacity, the load cells were omitted for the tests of specimens C1N and C2N. The loading assembly consisted of a stiffened distributing beam with two loading points each comprised of (from top to bottom) rollers, knife edges, and bearing plates as seen in Figure C-2(b).

The electrical resistance strain gauge locations varied by up to ±20 mm from the desired location. The strain gauges had to be applied directly on the longitudinal fibres of the GFRP reinforcement and not on the cross-wrapped fibres. Therefore, if required the strain gauges were moved to the nearest suitable locations and the as-built locations are provided for each specimen in the sections below. Wherever possible, the strain gauges were applied such that they were located on the side of the bar in the final reinforcement cage assembly. The strain gauges, 5 mm gauge length type KFG-5-120-C1-11 manufactured by Kyowa Electronic Instruments Co. Ltd., were applied using the procedure outlined in Chapter 3 using M-bond 200 adhesive. After applying each strain gauge, a 4 conductor wire was soldered to the leads of the strain gauge. The M-coat D

air drying acrylic coating from Vishay Micro-Measurements was applied to the strain gauge in a thin layer as a protective barrier against moisture (Figure C-3). The strain gauge and lead wires were then covered with a layer of clear silicon to prevent damage during placing of the concrete.

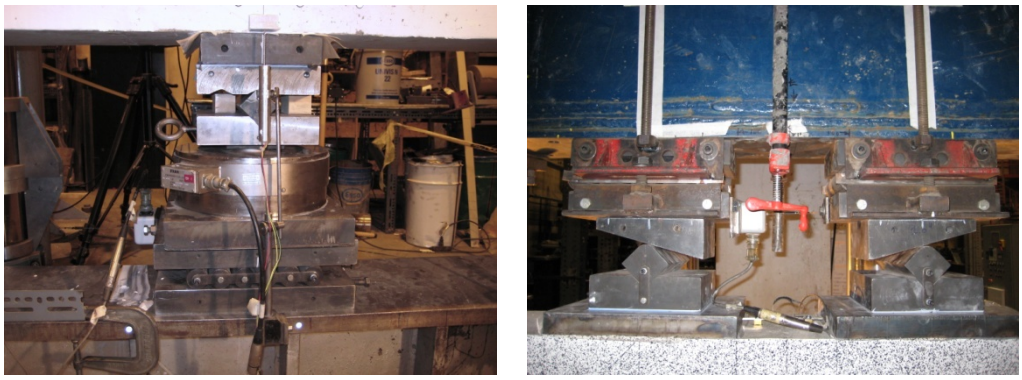

(a) (b)

Figure C-2: (a) typical reaction consisting of the bearing plate, knife edge, load cell, and rollers (specimen shown has h = 600 mm) and (b) typical loading points with rollers, knife edges, and bearing plates (specimen shown has h = 1000 mm).

Figure C-3: Instrumentation of the GFRP bars with strain gauges. Middle bar shows a strain gauge with wires attached and covered with M-coat D protective coating. The silicon protective coating has not been added yet.

Once all strain gauges were applied, the reinforcement cages were assembled using plastic ties and placed in the formwork (Figure C-4). The reinforcement was tied using wire to the formwork at both ends and at the middle to prevent floatation during placing of the concrete. Form oil was sprayed on the formwork prior to inserting the reinforcement cages. Figure C-5 shows the forms immediately prior to the placement of concrete.

Figure C-4: Rebar cage positioned in the 600 mm deep formwork (specimen B6H). The No. 3 transverse support bars seen in the center of the photograph are located at mid-span. Similar support bars were provided at both ends.

(a) (b)

Figure C-5: (a) 600 mm deep (specimen B5H left and B6H right) and (b) 1000 mm deep (specimen C1N left and C2N right) formwork ready for the concrete.

Steel lifting hooks were placed in the end regions of the specimens. The hooks were located well past the support location to ensure no interference in the force transfer mechanism during specimen testing.

Concrete was placed in a series of three lifts for the 600 and 1000 mm deep specimens. Two lifts were used for the 300 mm deep specimens. Each lift was compacted using internal vibration. Figure C-6(a) shows the vibration of the first lift of concrete in the 600 mm deep forms.

(a) (b)

Figure C-6: (a) vibrating concrete in the 600 mm deep formwork for specimen B5H and B6H and (b) typical test setup (specimen C1N shown).

Prior to testing, the front and back surface of the specimens were painted. A flat white acrylic latex paint was used. The back surface of the specimen was then speckled with flat black acrylic latex paint using an air sprayer. The paint was thinned with water and the airflow and nozzle opening adjusted to produce the correct speckle size needed for the DIC measurement system.

Once the specimens were placed into position in the test frame, the demountable instrumentation was installed. Using epoxy, thin aluminum plates having dimensions of approximately 10 mm x 20 mm were applied to the bottom surface of the specimens at the quarter span and mid-span locations where the vertical LVDTs were installed. The aluminum plates prevented the LVDTs from either breaking into air pockets during the test which may have been present under the surface of the concrete or cracks that may form at that location during testing. At the support locations, small angles were

attached to the concrete using epoxy to provide a measurement surface for the vertical LVDTs (top center of Figure C-2(a)).

The 45° strain rosettes consisted of LVDTs attached to threaded rods. The ¼" threaded rods were glued with epoxy into 20 mm deep holes drilled using a hammer drill. The circle diameter was 125 mm, 250 mm, and 350 mm for the specimens having h = 300 mm, 600 mm, and 1000 mm, respectively.

C.2 Comments on the Data in this Appendix

- The LVDTs were calibrated prior to the first test and the calibration was checked after the last specimen was tested. Intermediate checks were also conducted to ensure accuracy of all readings.
- The reported load is the total applied load which consisted of the machine load plus the weight of the loading assembly. Self-weight of the specimen was not included in this reported value.
- Quarter bridge configurations were used for all strain gauges. A four-wire measuring technique was used to eliminate lead-wire resistance.
- All instrumentation was checked immediately prior to commencement of loading to confirm correct measurements were being taken.
- All data channels were set to zero prior to initiating the test with the exception of the two support load cells. The support load cells were set to zero after the knife edges and bearing plates were placed on top of them but prior to the specimen being installed. The remaining channels were set to zero after the loading assembly had been installed (i.e. immediately prior to applying machine load).
- Measurements were continuously logged for the entire duration of the test.
- Data tables are provided for each specimen. These tables show a subset of data only for the loading stages at a regular time interval that varies for each specimen.
- The quarter span and mid-span deflection values reported have been adjusted for measured support settlement.
- Data for one set of strain rosettes is given for each specimen. In some specimens, cracks did not penetrate through both rosettes; therefore, the rosette data is for the rosette which contained cracks. In the instances were both rosettes contained cracks, the rosette data is presented for the shear span where failure occurred. The calculated orientation of the minimum principal strain was unreliable at low rosette strain readings due to reading accuracy of the LVDTs. Therefore, the principal strain angle is not shown in the figures until the calculated angle stabilized at higher load levels.

C.3 Specimen A1N

The displacement rate of specimen A1N was 0.1 mm/min of machine stroke. Flexural cracks at mid-span were first noticed during loading at approximately P = 130 kN and confirmed at load stage 2. At load stage 9 (P = 687 kN) localized crushing of the concrete from the inside edge of the loading plates to approximately 75 mm towards the mid-span was noticed on the front face. At P = 767 kN the specimen moved globally by approximately 10 mm towards end B (east) and the center LVDT (Δ_2) was displaced. The LVDT was reset and the data adjusted. As loading progressed, the upper 25 mm of concrete on the front face of the specimen between the loading plates was slowly forced upward while further crushing occurred along the inside edge of the loading plate. However, the concrete on the back half of the top compression zone was not forced upwards. This created a triangular block of concrete on the top front edge of the specimen that was forced upwards.

The DIC system recorded only localized crushing strains in the vicinity of the loading plates extending approximately one plate width into the main flexural region. At mid-span, the concrete strain at the extreme top of the compression zone was around 2200 με which was below the crushing strain determined from the companion cylinder tests. Overall, and be taking into account the load deflection behaviour, the specimen failed in flexural compression.

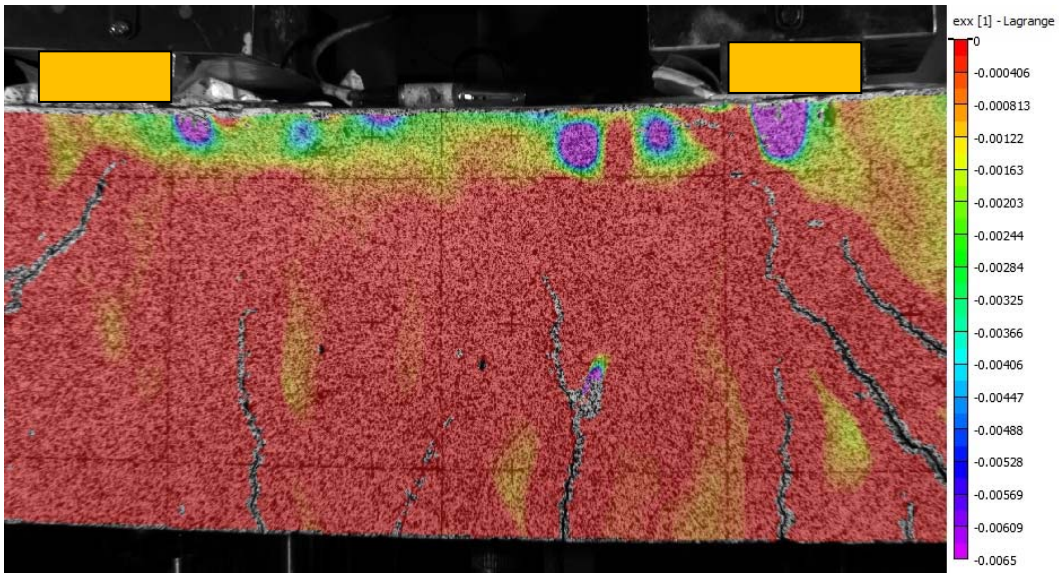

Figure C-7: Horizontal strain map (showing compression only) of the back surface of specimen A1N between the loading plates at the peak load.

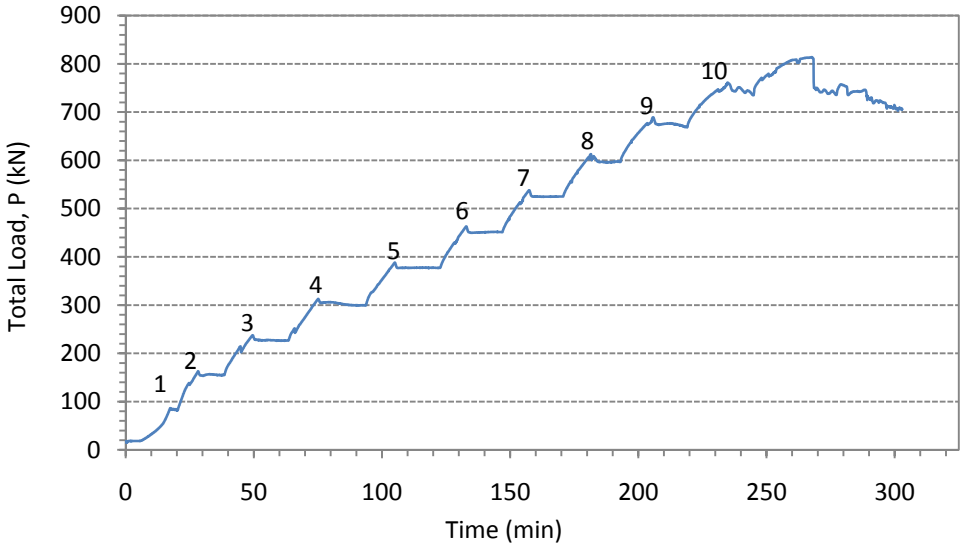

Figure C-8: Load – history of specimen A1N.

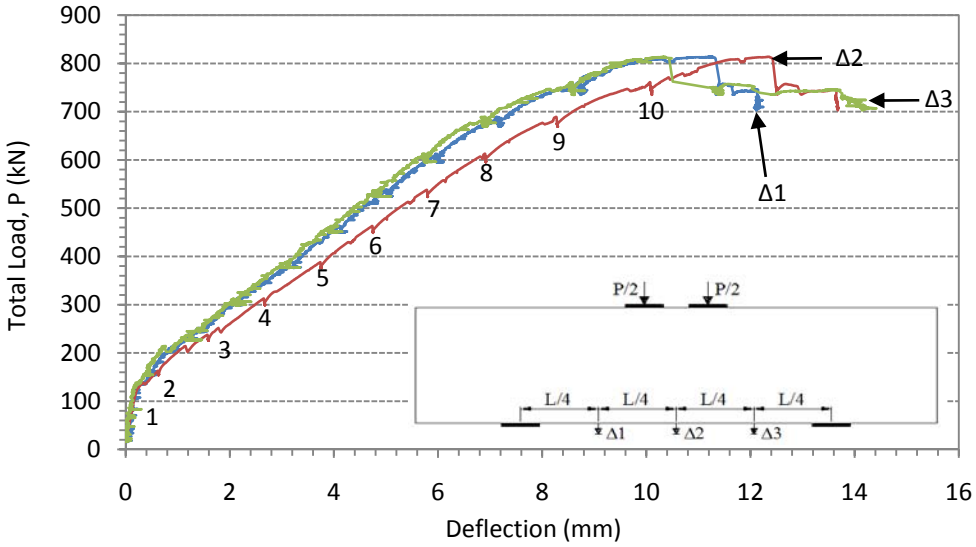

Figure C-9: Load – displacement response of specimen A1N.

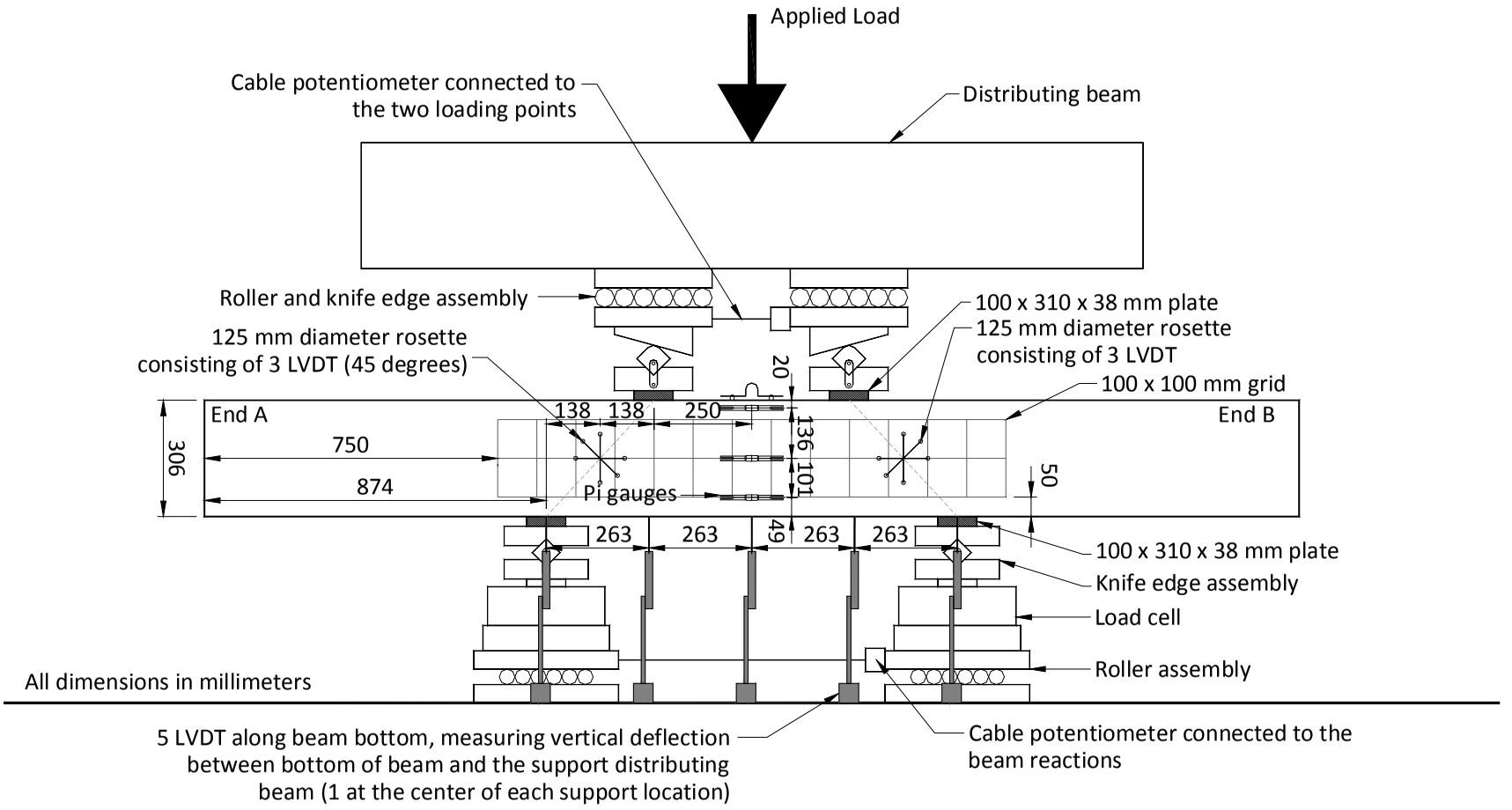

Figure C-10: Instrumentation drawing for specimen A1N.

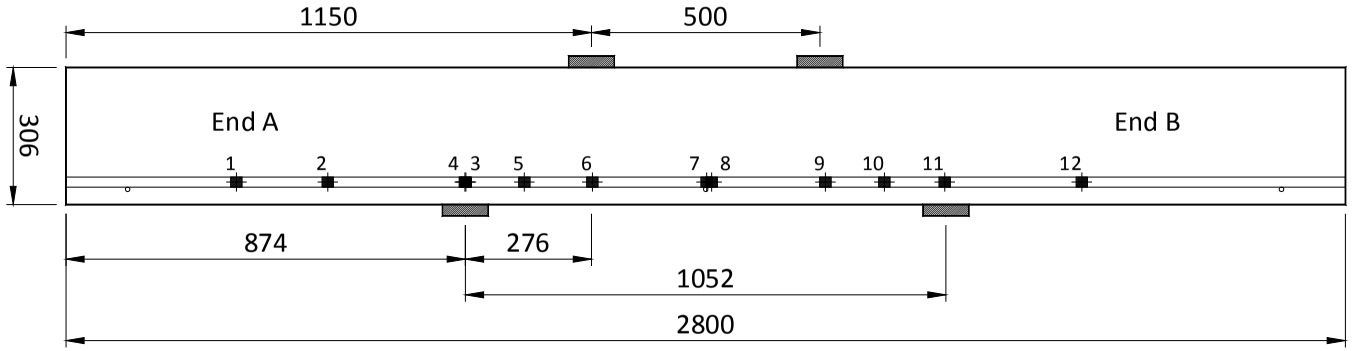

Strain Gauge Locations

Strain Gauge No.	Column	Distance from End A (mm)
1	F	373
2	C	573
3	C	875
4	B	873
5	C	1003
6	C	1152
7	C	1402
8	B	1413
9	C	1662
10	F	1791
11	C	1923
12	C	2223

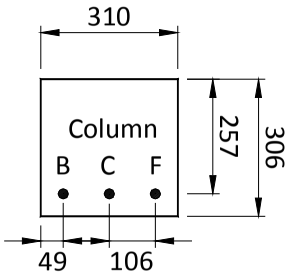

(3) - #7 GFRP Bars

Notes:
All dimensions in mm
Clear Cover: 38.1 mm
Concrete Strength: 40 MPa
Bar Length: 2800 mm

Figure C-11: Location of the strain gauges for specimen A1N (as-built).

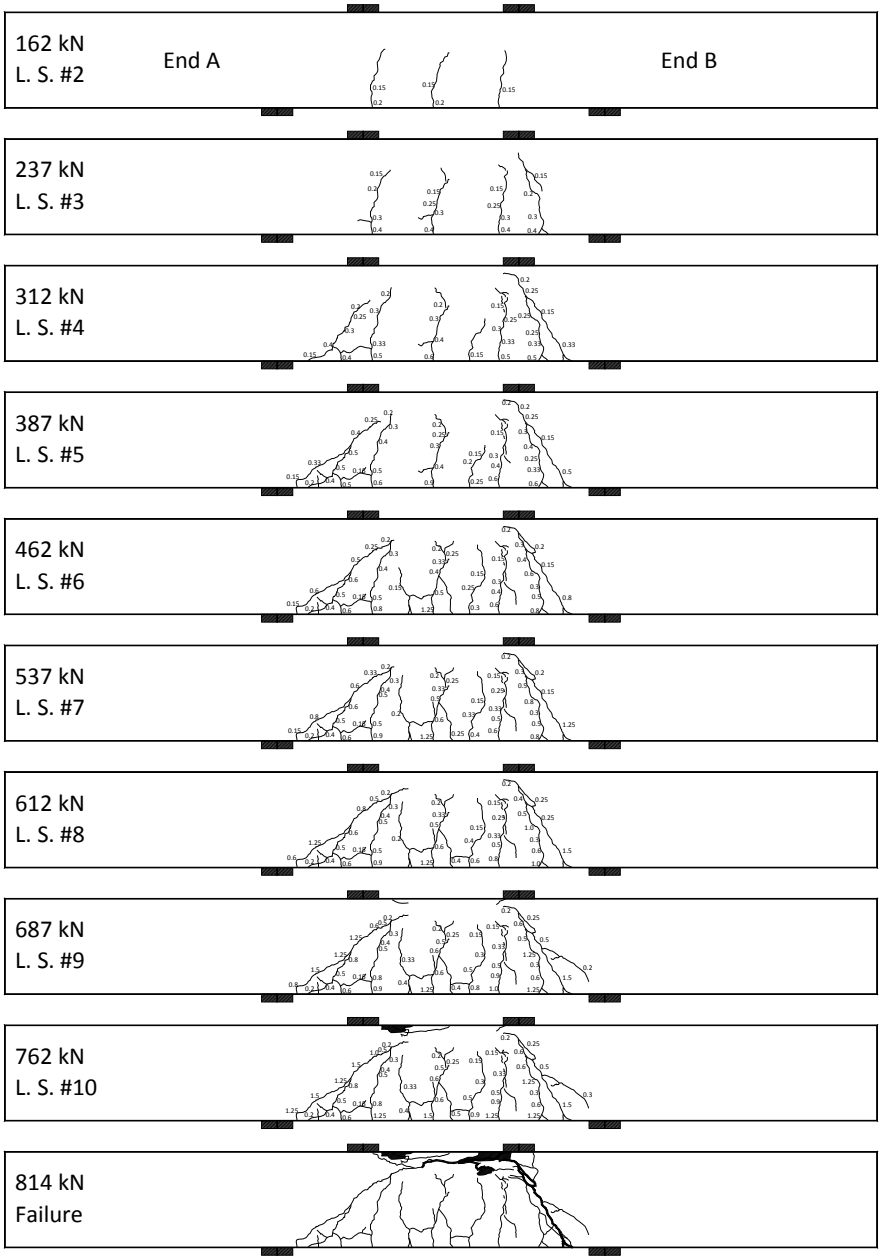

Figure C-12: Crack diagrams of specimen A1N showing the development of the cracks and the widths as loading progressed.

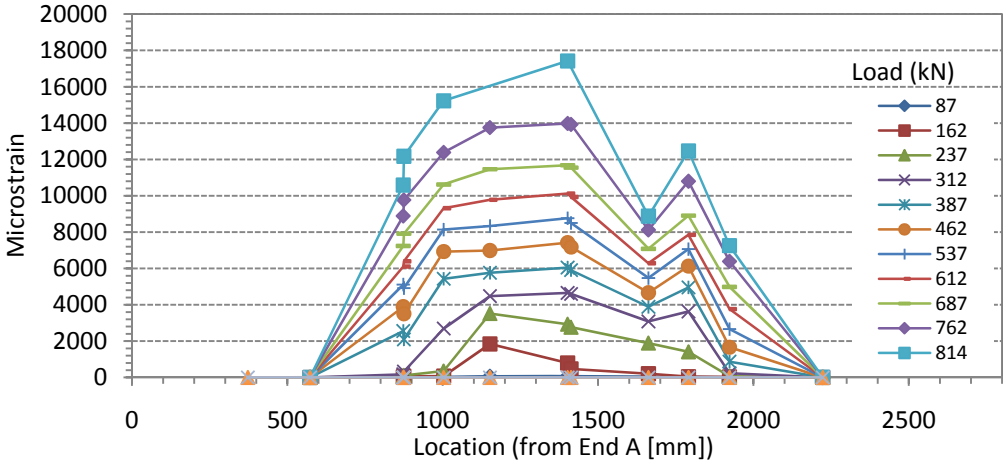

Figure C-13: Strain in the reinforcement as loading progressed.

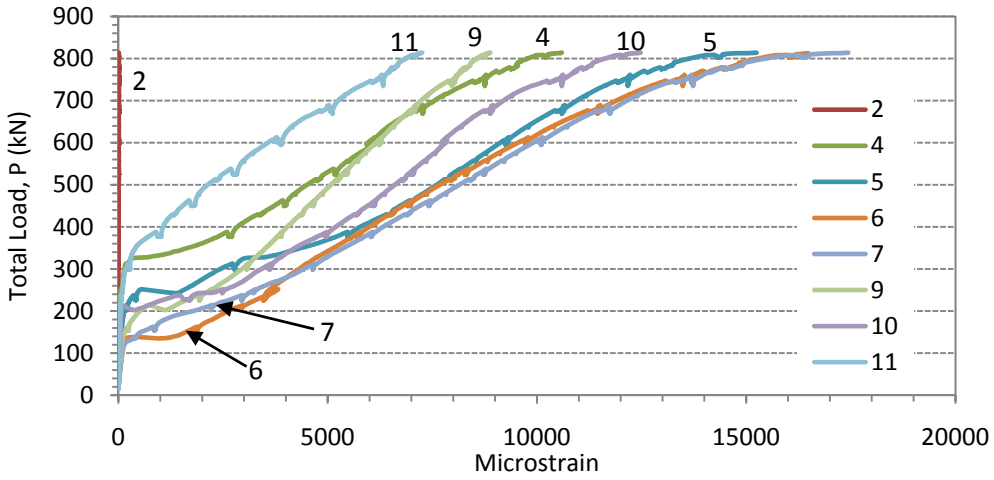

Figure C-14: Strain in the reinforcement.

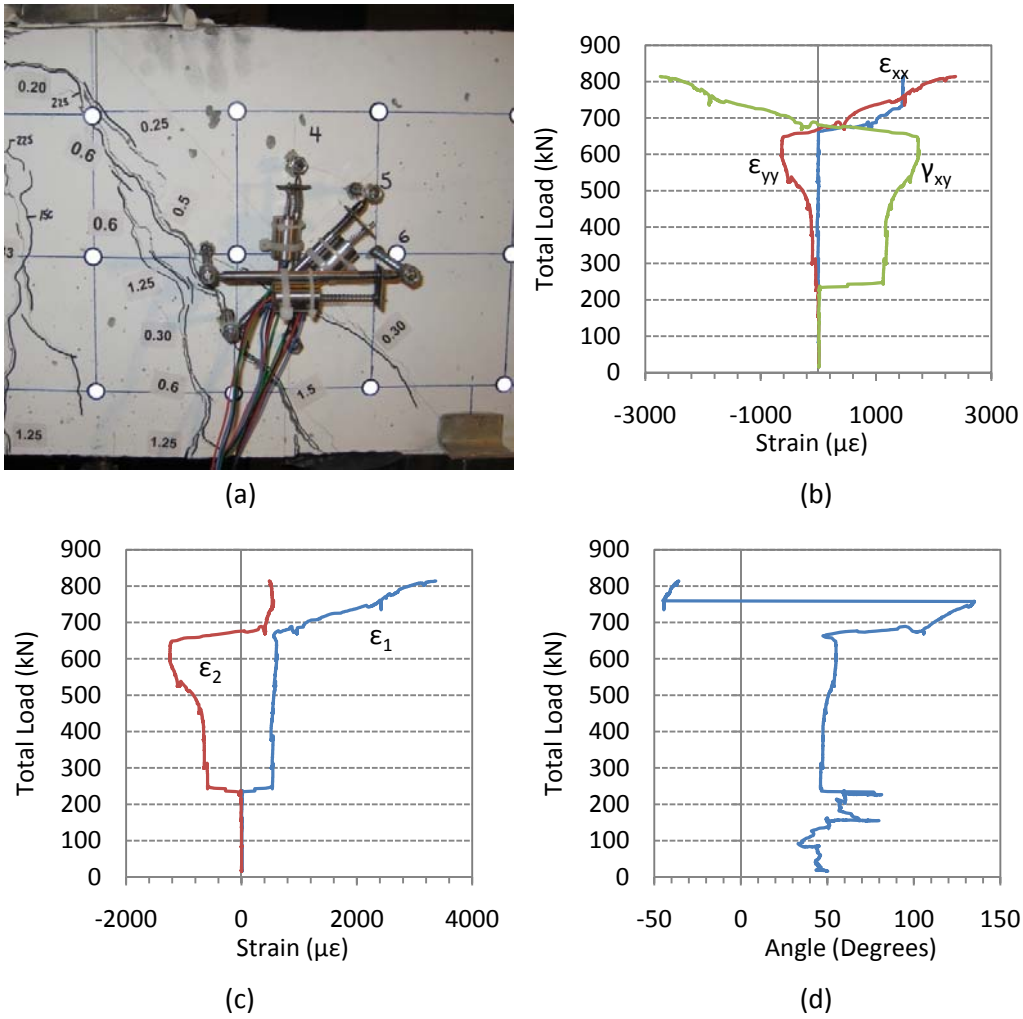

Figure C-15: (a) crack location through the rosette in shear span B at P= 814 kN, (b) strain components, (c) principal strains, and (d) the direction of the minimum principal strain (angle of inclination from a horizontal line towards mid-span).

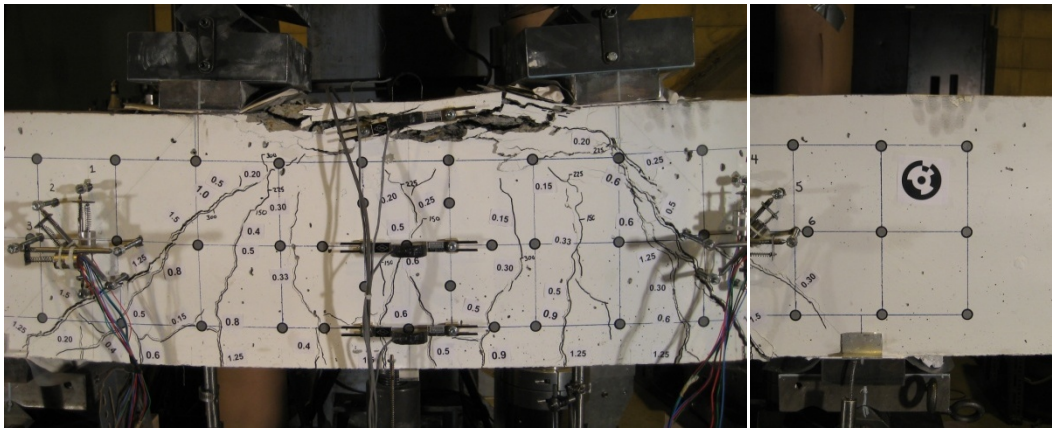

Figure C-16: Failure of specimen A1N with flexural crushing between the loading plates.

Table C-1: Subset of the collected data for specimen A1N.

			Displacements			Bottom Strain Gauges			
Load Stage	Time	Load, P	End A 1/4 Span	Mid-Span	End B 1/4 Span	2	4	5	6
(#)	(s)	(kN)	(mm)	(mm)	(mm)	(με)	(με)	(με)	(με)
	0	16	0.0	0.0	0.0	0	0	0	0
	250	18	0.0	0.0	0.0	0	0	0	0
	500	26	0.0	0.0	0.0	0	2	3	6
	750	43	0.1	0.1	0.0	0	6	9	20
	1000	77	0.1	0.1	0.1	0	14	22	52
1	1045	86	0.1	0.1	0.1	0	16	26	62
	1205	82	0.1	0.1	0.1	1	16	27	64
	1455	135	0.2	0.3	0.2	1	27	48	194
2	1695	163	0.5	0.6	0.5	1	31	79	1875
	2315	156	0.5	0.6	0.5	1	30	84	1880
	2565	199	0.7	1.0	0.6	1	41	137	2595
	2815	220	1.0	1.3	0.9	1	47	239	3131
3	2975	238	1.2	1.6	1.2	1	52	365	3543
	3750	226	1.3	1.6	1.2	1	51	421	3467
	4000	248	1.6	1.9	1.5	1	78	1516	3575
	4250	281	1.9	2.3	1.8	2	115	2098	4036
	4500	312	2.2	2.6	2.1	2	177	2706	4487
4	4505	313	2.2	2.7	2.1	2	179	2717	4495
	5635	302	2.1	2.7	2.2	2	241	2785	4414
	5885	339	2.6	3.1	2.5	3	1271	3981	4939
	6135	369	3.0	3.5	2.8	3	2186	4974	5460
5	6300	388	3.2	3.7	3.1	3	2589	5471	5785
	7365	377	3.2	3.8	3.1	4	2713	5477	5696
	7615	419	3.6	4.1	3.4	4	3127	6173	6297
	7865	450	4.0	4.6	3.8	5	3724	6736	6801
6	7975	463	4.1	4.7	3.9	5	3931	6960	7018
	8820	451	4.1	4.8	4.0	5	4005	6905	6935
	9070	493	4.5	5.2	4.5	5	4396	7495	7556
	9320	524	4.8	5.6	4.6	6	4896	7945	8097
7	9445	538	5.0	5.8	4.8	6	5138	8163	8364
	10245	525	5.0	5.8	4.9	7	5209	8083	8278
	10495	566	5.4	6.2	5.2	7	5612	8617	8911
	10745	596	5.7	6.6	5.5	8	5925	9068	9467
8	10890	613	5.9	6.9	5.7	8	6120	9328	9796
	11575	597	6.0	6.9	5.8	8	6098	9250	9722
	11825	638	6.3	7.3	6.1	9	6441	9750	10342
	12075	664	6.7	7.8	6.4	9	6846	10201	10915
	12325	687	7.1	8.2	6.8	10	7244	10627	11470
9	12350	689	7.1	8.3	6.9	10	7283	10666	11521
	13150	669	7.2	8.3	6.9	10	7271	10595	11449
	13400	709	7.5	8.7	7.3	11	7698	11104	12086
	13650	732	8.0	9.2	7.7	11	8150	11543	12636
	13900	743	8.4	9.7	8.2	11	8522	11939	13139
10	14085	761	8.7	10.1	8.5	12	8782	12227	13523
	14695	735	8.7	10.1	8.6	12	8752	12168	13482
	14945	771	8.8	10.5	8.8	12	9185	12733	14167
	15195	783	9.3	10.9	9.2	12	9513	13198	14738
	15445	801	9.7	11.3	9.3	11	9803	13686	15326
	15695	809	10.3	11.8	9.9	8	10143	14229	15946
	15945	813	11.0	12.2	10.2	7	10477	14822	-
Failure	16055	814	11.2	12.3	10.3	4	10590	15228	-

Table C-1 continued,

		Bottom Strain Gauges				Rosette shear span B		
Load Stage (#)	Load, P (kN)	7 (με)	9 (με)	10 (με)	11 (με)	ε_{xx} με	ε_{yy} με	γ_{xy} με
	16	0	0	0	0	5	4	8
	18	0	0	0	0	7	6	12
	26	7	5	2	2	8	7	13
	43	24	15	9	6	8	8	12
	77	62	38	22	14	8	8	10
1	86	73	46	26	16	8	8	11
	82	74	46	26	16	2	4	9
	135	360	89	45	26	7	6	10
2	163	823	215	46	31	8	5	13
	156	876	243	46	30	-1	-7	6
	199	1709	489	68	38	5	0	13
	220	2412	1473	865	54	7	-5	20
3	238	2955	1915	1454	66	8	-6	25
	226	2947	1944	1710	74	-12	-40	10
	248	3268	2221	2513	96	-4	-46	1123
	281	4047	2693	3130	132	0	-46	1131
	312	4665	3091	3641	234	3	-51	1140
4	313	4676	3097	3650	236	3	-51	1141
	302	4647	3069	3615	276	-10	-105	1174
	339	5168	3400	4038	338	-4	-100	1180
	369	5727	3715	4584	598	0	-101	1188
5	388	6075	3903	4988	891	1	-108	1197
	377	6038	3860	4947	1021	-22	-120	1163
	419	6658	4234	5470	1186	-17	-125	1175
	450	7201	4540	5957	1535	-4	-148	1222
6	463	7457	4685	6152	1692	0	-168	1249
	451	7417	4624	6037	1829	-7	-189	1262
	493	8021	5001	6509	2045	0	-248	1339
	524	8558	5330	6903	2468	4	-400	1501
7	538	8788	5488	7083	2685	5	-467	1573
	525	8717	5408	6964	2835	-14	-526	1594
	566	9310	5781	7422	3079	-4	-576	1664
	596	9837	6108	7761	3512	2	-631	1737
8	613	10135	6296	7858	3779	6	-629	1740
	597	10104	6206	7719	3908	-7	-637	1724
	638	10670	6545	8160	4135	2	-626	1730
	664	11183	6828	8526	4556	73	-74	1112
	687	11690	7084	8913	4991	844	312	-34
9	689	11739	7109	8951	5029	866	353	-97
	669	11746	6980	8880	5118	922	449	-287
	709	12323	7336	9339	5356	1176	591	-679
	732	12825	7634	9794	5719	1445	891	-1237
	743	13318	7913	10297	6068	1472	1289	-1654
10	761	13694	8088	10620	6289	1473	1481	-1845
	735	13729	7968	10591	6323	1459	1493	-1890
	771	14252	8173	10914	6480	1461	1586	-1975
	783	14858	8385	11276	6657	1464	1761	-2147
	801	15517	8584	11662	6883	1468	1975	-2354
	809	16245	8738	12009	7074	1469	2165	-2533
	813	17057	8840	12318	7202	1472	2310	-2671
Failure	814	17419	8881	12466	7253	1472	2370	-2732

C.4 Specimen A2N

The displacement rate of specimen A2N was 0.15 mm/min of machine stroke. Flexural cracks at mid-span were visually observed at load stage 1 (P = 87 kN). At load stage 2 (P = 137 kN), the MTS test frame unexpectedly experienced a fault resulting in the unloading of the specimen. Subsequently the specimen was reloaded to P = 137 kN and testing continued. After the maximum load was reached, the concrete on the inside edge of loading plate A started deteriorating. This was followed by a sudden drop in load as the main diagonal shear crack penetrated to the surface to the inside of loading plate A. The main diagonal crack in shear span A, from the inside edge of the reaction plate to the inside edge of the loading plate, initiated the shear compression failure.

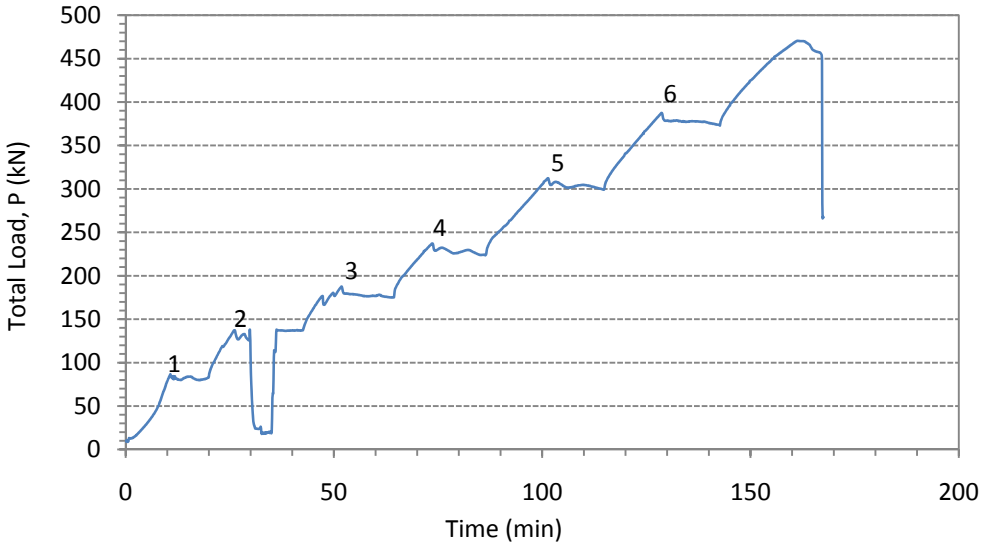

Figure C-17: Load – history of specimen A2N.

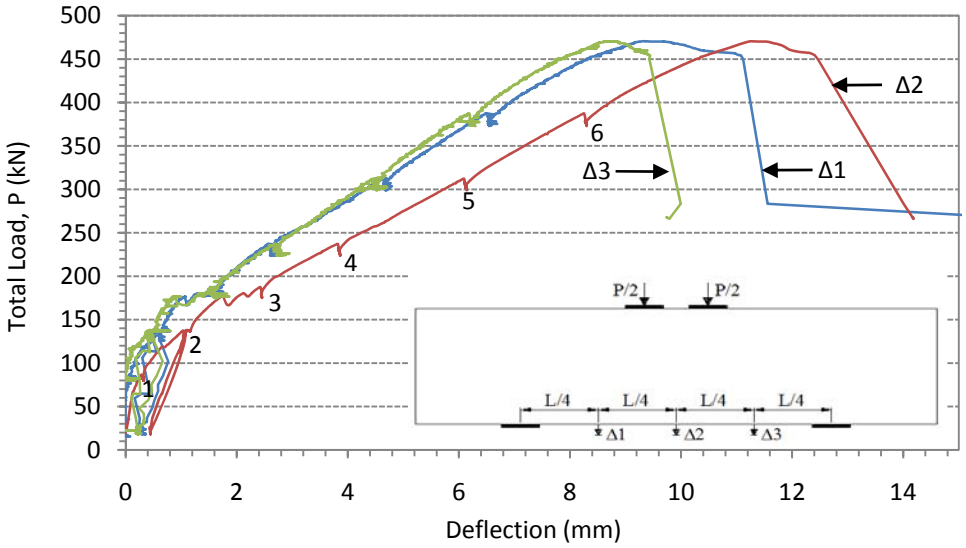

Figure C-18: Load – displacement response of specimen A2N.

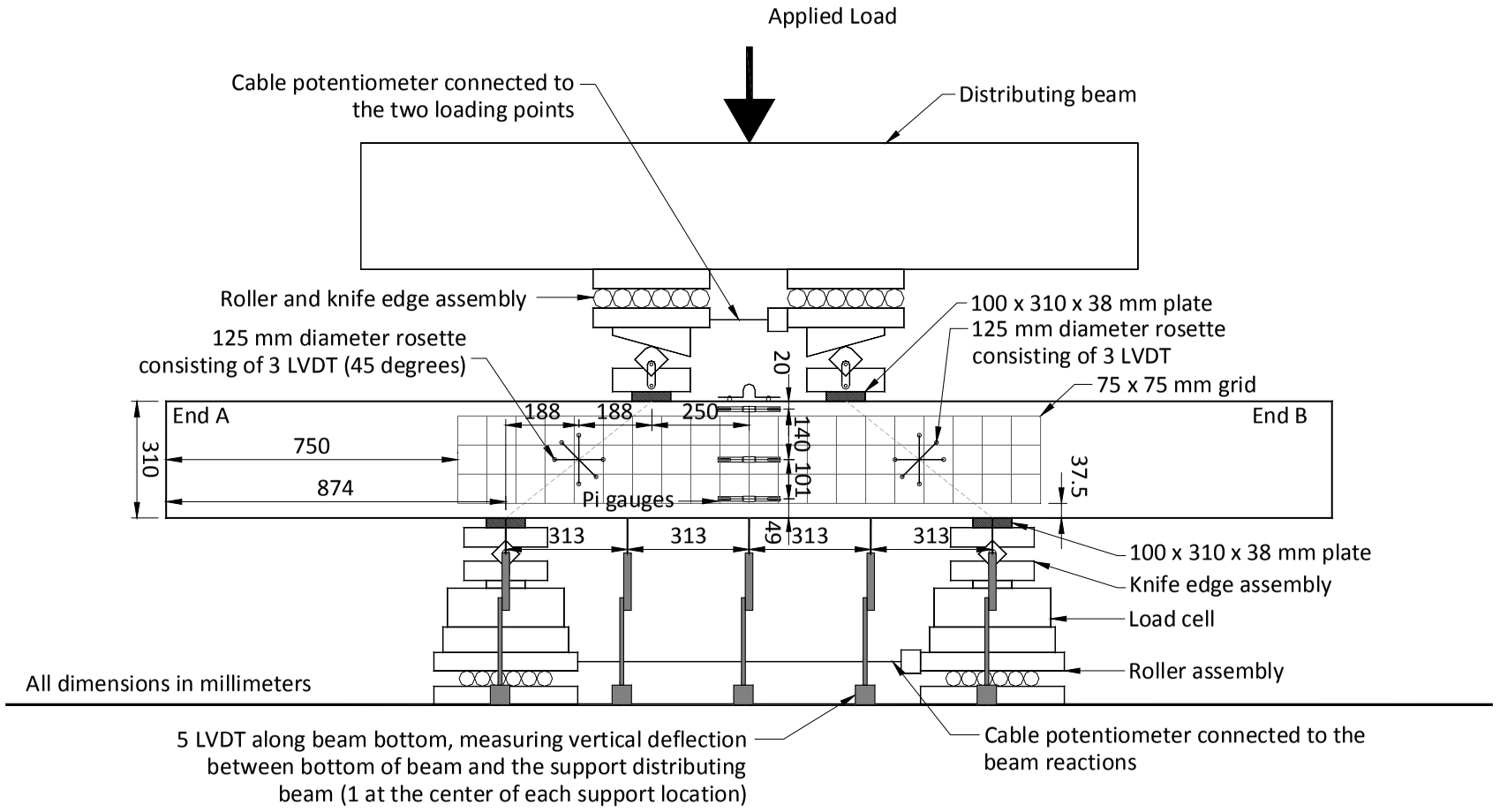

Figure C-19: Instrumentation drawing for specimen A2N.

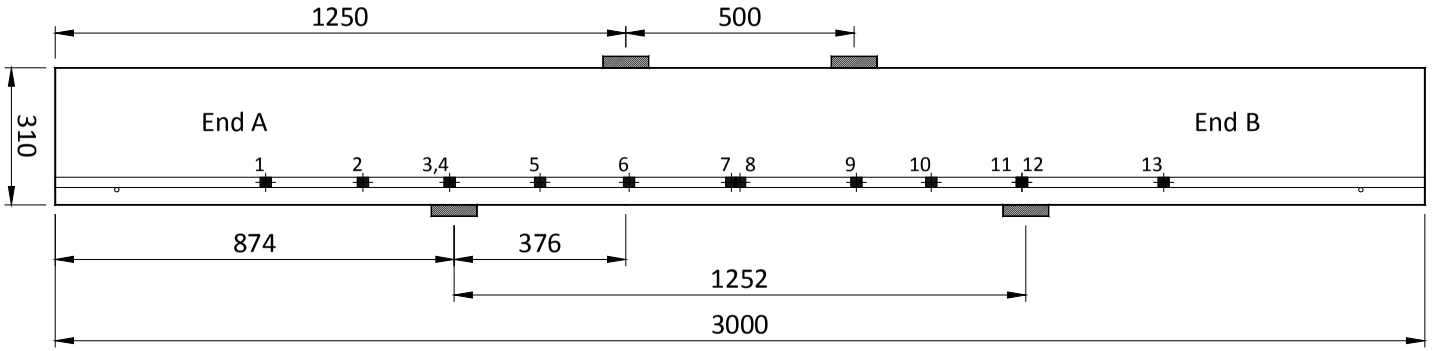

Strain Gauge Locations

Strain Gauge No.	Column	Distance from End A (mm)
1	C	461
2	C	674
3	C	864
4	B	864
5	F	1062
6	B	1257
7	C	1481
8	F	1500
9	B	1755
10	F	1919
11	C	2118
12	F	2117
13	F	2428

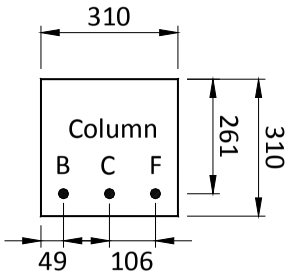

(3) - #7 GFRP Bars

Notes:
All dimensions in mm
Clear Cover: 38.1 mm
Concrete Strength: 45 MPa
Bar Length: 3000 mm

Figure C-20: Location of the strain gauges for specimen A2N (as-built).

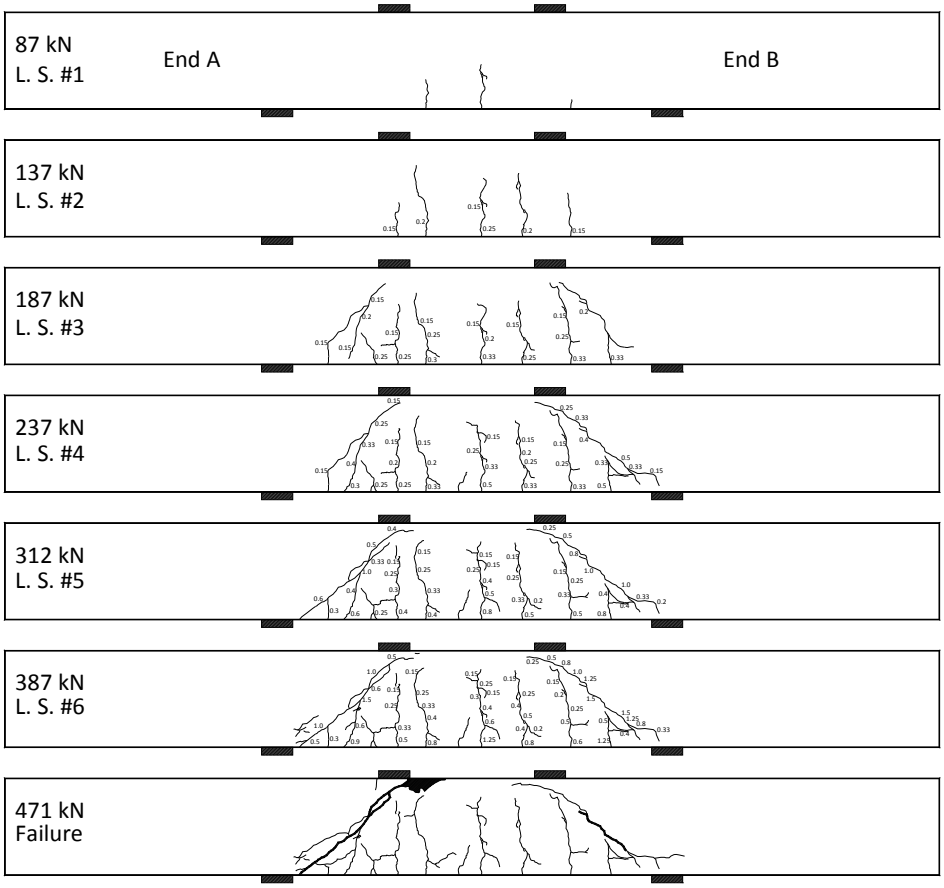

Figure C-21: Crack diagrams of specimen A2N showing the development of the cracks and the widths as loading progressed.

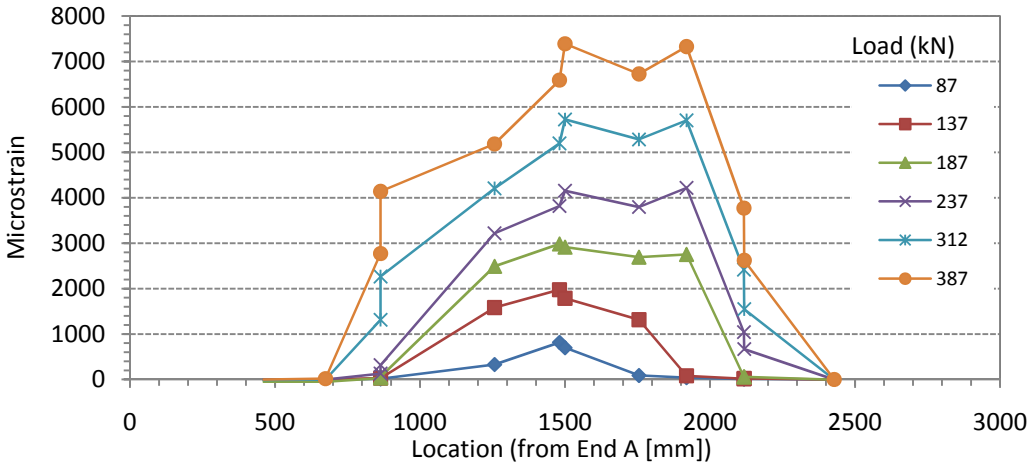

Figure C-22: Strain in the reinforcement as loading progressed.

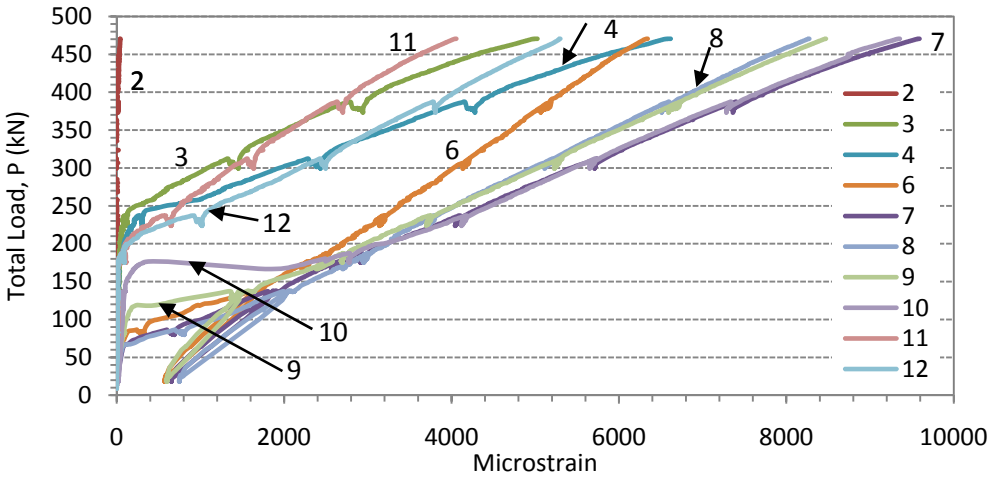

Figure C-23: Strain in the reinforcement.

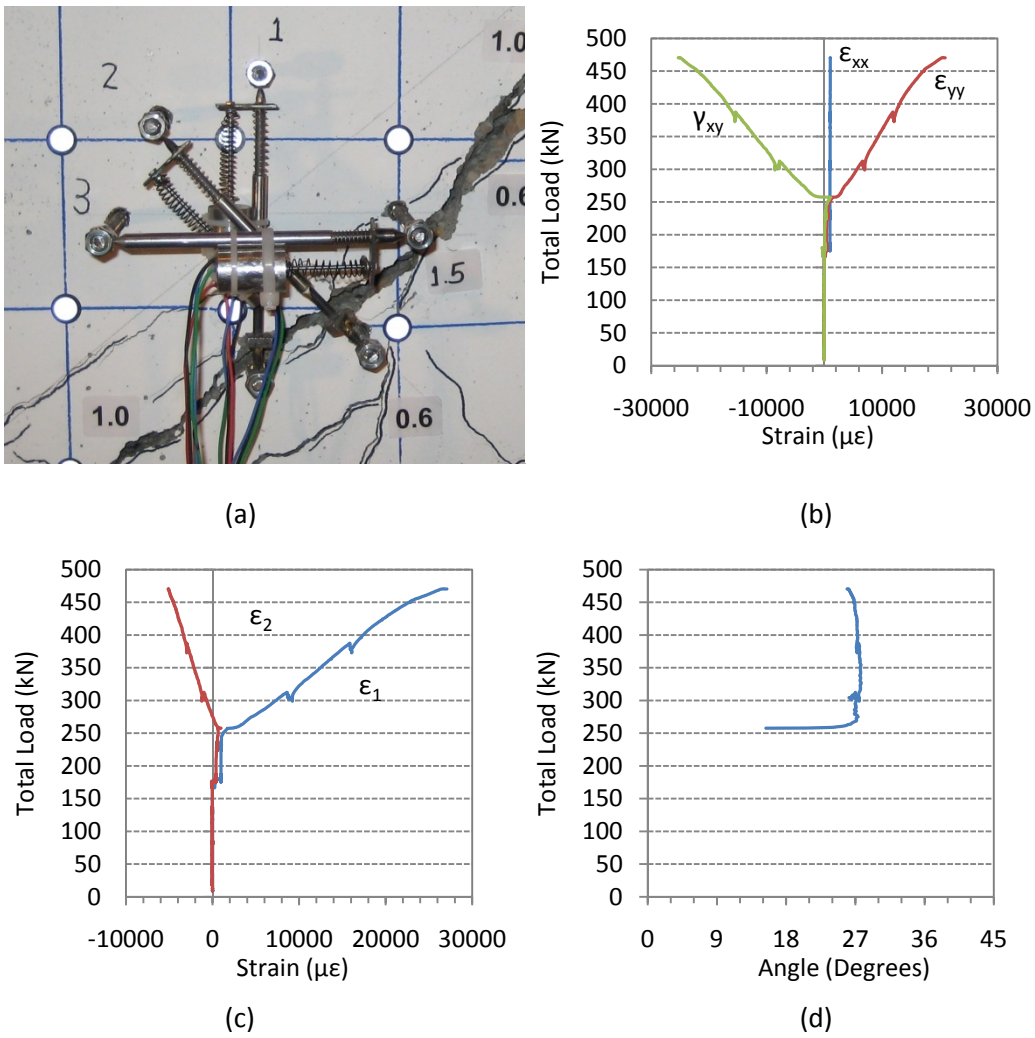

Figure C-24: (a) crack location through the rosette in shear span A at failure, (b) strain components, (c) principal strains, and (d) the direction of the minimum principal strain (angle of inclination from a horizontal line towards mid-span).

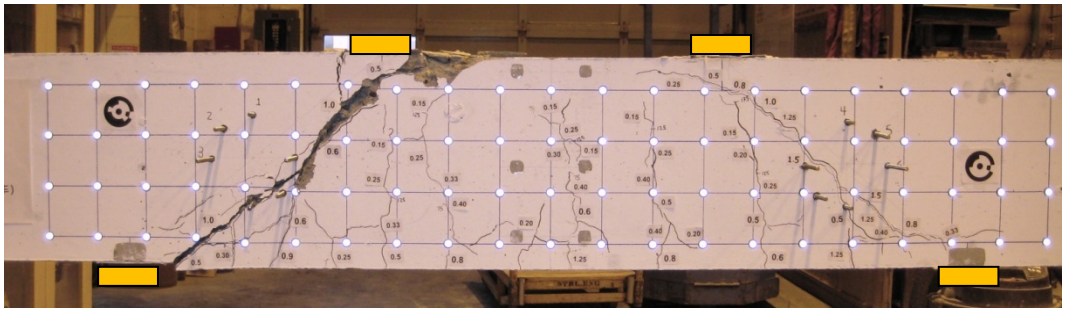

Figure C-25: Failure in shear span A as seen after removal of specimen A2N from testing machine.

Table C-2: Subset of the collected data for specimen A2N.

			Displacements			Bottom Strain Gauges				
Load Stage	Time	Load, P	End A 1/4 Span	Mid-Span	End B 1/4 Span	2	3	4	6	7
(#)	(s)	(kN)	(mm)	(mm)	(mm)	(με)	(με)	(με)	(με)	(με)
	0	9	0.0	0.0	0.0	-2	-1	-1	-2	-1
	200	20	-0.1	0.0	-0.1	-2	0	0	4	8
	400	40	0.0	0.1	-0.1	0	6	6	26	34
	600	79	0.0	0.2	0.0	-2	13	14	106	345
1	645	87	0.1	0.3	0.0	-4	14	14	240	599
	1145	81	0.1	0.3	0.0	0	16	15	326	692
	1345	112	0.2	0.6	0.1	-2	21	22	853	1255
	1545	135	0.5	1.0	0.4	-4	26	25	1534	1744
2	1570	137	0.6	1.0	0.4	0	29	27	1604	1806
	1770	126	0.7	1.1	0.5	-2	27	25	1585	1783
	1970	19	0.3	0.4	0.3	-5	3	-6	572	652
Unloaded	1990	18	0.3	0.4	0.2	-5	4	-6	572	652
	2040	19	0.3	0.4	0.2	-3	5	-4	576	654
	2090	20	0.2	0.4	0.2	-4	4	-5	576	653
	2140	114	0.4	1.0	0.3	0	25	20	1408	1595
2	2180	138	0.6	1.1	0.5	-2	29	24	1682	1908
	2555	137	0.7	1.2	0.5	-1	30	26	1718	1957
	2755	169	0.9	1.6	0.8	-24	26	16	2142	2474
	2955	178	1.2	2.0	1.4	-43	25	9	2342	2705
3	3110	188	1.6	2.4	1.5	-48	32	57	2496	2922
	3860	175	1.6	2.5	1.6	-4	53	90	2486	2909
	4060	206	1.9	2.9	1.9	-44	41	96	2759	3350
	4260	224	2.3	3.4	2.4	7	82	195	3040	3803
4	4415	237	2.6	3.8	2.7	-15	95	263	3189	4094
	5185	224	2.6	3.9	2.7	-9	122	304	3139	4044
	5385	251	3.0	4.3	3.1	-2	273	668	3389	4424
	5585	268	3.5	4.8	3.4	-9	555	1201	3602	4755
	5785	286	4.0	5.3	3.9	-16	845	1605	3862	5137
	5985	304	4.4	5.8	4.2	-23	1158	2050	4081	5523
5	6085	312	4.7	6.1	4.5	-3	1327	2285	4216	5738
	6890	299	4.7	6.1	4.5	-2	1454	2435	4134	5709
	7090	329	5.1	6.6	4.9	-43	1599	2686	4419	6130
	7290	348	5.5	7.1	5.3	-2	1975	3185	4693	6538
	7490	367	6.0	7.7	5.7	-21	2324	3621	4896	6931
	7690	385	6.4	8.2	6.1	-9	2702	4066	5133	7334
6	7720	387	6.5	8.2	6.2	18	2781	4150	5190	7398
	8560	373	6.5	8.3	6.3	16	2942	4281	5066	7362
	8760	402	7.0	8.8	6.6	2	3160	4587	5353	7809
	8960	421	7.4	9.3	7.0	17	3555	5047	5600	8217
	9160	437	7.9	9.8	7.4	-3	3956	5466	5798	8614
	9360	453	8.4	10.4	7.9	33	4371	5934	6034	9024
	9560	464	9.0	10.9	8.4	40	4778	6365	6222	9380
Failure	9685	471	9.4	11.3	8.7	44	5015	6606	6340	9588

Table C-2 continued,

		Bottom Strain Gauges					Rosette shear span A		
Load Stage	Load, P	8	9	10	11	12	ε_{xx}	ε_{yy}	γ_{xy}
(#)	(kN)	(με)	(με)	(με)	(με)	(με)	με	με	με
	9	-2	-3	-2	-4	-2	4	5	-3
	20	5	2	3	-3	0	-5	-1	-4
	40	29	22	14	5	3	-12	-7	-9
	79	423	74	35	12	7	-7	-5	0
1	87	697	80	39	10	7	-6	-4	-4
	81	811	87	41	15	8	-6	-3	-4
	112	1447	162	57	16	10	-5	0	-3
	135	1933	1237	76	20	14	-11	-5	-7
2	137	1996	1355	82	23	16	-11	-6	-7
	126	1965	1382	83	21	14	-20	-17	-9
	19	746	600	21	-11	-2	-31	-28	-6
Unloaded	18	746	598	21	-11	-2	-31	-28	-7
	19	748	599	22	-9	-2	-31	-28	-11
	20	749	597	22	-11	-2	-33	-29	-15
	114	1753	1295	75	14	13	-35	-30	-11
2	138	2083	1580	91	17	15	-35	-30	-13
	137	2124	1649	101	18	15	-25	-26	-10
	169	2656	2355	225	-5	10	-24	-24	-11
	178	2836	2505	2389	26	26	288	347	-263
3	188	2991	2699	2771	56	59	981	414	71
	175	2948	2692	2775	108	89	967	397	62
	206	3281	3069	3358	132	202	971	400	68
	224	3568	3457	3861	371	536	977	456	109
4	237	3791	3739	4171	554	904	980	532	183
	224	3712	3699	4118	651	1019	968	606	278
	251	4069	4071	4497	776	1215	970	972	643
	268	4356	4396	4814	978	1579	973	3080	-2888
	286	4698	4753	5170	1208	1946	969	4598	-4952
	304	5038	5115	5534	1419	2256	971	5938	-6865
5	312	5209	5297	5717	1559	2433	972	6627	-7784
	299	5112	5227	5650	1638	2497	994	6999	-8575
	329	5504	5565	6073	1761	2736	1001	7942	-10005
	348	5867	5956	6479	2040	3053	999	9226	-11877
	367	6204	6325	6870	2299	3386	1010	10453	-13512
	385	6532	6674	7273	2567	3721	1015	11688	-15181
6	387	6597	6731	7337	2629	3780	1015	11864	-15395
	373	6511	6592	7284	2702	3809	999	12088	-15512
	402	6913	7013	7727	2864	4071	1001	13167	-17053
	421	7259	7386	8142	3133	4375	1012	14482	-18815
	437	7553	7721	8520	3386	4666	1024	15943	-20456
	453	7873	8063	8799	3673	4968	1038	17434	-22283
	464	8132	8322	9145	3908	5206	1034	19361	-24130
Failure	471	8272	8470	9352	4052	5297	1028	20619	-25172

C.5 Specimen A3N

The displacement rate of specimen A3N was 0.1 mm/min of machine stroke. At failure, the main diagonal crack in shear span A extended to the inside edge of loading plate A resulting in movement along the crack and a sudden drop in load resistance. Failure occurred with very little warning. There was a momentary plateau in the load capacity at peak load prior to sudden failure. No crushing of concrete occurred in the constant moment region between the loading plate with the exception of the shear compression at the inside edge of loading plate A.

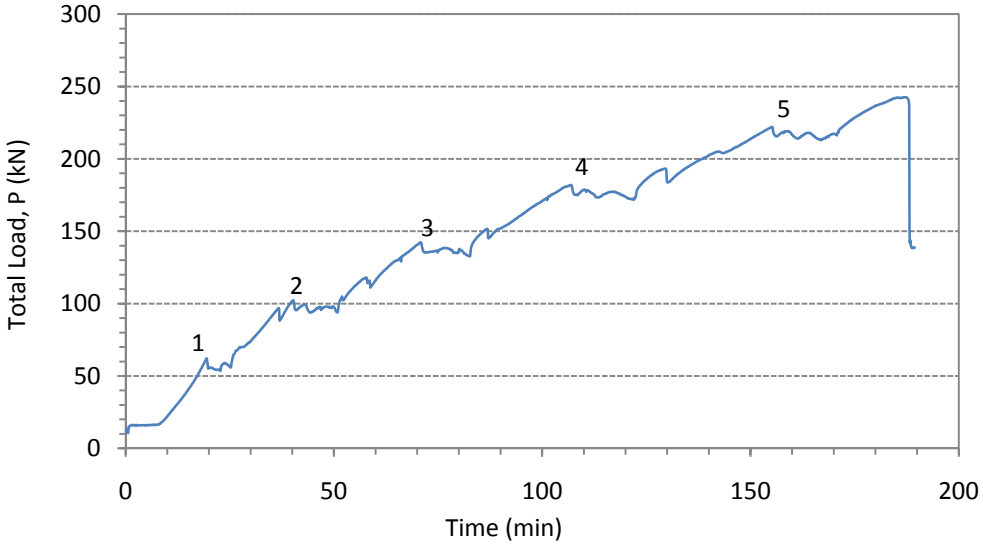

Figure C-26: Load – history of specimen A3N.

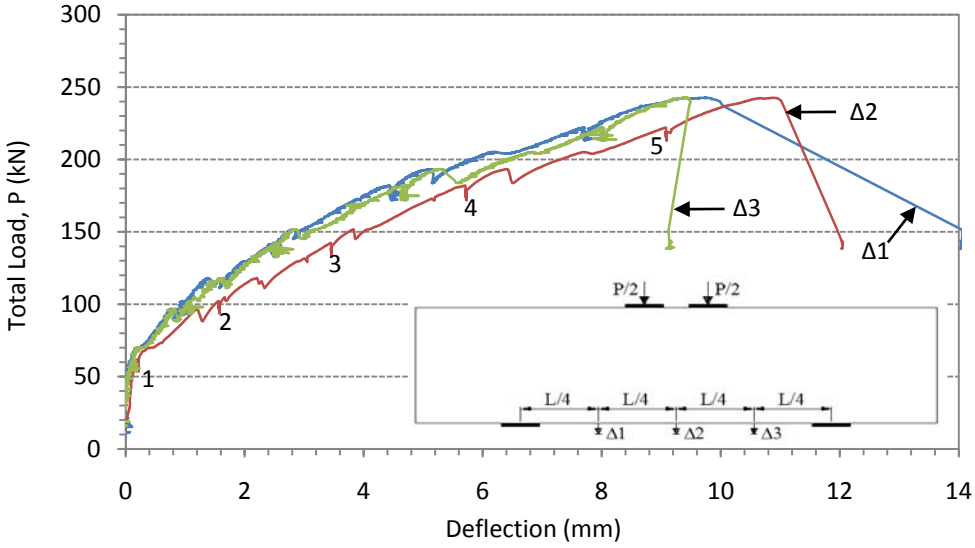

Figure C-27: Load – displacement response of specimen A3N.

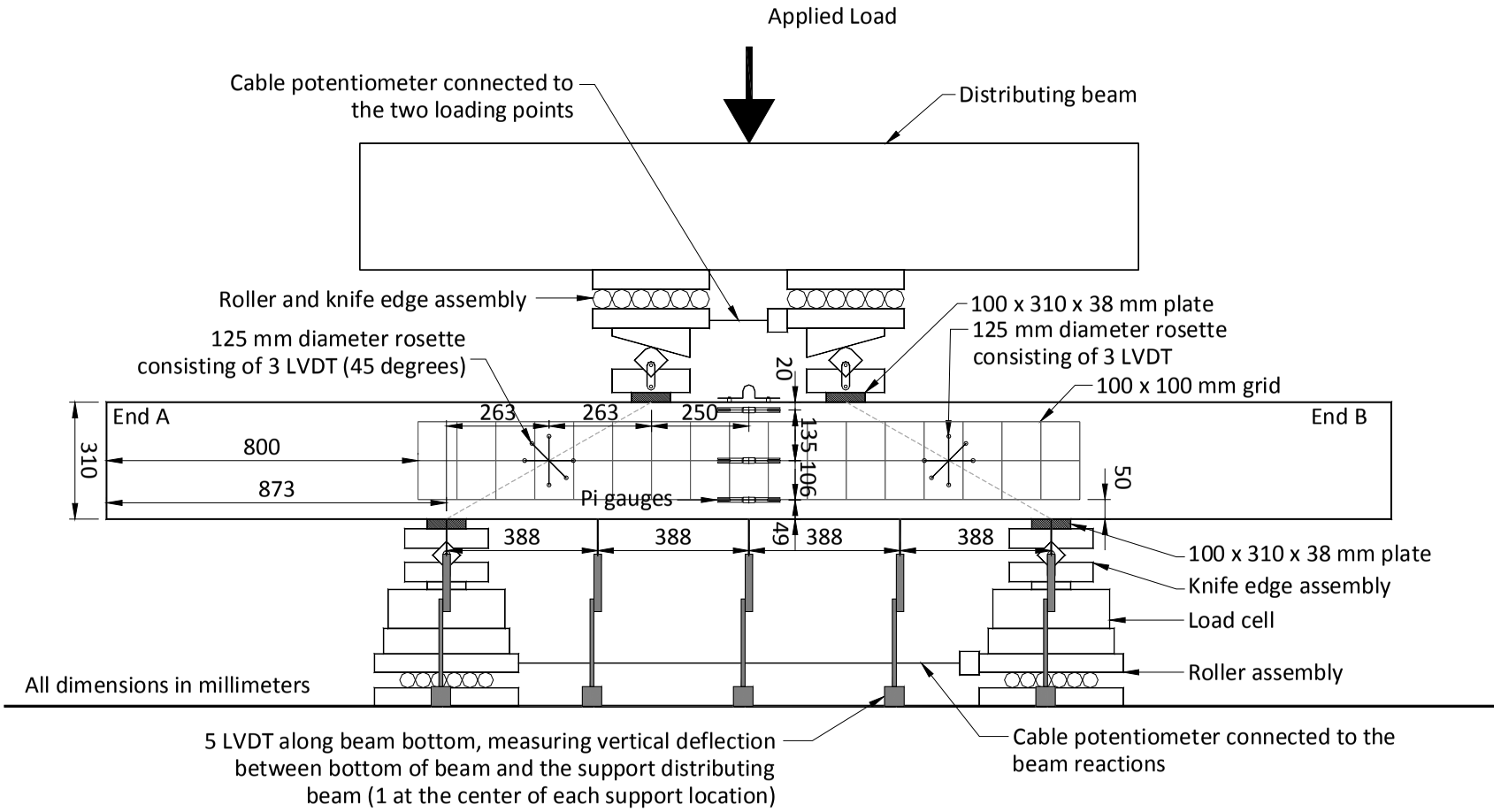

Figure C-28: Instrumentation drawing for specimen A3N.

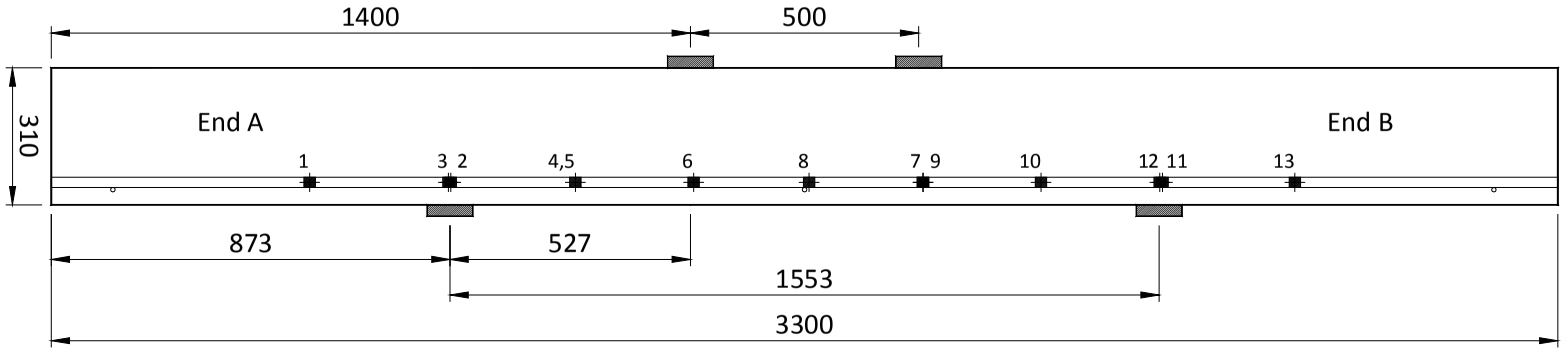

Strain Gauge Locations

Strain Gauge No.	Column	Distance from End A (mm)
1	F	566
2	F	875
3	C	870
4	C	1148
5	B	1148
6	C	1407
7	C	1909
8	B	1660
9	F	1910
10	C	2168
11	C	2434
12	F	2428
13	C	2724

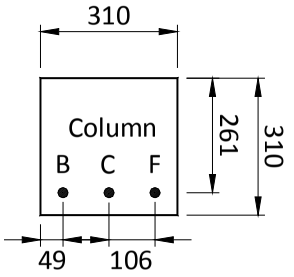

(3) - #7 GFRP Bars

Notes:
All dimensions in mm
Clear Cover: 38.1 mm
Concrete Strength: 41 MPa
Bar Length: 3300 mm

Figure C-29: Location of the strain gauges for specimen A3N (as-built).

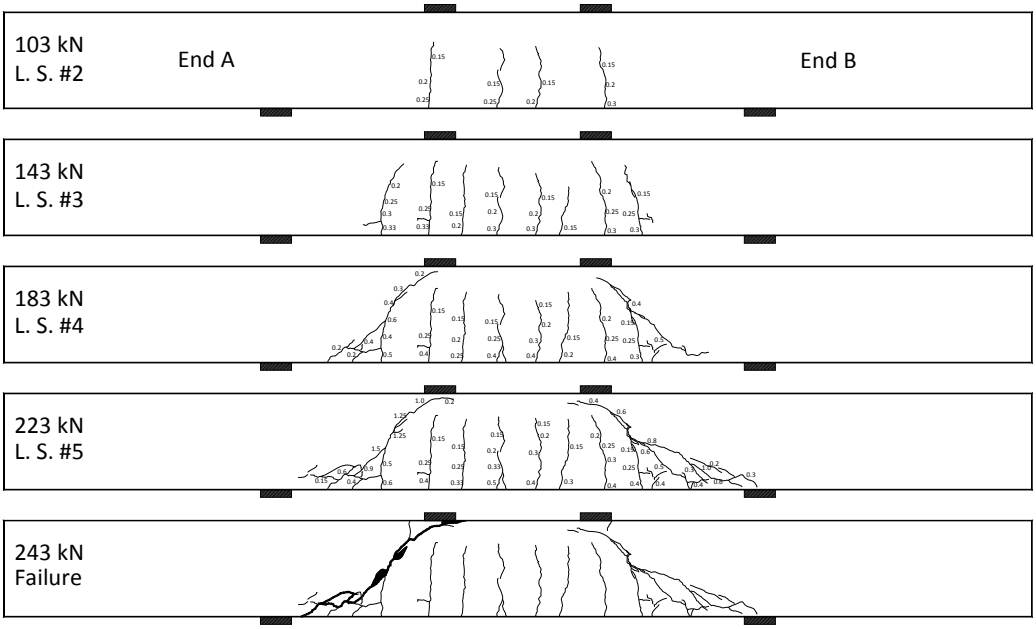

Figure C-30: Crack diagrams of specimen A3N showing the development of the cracks and the widths as loading progressed.

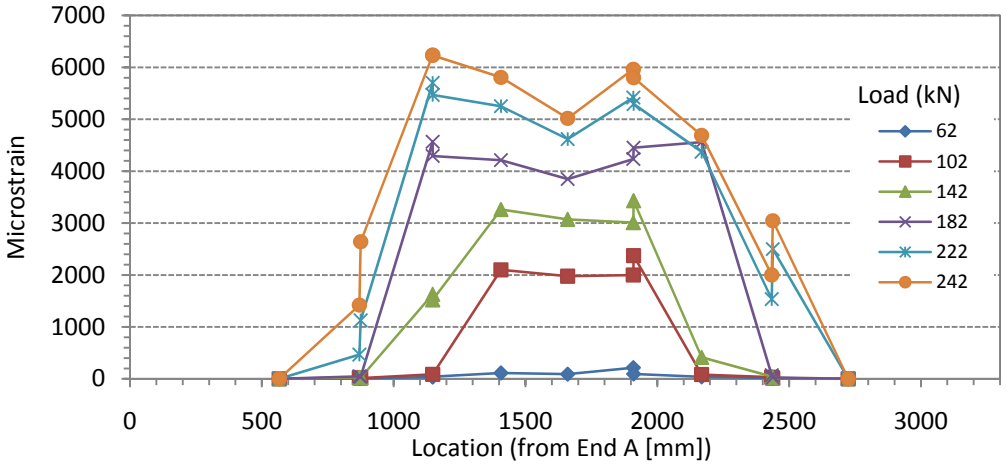

Figure C-31: Strain in the reinforcement as loading progressed.

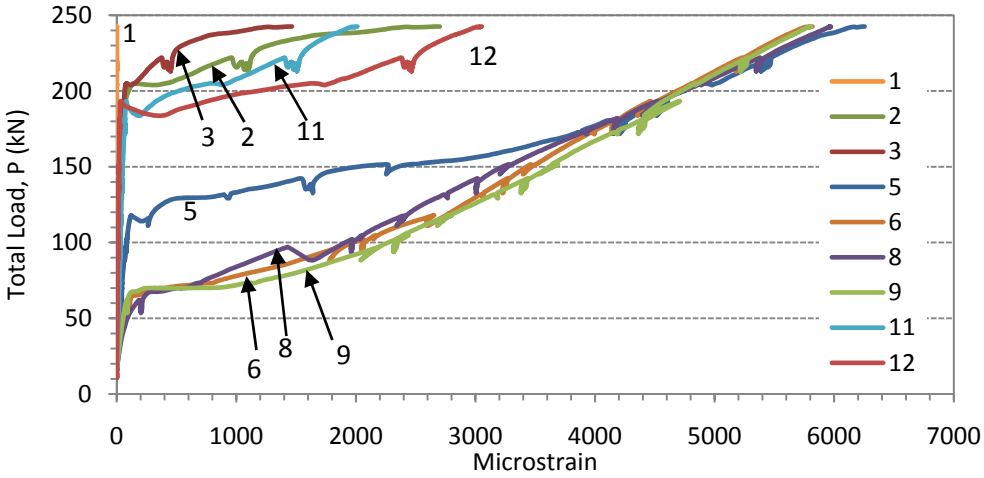

Figure C-32: Strain in the reinforcement.

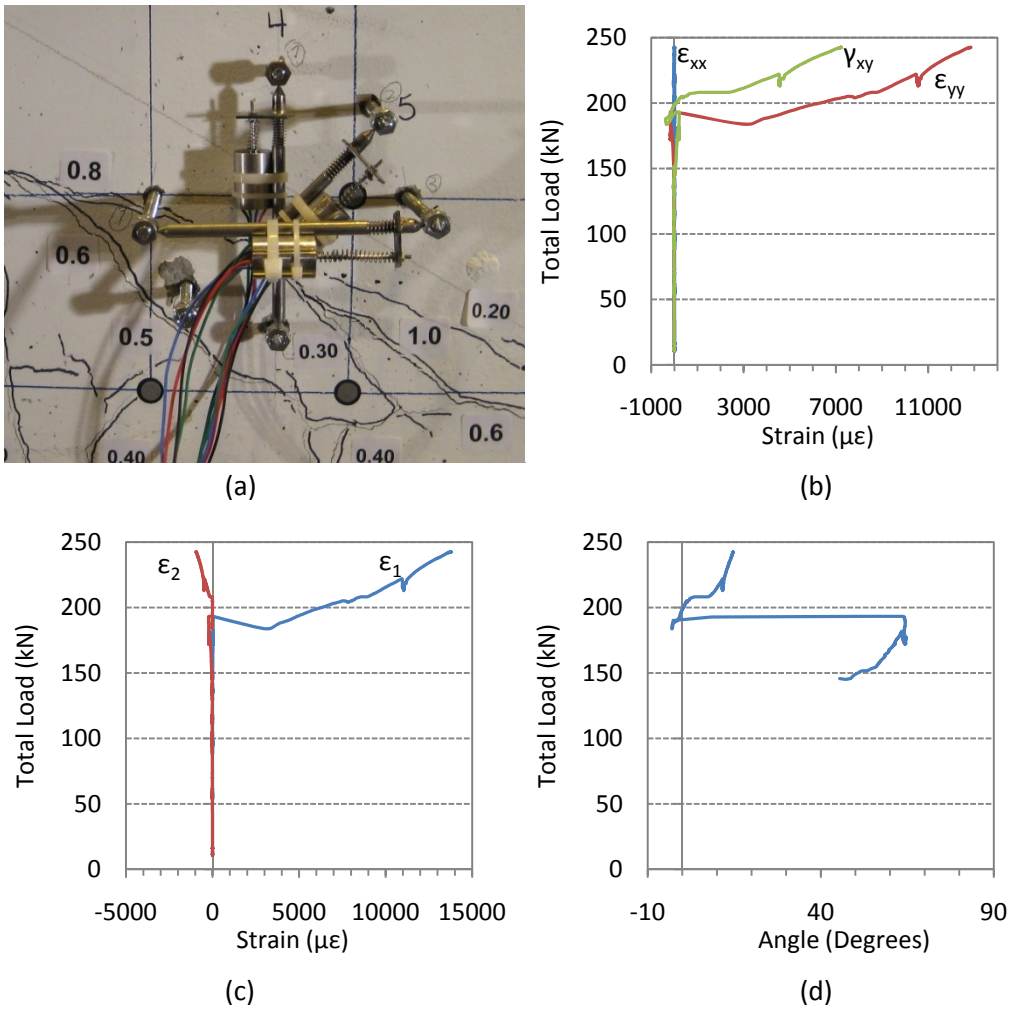

Figure C-33: (a) crack location through the rosette in shear span B at failure, (b) strain components, (c) principal strains, and (d) the direction of the minimum principal strain (angle of inclination from a horizontal line towards mid-span).

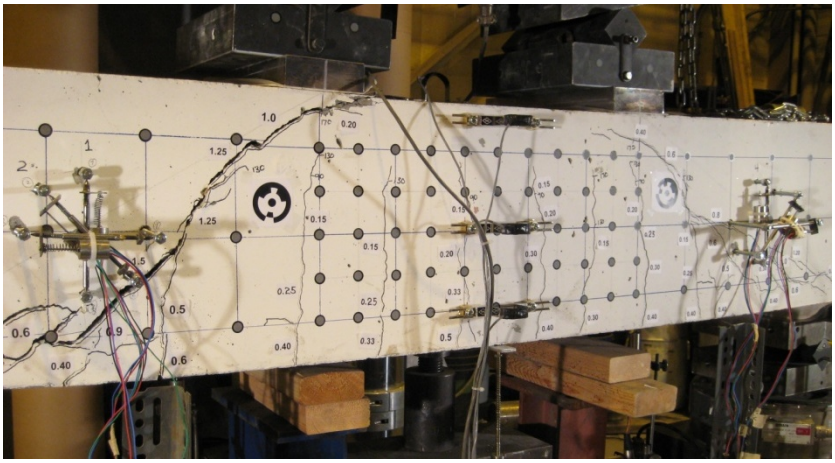

Figure C-34: Specimen A3N after failure.

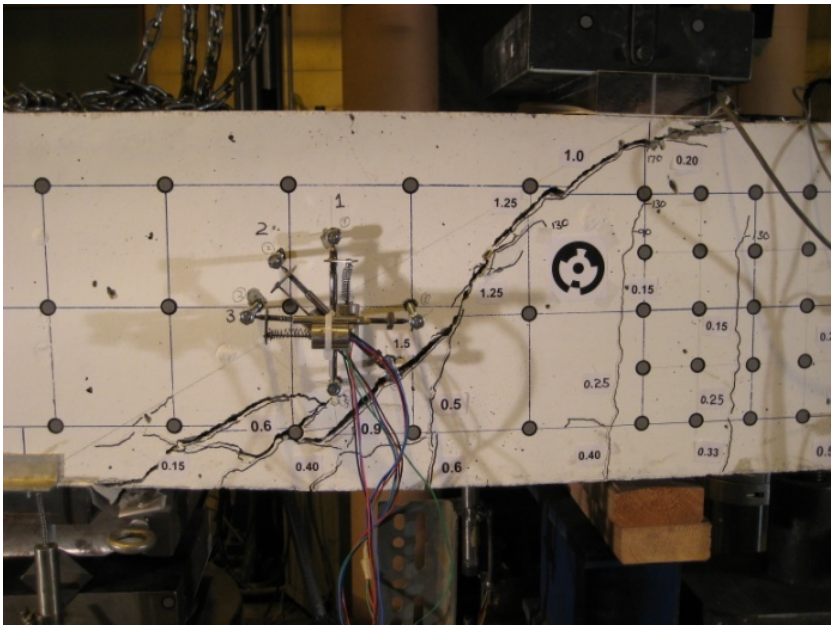

Figure C-35: Failure crack in shear span A.

Table C-3: Subset of collected data for specimen A3N.

			Displacements			Bottom Strain Gauges			
Load Stage	Time	Load, P	End A 1/4 Span	Mid-Span	End B 1/4 Span	1	2	3	5
(#)	(s)	(kN)	(mm)	(mm)	(mm)	(με)	(με)	(με)	(με)
	0	12	0.0	0.0	0.0	0	0	0	0
	250	16	0.0	0.0	-0.1	0	0	0	0
	500	17	0.1	0.0	-0.1	0	0	0	1
	750	31	0.0	0.1	0.0	0	3	3	11
	1000	48	0.1	0.1	0.0	0	5	7	26
1	1165	62	0.1	0.2	0.2	0	8	10	40
	1365	54	0.1	0.2	0.2	0	7	9	38
	1615	68	0.2	0.3	0.2	0	9	11	43
	1865	78	0.4	0.7	0.5	0	10	13	49
	2115	92	0.7	1.1	0.8	0	12	16	66
	2365	100	0.9	1.5	1.0	0	14	18	78
2	2410	102	1.0	1.6	1.1	0	14	19	82
	3050	94	1.0	1.6	1.1	0	14	18	83
	3300	112	1.2	1.9	1.4	0	16	21	101
	3550	113	1.6	2.4	1.7	0	15	21	266
	3800	126	1.9	2.7	2.0	0	17	24	400
	4050	135	2.2	3.1	2.2	0	19	27	1096
3	4245	142	2.5	3.4	2.6	0	20	28	1532
	4960	133	2.5	3.5	2.5	1	20	28	1640
	5210	152	2.8	3.8	2.8	0	21	31	2255
	5460	154	3.1	4.2	3.3	0	22	33	2712
	5710	162	3.4	4.6	3.7	0	23	35	3334
	5960	170	3.8	5.0	4.0	0	25	39	3743
	6210	177	4.1	5.4	4.4	0	28	41	4001
4	6410	182	4.4	5.7	4.7	0	34	45	4249
	7325	172	4.5	5.7	4.7	1	39	47	4207
	7575	189	4.8	6.1	5.0	1	44	50	4426
	7825	184	5.2	6.5	5.6	1	65	56	4514
	8075	194	5.5	6.9	6.0	1	75	60	4575
	8325	200	5.8	7.3	6.5	1	99	67	4755
	8575	204	6.3	7.8	6.9	1	214	97	4961
	8825	209	6.8	8.2	7.3	1	552	200	5112
	9075	216	7.3	8.7	7.7	1	747	280	5296
5	9310	222	7.7	9.1	8.0	1	960	377	5475
	10245	216	7.7	9.1	8.0	1	1113	459	5384
	10495	228	8.1	9.5	8.4	1	1207	511	5629
	10745	235	8.6	9.9	8.7	1	1549	714	5843
	10995	240	9.1	10.4	9.2	1	2192	1087	6066
Failure	11240	243	9.7	10.9	9.4	2	2702	1465	6254

Table C-3 continued,

		Bottom Strain Gauges					Rosette shear span B		
Load Stage	Load, P	6	8	9	11	12	ε_{xx}	ε_{yy}	γ_{xy}
(#)	(kN)	(με)	(με)	(με)	(με)	(με)	με	με	με
	12	0	0	0	0	0	-2	-2	-2
	16	0	0	0	0	0	-4	-3	-2
	17	2	2	2	0	0	-3	-3	-3
	31	21	27	20	6	2	-3	-1	-4
	48	48	77	49	12	4	-6	-2	-6
1	62	87	189	86	18	6	-6	-2	-5
	54	105	204	88	16	6	-6	-3	-9
	68	272	403	178	20	7	-8	-4	-9
	78	975	806	1369	23	8	-9	-4	-12
	92	1662	1255	1988	28	11	-9	-2	-11
	100	1967	1905	2262	31	12	-8	-1	-11
2	102	2059	1968	2345	31	12	-8	-1	-11
	94	2054	1965	2318	30	12	-16	-9	-23
	112	2409	2227	2592	35	14	-13	-10	-19
	113	2638	2354	2701	35	14	-9	-10	-20
	126	2925	2589	3009	40	16	-8	-6	-14
	135	3112	2824	3238	43	17	-8	-5	-11
3	142	3266	3015	3436	46	18	-7	-5	-8
	133	3227	3003	3380	44	18	-13	-12	-20
	152	3464	3277	3690	49	19	-13	-9	-17
	154	3548	3354	3683	52	19	-12	-34	63
	162	3712	3571	3861	56	21	-8	-51	88
	170	3895	3808	4071	60	23	-6	-74	113
	177	4074	4031	4289	64	24	-5	-111	153
4	182	4187	4185	4426	68	25	-3	-147	190
	172	4138	4156	4361	68	25	-16	-173	197
	189	4350	4384	4602	72	27	-11	-180	210
	184	4357	4395	4411	201	395	-8	3309	-351
	194	4530	4562	4582	341	780	-7	4998	-125
	200	4698	4750	4732	537	1219	-4	6426	100
	204	4809	4890	4839	860	1706	-1	7763	367
	209	4902	5004	4945	1035	1936	-1	8890	2535
	216	5070	5199	5117	1229	2164	-2	9732	3619
5	222	5230	5381	5276	1404	2381	-2	10480	4540
	216	5183	5351	5218	1520	2475	-16	10614	4555
	228	5385	5560	5433	1598	2588	-13	11213	5351
	235	5554	5752	5605	1743	2768	-5	11890	6162
	240	5694	5902	5733	1897	2939	0	12496	6859
Failure	243	5818	5970	5806	2012	3053	1	12850	7228

C.6 Specimen A4H

The displacement rate of specimen A4H was 0.15 mm/min of machine stroke. Early in the loading process, a diagonal crack formed approximately 200 mm to the inside of support B and extended slightly above the diagonal line drawn center to center of the loading and support plates. The crack became less inclined as it propagated towards the inside edge of the loading place. The diagonal crack width increased and a vertical crack formed to the outside of loading plate B from the top surface down to the diagonal shear crack. Even then, the specimen continued to resist increasingly more load as the diagonal crack grew in size and splitting cracks occurred around the reinforcement. Eventually the peak load was reached and the specimen continued to resist load for a short while longer before losing 70% of the load carrying capacity.

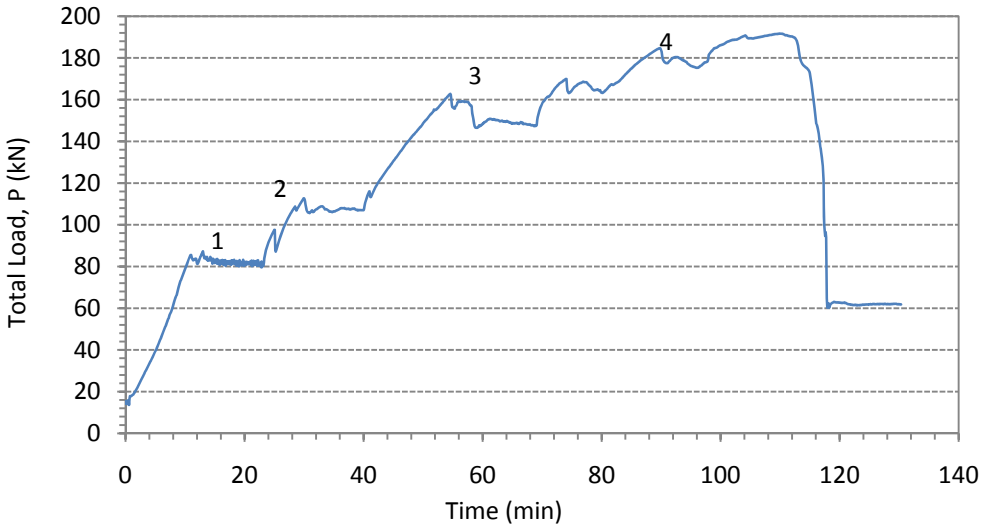

Figure C-36: Load – history of specimen A4H.

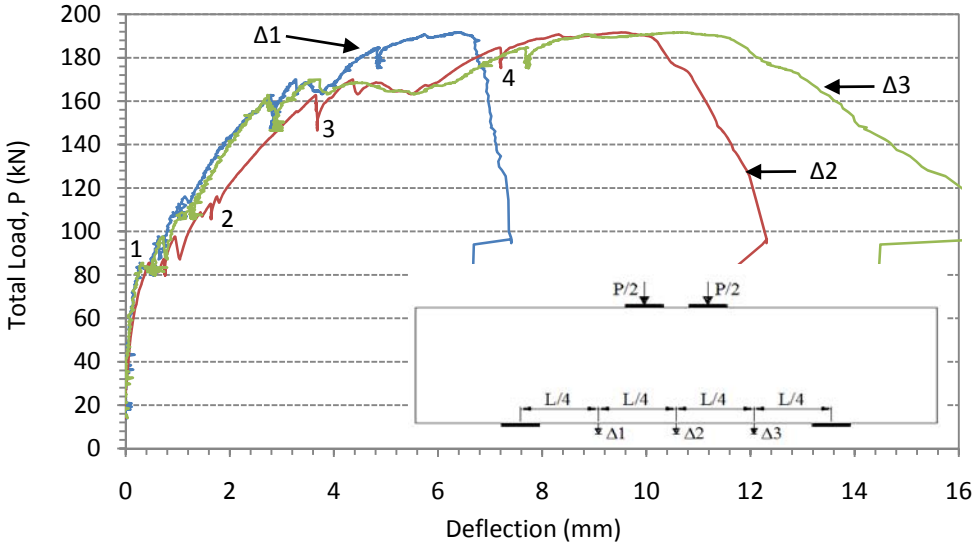

Figure C-37: Load – displacement response of specimen A4H.

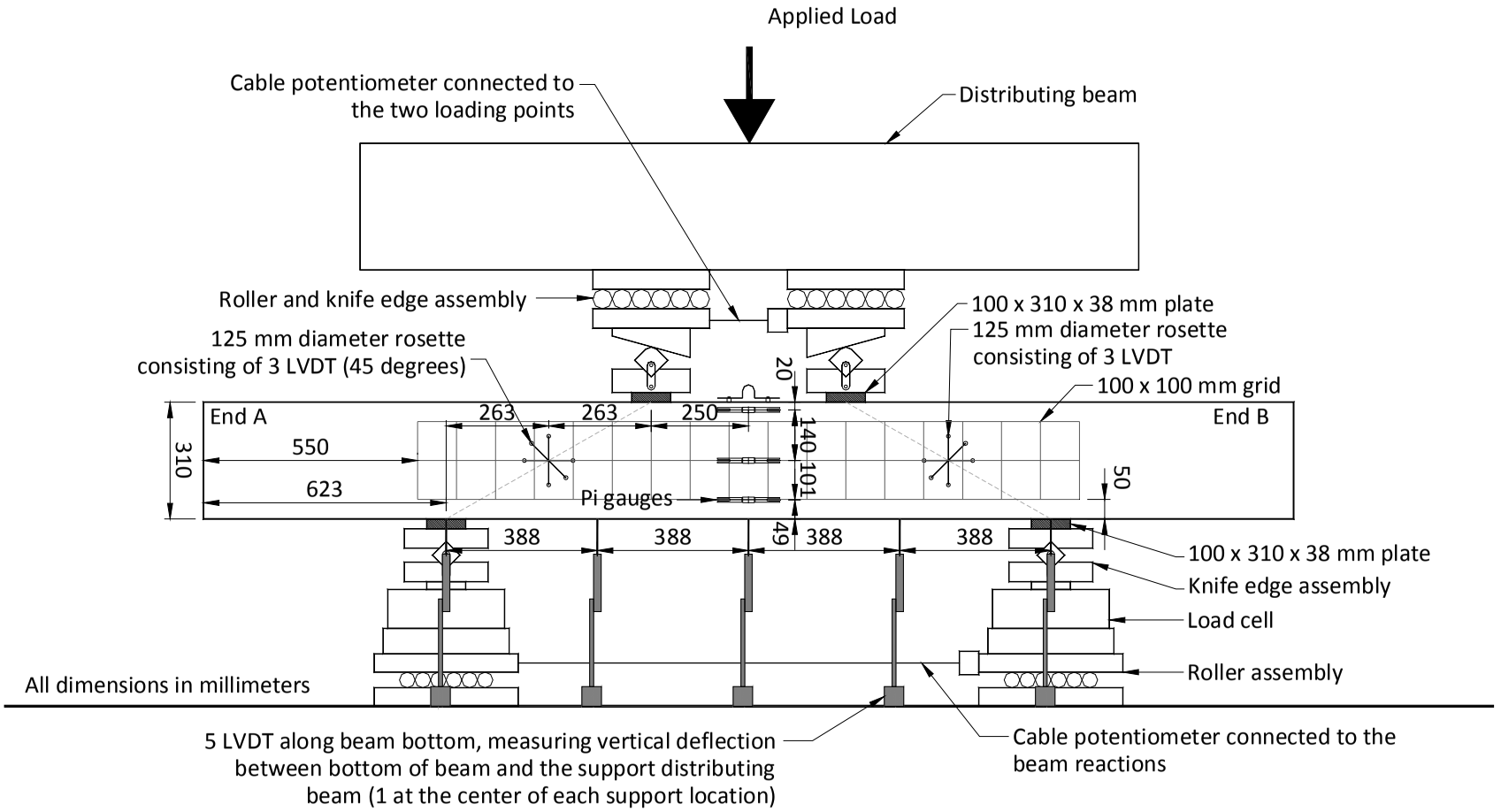

Figure C-38: Instrumentation drawing for specimen A4H.

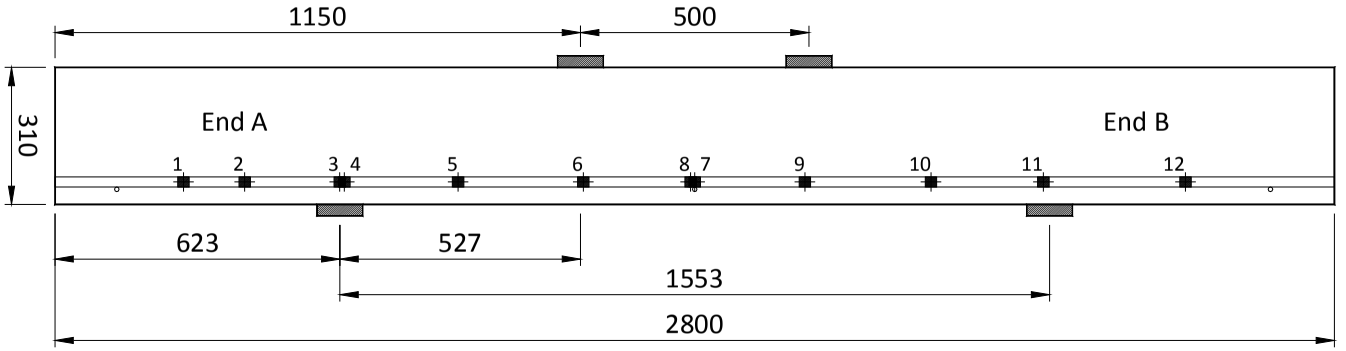

Strain Gauge Locations

Strain Gauge No.	Column	Distance from End A (mm)
1	C	281
2	F	415
3	F	623
4	C	633
5	C	882
6	F	1156
7	F	1400
8	C	1391
9	F	1641
10	F	1917
11	C	2163
12	C	2474

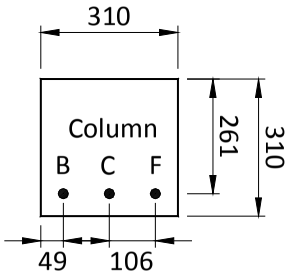

(3) - #7 GFRP Bars

Notes:
All dimensions in mm
Clear Cover: 38.1 mm
Concrete Strength: 65 MPa
Bar Length: 2800 mm

Figure C-39: Location of the strain gauges for specimen A4H (as-built).

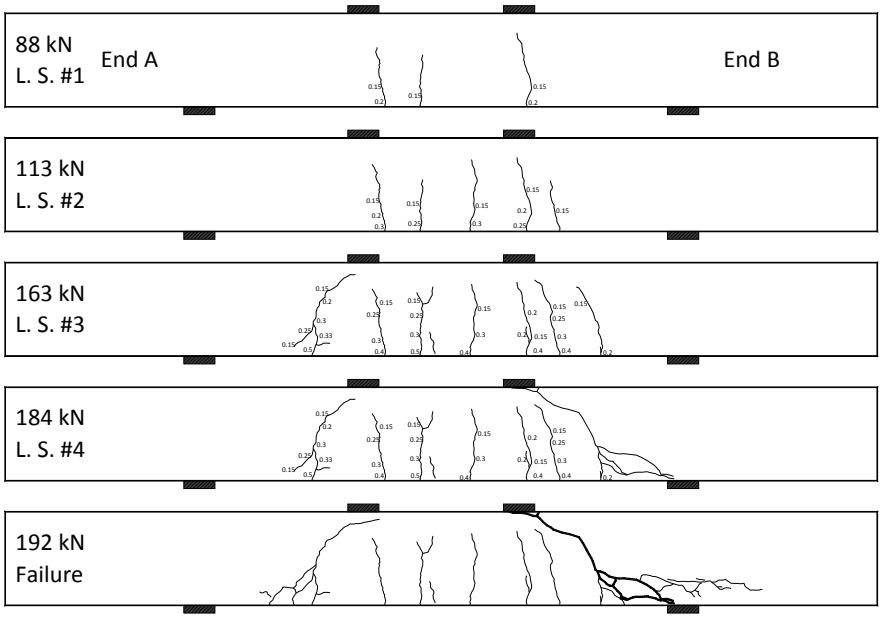

Figure C-40: Crack diagrams of specimen A4H showing the development of the cracks and the widths as loading progressed.

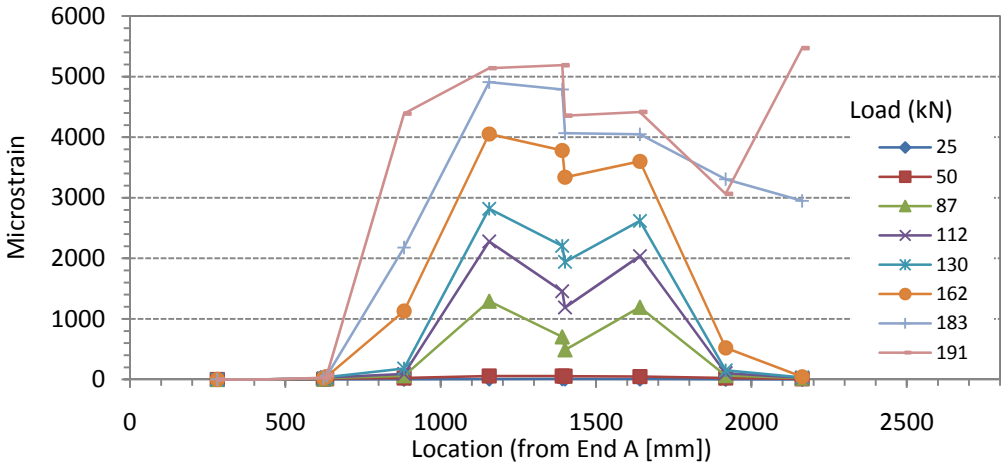

Figure C-41: Strain in the reinforcement as loading progressed.

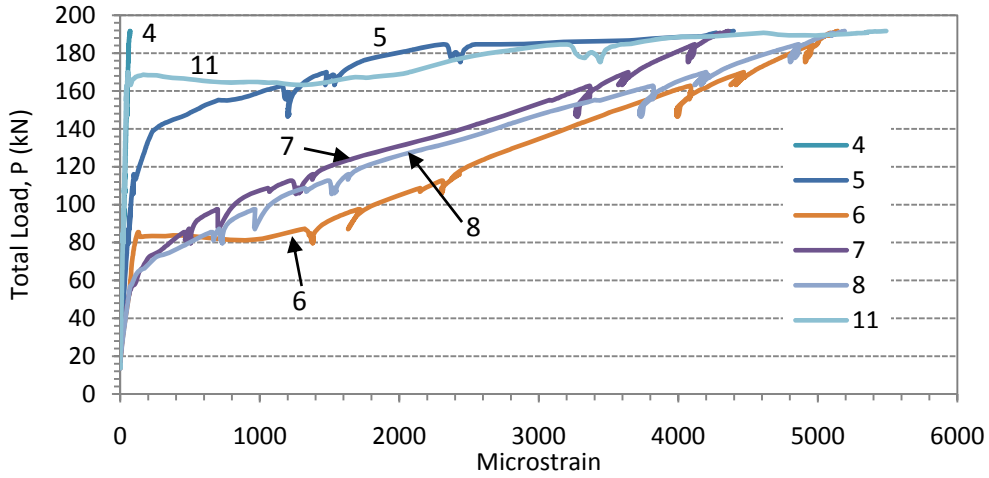

Figure C-42: Strain in the reinforcement.

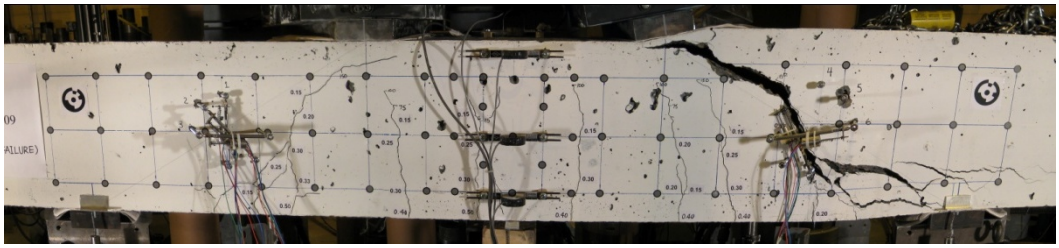

Figure C-43: Specimen B4H after failure.

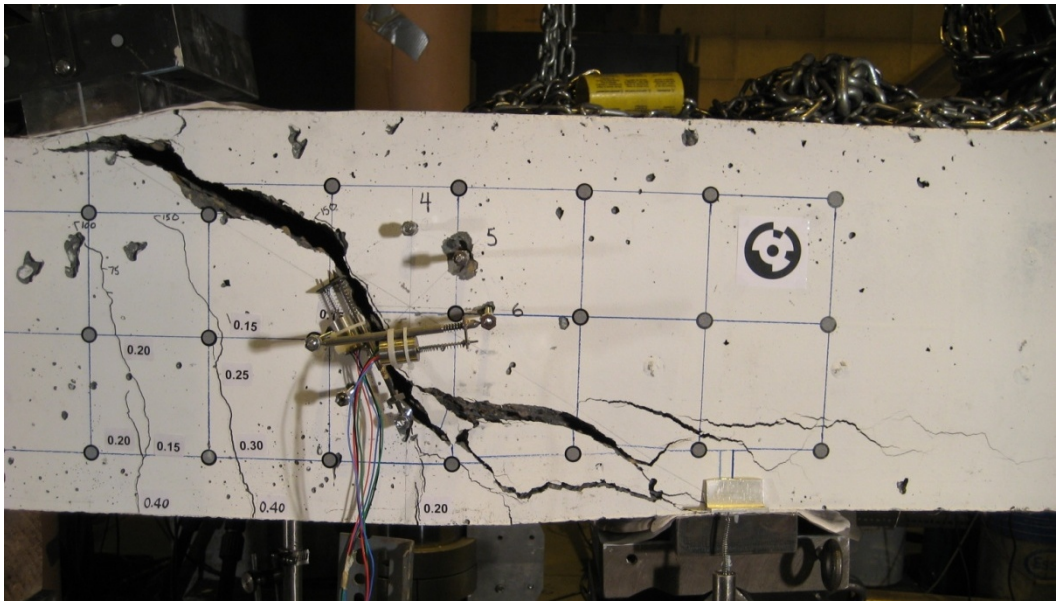

Figure C-44: Shear span B after failure.

Table C-4: Subset of the collected data for specimen A4H.

			Displacements			Bottom Strain Gauges					
Load Stage	Time	Load, P	End A 1/4 Span	Mid-Span	End B 1/4 Span	4	5	6	7	8	11
(#)	(s)	(kN)	(mm)	(mm)	(mm)	(με)	(με)	(με)	(με)	(με)	(με)
	0	15	0.0	0.0	0.0	0	0	0	0	0	0
	125	22	0.0	0.0	0.0	2	3	6	5	7	1
	250	34	0.0	0.0	0.0	6	12	25	23	27	5
	375	48	0.0	0.1	0.1	10	22	53	49	53	9
	500	65	0.1	0.2	0.1	16	37	78	136	128	14
	625	82	0.2	0.4	0.3	21	54	112	390	548	19
	750	84	0.5	0.7	0.5	22	57	1135	474	680	20
1	780	87	0.5	0.7	0.5	23	60	1323	492	709	21
	1375	80	0.6	0.8	0.6	23	60	1379	505	731	21
	1500	98	0.6	0.9	0.7	27	72	1705	691	957	24
	1625	102	0.8	1.3	0.9	29	78	1885	847	1107	26
	1750	109	1.0	1.5	1.2	31	88	2195	1106	1375	28
2	1800	113	1.0	1.6	1.3	32	93	2311	1231	1496	29
	2400	107	1.1	1.7	1.3	32	93	2305	1294	1546	28
	2525	118	1.3	1.9	1.5	35	130	2450	1444	1700	31
	2650	127	1.5	2.2	1.7	38	170	2725	1813	2066	33
	2775	135	1.7	2.5	1.9	40	210	3025	2231	2488	36
	2900	143	1.9	2.8	2.1	43	316	3300	2579	2806	38
	3025	150	2.3	3.1	2.3	45	543	3563	2871	3126	40
	3150	156	2.5	3.4	2.6	47	856	3816	3131	3490	42
	3275	163	2.8	3.7	2.7	50	1159	4087	3365	3817	43
3	3275	163	2.8	3.7	2.7	50	1159	4087	3365	3817	43
	4145	148	2.8	3.7	2.9	48	1209	3987	3264	3723	44
	4270	162	3.0	4.0	3.2	51	1280	4193	3415	3903	48
	4395	168	3.2	4.2	3.5	53	1414	4407	3587	4127	52
	4520	166	3.3	4.6	4.0	53	1483	4410	3595	4149	86
	4645	168	3.6	4.9	4.6	54	1533	4475	3644	4216	243
	4770	164	3.7	5.3	5.3	53	1537	4430	3610	4177	1026
	4895	167	3.9	5.7	5.9	54	1556	4471	3642	4217	1665
	5020	171	4.1	6.1	6.5	55	1611	4553	3716	4310	2127
	5145	177	4.3	6.5	6.9	57	1780	4715	3871	4514	2422
	5270	181	4.6	6.8	7.3	59	2068	4850	4009	4704	2783
4	5385	185	4.8	7.2	7.7	60	2317	4959	4117	4862	3183
	5870	179	4.9	7.2	7.7	59	2447	4909	4069	4800	3455
	5995	186	5.2	7.5	8.0	62	3230	5004	4178	4942	3735
	6120	189	5.5	7.9	8.5	65	4041	5042	4242	5029	4032
	6245	191	5.7	8.3	8.9	68	4267	5088	4297	5104	4600
	6370	190	6.0	8.8	9.6	69	4295	5088	4299	5112	5114
	6495	191	6.2	9.2	10.2	70	4351	5118	4332	5157	5347
Failure	6595	192	6.4	9.5	10.6	71	4396	5143	4359	5193	5491

C.7 Specimen B1N

The displacement rate of specimen B1N was 0.1 mm/min of machine stroke. An initial peak load was reach at approximately P = 1273 kN. At P = 1273 kN, the main diagonal cracks in both shear spans had extended to near the top of the specimen towards the inside edge of the loading plate and were starting to become horizontal. Subsequently, crushing of concrete commenced in the flexural compression zone at mid-span. The load carrying capacity dropped slightly but was regained followed by 8% drop due to further deterioration of the flexural region. The diagonal cracks had propagated such that they joined horizontally approximately 60 mm below the top of the beam. The concrete above was completely crushed yet the specimen continued to support and resist additional load until the peak load was reached. At this point, the crushing of the concrete had extended to 1/3 of the specimen depth and a horizontal splitting crack was forming to the right of support A. The main diagonal crack width had increased significantly and the center of the specimen had moved downwards vertically along the two diagonal shear cracks.

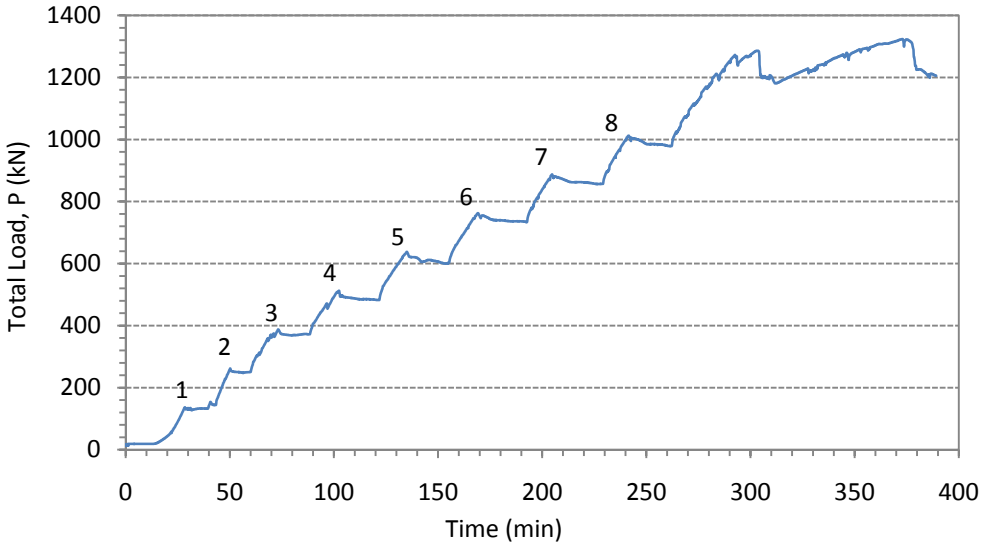

Figure C-45: Load – history of specimen B1N.

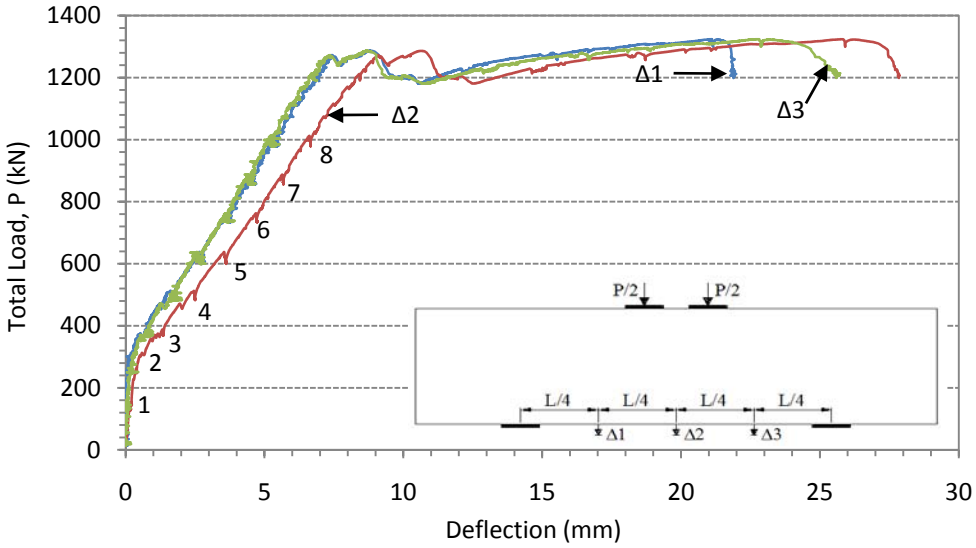

Figure C-46: Load – displacement response of specimen B1N.

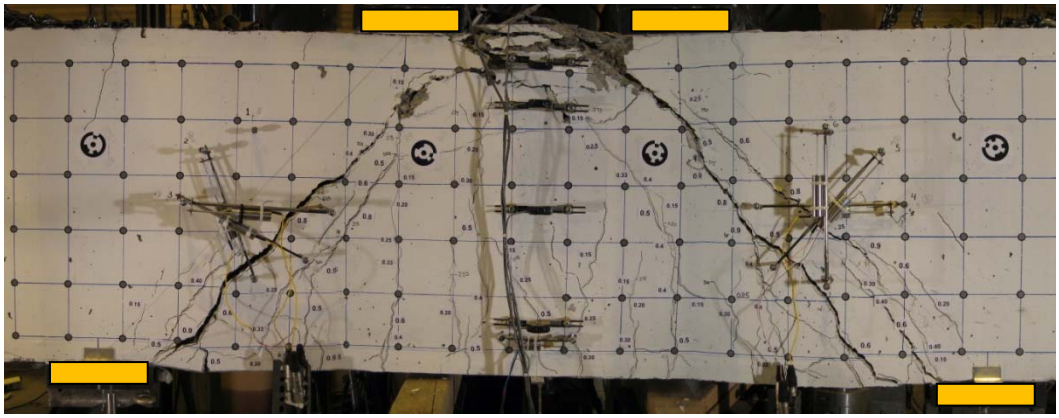

Figure C-47: Specimen B1N at the conclusion of the test.

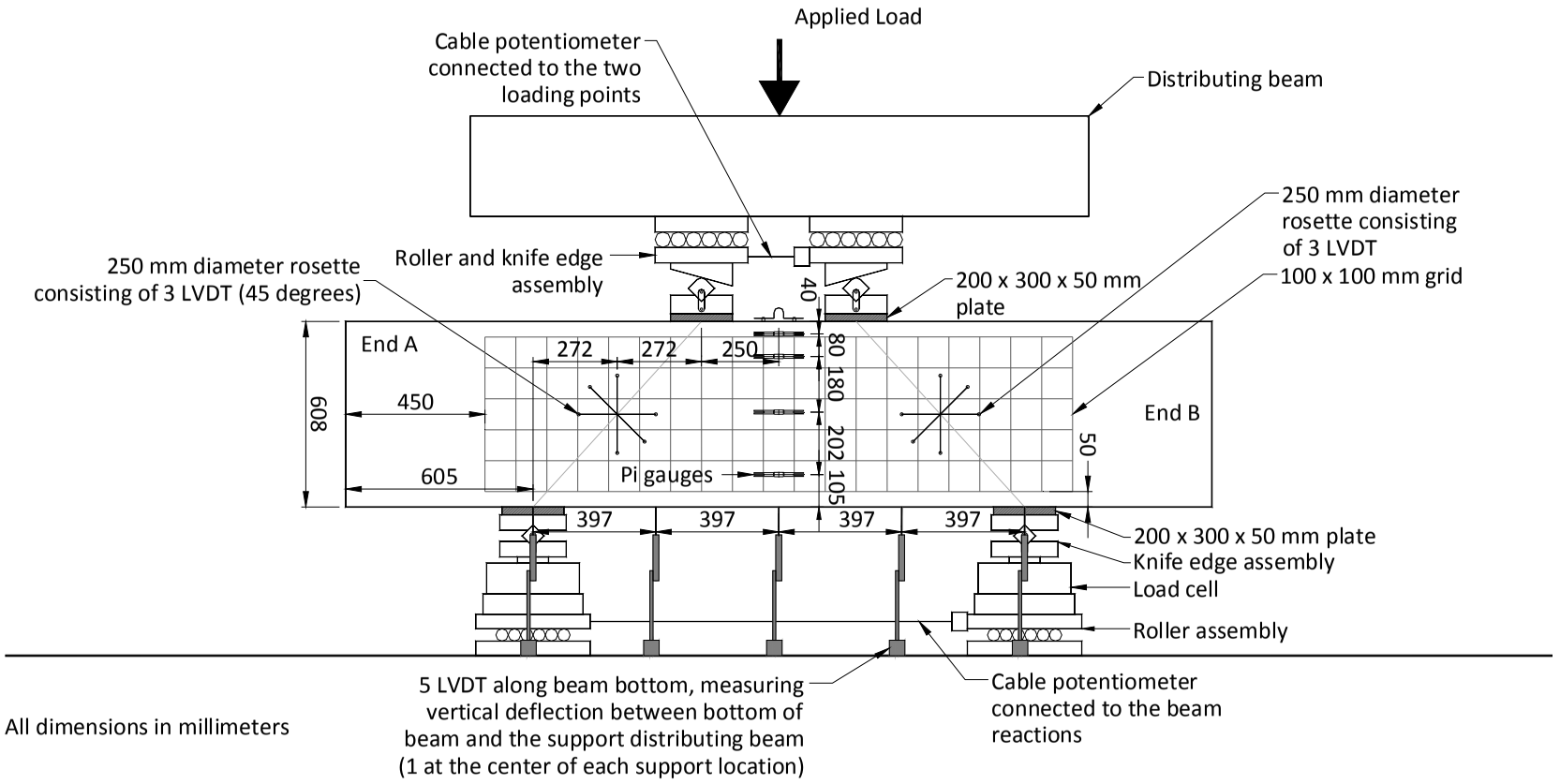

Figure C-48: Instrumentation drawing for specimen B1N.

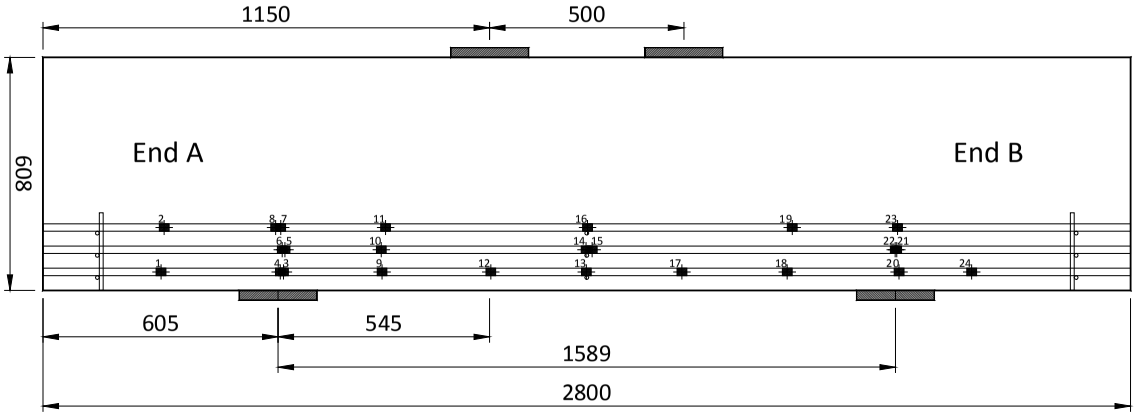

Strain Gauge Locations

Strain Gauge No.	Row	Column	Distance from End A (mm)	Strain Gauge No.	Row	Column	Distance from End A (mm)
1	B	F	304	13	B	C	1399
2	T	C	312	14	M	F	1398
3	B	B	619	15	M	B	1414
4	B	F	611	16	T	B	1402
5	M	F	623	17	B	C	1643
6	M	B	616	18	B	C	1916
7	T	F	612	19	T	C	1929
8	T	C	599	20	B	F	2204
9	B	C	873	21	M	F	2198
10	M	F	871	22	M	B	2194
11	T	F	882	23	T	C	2200
12	B	F	1153	24	B	B	2391

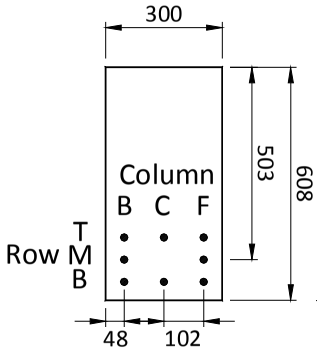

(8) - #6 GFRP Bars

Notes:
All dimensions in mm
Clear Cover: 38.1 mm
Concrete Strength: 41 MPa
Bar Length: 2800 mm

Figure C-49: Location of the strain gauges for specimen B1N (as-built).

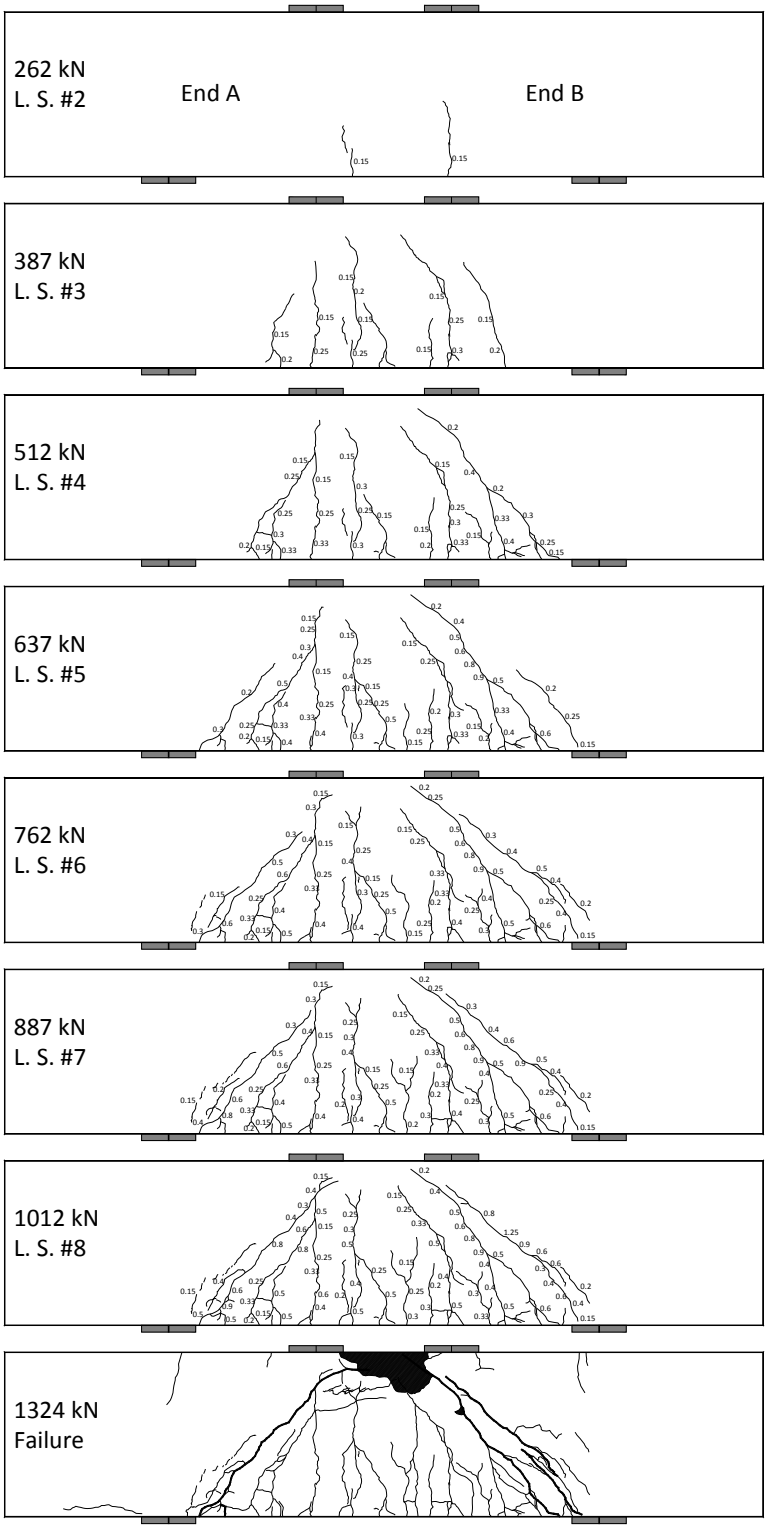

Figure C-50: Crack diagrams of specimen B1N showing the development of the cracks and the widths as loading progressed.

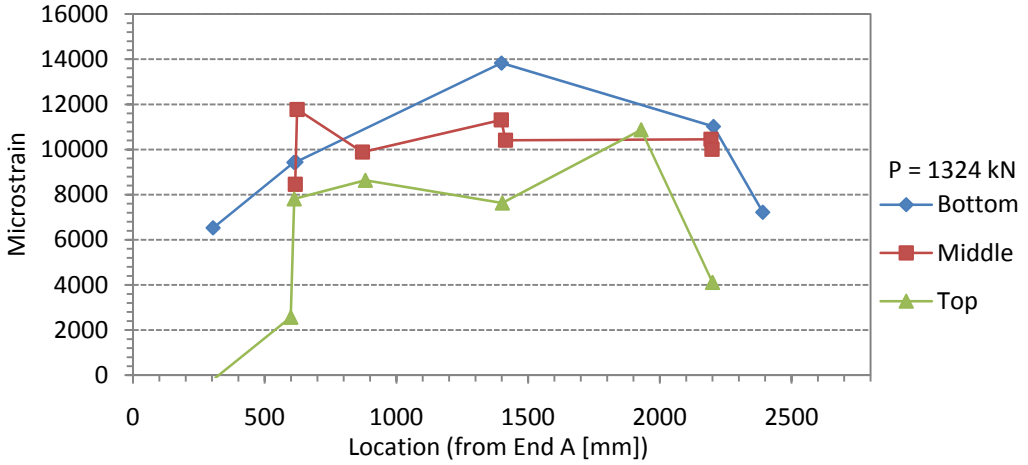

Figure C-51: Strain distribution in the bottom, middle, and top reinforcement at peak load.

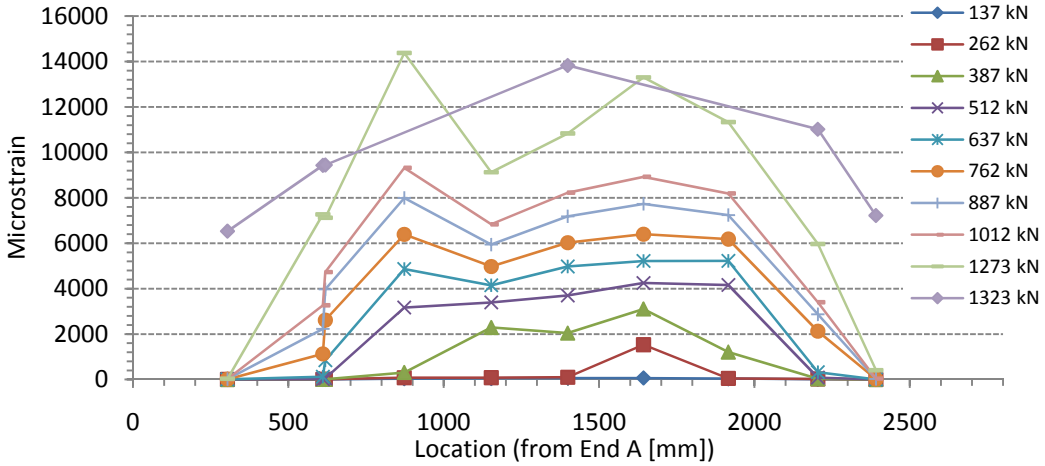

Figure C-52: Strain in the bottom reinforcement layer as loading progressed.

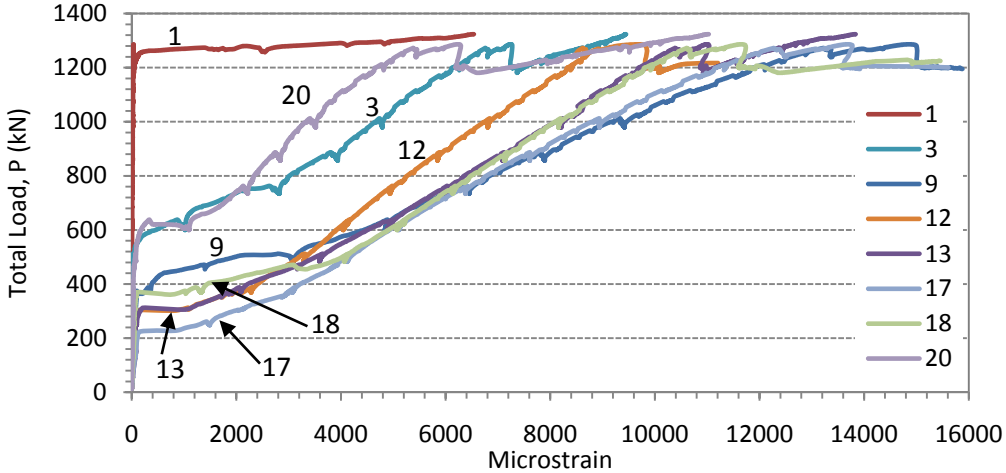

Figure C-53: Strain in the bottom reinforcement layer.

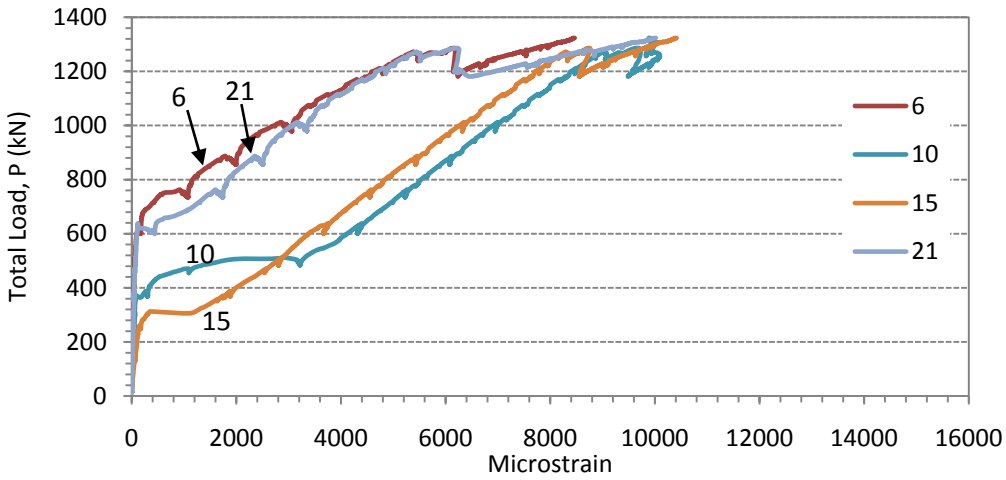

Figure C-54: Strain in the middle reinforcement layer.

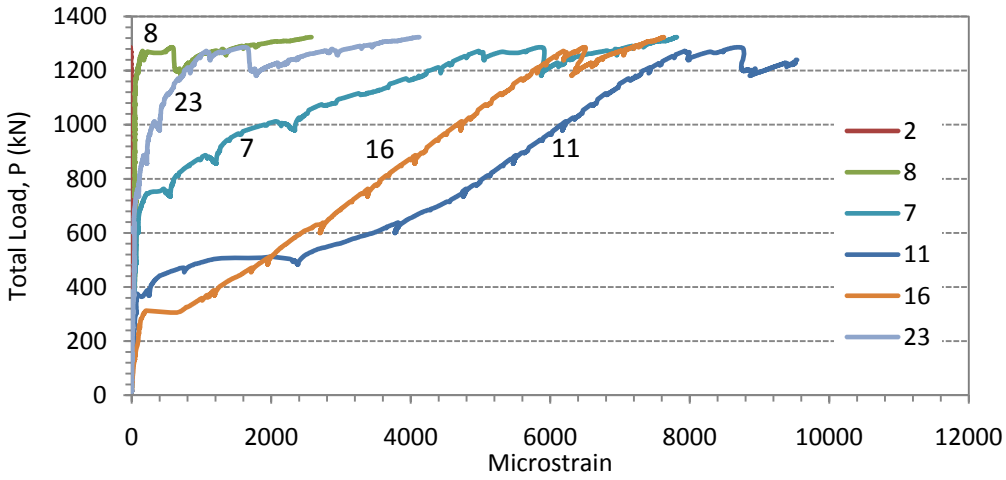

Figure C-55: Strain in the top reinforcement layer.

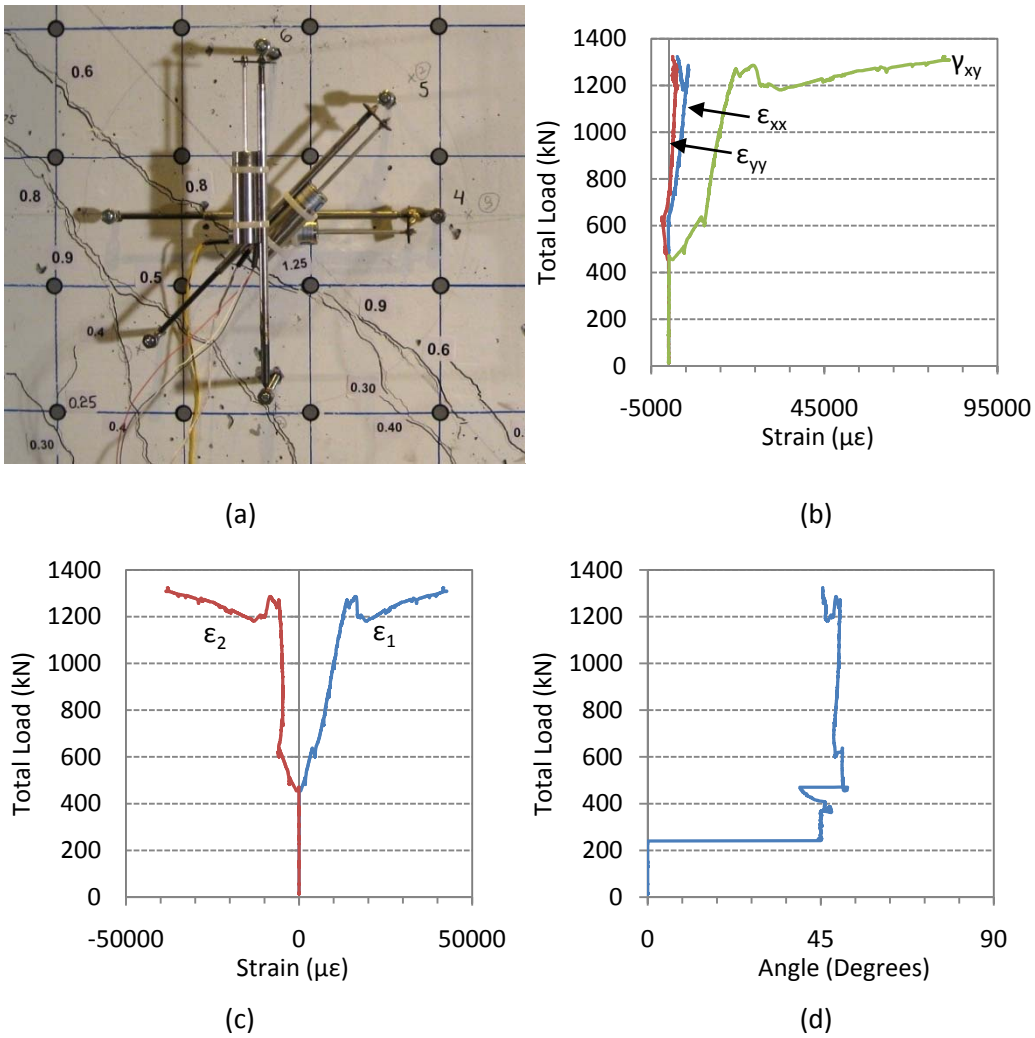

Figure C-56: (a) crack location through the rosette in shear span B at P= 1012 kN, (b) strain components, (c) principal strains, and (d) the direction of the minimum principal strain (angle of inclination from a horizontal line towards mid-span).

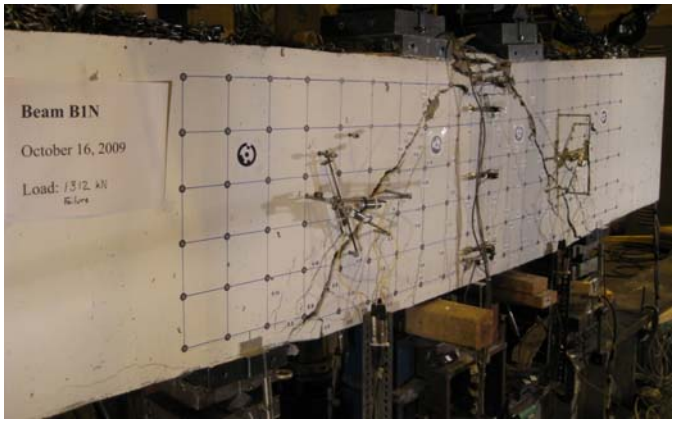

Figure C-57: Specimen B1N at the conclusion of the test, end A on the left, end B on the right.

Table C-5: Subset of the collected data for specimen B1N.

			Displacements			Bottom Strain Gauges				
Load Stage	Time	Load, P	End A 1/4 Span	Mid-Span	End B 1/4 Span	1	3	9	13	17
(#)	(s)	(kN)	(mm)	(mm)	(mm)	(με)	(με)	(με)	(με)	(με)
	0	16	0.0	0.0	0.0	0	0	0	0	0
	375	19	0.0	0.0	-0.1	0	0	0	0	1
	750	19	0.0	0.0	0.0	0	0	0	0	1
	1125	37	0.0	0.0	0.0	0	1	5	9	10
	1500	90	0.1	0.1	0.0	0	2	21	38	37
1	1700	136	0.0	0.2	0.1	1	3	34	71	63
	2375	133	0.0	0.2	0.1	1	3	35	72	67
	2750	195	0.0	0.2	0.2	1	5	52	80	101
2	3010	262	0.1	0.4	0.3	2	7	74	87	1421
	3605	252	0.1	0.4	0.2	2	6	75	97	1498
	3980	334	0.3	0.8	0.4	3	7	86	1421	2482
	4355	380	0.7	1.3	0.7	3	7	280	1980	3054
3	4395	388	0.7	1.3	0.8	3	8	313	2052	3110
	5305	372	0.7	1.4	0.9	3	7	362	2095	3072
	5680	451	1.1	1.8	1.1	4	11	916	2942	3756
	6055	503	1.5	2.3	1.7	5	16	2026	3546	4132
4	6145	512	1.6	2.5	1.8	5	20	2806	3651	4214
	7305	482	1.8	2.5	1.8	5	49	3095	3591	4120
	7680	572	2.1	2.9	2.1	5	176	3965	4238	4693
	8055	631	2.7	3.5	2.5	8	783	4809	4899	5170
5	8100	638	2.6	3.5	2.6	8	861	4881	4990	5230
	9225	599	2.7	3.6	2.7	8	1020	4843	4886	5100
	9600	674	3.0	4.0	3.0	9	1178	5264	5267	5582
	9975	738	3.5	4.5	3.4	11	2005	6008	5807	6166
6	10150	763	3.7	4.7	3.6	13	2634	6403	6033	6406
	11560	734	3.8	4.7	3.7	13	2825	6453	6010	6375
	11935	827	4.1	5.2	4.0	15	3237	7126	6579	7022
7	12285	887	4.5	5.6	4.3	17	3804	7813	7115	7609
	13745	857	4.6	5.7	4.4	17	3940	7896	7086	7609
	14120	948	5.0	6.1	4.8	19	4317	8571	7664	8286
8	14485	1012	5.4	6.6	5.2	21	4734	9328	8234	8932
	16205	1080	6.0	7.3	5.8	24	5245	10329	8758	9824
	16580	1145	6.4	7.8	6.2	27	5700	11178	9257	10526
	16955	1203	6.9	8.3	6.6	30	6171	11942	9736	11220
	17330	1243	7.2	8.7	7.0	32	6512	12653	10095	11789
9	17555	1272	7.4	9.1	7.4	34	6759	13221	10387	12269
	17930	1266	8.3	10.1	8.2	33	7047	14150	10739	13118
	18305	1207	9.6	11.3	9.3	35	7242	15081	10870	13575
	18680	1186	10.5	12.4	10.6	41	7377	-	10937	16895
	19055	1198	11.1	13.3	11.6	45	7468	-	11133	-
	19430	1217	11.7	14.1	12.3	52	7675	-	11387	-
	19805	1226	12.3	14.9	13.1	70	7883	-	11640	-
	20180	1248	13.1	15.8	14.1	127	8111	-	11887	-
	20555	1268	14.5	17.5	15.5	825	8518	-	12283	-
	20930	1279	15.8	19.1	17.1	2940	8760	-	12520	-
	21305	1293	17.2	20.7	18.6	4555	9017	-	12811	-
	21680	1307	18.5	22.4	19.9	5461	9212	-	13170	-
	22055	1312	19.9	24.2	21.5	6140	9326	-	13504	-
Failure	22380	1324	21.1	25.8	22.7	6534	9446	-	13835	-

Table C-5 continued,

		Middle Strain Gauges			Top Strain Gauges					Rosette shear span B		
Load Stage	Load, P	6	10	15	2	7	8	11	16	ε_{xx}	ε_{yy}	γ_{xy}
(#)	(kN)	(με)	(με)	(με)	(με)	(με)	(με)	(με)	(με)	με	με	με
	16	0	0	0	0	0	0	0	0	0	1	0
	19	0	0	0	0	0	0	0	0	0	-1	2
	19	0	0	0	0	0	0	0	0	0	-1	1
	37	2	3	7	0	1	2	2	5	0	-1	-1
	90	8	14	30	0	6	7	9	20	-1	-2	-1
1	136	13	23	57	-1	10	11	16	39	-1	-1	-1
	133	13	23	61	-1	10	11	17	44	1	1	-2
	195	20	35	98	-1	15	17	27	88	2	1	0
2	262	28	49	151	-2	22	24	39	110	1	1	92
	252	27	50	174	-2	22	24	41	117	3	2	94
	334	35	61	1435	-2	31	33	65	856	3	3	91
	380	41	233	1830	-2	37	40	198	1142	9	1	82
3	388	42	266	1881	-2	38	40	223	1176	9	1	84
	372	41	308	1891	-2	37	40	256	1192	7	3	90
	451	50	691	2418	-3	47	48	495	1595	-17	2	110
	503	56	1828	2804	-3	55	55	1175	1923	-33	-856	4011
4	512	59	2926	2874	-3	59	57	2008	1985	-36	-947	4475
	482	61	3217	2803	-3	60	57	2384	1950	-42	-955	4534
	572	79	3936	3208	-4	66	65	3105	2277	-50	-1362	6676
	631	132	4343	3685	-4	83	64	3753	2697	-58	-1888	9197
5	638	143	4396	3747	-4	86	64	3818	2744	-60	-1928	9459
	599	174	4317	3666	-5	91	61	3774	2702	97	-1266	10332
	674	205	4663	3989	-5	107	65	4138	2926	773	-538	11000
	738	514	5098	4409	-6	197	64	4683	3251	1477	69	11616
6	763	915	5263	4580	-6	459	44	4796	3387	1831	306	11791
	734	1079	5224	4552	-6	555	43	4752	3382	1950	434	11656
	827	1308	5708	5019	-7	703	43	5186	3729	2423	668	12447
7	887	1785	6121	5459	-7	1056	42	5511	4069	2919	941	13128
	857	1997	6080	5428	-8	1211	44	5469	4058	3000	1051	13161
	948	2261	6568	5910	-8	1409	45	5896	4401	3398	1190	13962
8	1012	2846	6994	6354	-9	2062	43	6223	4730	3815	1389	14780
	1080	3502	7572	6911	-10	2914	45	6660	5150	4349	1674	15929
	1145	4083	7996	7339	-11	3686	52	6985	5467	4758	1879	16877
	1203	4654	8428	7750	-12	4308	81	7366	5775	5159	2082	17843
	1243	5073	8756	8057	-12	4681	115	7676	6008	5476	2187	18704
9	1272	5383	9016	8293	-13	4970	157	7928	6188	5734	2271	19421
	1266	5929	9394	8537	-14	5545	429	8389	6341	5667	2290	22625
	1207	6147	9583	8582	-15	5876	623	8751	6361	5091	2010	26445
	1186	6243	9512	8574	-15	5879	702	8882	6326	4290	2093	31394
	1198	6317	9607	8690	-16	5910	739	9043	6381	3962	2517	36883
	1217	6509	9783	8881	-16	6024	778	9250	6504	3813	1949	41704
	1226	6730	9918	9068	-18	6163	840	9458	6636	3699	1412	46005
	1248	6950	10056	9249	-20	6332	919	9684	6758	3562	1199	50873
	1268	7350	10047	9527	-30	6691	1125	9837	6965	3407	1362	57701
	1279	7611	9890	9715	-50	7005	1419	9929	7111	3181	1726	65132
	1293	7902	9979	9913	-71	7286	1700	9801	7261	3047	1768	73105
	1307	8164	10041	10097	-93	7512	2040	9395	7398	2938	1444	79203
	1312	8308	9916	10258	-112	7687	2327	8879	7513	2679	1161	79188
Failure	1324	8463	9887	10414	-124	7813	2572	8629	7630	2537	1218	79830

C.8 Specimen B2N

The displacement rate of specimen B2N was 0.1 mm/min of machine stroke. At P = 792 kN, the specimen globally moved approximately 10 mm towards end A (west) which disrupted the center LVDT (Δ_2). The LVDT was reset and the data adjusted. The main diagonal cracks in each shear span extended towards the inside of the loading plates where they became almost horizontal at a depth of approximately 60 mm from the top surface. Failure of specimen B2N was sudden. The main diagonal crack in shear span A propagated through the horizontal compression zone, emerging to the inside of loading plate A which resulted in movement along the diagonal crack and immediate loss of load carrying capacity.

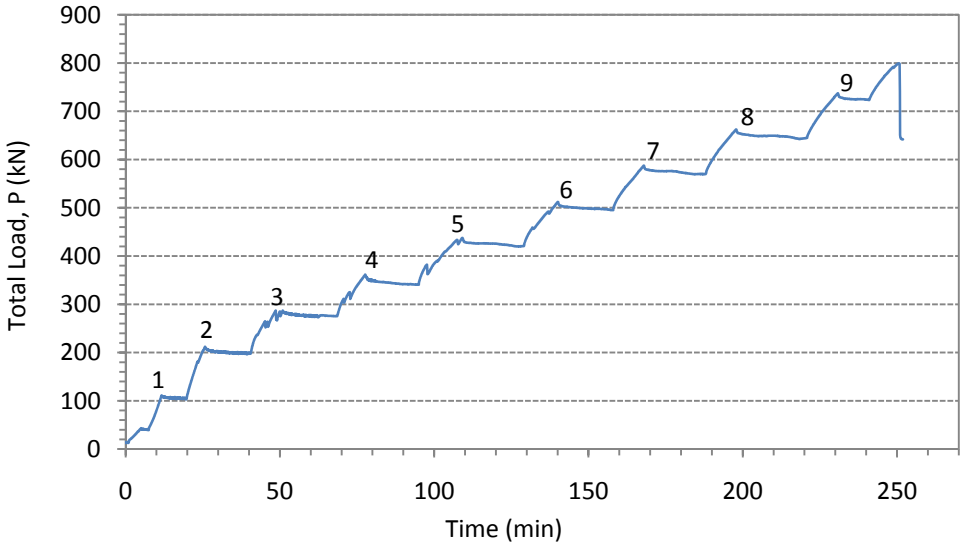

Figure C-58: Load – history of specimen B2N.

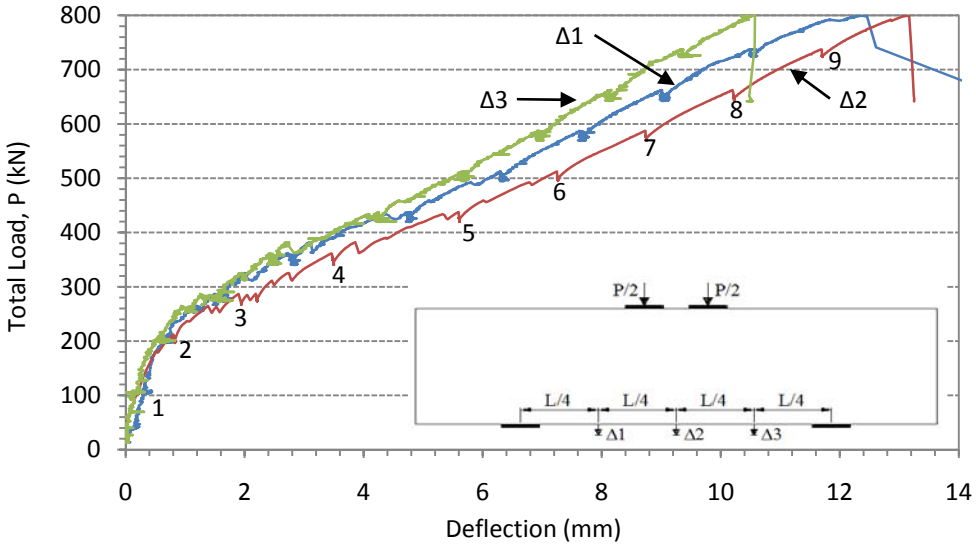

Figure C-59: Load – displacement response of specimen B2N.

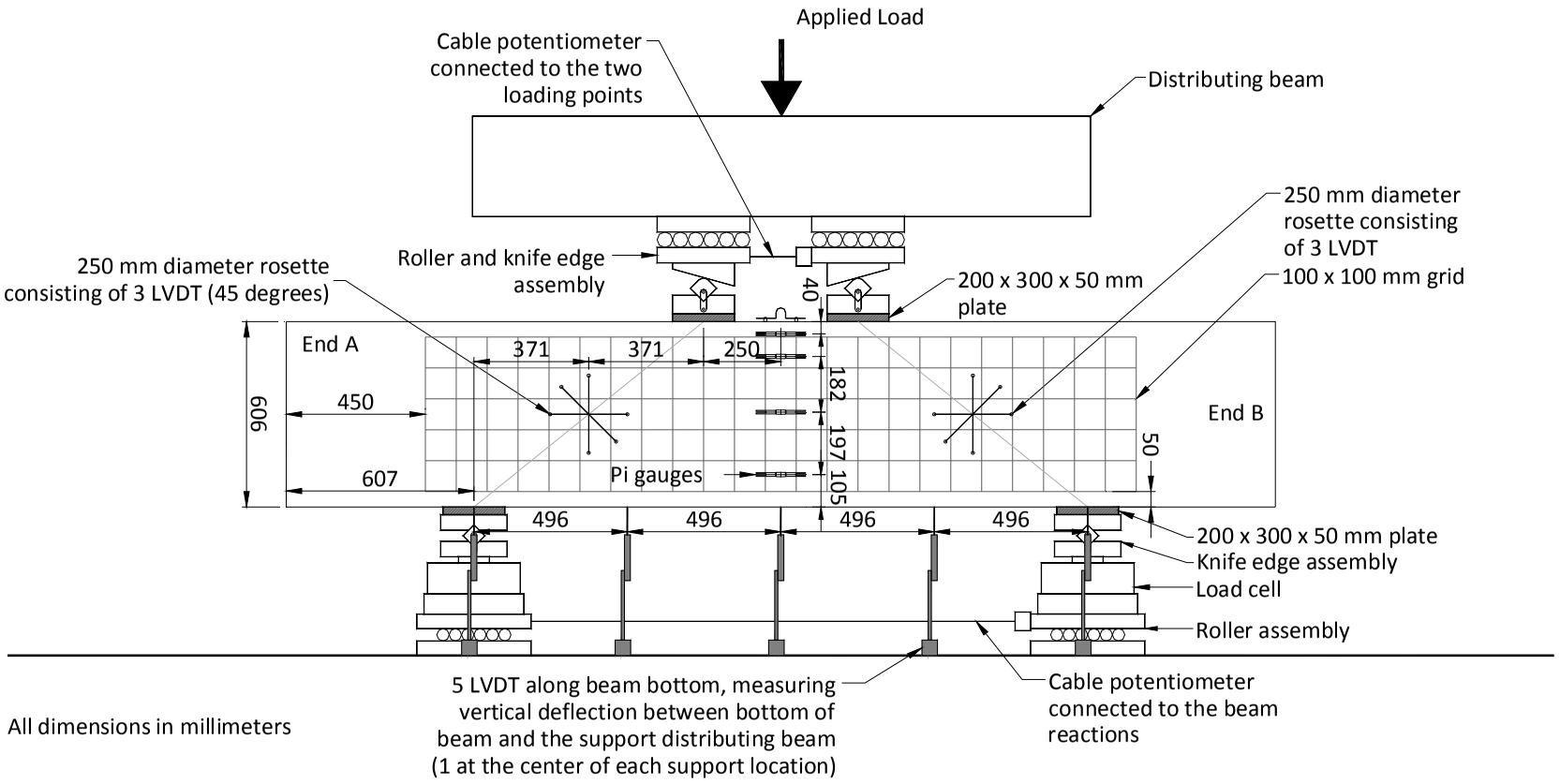

Figure C-60: Instrumentation drawing for specimen B2N.

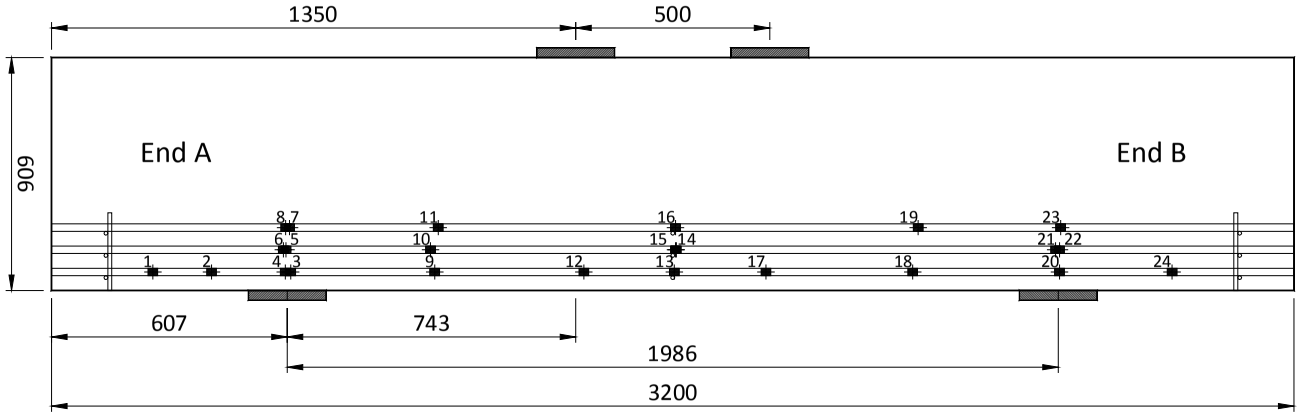

Strain Gauge Locations

Strain Gauge No.	Row	Column	Distance from End A (mm)	Strain Gauge No.	Row	Column	Distance from End A (mm)
1	B	F	261	13	B	C	1604
2	B	F	412	14	M	B	1609
3	B	F	616	15	M	F	1607
4	B	C	602	16	T	C	1607
5	M	B	604	17	B	C	1840
6	M	F	597	18	B	F	2218
7	T	F	613	19	T	B	2232
8	T	B	603	20	B	C	2596
9	B	F	987	21	M	F	2586
10	M	F	976	22	M	B	2596
11	T	F	996	23	T	C	2599
12	B	C	1371	24	B	C	2886

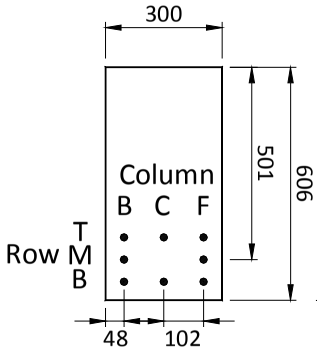

(8) - #6 GFRP Bars

Notes:
All dimensions in mm
Clear Cover: 38.1 mm
Concrete Strength: 40 MPa
Bar Length: 3200 mm

Figure C-61: Location of the strain gauges for specimen B2N (as-built).

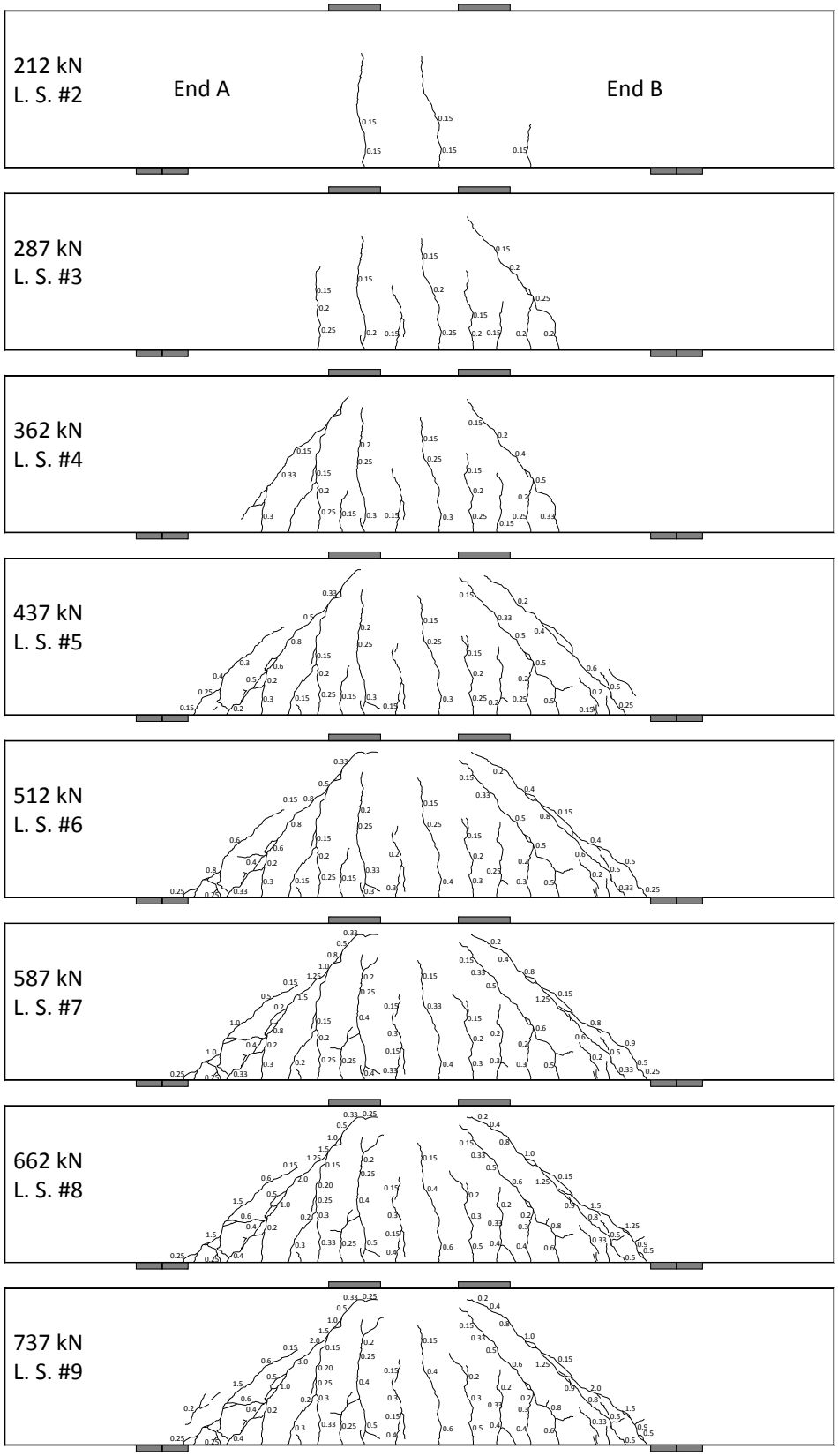
212 kN
L. S. #2
End A
End B
287 kN
L. S. #3
362 kN
L. S. #4
437 kN
L. S. #5
512 kN
L. S. #6
587 kN
L. S. #7
662 kN
L. S. #8
737 kN
L. S. #9

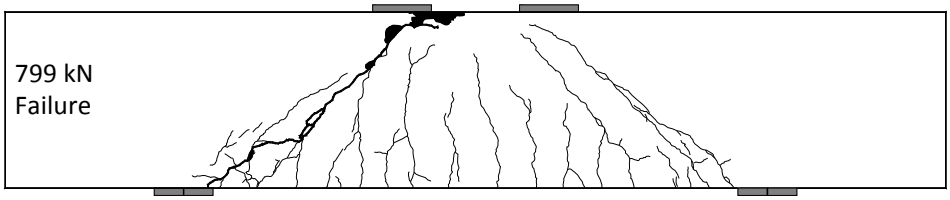

Figure C-62: Crack diagrams of specimen B2N showing the development of the cracks and the widths as loading progressed.

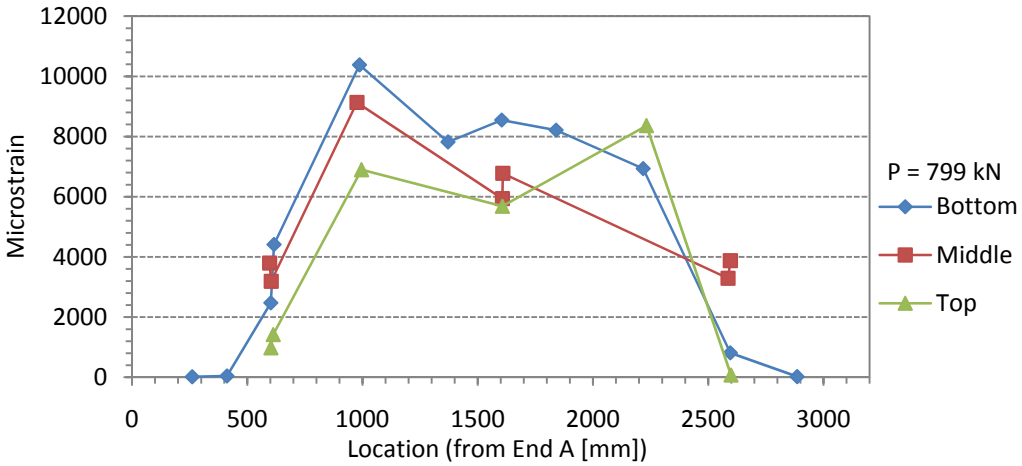

Figure C-63: Strain distribution in the bottom, middle, and top reinforcement at peak load.

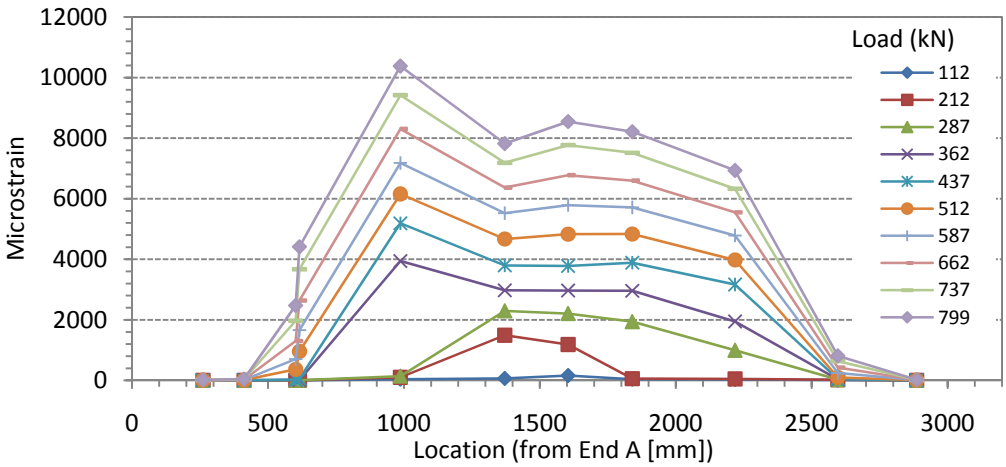

Figure C-64: Strain in the bottom reinforcement layer as loading progressed.

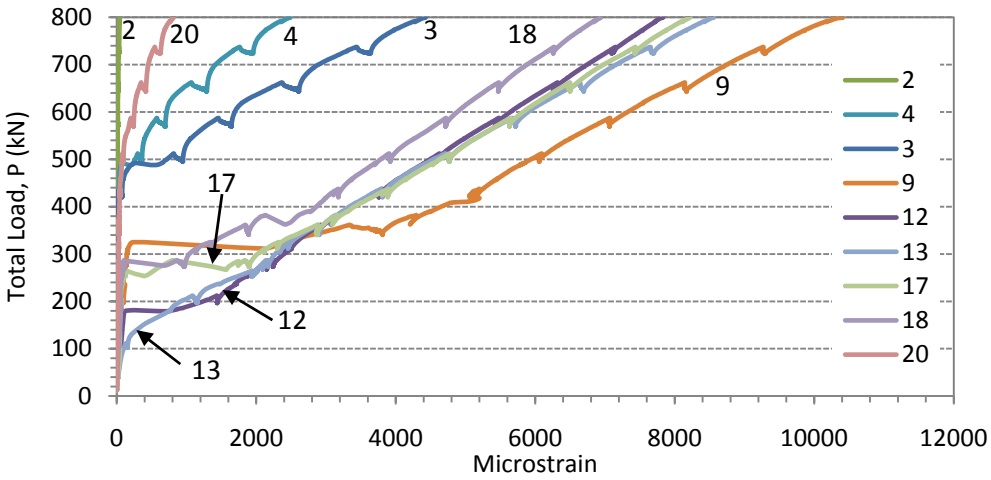

Figure C-65: Strain in the bottom reinforcement layer.

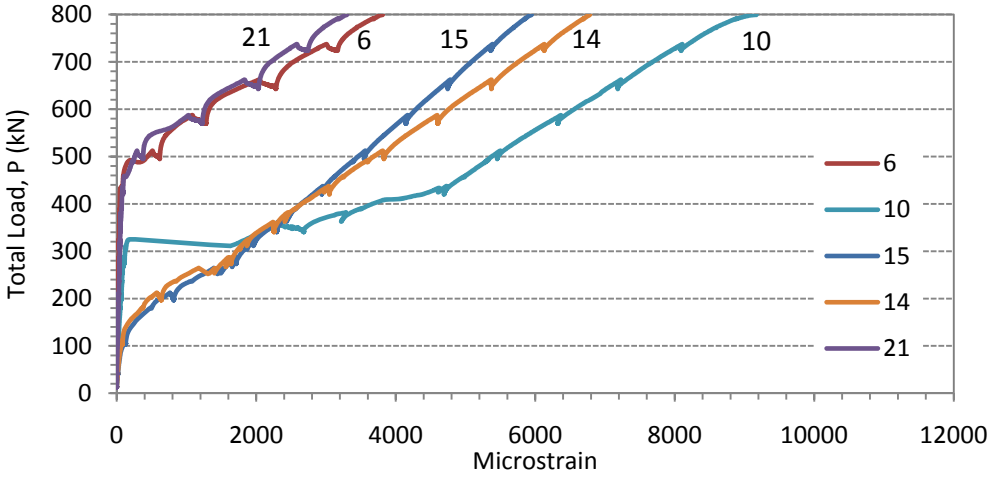

Figure C-66: Strain in the middle reinforcement layer.

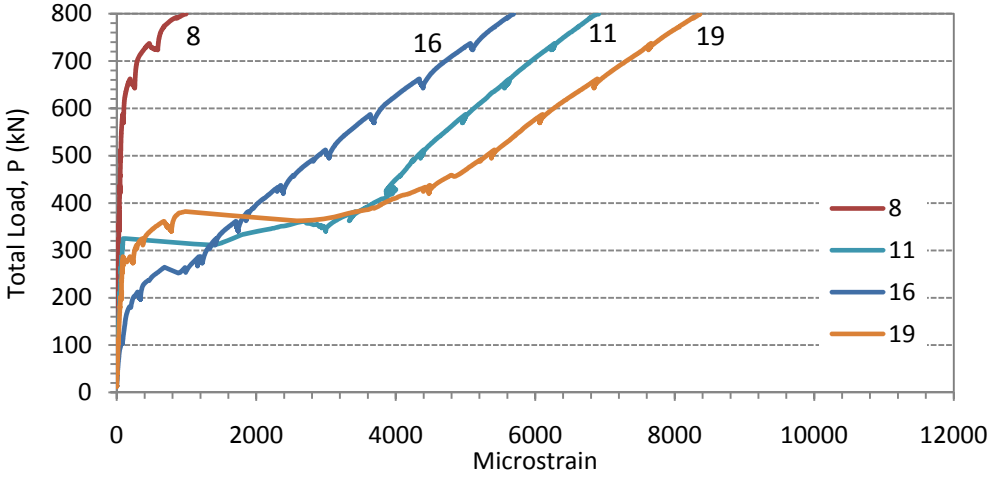

Figure C-67: Strain in the top reinforcement layer.

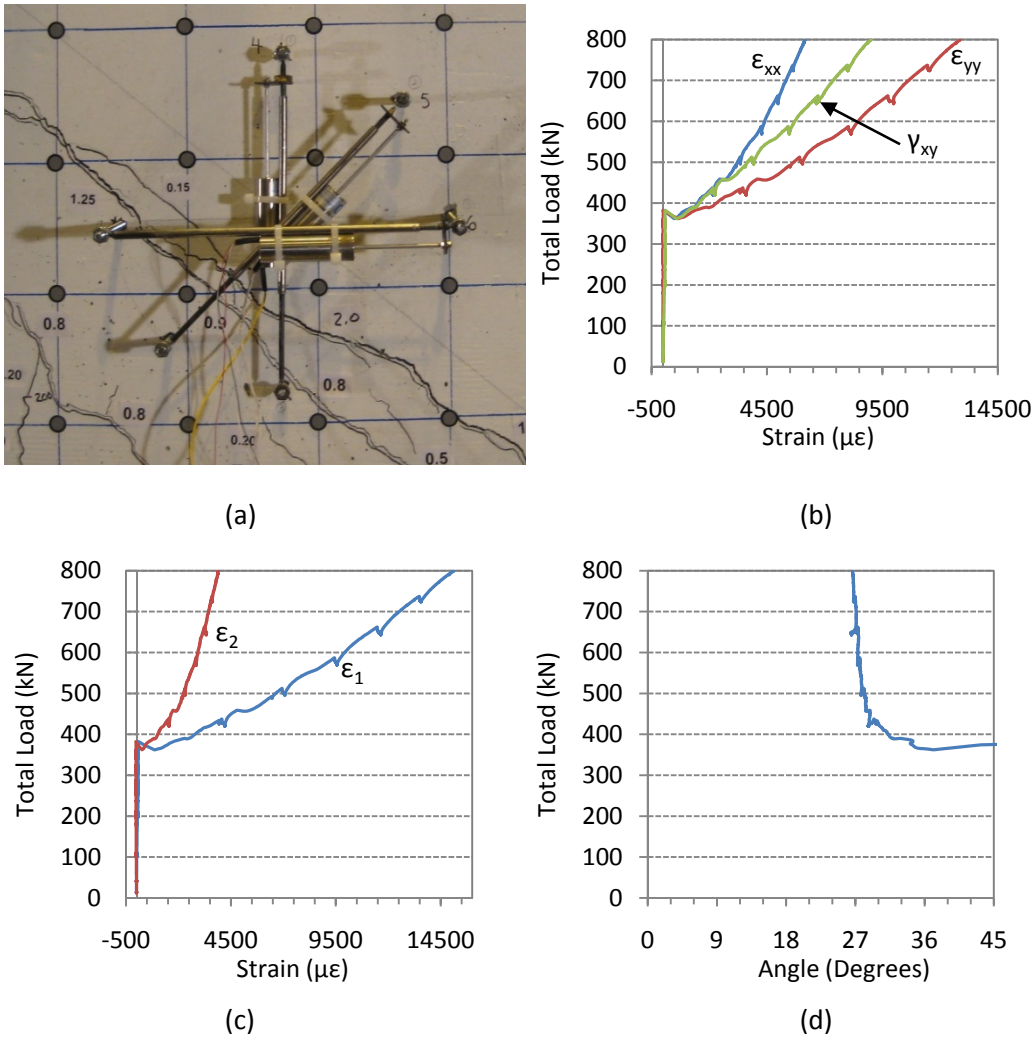

Figure C-68: (a) crack location through the rosette in shear span B at failure, (b) strain components, (c) principal strains, and (d) the direction of the minimum principal strain (angle of inclination from a horizontal line towards mid-span).

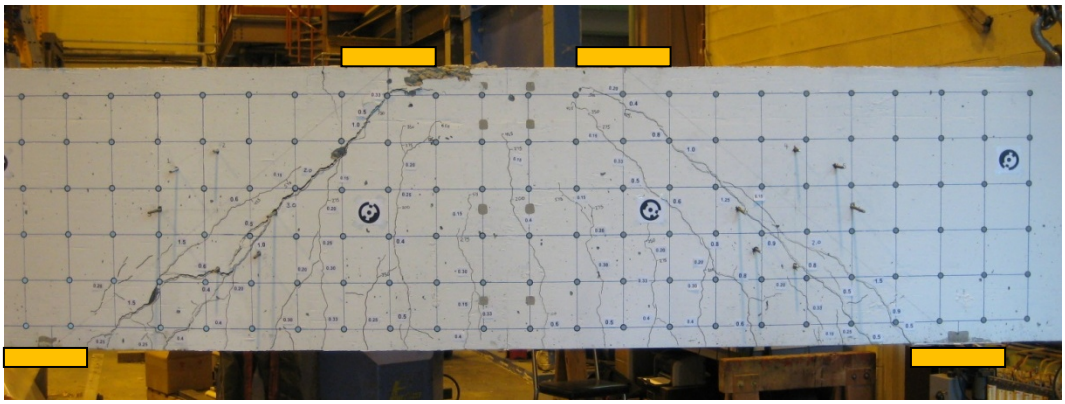

Figure C-69: Specimen B2N after testing with failure crack in shear span A (left).

Table C-6: Subset of the collected data for specimen B2N.

			Displacements			Bottom Strain Gauges				
Load Stage	Time	Load, P	End A 1/4 Span	Mid-Span	End B 1/4 Span	2	3	9	12	13
(#)	(s)	(kN)	(mm)	(mm)	(mm)	(με)	(με)	(με)	(με)	(με)
	0	13	0.0	0.0	0.0	0	0	0	0	0
	200	31	0.1	0.0	0.0	0	0	5	9	12
	400	41	0.1	0.0	0.0	0	0	9	16	22
	600	80	0.2	0.1	0.1	0	0	24	40	60
1	700	111	0.3	0.2	0.2	0	0	38	60	131
	1180	103	0.3	0.2	0.1	0	0	39	61	156
	1380	175	0.5	0.5	0.4	1	2	71	104	699
2	1545	212	0.7	0.8	0.6	2	3	85	1434	1084
	2420	198	0.8	0.8	0.6	2	3	98	1441	1154
	2620	248	1.0	1.2	0.8	3	4	97	1790	1635
	2820	268	1.3	1.7	1.2	3	5	107	2009	2008
	3020	278	1.6	2.1	1.5	3	6	120	2205	2129
3	3055	287	1.7	2.2	1.6	3	7	124	2261	2161
	4105	275	1.6	2.2	1.6	3	7	134	2239	2177
	4305	317	1.9	2.6	1.9	4	8	179	2448	2408
	4505	339	2.4	3.1	2.2	4	7	2750	2686	2621
4	4660	361	2.7	3.5	2.4	4	9	3340	2924	2884
	5700	341	2.8	3.5	2.5	5	11	3812	2875	2901
	5900	366	3.1	4.0	2.9	5	13	4224	3085	3093
	6100	394	3.6	4.5	3.4	5	16	4556	3314	3273
	6300	418	4.0	5.0	3.8	5	18	5200	3586	3549
	6500	430	4.6	5.5	4.2	6	47	5127	3744	3736
5	6545	437	4.8	5.6	4.2	7	57	5197	3804	3786
	7735	421	4.7	5.6	4.3	7	77	5154	3756	3811
	7935	457	5.1	6.1	4.7	8	94	5442	4031	4045
	8135	483	5.6	6.6	5.1	9	174	5715	4306	4316
	8335	503	6.1	7.1	5.5	12	743	5977	4526	4580
6	8405	512	6.3	7.2	5.7	12	817	6092	4630	4714
	9480	495	6.3	7.3	5.6	13	948	6057	4582	4771
	9680	537	6.8	7.7	6.1	14	1022	6417	4907	5058
	9880	562	7.2	8.2	6.6	14	1205	6734	5183	5352
7	10075	587	7.6	8.7	6.9	15	1455	7072	5479	5671
	11275	570	7.7	8.8	7.0	16	1646	7064	5425	5722
	11475	610	8.1	9.2	7.3	17	1735	7446	5745	6002
	11675	638	8.5	9.7	7.7	18	2027	7784	6042	6330
8	11870	662	9.0	10.2	8.2	19	2368	8144	6320	6640
	13245	645	9.0	10.2	8.1	23	2615	8171	6255	6698
	13445	684	9.4	10.7	8.5	24	2746	8553	6578	6980
	13645	712	9.9	11.2	8.8	26	3055	8905	6875	7309
	13845	737	10.6	11.7	9.3	30	3427	9262	7146	7641
9	13850	737	10.5	11.7	9.4	30	3437	9270	7152	7649
	14460	723	10.5	11.7	9.3	34	3642	9304	7092	7700
	14660	760	11.0	12.2	9.8	36	3827	9684	7404	7998
	14860	785	11.6	12.7	10.3	40	4155	10056	7661	8327
Failure	15035	799	12.4	13.1	10.4	44	4428	10413	7832	8560

Table C-6 continued,

		Middle Strain Gauges			Top Strain Gauges			Rosette shear span B		
Load Stage	Load, P	6	10	14	8	11	16	ε_{xx}	ε_{yy}	γ_{xy}
(#)	(kN)	(με)	(με)	(με)	(με)	(με)	(με)	με	με	με
	13	0	0	0	0	0	0	1	0	-1
	31	1	3	8	2	2	6	1	-1	2
	41	2	6	14	3	4	12	1	-1	0
	80	4	15	39	6	10	33	1	-1	15
1	111	7	24	73	9	16	77	1	-1	27
	103	7	26	81	8	17	86	6	-2	26
	175	13	49	332	15	34	163	14	-1	49
2	212	17	61	574	19	44	298	33	-2	69
	198	17	65	642	17	45	340	39	0	75
	248	22	78	958	21	59	533	45	0	78
	268	24	87	1463	23	62	1049	46	0	81
	278	26	100	1599	24	69	1184	46	1	89
3	287	27	103	1625	25	71	1204	46	1	89
	275	27	111	1641	24	73	1233	58	0	85
	317	31	144	1824	28	88	1376	57	-1	83
	339	33	2071	2006	31	1972	1518	59	0	81
4	361	36	2313	2241	34	2677	1708	59	0	79
	341	37	2684	2255	32	2996	1743	61	2	82
	366	40	3230	2419	35	3346	1861	627	902	768
	394	43	3566	2593	38	3610	1984	1417	2175	1489
	418	47	4299	2839	41	3918	2180	1767	2805	1849
	430	66	4657	2994	46	3890	2317	2079	3354	2125
5	437	72	4727	3038	46	3928	2351	2130	3444	2175
	421	84	4692	3049	45	3864	2389	2165	3601	2242
	457	95	4984	3253	49	4061	2537	2645	4472	2787
	483	138	5229	3490	53	4209	2727	3045	5264	3387
	503	460	5406	3714	53	4335	2913	3251	5712	3693
6	512	513	5500	3815	55	4403	2994	3333	5908	3839
	495	617	5455	3832	57	4355	3045	3345	6044	3923
	537	670	5791	4078	62	4594	3218	3618	6560	4294
	562	828	6071	4325	71	4797	3420	3973	7416	4955
7	587	1082	6368	4594	85	5003	3635	4245	8024	5419
	570	1283	6324	4605	98	4956	3688	4265	8156	5475
	610	1365	6670	4848	106	5206	3863	4470	8604	5822
	638	1660	6969	5118	136	5429	4101	4719	9144	6281
8	662	2040	7229	5370	191	5633	4336	4968	9736	6712
	645	2287	7182	5372	260	5555	4392	4976	9988	6660
	684	2405	7517	5617	275	5808	4578	5193	10344	7151
	712	2674	7816	5877	330	6051	4824	5422	10880	7546
	737	2998	8103	6126	463	6274	5066	5631	11436	7973
9	737	3006	8110	6132	467	6279	5072	5635	11448	7981
	723	3169	8092	6128	589	6229	5107	5639	11552	8009
	760	3325	8431	6376	628	6501	5307	5839	12028	8373
	785	3587	8780	6623	769	6733	5532	6044	12528	8732
Failure	799	3812	9171	6784	995	6913	5692	6149	12876	9007

C.9 Specimen B3N

The displacement rate of specimen B3N was 0.2 mm/min of machine stroke. The main diagonal cracks in both shear spans propagated towards the loading plates and become more horizontal at approximately 100 mm from the top of the specimen. Both cracks advanced underneath the loading plate towards the mid-span. Shear compression failure occurred near the inside edge of loading plate A. No additional crushing of the flexural compression region was observed. Failure of specimen B3N occurred with no warning and resulted in an immediate loss in load carrying ability.

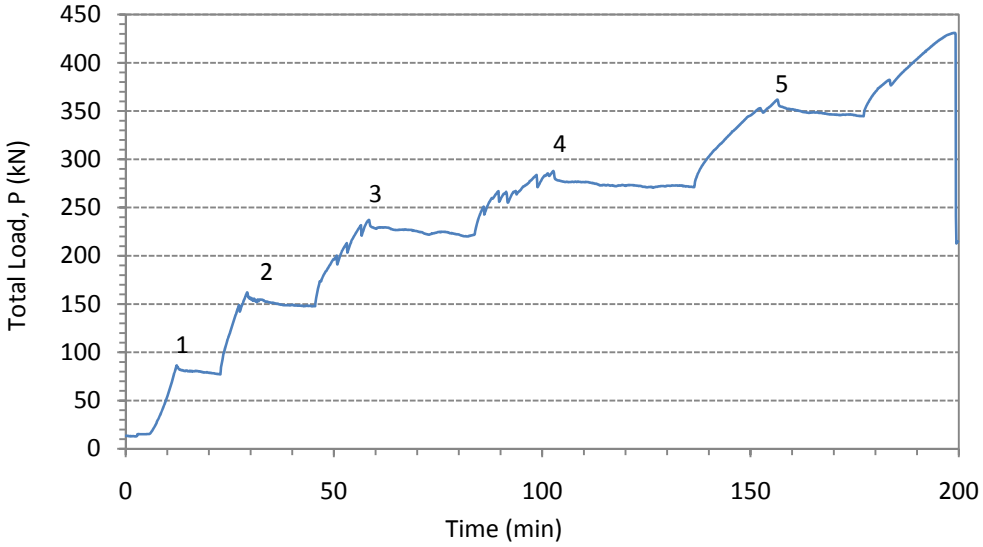

Figure C-70: Load – history of specimen B3N.

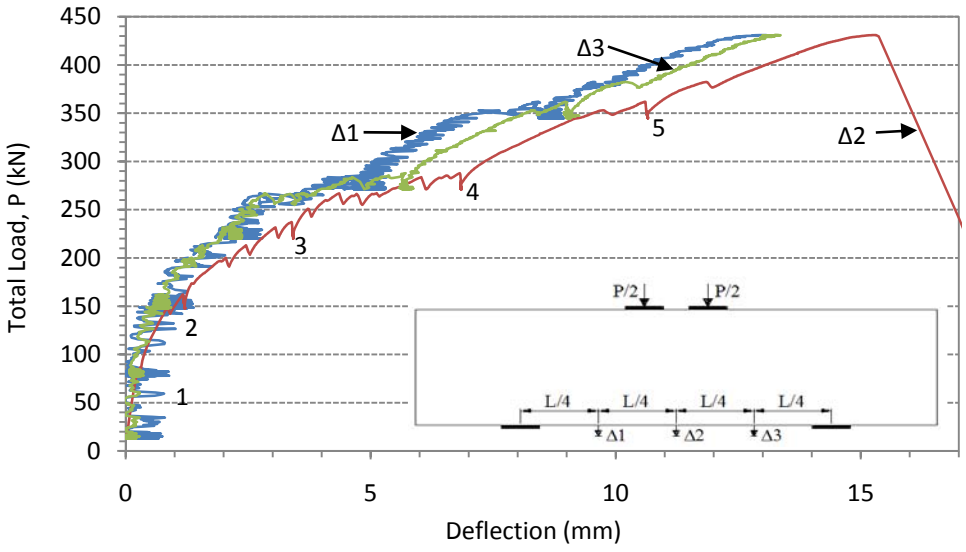

Figure C-71: Load – displacement response of specimen B3N. Measured deflections at the quarter-spans (Δ_1 and Δ_3) contained signal noise.

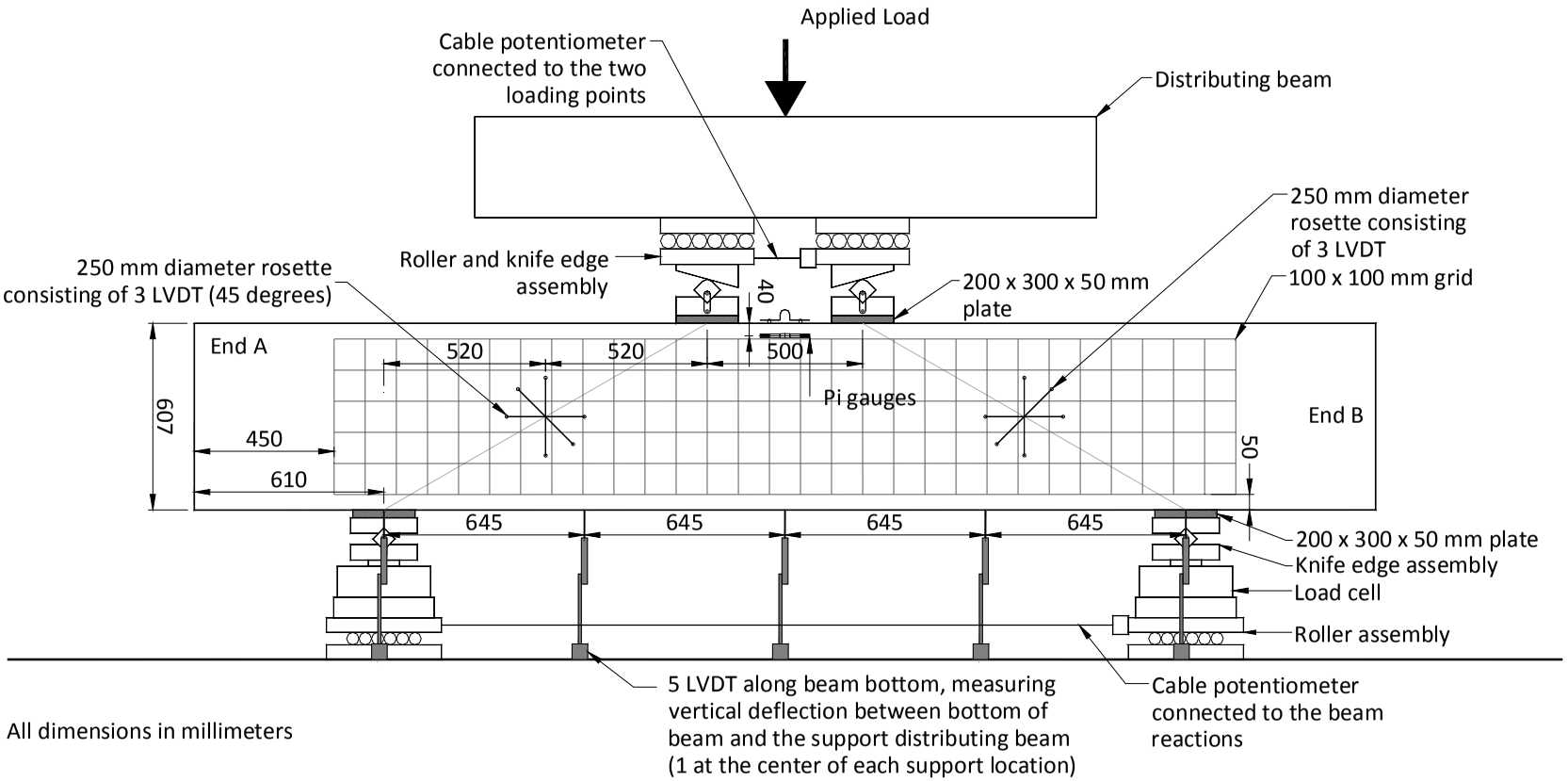

Figure C-72: Instrumentation drawing for specimen B3N.

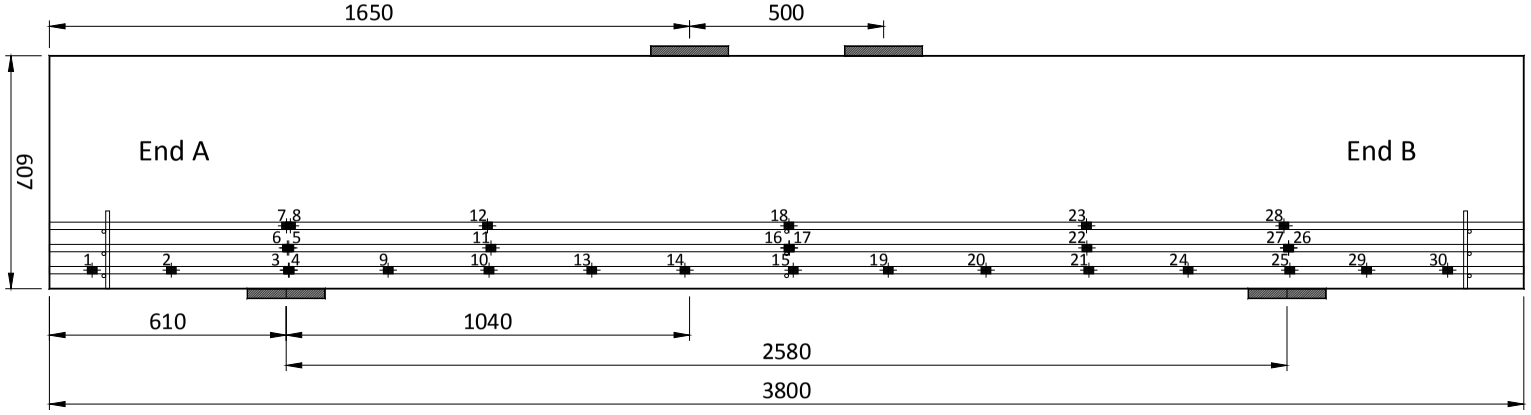

Strain Gauge Locations

Strain Gauge No.	Row	Column	Distance from End A (mm)	Strain Gauge No.	Row	Column	Distance from End A (mm)
1	B	F	110	16	M	F	1906
2	B	F	314	17	M	B	1907
3	B	C	616	18	T	C	1906
4	B	F	618	19	B	C	2162
5	M	F	617	20	B	C	2414
6	M	B	613	21	B	C	2679
7	T	C	611	22	M	F	2674
8	T	F	610	23	T	C	2673
9	B	C	873	24	B	F	2935
10	B	C	1133	25	B	C	3197
11	M	F	1138	26	M	F	3194
12	T	C	1129	27	M	B	3194
13	B	C	1398	28	T	F	3182
14	B	C	1638	29	B	F	3395
15	B	C	1917	30	B	F	3604

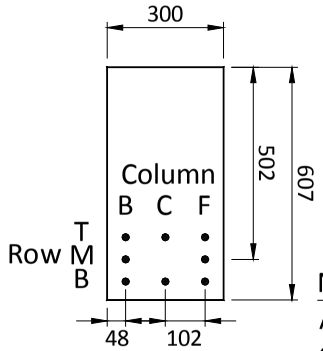

(8) - #6 GFRP Bars

Notes:
All dimensions in mm
Clear Cover: 38.1 mm
Concrete Strength: 41 MPa
Bar Length: 3800 mm

Figure C-73: Location of the strain gauges for specimen B3N (as-built).

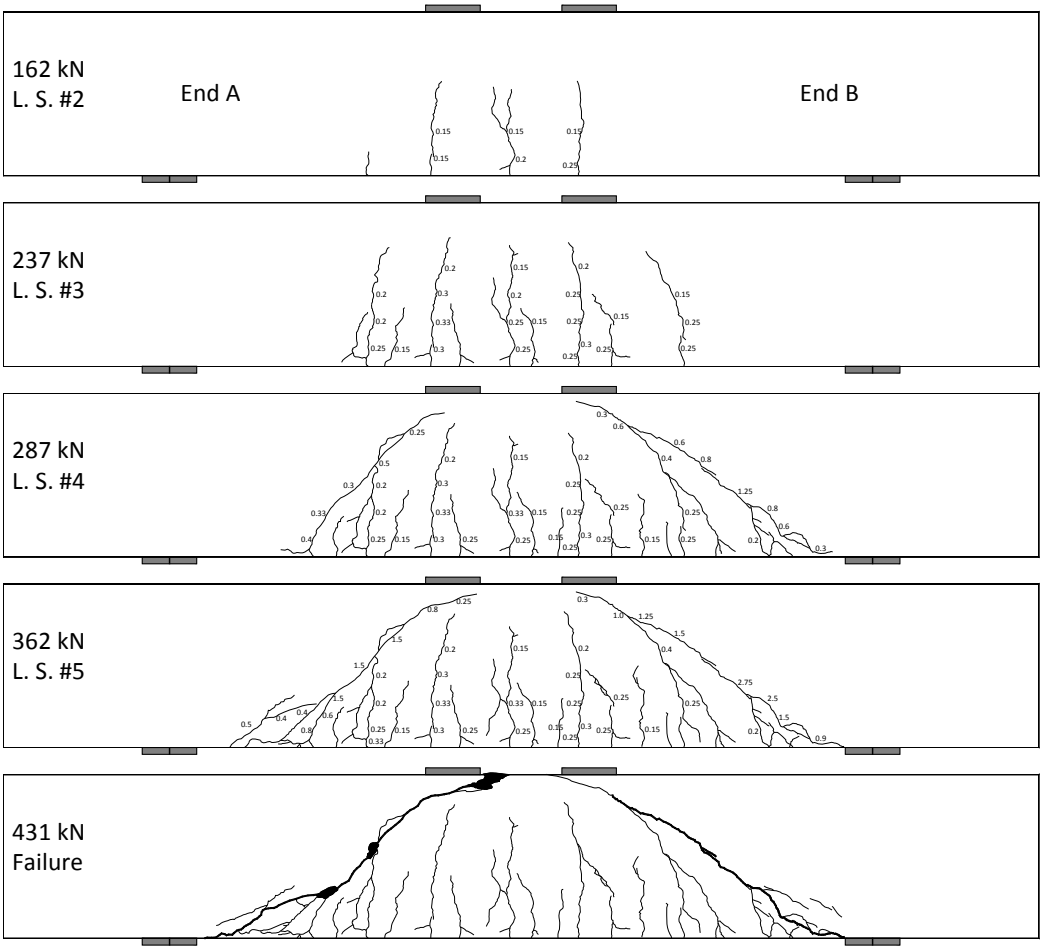

Figure C-74: Crack diagrams of specimen B3N showing the development of the cracks and the widths as loading progressed.

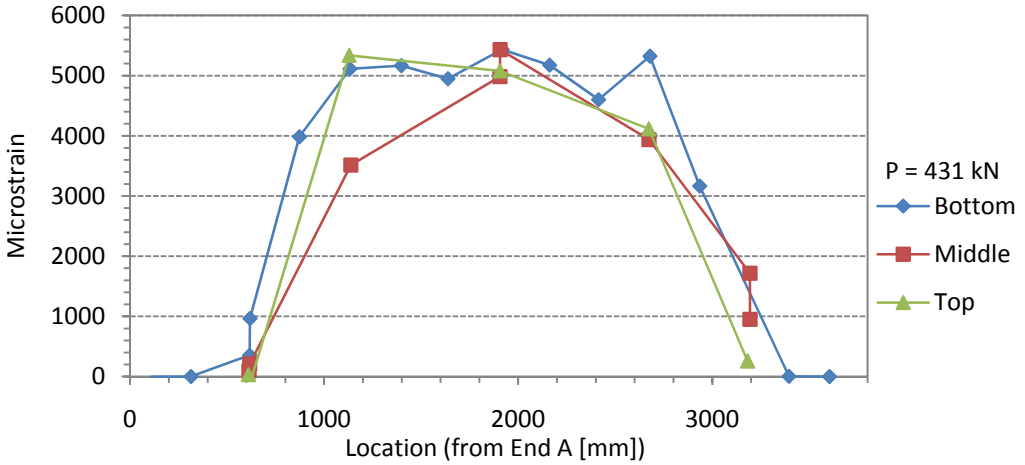

Figure C-75: Strain distribution in the bottom, middle, and top reinforcement at peak load.

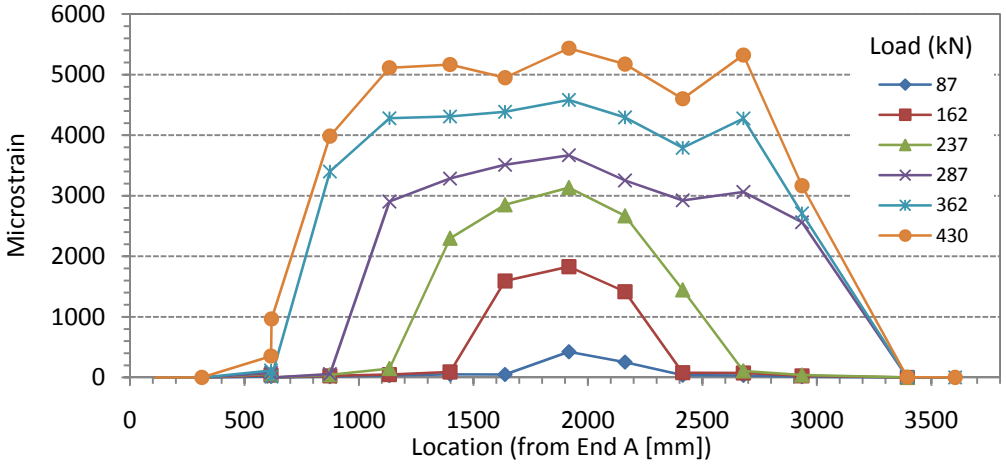

Figure C-76: Strain in the bottom reinforcement layer as loading progressed.

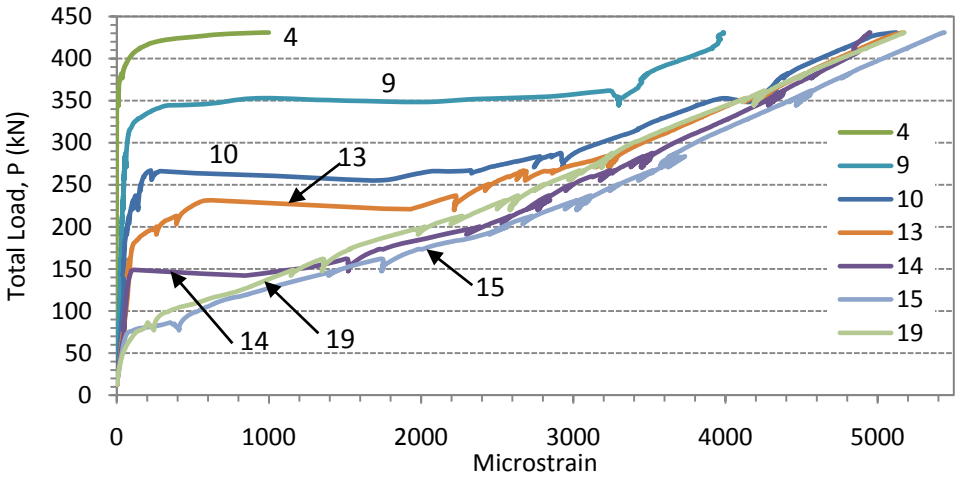

Figure C-77: Strain in the bottom reinforcement layer.

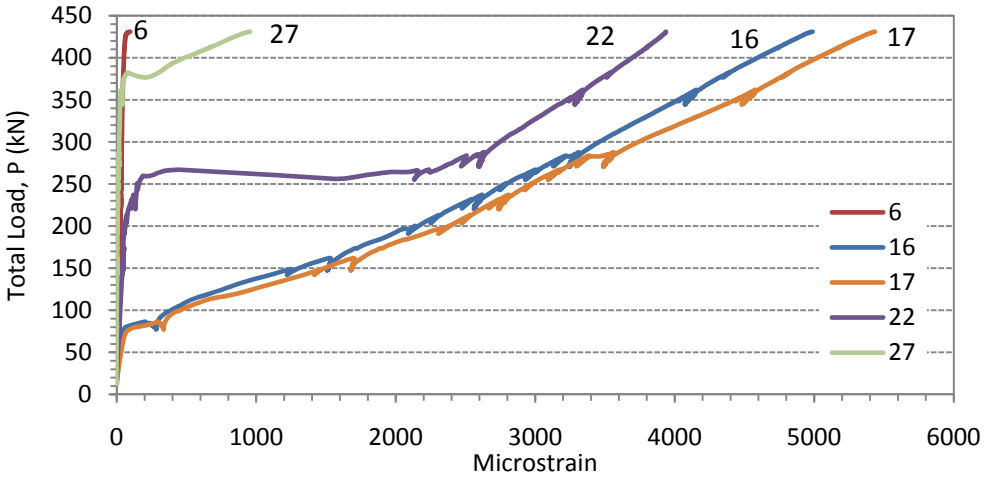

Figure C-78: Strain in the middle reinforcement layer.

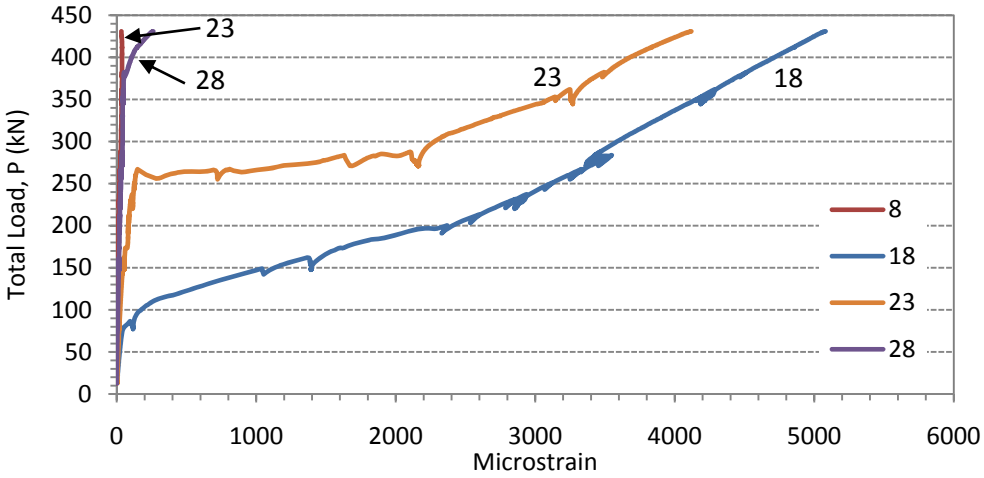

Figure C-79: Strain in the top reinforcement layer.

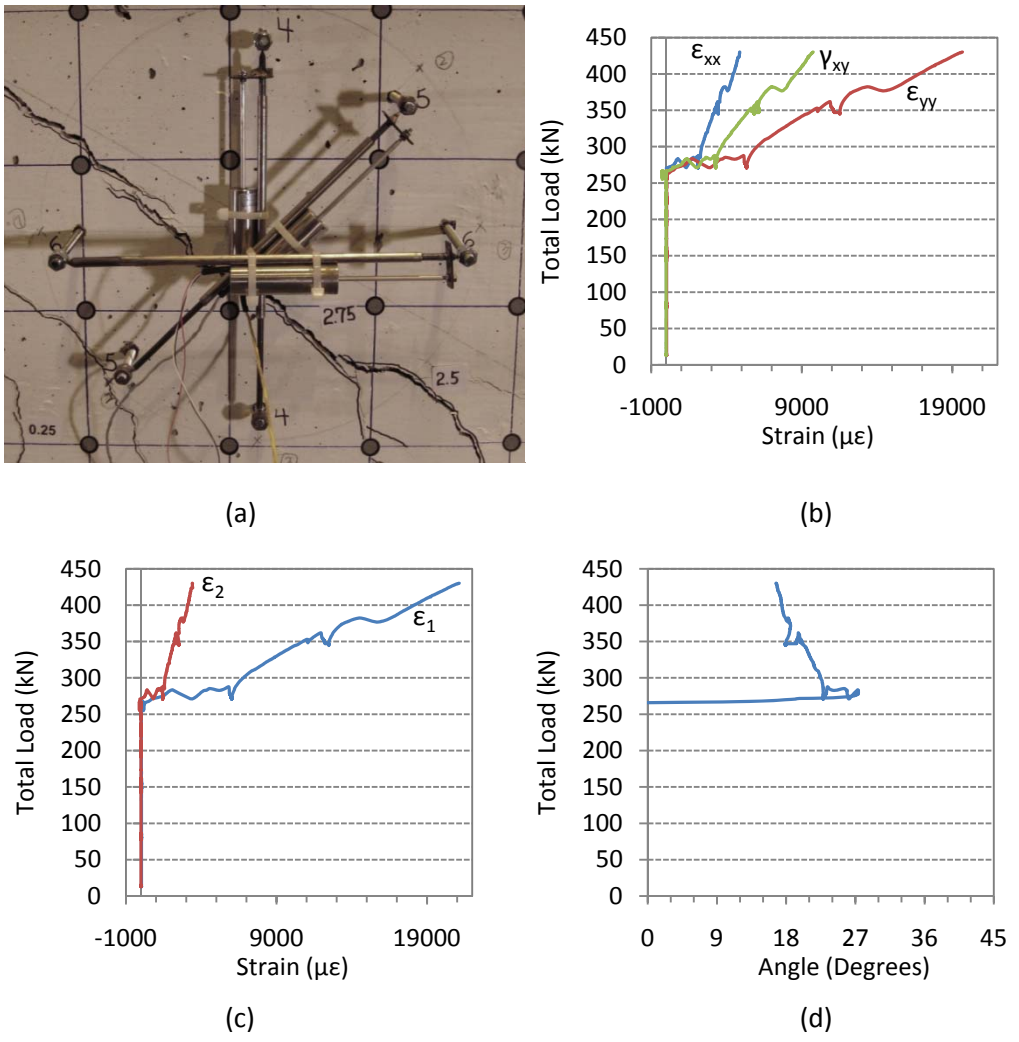

Figure C-80: (a) crack location through the rosette in shear span B at failure, (b) strain components, (c) principal strains, and (d) the direction of the minimum principal strain (angle of inclination from a horizontal line towards mid-span).

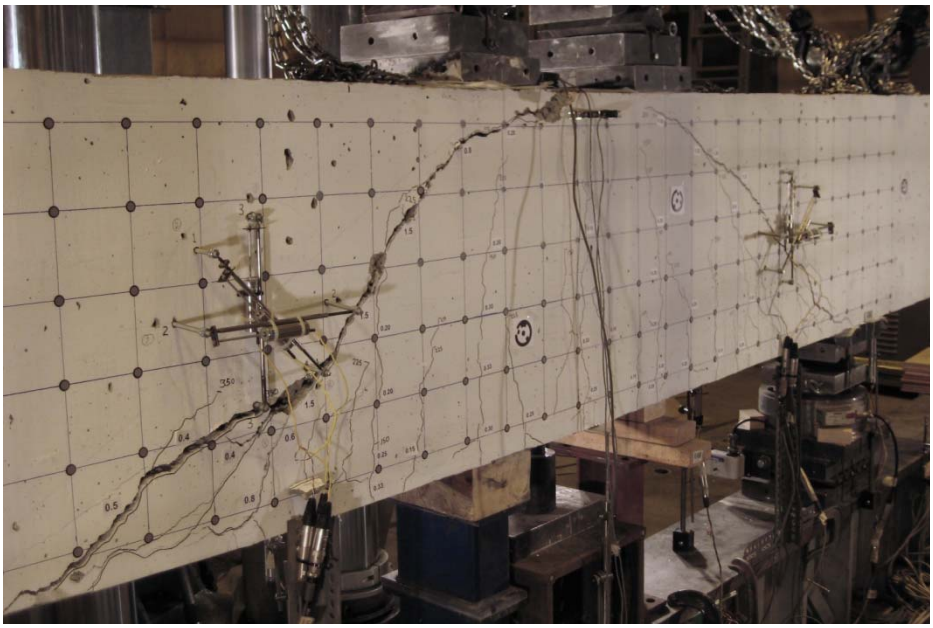

Figure C-81: Specimen B3N after failure. Failure surface is in shear span A (left).

Table C-7: Subset of the collected data for specimen B3N.

			Displacements			Bottom Strain Gauges						
Load Stage	Time	Load, P	End A 1/4 Span	Mid-Span	End B 1/4 Span	2	4	9	10	13	14	15
(#)	(s)	(kN)	(mm)	(mm)	(mm)	(με)	(με)	(με)	(με)	(με)	(με)	(με)
	0	13	0.0	0.0	0.0	-2	-2	2	2	2	2	1
	150	13	0.3	0.0	0.2	-2	-2	2	3	2	2	1
	300	15	0.0	0.0	0.0	-2	-2	2	3	2	2	2
	450	28	0.6	0.1	0.2	-2	-2	4	8	10	11	12
	600	54	-0.1	0.1	0.0	-2	-2	8	19	26	31	38
1	735	86	0.1	0.3	0.1	-2	-3	14	32	49	49	351
	1360	77	0.4	0.3	0.2	-2	-2	13	30	49	45	409
	1510	122	0.3	0.6	0.3	-2	-2	19	45	73	67	898
	1660	146	0.4	0.9	0.5	-2	-2	23	42	69	993	1421
2	1755	162	0.5	1.2	0.7	-2	-2	26	48	83	1518	1749
	2730	148	0.5	1.2	0.6	-2	-2	25	44	85	1521	1739
	2880	184	0.8	1.6	1.0	-2	-2	30	54	129	1958	2226
	3030	199	1.3	2.0	1.4	-2	-2	33	67	254	2357	2551
	3180	213	1.7	2.4	1.6	-2	-2	36	80	385	2580	2722
	3330	225	2.2	2.9	2.0	-2	-2	39	98	499	2757	2921
	3480	236	2.5	3.3	2.3	-2	-2	42	119	2188	2817	3087
3	3505	237	2.6	3.4	2.3	-2	-2	42	124	2229	2840	3115
	4960	221	2.4	3.4	2.2	-2	-1	41	140	2216	2765	3022
	5110	244	2.3	3.6	2.3	-2	-1	45	151	2363	2916	3214
	5260	258	2.4	4.0	2.6	-2	-1	48	173	2550	3091	3399
	5410	260	3.0	4.5	3.2	-2	-1	49	240	2642	3197	3460
	5560	263	3.5	5.0	3.5	-2	-1	48	1974	2764	3232	3494
	5710	270	3.6	5.4	3.9	-2	-1	51	2441	2938	3309	3574
	5860	280	4.5	5.9	4.5	-2	-1	53	2679	3143	3412	3686
	6010	281	4.5	6.3	5.1	-2	-1	54	2790	3203	3445	3701
	6160	288	5.3	6.8	5.7	-2	-1	57	2918	3293	3519	3676
4	6160	288	5.3	6.8	5.7	-2	-1	57	2918	3293	3519	3676
	8190	271	5.2	6.8	5.7	-2	-1	61	2933	3232	3446	3572
	8340	297	5.5	7.2	6.1	-2	0	67	3134	3423	3635	3773
	8490	310	5.5	7.7	6.4	-1	0	77	3347	3592	3788	3919
	8640	321	6.1	8.2	6.9	-1	1	104	3482	3729	3929	4056
	8790	332	6.3	8.6	7.6	-1	0	173	3630	3860	4059	4193
	8940	343	6.6	9.1	7.8	-1	1	297	3793	3997	4184	4329
	9090	351	7.5	9.6	8.2	-1	1	785	3928	4102	4278	4434
	9240	352	7.8	10.1	8.5	-1	4	2441	4218	4171	4291	4454
	9390	362	8.4	10.6	9.0	-1	9	3243	4335	4299	4384	4566
5	9390	362	8.4	10.6	9.0	-1	9	3243	4335	4299	4384	4566
	10630	345	8.6	10.7	9.1	-1	13	3299	4187	4199	4281	4464
	10780	368	9.2	11.1	9.4	-1	14	3433	4314	4366	4444	4642
	10930	379	9.4	11.6	9.9	0	26	3465	4372	4482	4564	4772
	11080	381	9.8	12.2	10.7	0	39	3483	4410	4522	4598	4806
	11230	393	10.3	12.7	11.1	0	59	3620	4530	4649	4716	4940
	11380	403	10.8	13.2	11.6	0	92	3777	4655	4771	4821	5068
	11530	413	11.2	13.7	12.1	0	155	3917	4785	4898	4848	5198
	11680	421	12.0	14.2	12.5	0	297	3958	4896	5006	4887	5308
	11830	429	12.5	14.8	13.0	1	659	3966	5008	5112	4932	5399
Failure	11935	431	13.0	15.3	13.3	1	999	3988	5124	5172	4951	5439

Table C-7 continued,

		Middle Strain Gauges			Top Strain Gauges			Rosette shear span B		
Load Stage (#)	Load, P (kN)	6 (με)	16 (με)	22 (με)	18 (με)	23 (με)	28 (με)	ε_{xx} με	ε_{yy} με	γ_{xy} με
	13	-1	0	-1	2	3	-2	2	21	-18
	13	-1	0	-1	2	3	-2	2	21	-19
	15	-1	0	-1	3	3	-1	2	20	-19
	28	1	8	3	9	6	0	1	21	-19
	54	5	25	10	24	12	3	2	21	-20
1	86	10	202	20	96	20	7	1	21	-19
	77	9	284	20	118	20	7	2	20	-19
	122	15	704	31	485	32	11	2	19	-19
	146	18	1253	41	1081	42	14	2	19	-20
2	162	21	1533	47	1379	52	16	2	19	-18
	148	19	1510	45	1393	54	16	1	19	-17
	184	23	1872	48	1824	81	19	2	17	-13
	199	25	2126	58	2343	83	21	2	17	-14
	213	27	2302	71	2585	87	23	2	15	-13
	225	29	2456	94	2761	96	24	3	18	-17
	236	30	2595	118	2912	107	26	2	17	-15
3	237	30	2619	121	2938	111	26	2	17	-14
	221	29	2561	134	2852	115	26	2	17	-14
	244	31	2719	143	3033	122	29	2	17	-15
	258	33	2884	181	3213	134	30	2	16	-15
	260	33	2952	1767	3274	358	31	2	18	-180
	263	33	2987	2181	3307	757	31	1	71	-280
	270	33	3058	2340	3383	1164	33	3	605	458
	280	34	3167	2454	3497	1539	35	644	1456	1149
	281	34	3201	2546	3522	1804	38	1604	3479	2383
	288	35	3313	2631	3464	2104	40	2118	5129	3202
4	288	35	3313	2631	3464	2104	40	2118	5129	3202
	271	34	3244	2594	3364	2165	40	2124	5353	3289
	297	36	3430	2723	3559	2253	42	2327	5898	3598
	310	37	3569	2837	3696	2398	43	2517	6616	3969
	321	38	3694	2944	3819	2584	43	2741	7424	4366
	332	39	3818	3047	3941	2768	42	2885	8224	4803
	343	40	3941	3148	4066	2973	42	3071	9082	5218
	351	42	4035	3235	4164	3111	43	3222	9804	5530
	352	42	4058	3264	4185	3163	44	3265	10204	5741
	362	43	4156	3341	4288	3249	46	3416	10878	6077
5	362	43	4156	3341	4288	3249	46	3416	10878	6077
	345	42	4074	3283	4185	3269	47	3453	11533	5851
	368	44	4233	3405	4356	3354	49	3573	11961	6329
	379	47	4346	3504	4473	3450	52	3704	12788	6767
	381	48	4385	3540	4507	3512	69	4179	15196	7981
	393	50	4509	3631	4631	3604	91	4363	16192	8309
	403	52	4626	3719	4745	3713	114	4518	17043	8699
	413	55	4748	3803	4862	3840	149	4649	17894	9082
	421	60	4853	3872	4961	3966	198	4741	18773	9391
	429	70	4944	3926	5043	4072	239	4865	19459	9670
Failure	431	96	4988	3937	5081	4119	261	4873	19839	9811

C.10 Specimen B4N

The displacement rate of specimen B4N was 0.15 mm/min of machine stroke. The main diagonal cracks in both shear spans coincided with the diagonal line between the center of the loading and support plates. At approximately 50 mm from the top surface, both diagonal cracks deviated from the diagonal line towards a more horizontal trajectory. At load stage 8 (P = 812 kN) a small vertical crack had formed from the tip of the main diagonal crack in shear span B to the inside edge of the loading plate B. Failure occurred when the main diagonal crack in shear span B penetrated to the inside and outside edge of the loading plate B producing a triangular shaped piece of concrete immediately below the plate. Load carrying capacity of specimen B4N deteriorated and sliding occurred along the diagonal crack in shear span B.

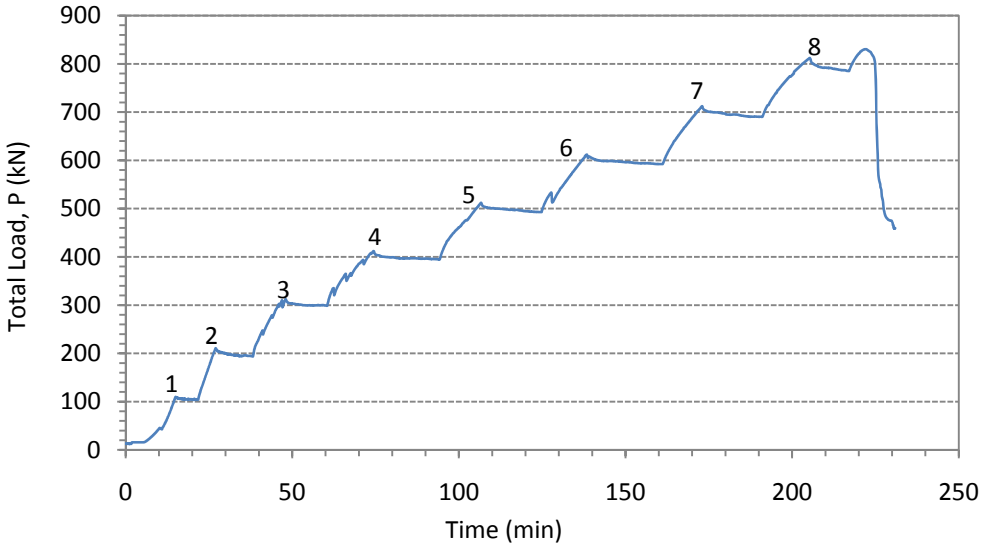

Figure C-82: Load – history of specimen B4N.

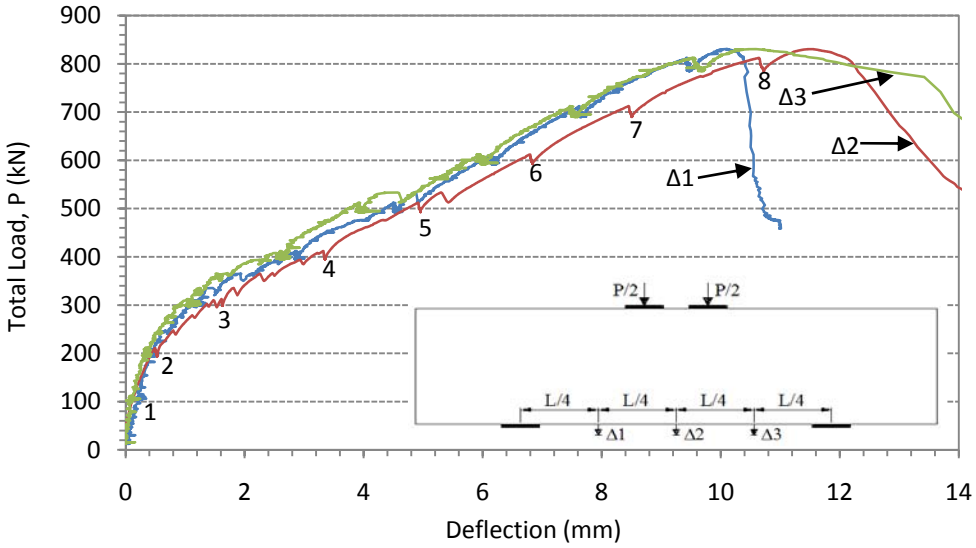

Figure C-83: Load – displacement response of specimen B4N.

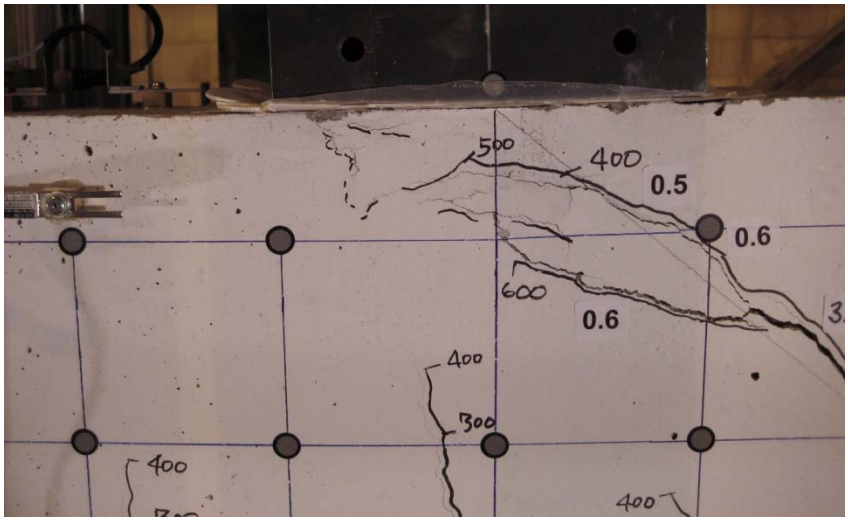

Figure C-84: Cracks beneath loading plate B at load stage 8 (P= 812 kN).

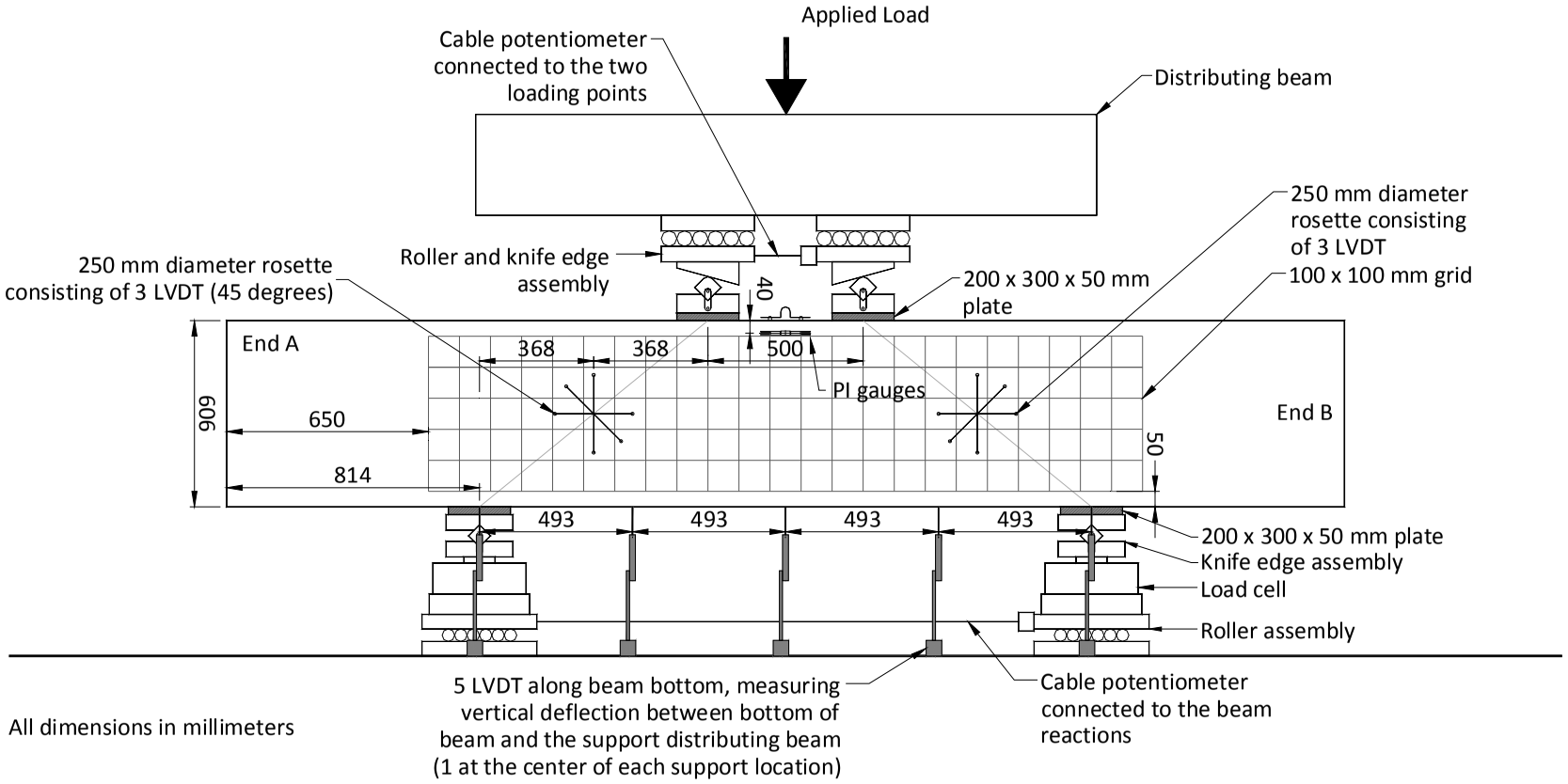

Figure C-85: Instrumentation drawing for specimen B4N.

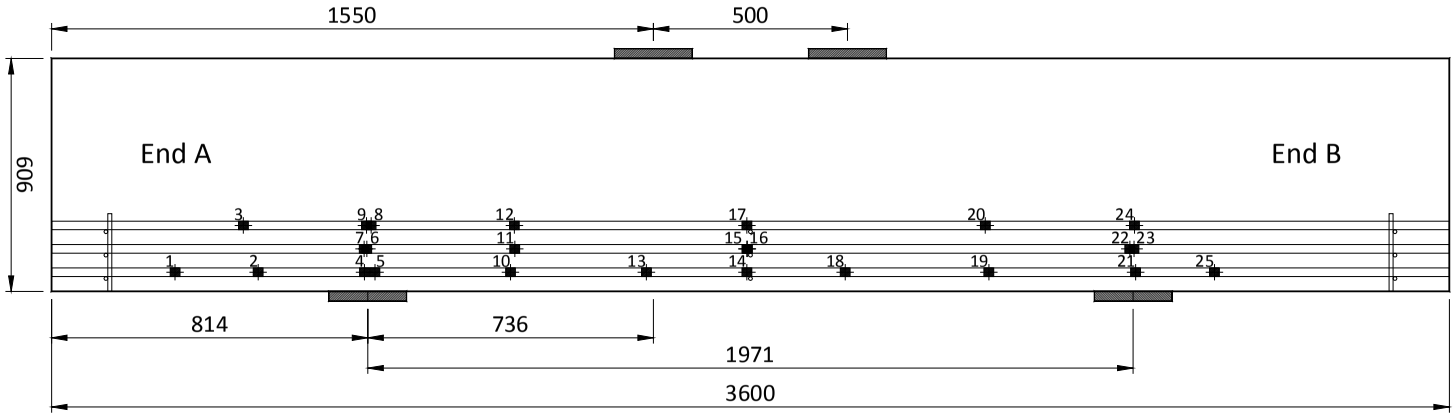

Strain Gauge Locations

Strain Gauge No.	Row	Column	Distance from End A (mm)	Strain Gauge No.	Row	Column	Distance from End A (mm)
1	B	C	318	14	B	C	1791
2	B	B	532	15	M	F	1791
3	T	C	494	16	M	B	1792
4	B	C	806	17	T	C	1791
5	B	B	833	18	B	C	2044
6	M	F	812	19	B	C	2414
7	M	B	805	20	T	F	2405
8	T	F	823	21	B	C	2792
9	T	C	811	22	M	B	2777
10	B	B	1182	23	M	F	2788
11	M	B	1193	24	T	B	2789
12	T	C	1192	25	B	C	2995
13	B	B	1532				

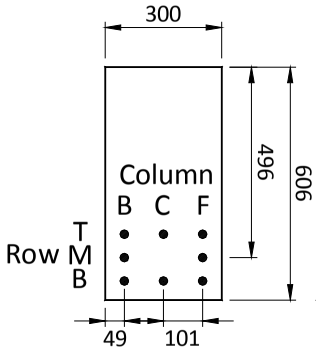

(8) - #7 GFRP Bars

Notes:
All dimensions in mm
Clear Cover: 38.1 mm
Concrete Strength: 41 MPa
Bar Length: 3600 mm

Figure C-86: Location of the strain gauges for specimen B4N (as-built).

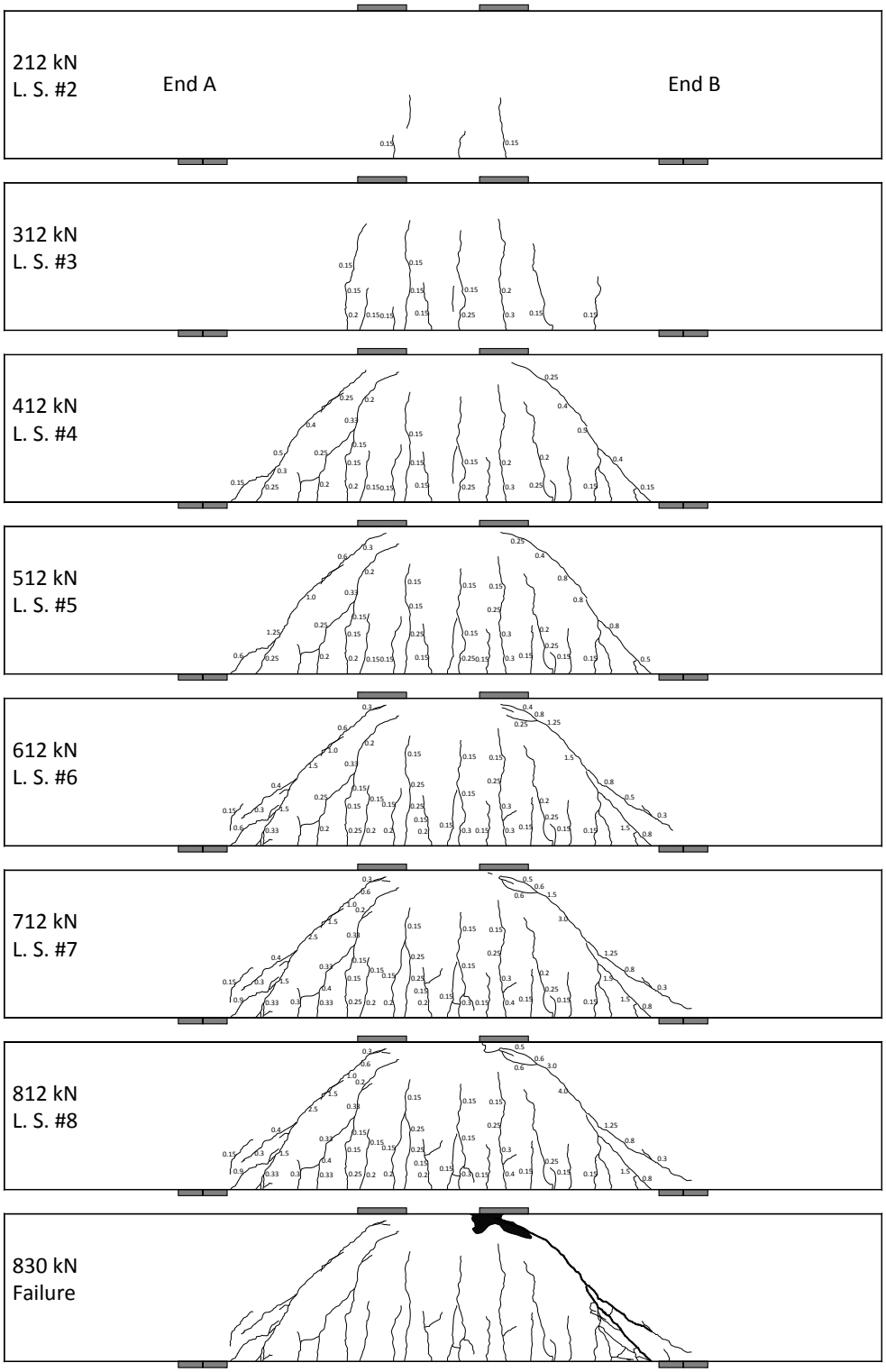

Figure C-87: Crack diagrams of specimen B4N showing the development of the cracks and the widths as loading progressed.

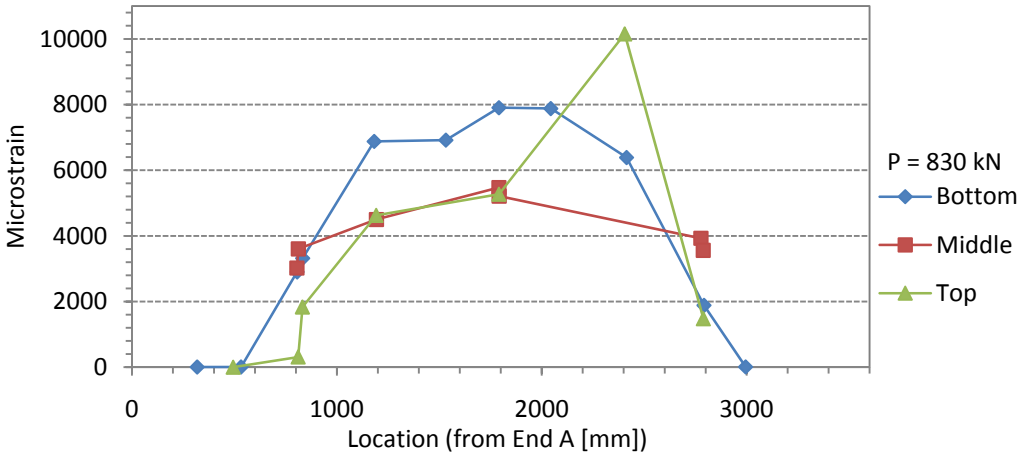

Figure C-88: Strain distribution in the bottom, middle, and top reinforcement at peak load.

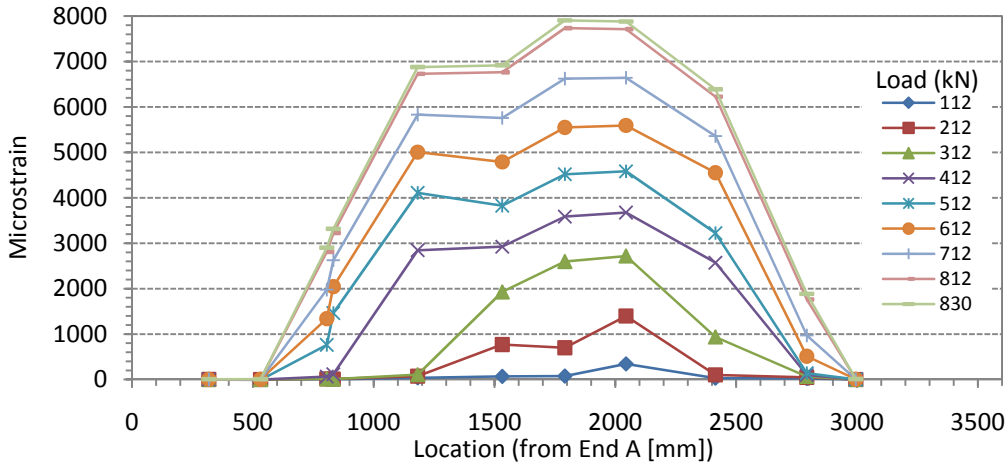

Figure C-89: Strain in the bottom reinforcement layer as loading progressed.

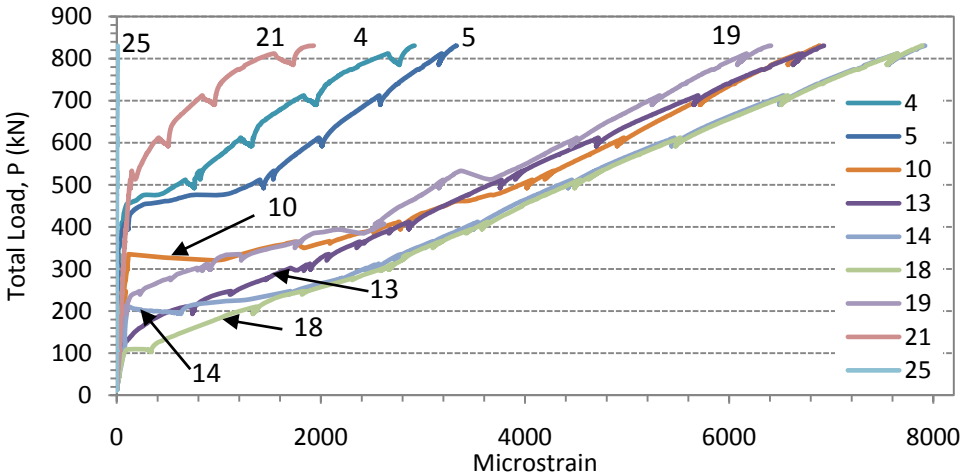

Figure C-90: Strain in the bottom reinforcement layer.

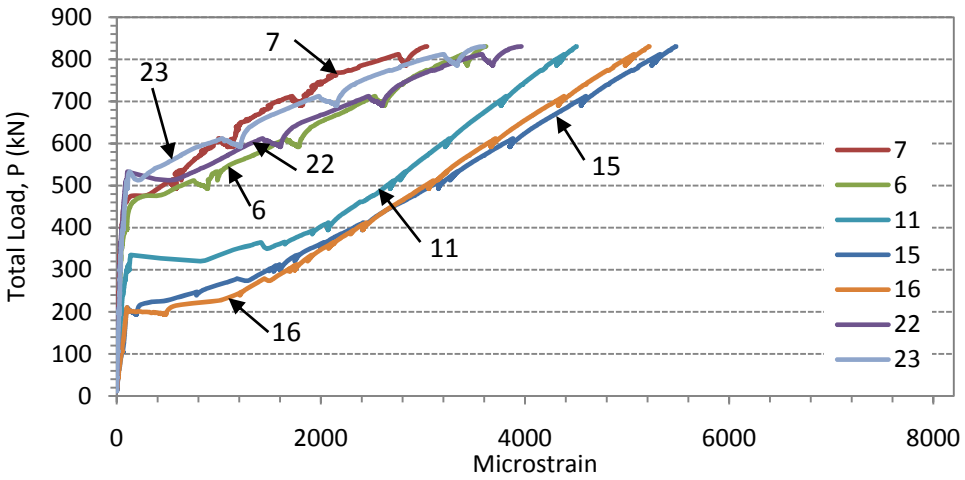

Figure C-91: Strain in the middle reinforcement layer.

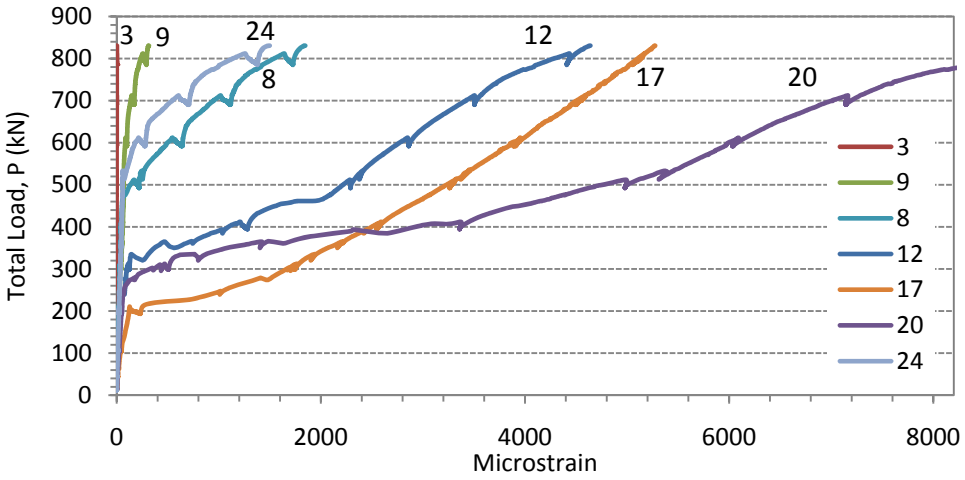

Figure C-92: Strain in the top reinforcement layer.

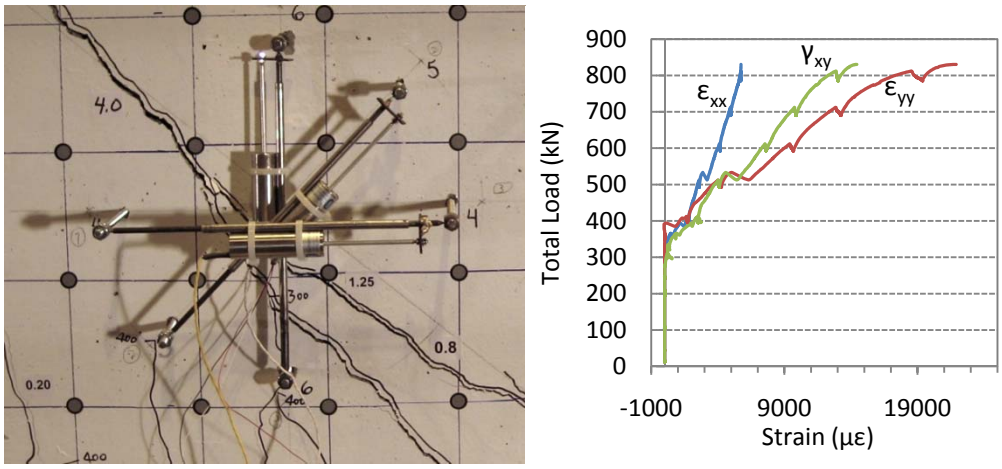

(a) (b)

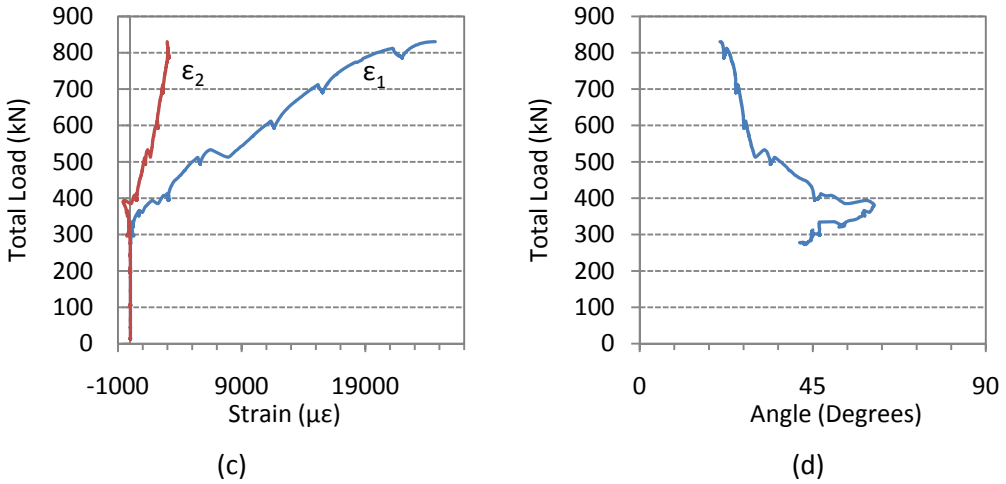

Figure C-93: (a) crack location through the rosette in shear span B at P= 812 kN, (b) strain components, (c) principal strains, and (d) the direction of the minimum principal strain (angle of inclination from a horizontal line towards mid-span).

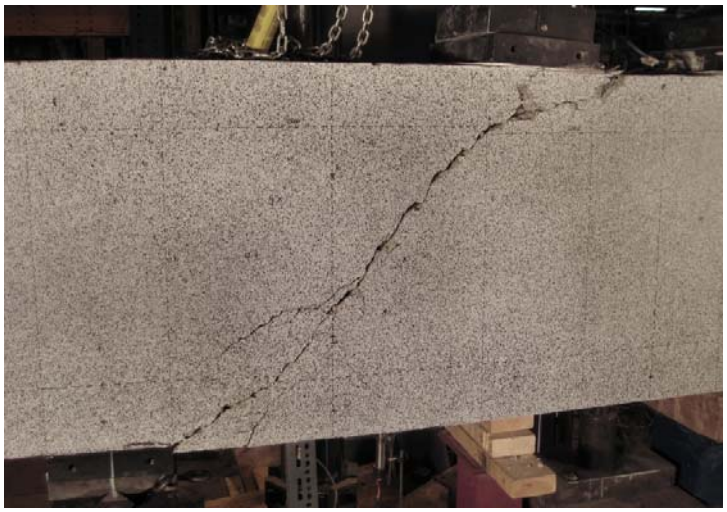

Figure C-94: Back side of specimen B4N showing the failure surface in shear span B.

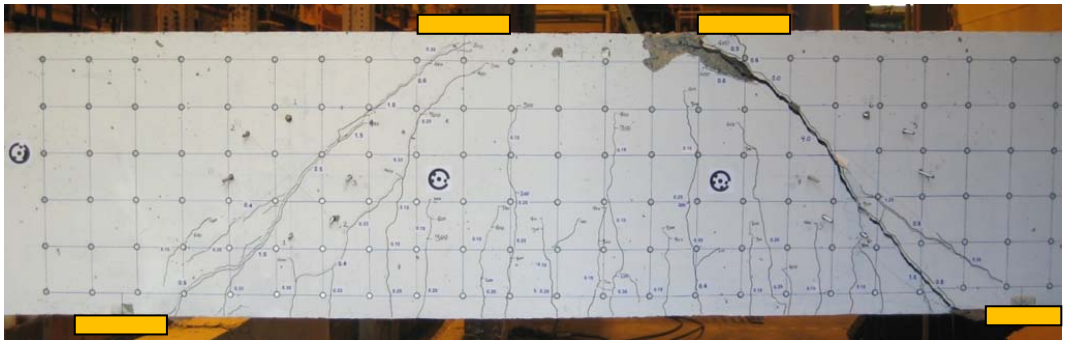

Figure C-95: Specimen B4N after testing, end A on left, end B on right.

Table C-8: Subset of the collected data for specimen B4N.

			Displacements			Bottom Strain Gauges					
Load Stage	Time	Load, P	End A 1/4 Span	Mid-Span	End B 1/4 Span	5	10	13	14	18	25
(#)	(s)	(kN)	(mm)	(mm)	(mm)	(με)	(με)	(με)	(με)	(με)	(με)
	0	13	0.0	0.0	0.0	0	0	0	0	0	0
	200	16	0.0	0.0	0.0	0	0	1	1	1	0
	400	21	0.1	0.0	0.0	1	2	4	4	5	0
	600	44	0.1	0.0	0.1	2	11	18	22	20	0
	800	79	0.1	0.1	0.2	4	24	42	50	48	0
1	900	110	0.3	0.1	0.1	6	36	65	76	180	1
	1300	104	0.2	0.1	0.1	5	35	65	72	338	0
	1500	172	0.3	0.3	0.2	9	56	303	86	893	1
2	1620	211	0.4	0.5	0.4	11	70	675	120	1364	1
	2290	194	0.4	0.5	0.4	10	68	742	630	1335	0
	2490	244	0.7	0.9	0.5	11	67	1142	1714	1844	0
	2690	287	1.0	1.2	0.8	14	93	1545	2298	2429	1
3	2880	312	1.2	1.6	1.0	13	107	1892	2567	2705	1
	3625	299	1.2	1.6	1.1	8	102	1898	2553	2665	0
	3825	340	1.6	2.0	1.4	9	1295	2153	2839	2921	0
	4025	361	2.0	2.4	1.6	25	1999	2396	3072	3154	1
	4225	388	2.4	2.8	2.0	50	2427	2627	3312	3403	1
	4425	407	2.8	3.2	2.6	81	2717	2822	3494	3592	1
4	4465	412	2.8	3.3	2.6	91	2767	2866	3538	3634	1
	5655	395	2.9	3.4	2.7	114	2779	2862	3497	3578	1
	5855	443	3.3	3.7	2.9	184	3123	3139	3813	3921	1
	6055	468	3.7	4.2	3.3	601	3532	3360	4030	4124	1
	6255	492	4.3	4.6	3.7	1232	3873	3575	4255	4350	2
5	6400	512	4.5	4.9	3.9	1401	4070	3768	4458	4541	2
	7490	493	4.6	5.0	4.0	1439	4018	3756	4422	4486	2
	7690	514	4.9	5.4	4.6	1533	4195	3905	4568	4627	3
	7890	550	5.3	5.9	5.1	1640	4440	4126	4838	4905	3
	8090	581	5.8	6.3	5.6	1802	4706	4416	5142	5206	4
	8290	611	6.2	6.8	5.9	1971	4957	4707	5447	5510	4
6	8300	612	6.1	6.8	6.0	1979	4968	4716	5461	5521	4
	9660	592	6.2	6.8	6.0	2011	4901	4701	5436	5477	5
	9860	636	6.6	7.2	6.4	2130	5181	4963	5746	5799	5
	10060	668	6.9	7.7	6.8	2307	5437	5261	6057	6119	6
	10260	696	7.4	8.2	7.3	2474	5663	5531	6355	6403	6
7	10380	712	7.6	8.5	7.5	2572	5796	5696	6533	6574	7
	11460	690	7.7	8.5	7.6	2582	5713	5652	6492	6509	7
	11660	732	8.0	8.9	7.8	2706	5973	5910	6790	6819	7
	11860	762	8.5	9.4	8.3	2871	6213	6191	7084	7113	7
	12060	786	8.9	9.9	8.9	3026	6425	6438	7350	7371	8
	12260	807	9.3	10.5	9.4	3150	6629	6659	7588	7596	9
8	12315	812	9.4	10.6	9.6	3183	6681	6712	7647	7649	9
	13025	785	9.5	10.7	9.7	3155	6574	6624	7562	7545	9
	13225	825	9.9	11.2	10.2	3285	6829	6867	7849	7826	10
Failure	13320	830	10.1	11.5	10.5	3327	6888	6928	7918	7891	10

Table C-8 continued,

		Middle Strain Gauges			Top Strain Gauges			Rosette shear span B		
Load Stage	Load, P	6	11	15	8	12	17	ε_{xx}	ε_{yy}	γ_{xy}
(#)	(kN)	(με)	(με)	(με)	(με)	(με)	(με)	με	με	με
	13	0	0	0	0	0	0	0	1	0
	16	1	0	0	0	0	3	0	1	1
	21	1	1	3	1	1	4	0	1	1
	44	4	6	14	3	5	11	0	1	4
	79	9	14	33	7	12	25	0	1	1
1	110	13	22	57	9	18	43	0	0	3
	104	12	21	59	9	19	47	1	0	0
	172	21	37	84	15	35	103	1	1	3
2	211	25	46	102	19	45	126	2	1	6
	194	24	44	195	19	44	233	1	2	6
	244	29	64	799	24	77	1024	2	2	11
	287	35	88	1382	28	93	1567	2	3	69
3	312	38	115	1594	33	115	1760	3	3	224
	299	38	121	1602	34	124	1745	19	4	220
	340	42	1062	1818	39	327	1986	167	6	415
	361	56	1589	2026	39	678	2198	446	12	860
	388	69	1869	2223	42	966	2400	1025	-47	1812
	407	86	2042	2383	43	1170	2556	1751	1448	2375
4	412	90	2075	2420	43	1210	2592	1812	1630	2464
	395	99	2070	2406	44	1282	2548	1812	1769	2521
	443	119	2274	2651	49	1474	2811	2024	2140	2751
	468	193	2451	2846	60	2030	3004	2252	2823	3213
	492	557	2604	3026	114	2174	3172	2422	3379	3599
5	512	752	2715	3178	169	2284	3317	2594	4036	4010
	493	892	2679	3152	219	2290	3260	2608	4276	4116
	514	988	2778	3267	254	2378	3373	3212	6384	5492
	550	1119	2924	3451	308	2489	3566	3532	7508	6312
	581	1408	3090	3659	425	2659	3750	3785	8384	6911
	611	1649	3252	3873	545	2840	3962	4112	9352	7520
6	612	1648	3259	3881	544	2848	3951	4124	9396	7544
	592	1786	3218	3853	644	2861	3908	4188	9684	7624
	636	1891	3391	4067	675	3011	4117	4312	10332	8180
	668	2158	3566	4286	796	3206	4330	4568	11248	8752
	696	2389	3724	4480	929	3394	4480	4816	12220	9380
7	712	2530	3816	4598	1018	3506	4593	4960	12864	9752
	690	2627	3762	4547	1115	3504	4491	4964	13256	9884
	732	2748	3926	4753	1166	3655	4719	5160	13936	10392
	762	2933	4085	4954	1280	3866	4890	5396	15032	11020
	786	3147	4222	5132	1435	4128	5028	5584	16380	11756
	807	3344	4352	5286	1598	4374	5144	5700	17956	12592
8	812	3391	4385	5323	1638	4432	5170	5728	18488	12856
	785	3436	4308	5240	1727	4408	5053	5728	19388	13036
	825	3561	4467	5435	1798	4580	5242	5736	20644	13908
Failure	830	3616	4505	5480	1844	4638	5274	5740	21904	14444

C.11 Specimen B5H

The displacement rate of specimen B5H was 0.15 mm/min of machine stroke. At a load of P = 518 kN the specimen rolled approximately 5 mm towards end A disrupting the quarter-span vertical LVDTs. At P = 1200 kN, further global movement of approximately 10 mm occurred towards end A (west). The deflection data was adjusted in both instances. The diagonal shear crack in shear span B closely followed the diagonal line drawn from the center of the support plate to the center of the loading plate. Two small parallel horizontal cracks were observed to extend under loading plate B. The specimen exhibited extremely brittle failure. The failure occurred along the main diagonal shear crack in span B. Significant damage to the concrete occurred along the diagonal crack in shear span B with large pieces of concrete being ejected.

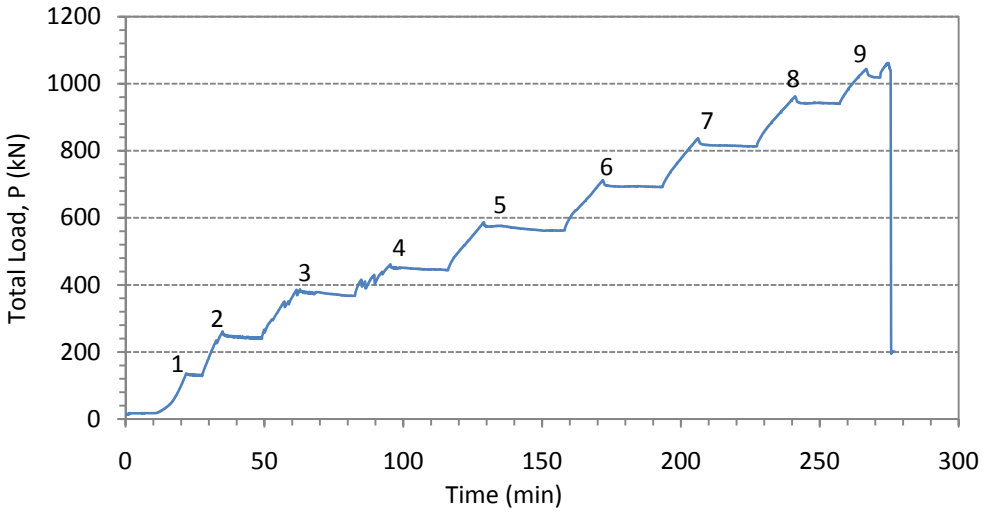

Figure C-96: Load – history of specimen B5H.

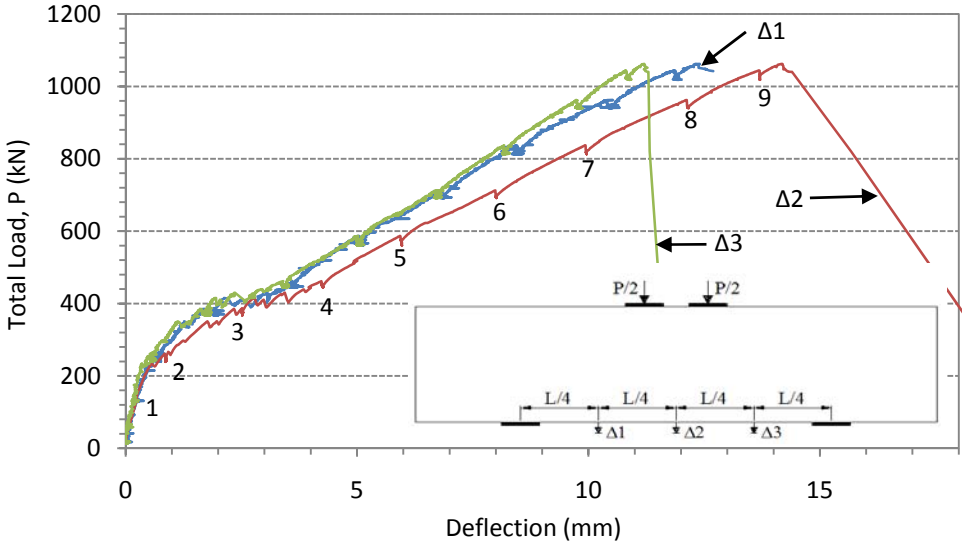

Figure C-97: Load – deflection response of specimen B5H.

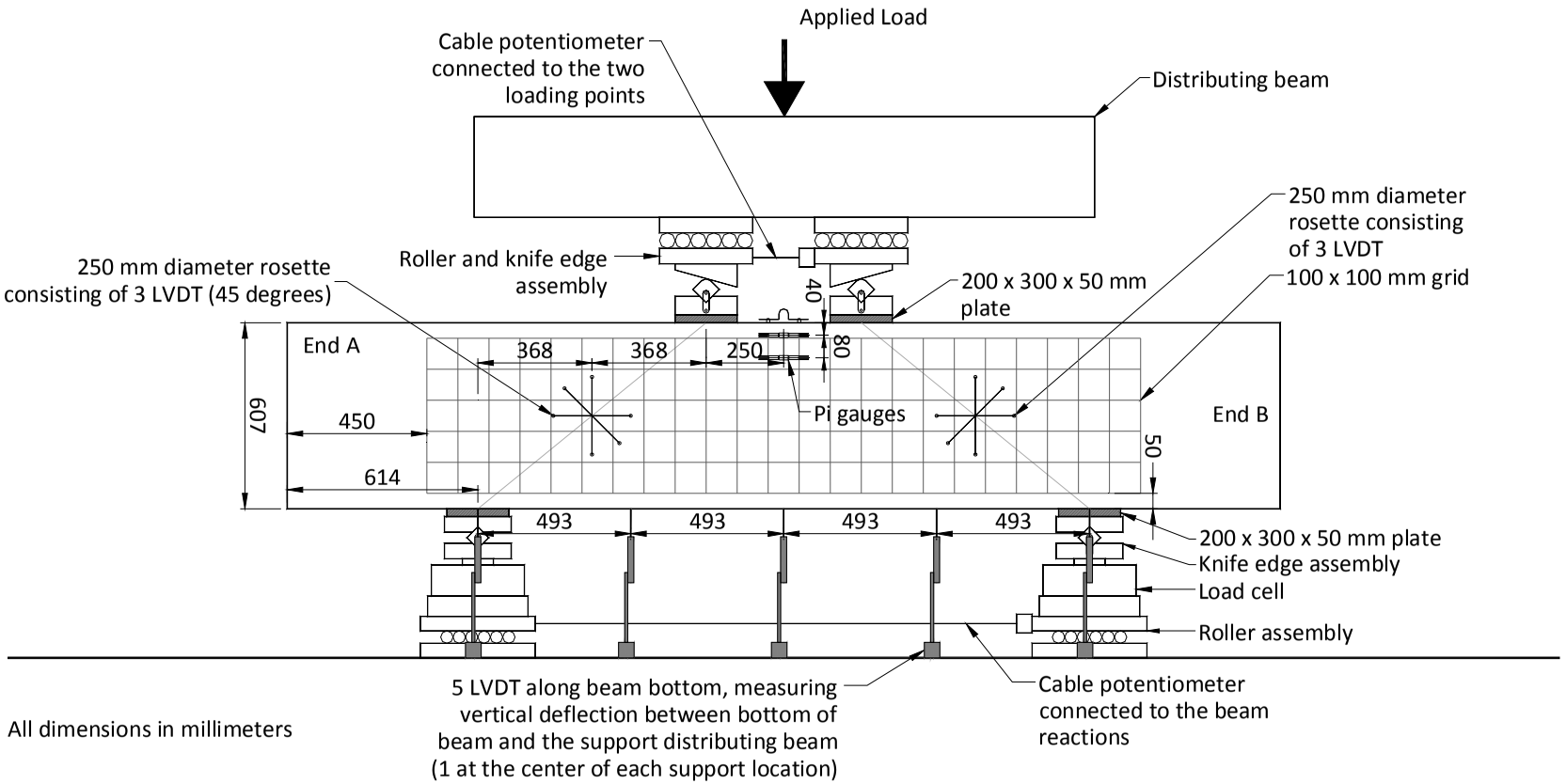

Figure C-98: Instrumentation drawing for specimen B5H.

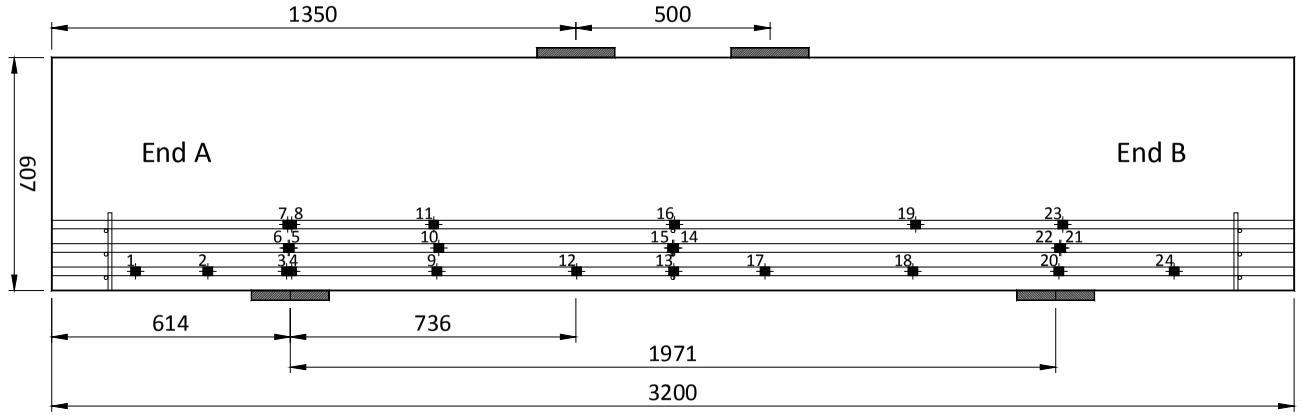

Strain Gauge Locations

Strain Gauge No.	Row	Column	Distance from End A (mm)	Strain Gauge No.	Row	Column	Distance from End A (mm)
1	B	C	216	13	B	F	1602
2	B	C	402	14	M	B	1602
3	B	F	605	15	M	F	1599
4	B	C	618	16	T	C	1604
5	M	F	612	17	B	C	1837
6	M	B	609	18	B	F	2218
7	T	F	608	19	T	C	2225
8	T	B	618	20	B	F	2594
9	B	C	992	21	M	B	2599
10	M	F	997	22	M	F	2596
11	T	F	984	23	T	C	2604
12	B	F	1352	24	B	F	2891

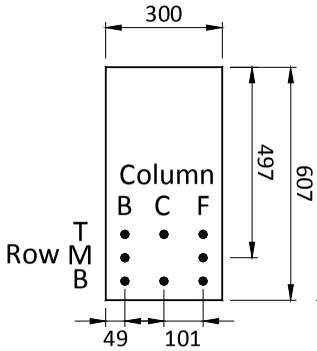

(8) - #7 GFRP Bars

Notes:
All dimensions in mm
Clear Cover: 38.1 mm
Concrete Strength: 66 MPa
Bar Length: 3200 mm

Figure C-99: Location of the strain gauges for specimen B5H (as-built).

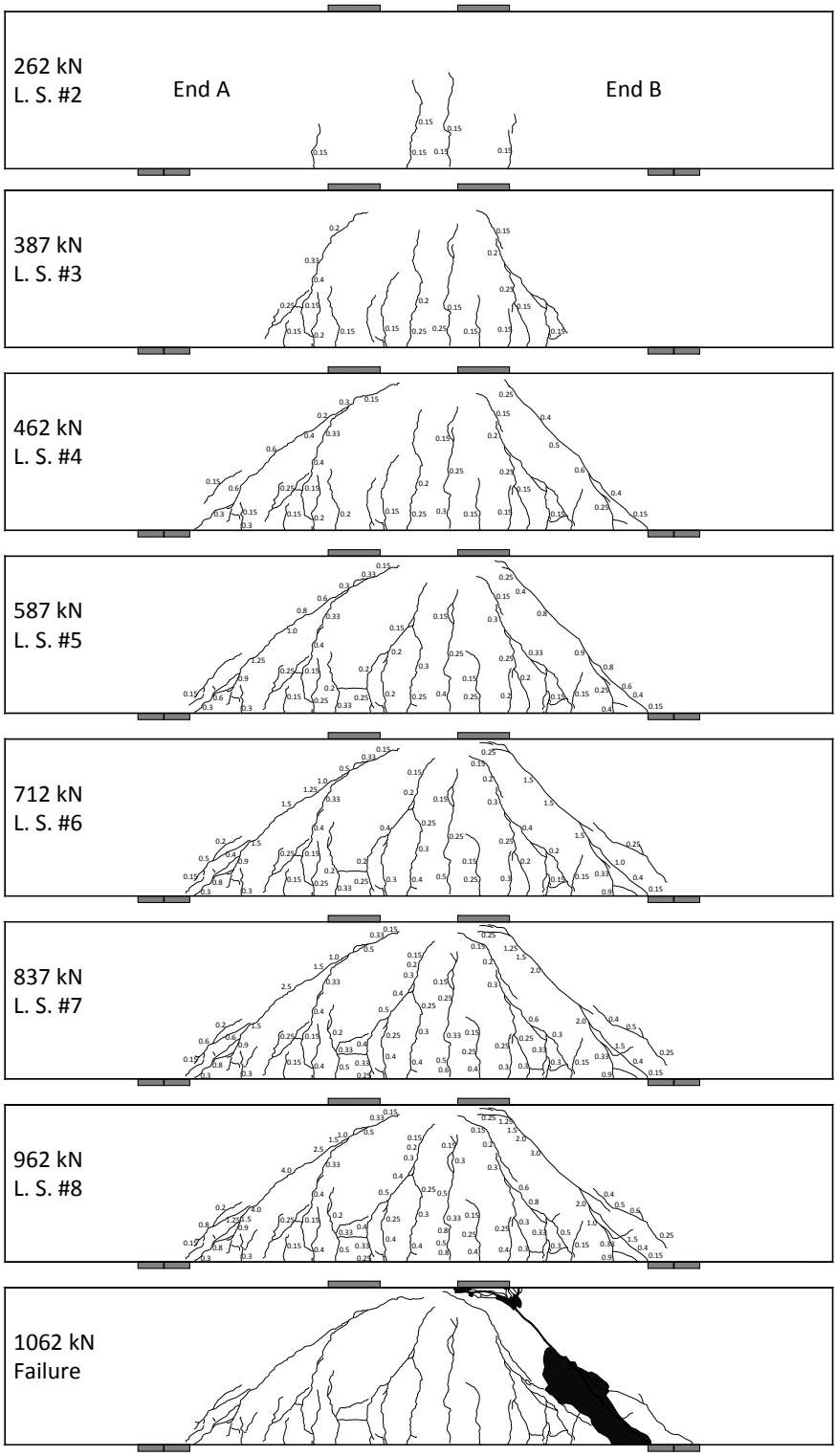

Figure C-100: Crack diagrams of specimen B5H showing the development of the cracks and the widths as loading progressed.

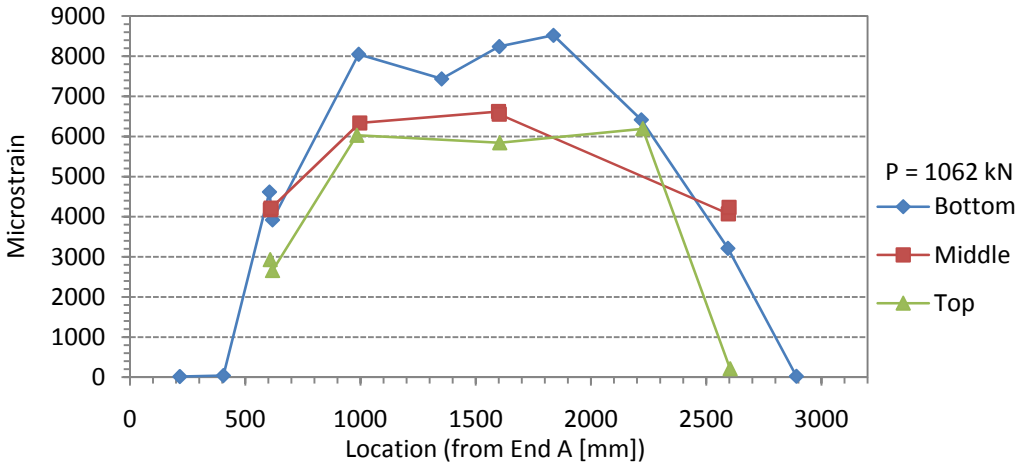

Figure C-101: Strain distribution in the bottom, middle, and tip reinforcement at peak load.

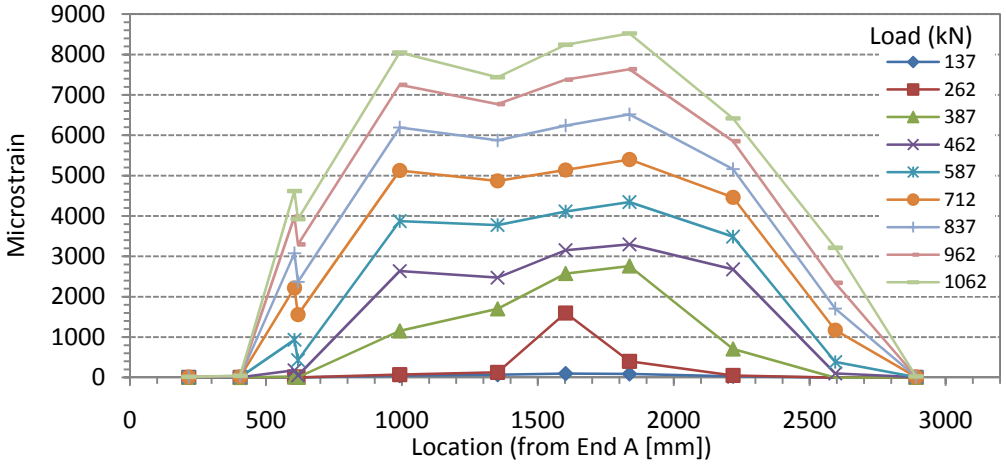

Figure C-102: Strain in the bottom reinforcement layer as loading progressed.

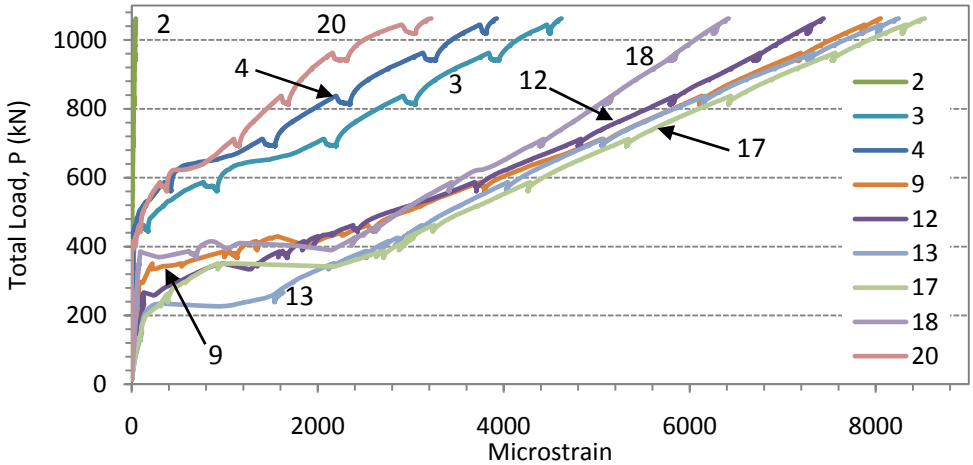

Figure C-103: Strain in the bottom reinforcement layer.

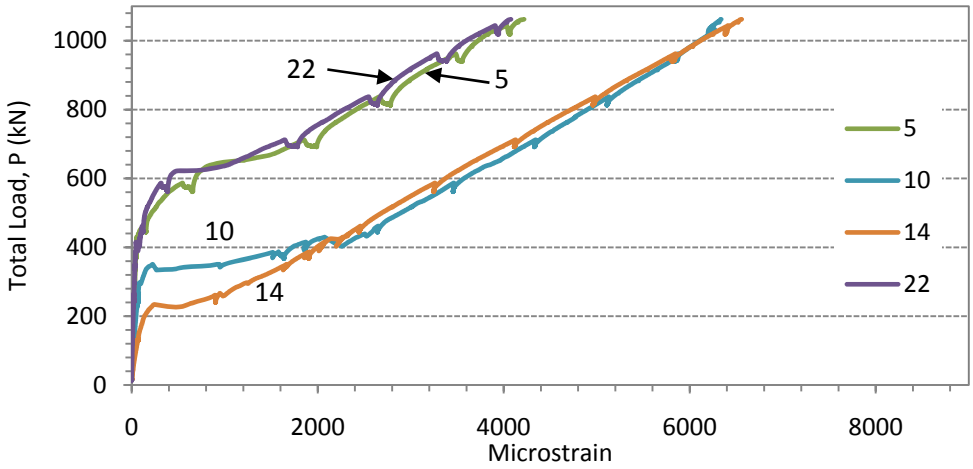

Figure C-104: Strain in the middle reinforcement layer.

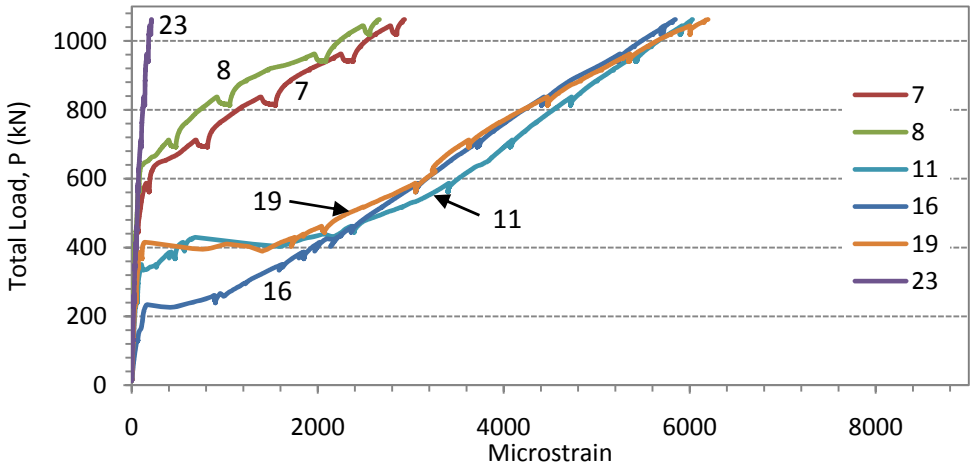

Figure C-105: Strain in the top reinforcement layer.

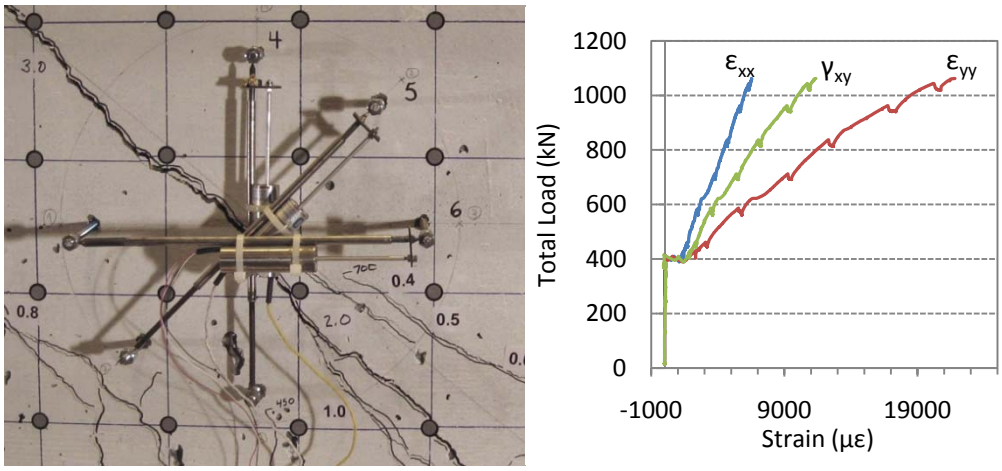

(a) (b)

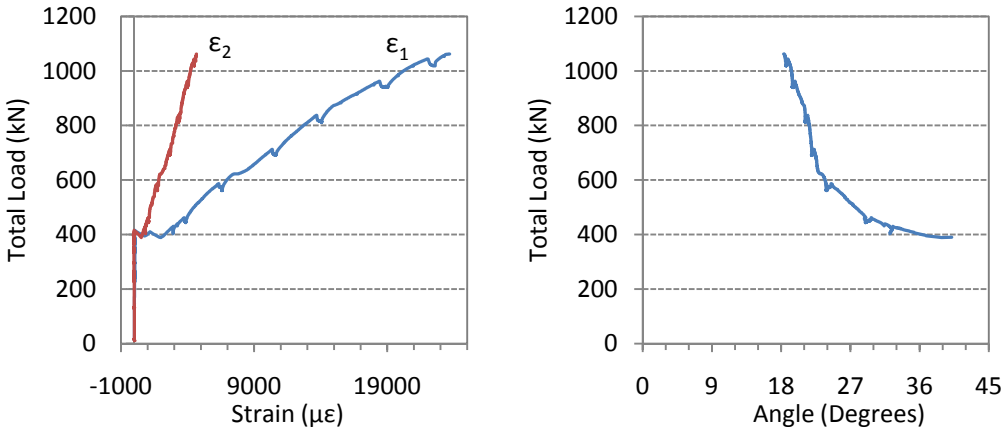

(c) (d)

Figure C-106: (a) crack location through the rosette in shear span B at P= 962 kN, (b) strain components, (c) principal strains, and (d) the direction of the minimum principal strain (angle of inclination from a horizontal line towards mid-span).

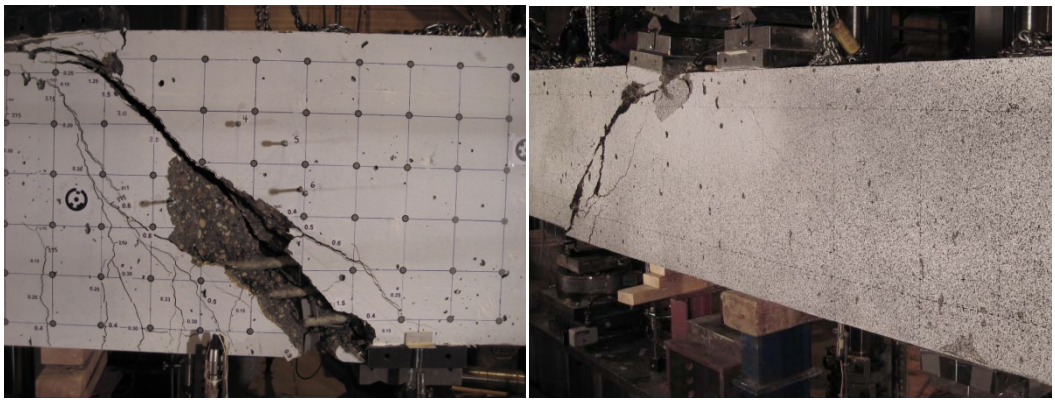

(a) (b)

Figure C-107: Failure of specimen B5H in shear span B (a) showing the front side and (b) the back side of the specimen.

Table C-9: Subset of the collected data in specimen B5H.

			Displacements			Bottom Strain Gauges				
Load Stage	Time	Load, P	End A 1/4 Span	Mid-Span	End B 1/4 Span	2	4	9	12	13
(#)	(s)	(kN)	(mm)	(mm)	(mm)	(με)	(με)	(με)	(με)	(με)
	0	14	0.0	0.0	0.0	1	0	1	0	0
	250	17	0.0	0.0	0.0	1	1	1	0	0
	500	18	0.0	0.0	0.0	2	1	2	0	0
	750	23	0.0	0.0	-0.1	2	2	4	3	3
	1000	51	0.1	0.1	0.0	2	1	13	16	19
	1250	116	0.2	0.2	0.1	3	3	37	53	73
1	1310	136	0.2	0.2	0.1	3	3	45	65	93
	1630	130	0.2	0.2	0.2	3	3	45	66	95
	1880	210	0.5	0.5	0.3	3	4	76	110	153
2	2095	261	0.8	0.8	0.5	3	4	70	119	1536
	2945	239	0.7	0.9	0.5	3	3	67	120	1535
	3195	298	1.0	1.3	0.8	3	5	124	512	1745
	3445	334	1.4	1.8	1.2	3	6	220	1283	2113
	3695	385	1.7	2.3	1.6	3	7	987	1587	2502
3	3770	387	1.9	2.5	1.7	3	8	1053	1625	2528
	4955	367	1.9	2.5	1.7	2	6	1133	1672	2522
	5205	393	2.7	3.1	2.1	2	7	1350	1839	2685
	5455	423	3.1	3.7	2.8	3	9	2054	2000	2905
	5705	459	3.6	4.2	3.3	5	36	2502	2347	3099
4	5725	462	3.6	4.2	3.4	5	38	2543	2381	3120
	6965	444	3.6	4.3	3.4	5	49	2594	2428	3093
	7215	502	4.0	4.8	3.9	5	83	2948	2786	3399
	7465	541	4.5	5.3	4.4	8	210	3296	3251	3692
	7715	583	5.0	5.9	5.0	10	337	3708	3651	4014
5	7740	587	5.0	5.9	5.0	10	352	3750	3686	4042
	9490	563	5.1	6.0	5.0	11	423	3799	3706	4028
	9740	623	5.6	6.5	5.5	11	499	4184	4029	4343
	9990	660	6.2	7.2	6.0	14	997	4560	4355	4631
	10240	701	6.7	7.8	6.6	16	1330	4951	4731	4971
6	10315	712	6.8	8.0	6.8	17	1407	5059	4830	5076
	11605	693	6.9	8.0	6.7	18	1543	5056	4800	5061
	11855	752	7.3	8.6	7.2	19	1669	5412	5144	5423
	12105	794	7.9	9.2	7.7	21	1920	5774	5500	5786
	12355	836	8.5	9.9	8.2	24	2181	6116	5827	6152
7	12370	837	8.4	9.9	8.2	24	2197	6133	5843	6168
	13640	813	8.5	10.0	8.2	26	2349	6107	5787	6143
	13890	874	9.0	10.6	8.7	27	2484	6442	6110	6507
	14140	913	9.6	11.2	9.1	30	2729	6764	6412	6867
	14390	951	10.2	11.9	9.6	33	3030	7095	6682	7224
8	14470	962	10.4	12.1	9.7	34	3131	7195	6760	7331
	15430	940	10.5	12.2	9.9	36	3270	7159	6683	7271
	15680	995	11.0	12.8	10.2	38	3417	7482	6982	7630
	15930	1034	11.7	13.5	10.7	40	3667	7795	7240	7969
	16180	1019	11.9	13.7	10.9	41	3800	7857	7269	8026
	16430	1056	12.3	14.0	11.1	43	3885	8001	7397	8185
Failure	16480	1062	12.4	14.2	11.2	43	3925	8053	7440	8247

Table C-9 continued,

		Middle Strain Gauges			Top Strain Gauges			Rosette shear span B		
Load Stage	Load, P	5	10	14	7	11	16	ε_{xx}	ε_{yy}	γ_{xy}
(#)	(kN)	(με)	(με)	(με)	(με)	(με)	(με)	με	με	με
	14	0	0	0	0	0	0	0	2	-2
	17	0	0	1	0	0	1	1	2	-1
	18	0	0	1	0	0	1	0	1	-1
	23	0	1	4	0	1	4	1	2	-1
	51	3	7	16	2	5	14	1	2	-1
	116	10	22	55	9	15	45	2	3	-1
1	136	12	27	68	11	19	59	2	3	4
	130	13	28	69	11	19	65	3	5	10
	210	22	49	160	20	35	126	2	5	26
2	261	29	67	895	26	61	885	3	6	58
	239	28	67	900	26	60	900	5	9	64
	298	34	103	1265	31	69	1233	5	8	73
	334	39	297	1627	36	130	1583	4	7	102
	385	45	1516	1892	41	402	1831	4	8	108
3	387	45	1578	1909	41	425	1850	5	7	-37
	367	46	1638	1903	42	467	1850	7	10	-37
	393	48	1862	2018	44	570	1973	1143	1546	1516
	423	65	2378	2256	54	1819	2192	1432	2363	1958
	459	117	2630	2442	59	2331	2358	1673	3016	2295
4	462	124	2650	2459	61	2358	2375	1713	3081	2314
	444	154	2642	2442	69	2391	2359	1718	3204	2372
	502	217	2905	2699	86	2738	2599	1918	3797	2707
	541	332	3178	2952	108	3116	2821	2243	4538	2979
	583	518	3438	3234	147	3389	3059	2504	5453	3429
5	587	545	3461	3259	155	3410	3078	2525	5543	3478
	563	658	3455	3246	189	3399	3053	2531	5814	3608
	623	750	3719	3510	219	3637	3286	2909	6915	4168
	660	1333	4001	3749	414	3867	3465	3354	8065	4757
	701	1761	4267	4042	634	4039	3689	3663	8980	5270
6	712	1853	4345	4129	692	4093	3749	3773	9255	5402
	693	1990	4329	4113	817	4068	3715	3783	9530	5539
	752	2136	4607	4402	904	4288	3957	4092	10356	5990
	794	2379	4864	4687	1114	4505	4183	4407	11283	6493
	836	2651	5118	4973	1372	4721	4424	4697	12255	7016
7	837	2666	5131	4986	1388	4732	4435	4705	12308	7059
	813	2785	5109	4959	1548	4717	4408	4713	12684	7232
	874	2931	5376	5244	1654	4940	4652	5012	13526	7661
	913	3148	5624	5511	1880	5155	4916	5250	14996	8367
	951	3409	5812	5766	2168	5375	5177	5533	16332	8988
8	962	3485	5880	5849	2250	5440	5252	5646	16765	9199
	940	3556	5827	5808	2381	5415	5212	5650	17381	9472
	995	3702	6079	6088	2499	5637	5455	5944	18344	9943
	1034	3950	6230	6342	2711	5861	5689	6255	19725	10522
	1019	4063	6211	6385	2836	5900	5698	6344	20599	10866
	1056	4151	6308	6512	2907	5998	5806	6513	21377	11186
Failure	1062	4218	6339	6559	2934	6030	5847	6546	21802	11358

C.12 Specimen B6H

The displacement rate of specimen B6H was 0.15 mm/min of machine stroke. By load stage 4, a diagonal crack in shear span A had propagated above the diagonal line drawn between the centerlines of the loading and support plates. This crack became progressively less inclined and propagated towards the loading point. After load stage 5, the load carrying capacity of the specimen increased until a vertical crack formed 250 mm outside the outer edge of loading plate A that intersected the main diagonal crack. The formation of the vertical crack at P = 357 kN resulted in the load carrying capacity of the specimen to decrease by 10%. As loading continued, the diagonal crack in shear span A grew until failure of the specimen occurred due to the vertical crack in shear span A.

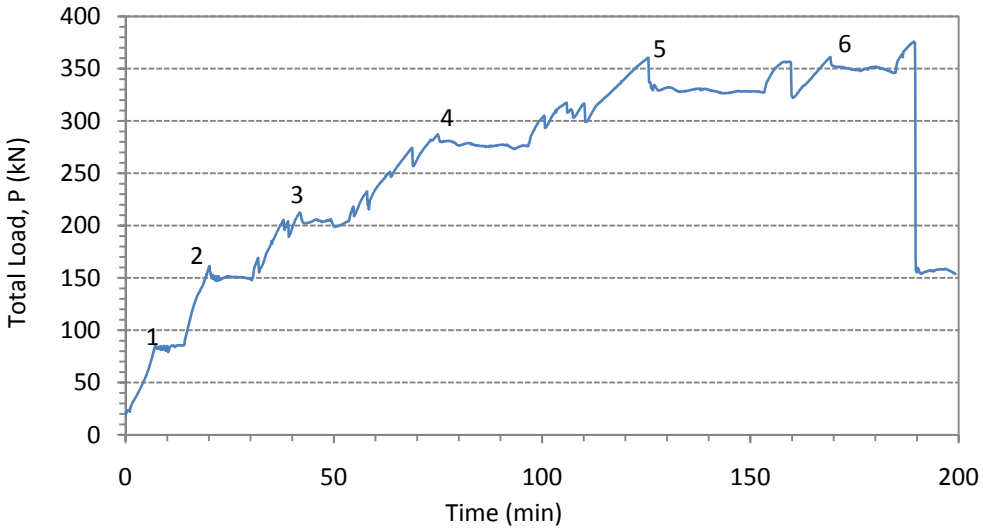

Figure C-108: Load – history of specimen B6H.

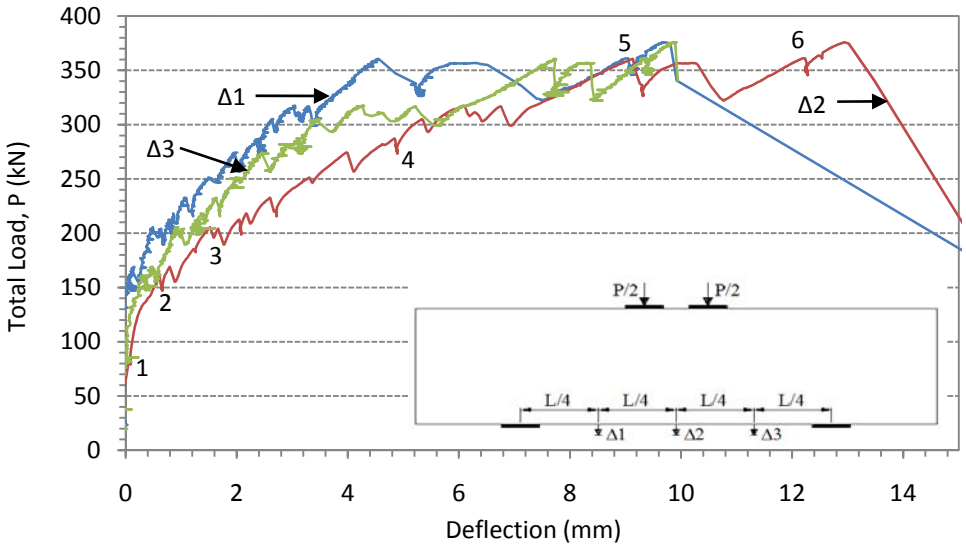

Figure C-109: Load – deflection response of specimen B6H.

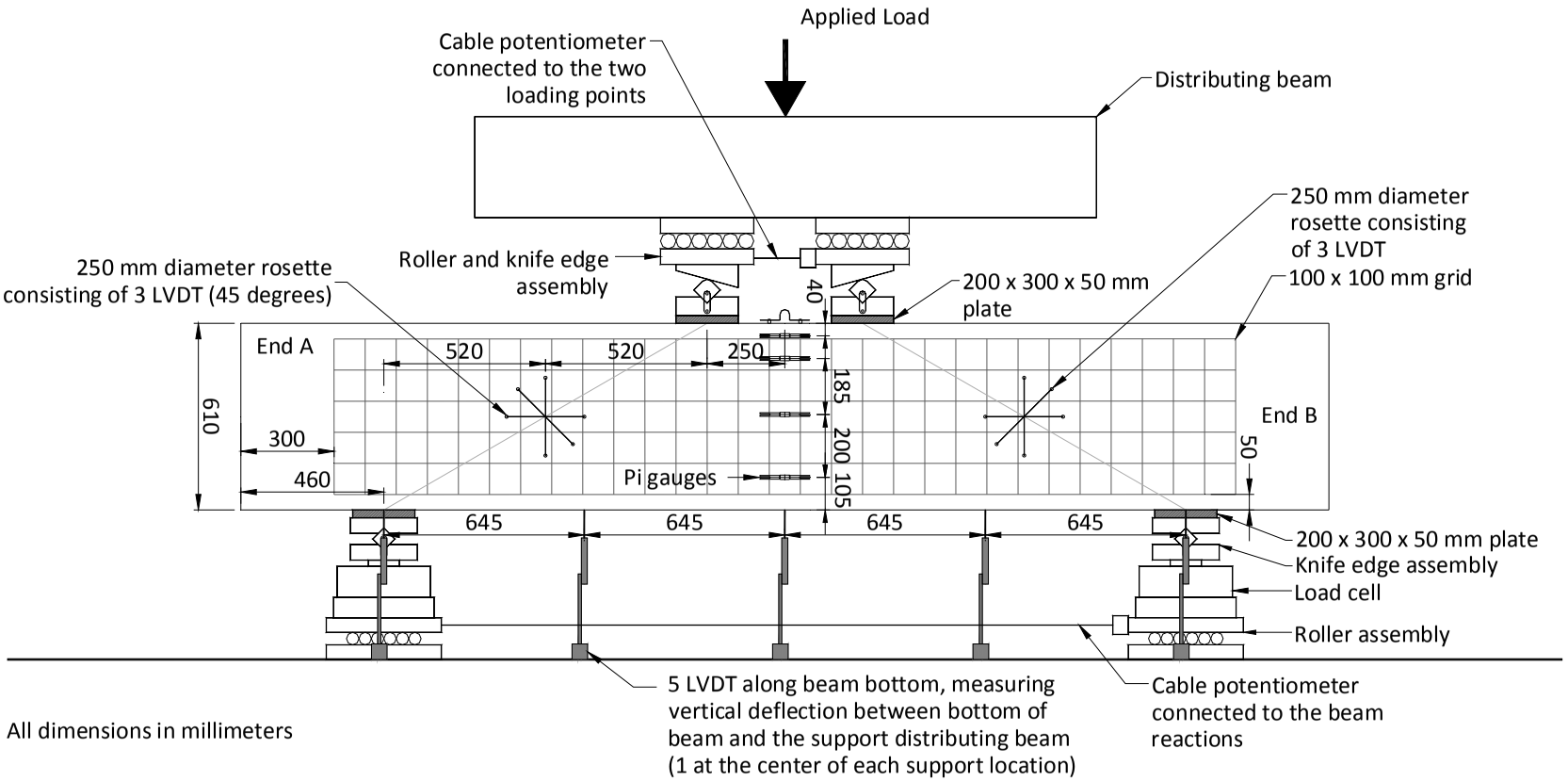

Figure C-110: Instrumentation drawing for specimen B6H.

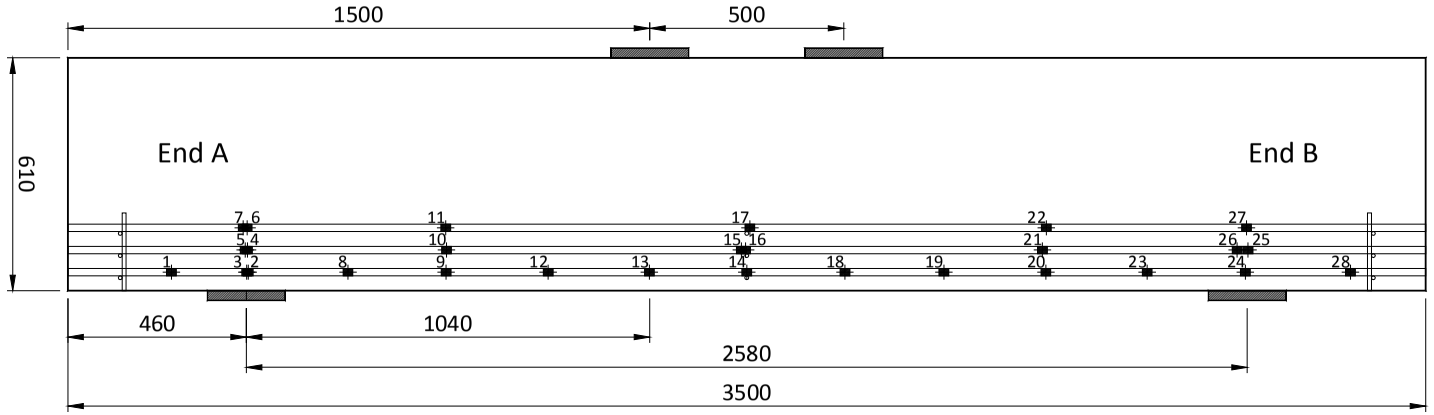

Strain Gauge Locations

Strain Gauge No.	Row	Column	Distance from End A (mm)	Strain Gauge No.	Row	Column	Distance from End A (mm)
1	B	B	627	15	M	B	1736
2	B	B	465	16	M	F	1747
3	B	F	461	17	T	C	1758
4	M	B	463	18	B	F	2003
5	M	F	457	19	B	C	2258
6	T	F	462	20	B	C	2521
7	T	C	452	21	M	F	2512
8	B	C	722	22	T	C	2522
9	B	C	975	23	B	C	2782
10	M	B	976	24	B	C	3035
11	T	C	974	25	M	B	3042
12	B	F	1238	26	M	F	3014
13	B	C	1499	27	T	F	3038
14	B	C	1750	28	B	B	3306

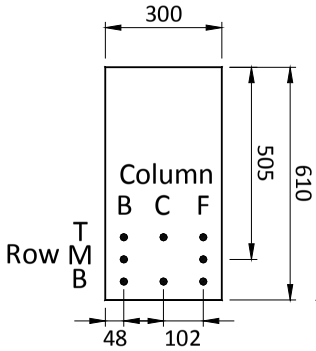

(8) - #6 GFRP Bars

Notes:
All dimensions in mm
Clear Cover: 38.1 mm
Concrete Strength: 69 MPa
Bar Length: 3500 mm

Figure C-111: Location of the strain gauges for specimen B6H (as-built).

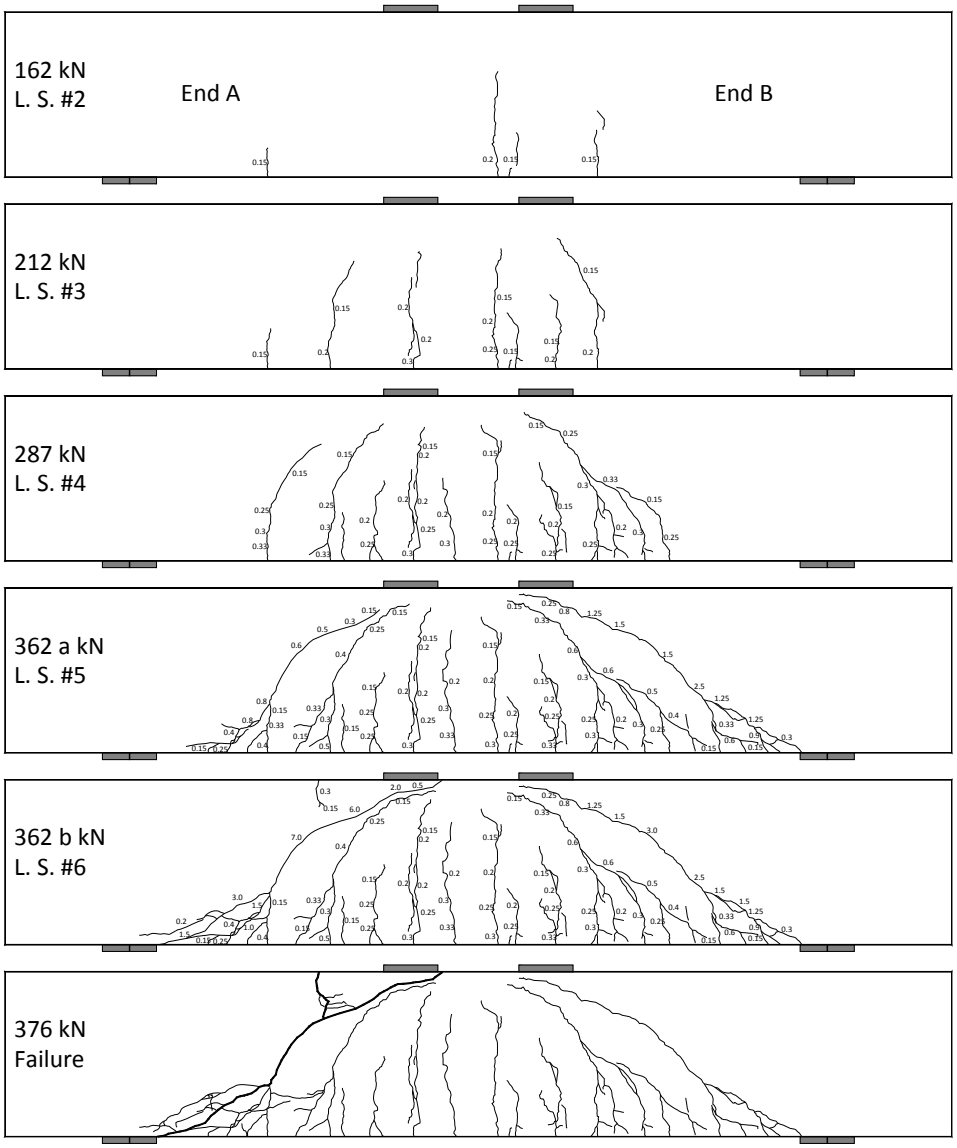

Figure C-112: Crack diagrams of specimen B6H showing the development of the cracks and the widths as loading progressed.

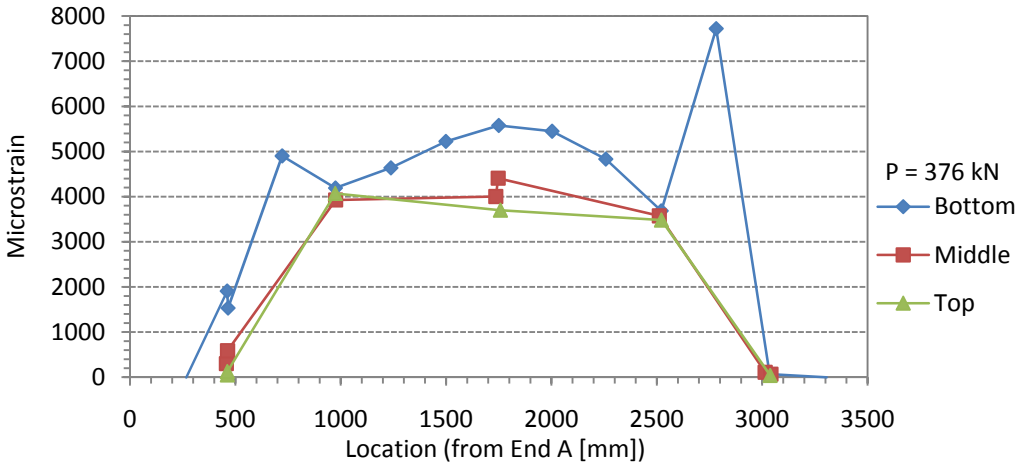

Figure C-113: Strain distribution in the bottom, middle, and top reinforcement at the peak load.

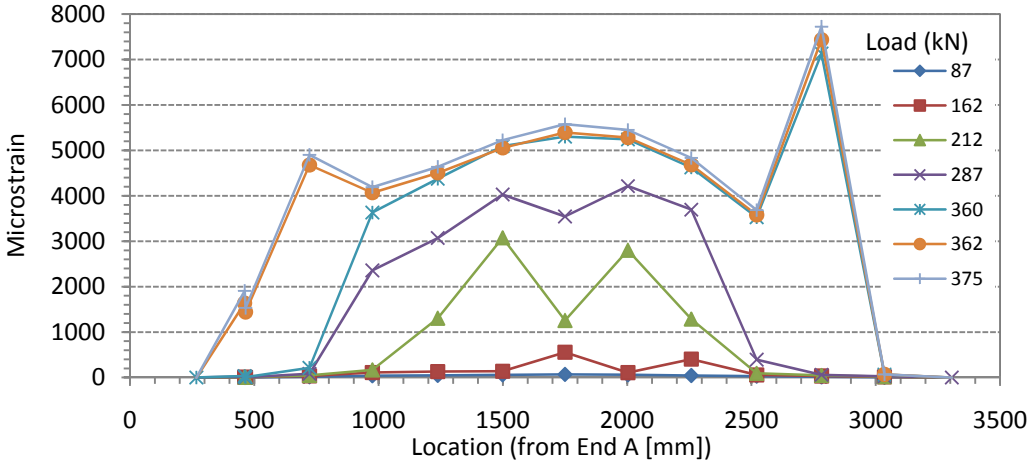

Figure C-114: Strain in the bottom reinforcement layer as loading progressed.

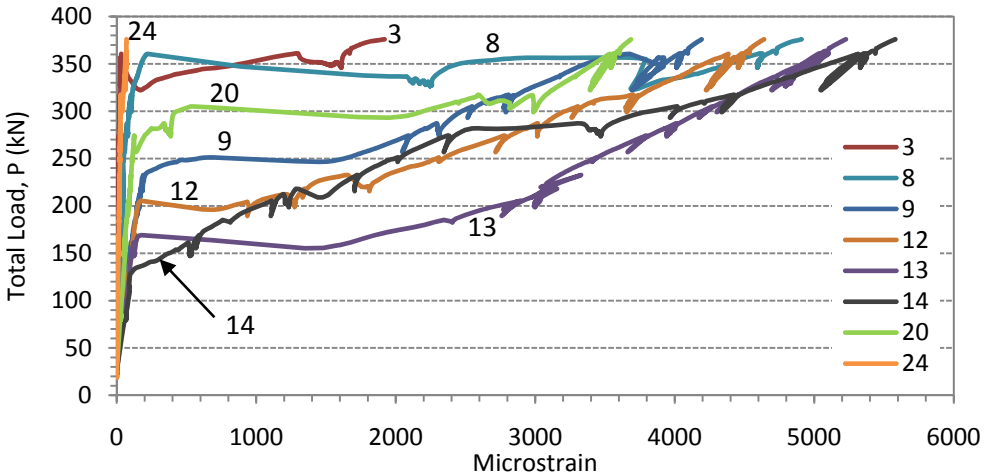

Figure C-115: Strain in the bottom reinforcement layer.

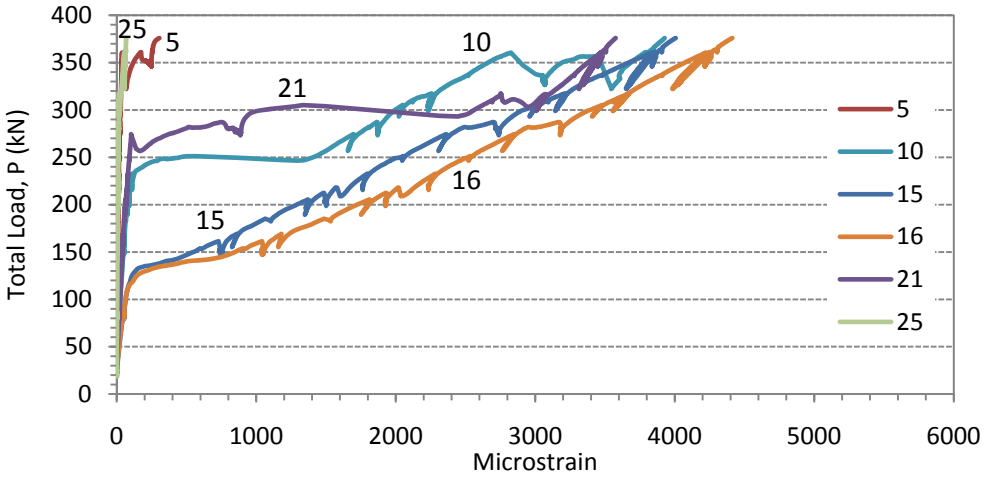

Figure C-116: Strain in the middle reinforcement layer.

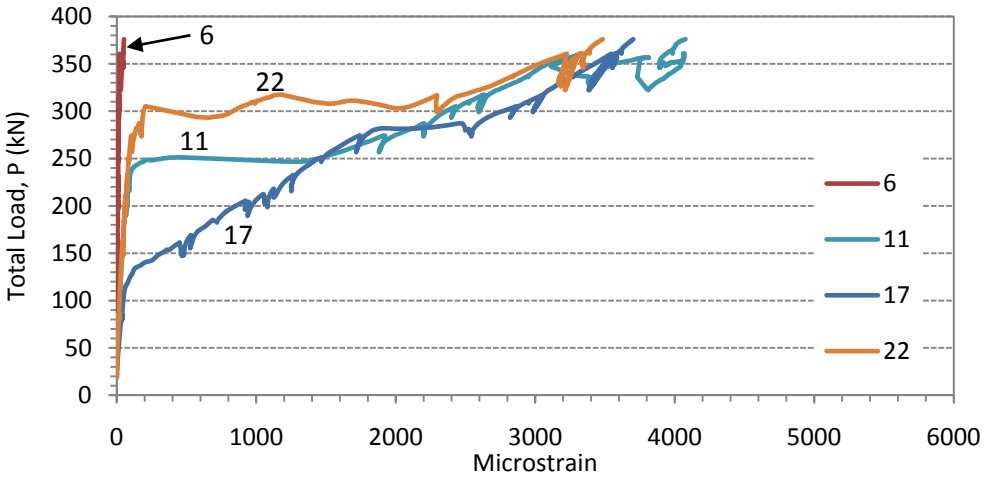

Figure C-117: Strain in the top reinforcement layer.

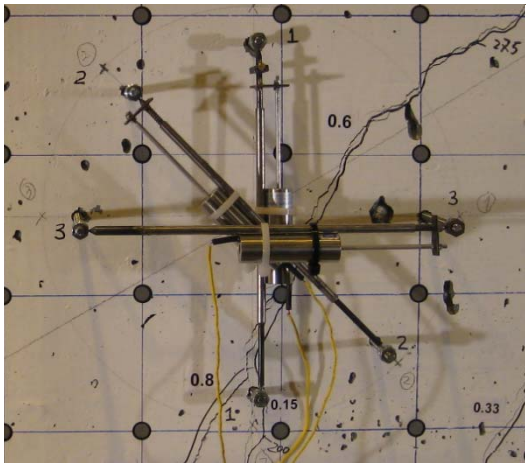

(a)

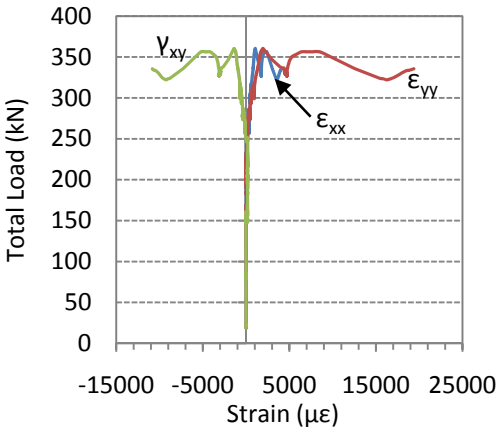

(b)

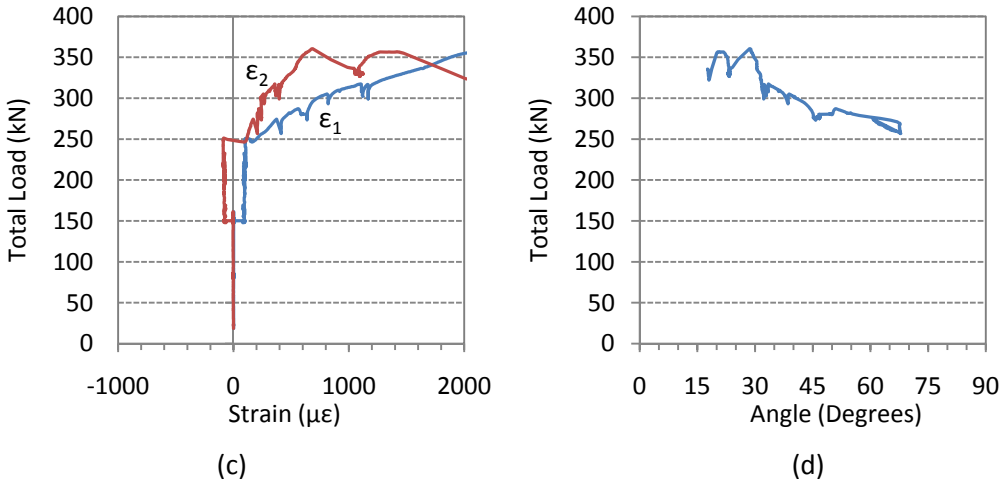

Figure C-118: (a) crack location through the rosette in shear span A at P= 360 kN, (b) strain components, (c) principal strains, and (d) the direction of the minimum principal strain (angle of inclination from a horizontal line towards mid-span).

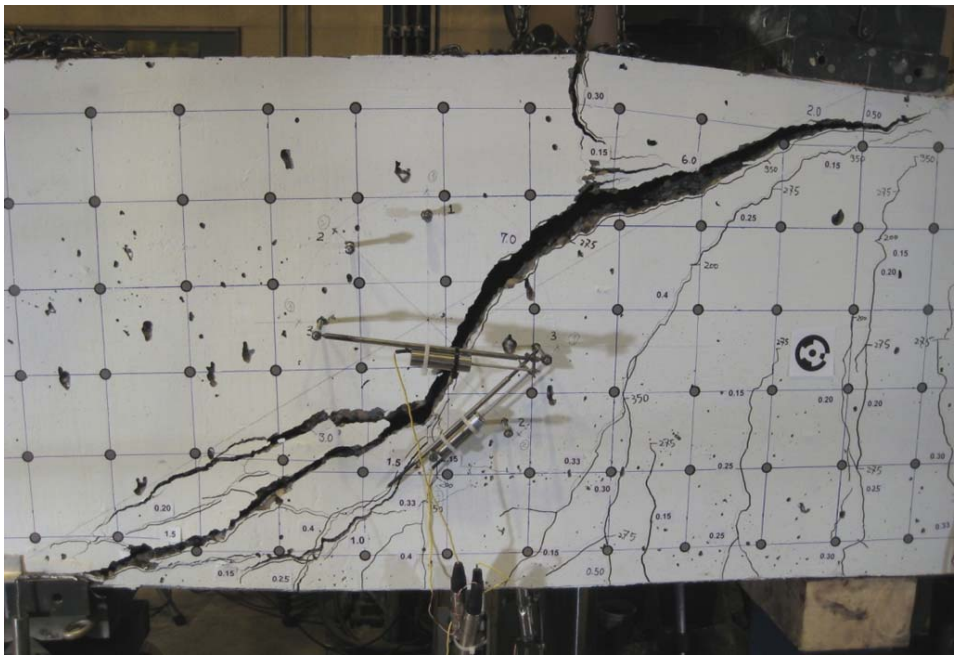

Figure C-119: Failure of specimen B6H in shear span A.

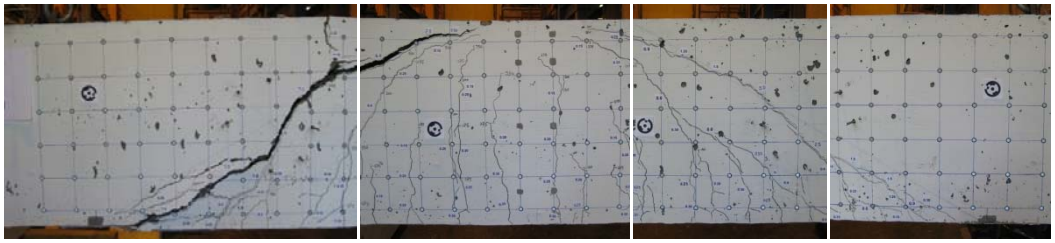

Figure-C-120: Specimen B6H after being removed from the test frame (end A on left, B on right).

Table C-10: Subset of the collected data for specimen B6H.

			Displacements			Bottom Strain Gauges						
Load Stage (#)	Time (s)	Load, P (kN)	End A 1/4 Span (mm)	Mid-Span (mm)	End B 1/4 Span (mm)	1 (με)	3 (με)	8 (με)	9 (με)	12 (με)	13 (με)	14 (με)
	0	19	-0.1	0.0	0.0	0	0	0	0	0	0	0
	150	36	-0.1	0.0	-0.1	0	0	3	6	7	9	10
	300	57	-0.1	0.0	0.0	0	1	7	18	22	25	31
1	430	86	-0.1	0.1	0.0	0	3	14	37	44	52	63
	785	86	-0.1	0.1	0.0	0	3	15	39	48	57	69
	935	112	-0.1	0.2	0.0	0	4	21	55	67	81	92
	1085	140	0.0	0.4	0.1	0	6	28	79	98	96	224
2	1210	161	0.1	0.6	0.5	0	7	34	103	124	122	514
	1820	148	0.1	0.7	0.4	0	6	32	103	122	128	536
	1970	162	0.3	1.0	0.6	0	7	35	110	116	1693	581
	2120	185	0.4	1.3	0.8	0	8	41	136	135	2419	829
	2270	205	0.5	1.5	0.9	0	10	43	166	167	2883	1103
	2420	201	0.7	1.9	1.2	0	10	42	151	978	2858	1128
3	2510	212	0.8	2.0	1.3	0	10	45	163	1211	3042	1194
	3195	204	0.8	2.1	1.3	-1	10	44	163	1280	3000	1237
	3345	217	0.9	2.3	1.5	-1	11	47	172	1355	3062	1555
	3495	221	1.2	2.7	1.7	0	11	46	186	1799	3051	1705
	3645	239	1.3	3.0	1.8	0	12	47	271	2053	3256	1815
	3795	250	1.5	3.3	2.0	0	12	43	595	2298	3427	1998
	3945	259	1.8	3.6	2.3	0	14	54	1826	2475	3557	2130
	4095	272	2.0	3.9	2.5	0	16	59	2053	2733	3758	2329
	4245	269	2.1	4.3	2.6	0	16	61	2079	2769	3758	2385
	4395	282	2.3	4.6	2.9	0	18	69	2211	2927	3929	2590
4	4495	287	2.5	4.8	3.1	0	18	73	2292	3014	4009	3303
	5795	276	2.4	4.9	3.1	0	18	80	2313	3017	3945	3476
	5945	298	2.5	5.1	3.3	0	21	86	2456	3190	4174	3769
	6095	298	2.7	5.5	3.8	0	21	89	2531	3285	4213	3995
	6245	313	2.9	5.8	4.1	0	23	97	2694	3474	4392	4285
	6395	310	3.1	6.2	4.6	0	23	103	2788	3671	4392	4381
	6545	312	3.3	6.6	5.1	0	24	106	2802	3688	4405	4392
	6695	305	3.4	7.1	5.8	0	24	107	2803	3676	4342	4363
	6845	319	3.6	7.4	6.2	1	26	112	2885	3772	4469	4481
	6995	328	3.8	7.8	6.6	0	27	124	3020	3892	4584	4645
	7145	338	4.1	8.2	7.0	1	29	149	3181	4051	4738	4862
	7295	347	4.2	8.5	7.3	1	30	169	3319	4171	4880	5048
	7445	356	4.4	8.9	7.6	1	31	194	3511	4316	5032	5229
5	7530	360	4.6	9.1	7.7	1	32	220	3678	4385	5103	5314
	9200	327	5.3	9.3	7.7	0	25	2258	3728	4259	4789	5082
	9350	350	5.5	9.6	8.0	0	27	2445	3841	4365	4952	5229
	9500	356	6.0	10.0	8.1	0	26	3115	3880	4423	5021	5313
	9650	324	7.6	10.8	8.5	-5	194	3743	3700	4231	4702	5051
	9800	335	8.1	11.2	8.7	-5	339	4024	3793	4300	4786	5124
	9950	346	8.5	11.6	9.0	-5	741	4312	3894	4372	4883	5211
	10100	358	8.9	12.0	9.3	-5	1148	4535	3998	4453	4999	5318
6	10155	361	9.0	12.2	9.4	-5	1300	4627	4048	4495	5055	5374
	11090	346	9.1	12.3	9.4	-5	1612	4591	4013	4454	4979	5329
	11240	369	9.4	12.6	9.6	-5	1716	4758	4118	4562	5133	5474
Failure	11355	376	9.7	12.9	9.9	-6	1920	4909	4193	4641	5227	5581

Table C-10 continued,

		Middle Strain Gauges			Top Strain Gauges			Rosette shear span B		
Load Stage (#)	Load, P (kN)	5 (με)	10 (με)	16 (με)	6 (με)	17 (με)	22 (με)	ε_{xx} με	ε_{yy} με	γ_{xy} με
	19	0	0	0	0	0	0	1	1	1
	36	1	4	7	0	6	3	1	-1	-1
	57	2	10	22	1	17	8	0	-2	-2
1	86	4	21	46	2	35	16	0	-2	-2
	86	4	22	52	2	39	17	0	-1	-2
	112	6	31	83	3	59	24	0	-3	-3
	140	8	43	488	5	194	33	1	-3	-3
2	161	10	53	1042	6	451	41	1	-3	-3
	148	9	51	1053	5	481	43	-11	25	141
	162	10	54	1188	6	541	46	-11	26	179
	185	12	66	1539	7	726	53	-10	26	175
	205	13	83	1802	8	915	60	-10	25	176
	201	13	81	1814	8	973	61	-8	23	174
3	212	14	87	1931	8	1051	66	-7	23	168
	204	14	89	1928	8	1083	66	-7	23	179
	217	15	94	2121	9	1159	70	-8	24	156
	221	15	109	2236	9	1251	74	-2	21	197
	239	16	175	2363	10	1332	81	-2	20	194
	250	17	465	2521	12	1456	87	-9	22	187
	259	19	1527	2639	12	1557	93	254	154	-104
	272	20	1668	2813	12	1706	102	313	207	-164
	269	20	1692	2820	12	1750	118	384	239	-144
	282	22	1805	2956	13	1930	140	393	301	-257
4	287	23	1864	3167	13	2458	160	424	353	-333
	276	22	1872	3181	14	2546	179	442	440	-397
	298	25	1982	3367	15	2735	190	442	503	-470
	298	25	2035	3435	15	2838	812	483	613	-540
	313	27	2158	3598	16	2989	1049	548	770	-614
	310	28	2240	3622	16	3025	1624	589	887	-683
	312	28	2249	3629	16	3028	2221	590	913	-697
	305	28	2244	3585	16	3000	2338	616	949	-694
	319	30	2299	3680	17	3066	2511	643	1006	-726
	328	32	2391	3782	18	3158	2701	728	1157	-838
	338	34	2526	3915	19	3278	2848	827	1370	-979
	347	35	2630	4038	20	3394	2989	891	1515	-1089
	356	37	2749	4161	21	3497	3144	975	1724	-1210
5	360	37	2825	4222	21	3546	3226	1065	1966	-1391
	327	36	3068	4022	22	3402	3188	1763	4734	-3119
	350	38	3189	4148	24	3492	3240	1886	5252	-3447
	356	42	3362	4213	26	3545	3289	2170	6977	-4421
	324	70	3555	3989	29	3387	3214	-	-	-
	335	83	3602	4055	33	3431	3236	-	-	-
	346	108	3653	4131	37	3484	3264	-	-	-
	358	153	3759	4218	40	3548	3305	-	-	-
6	361	174	3801	4262	42	3583	3332	-	-	-
	346	249	3777	4215	47	3553	3343	-	-	-
	369	264	3870	4332	49	3640	3410	-	-	-
Failure	376	305	3927	4412	52	3702	3485	-	-	-

C.13 Specimen C1N

The displacement rate of specimen C1N was 0.15 mm/min of machine stroke. Diagonal cracks propagated from the inside edge of the support plates towards the inside edge of the loading plates. At the peak load, the specimen rolled approximately 40 mm towards end B. The test was paused to investigate the stability of the specimen and brittle failure occurred within seconds. The diagonal crack from shear span B penetrated through the flexural compression zone resulting in crushing and a sudden drop in load carrying ability.

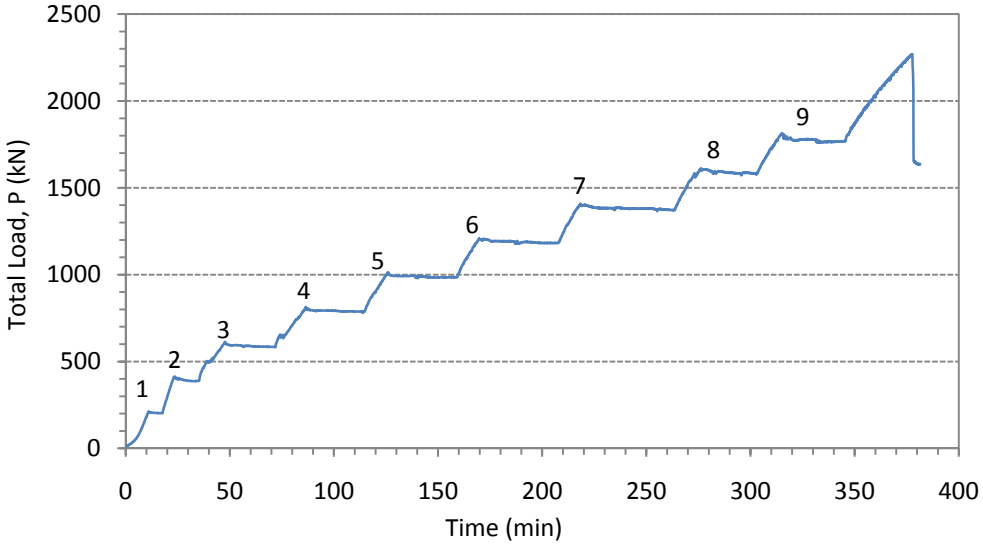

Figure C-121: Load – history of specimen C1N.

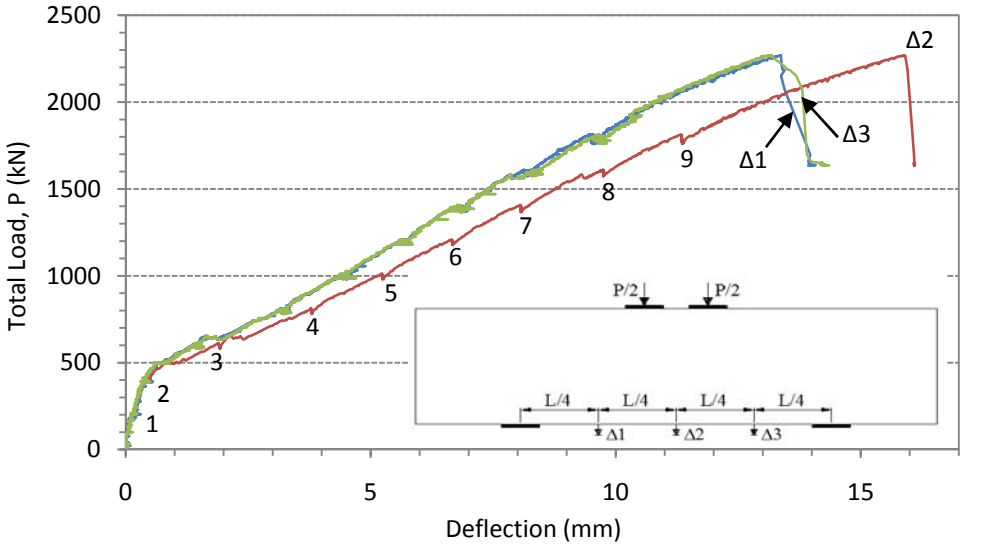

Figure C-122: Load – displacement response of specimen C1N.

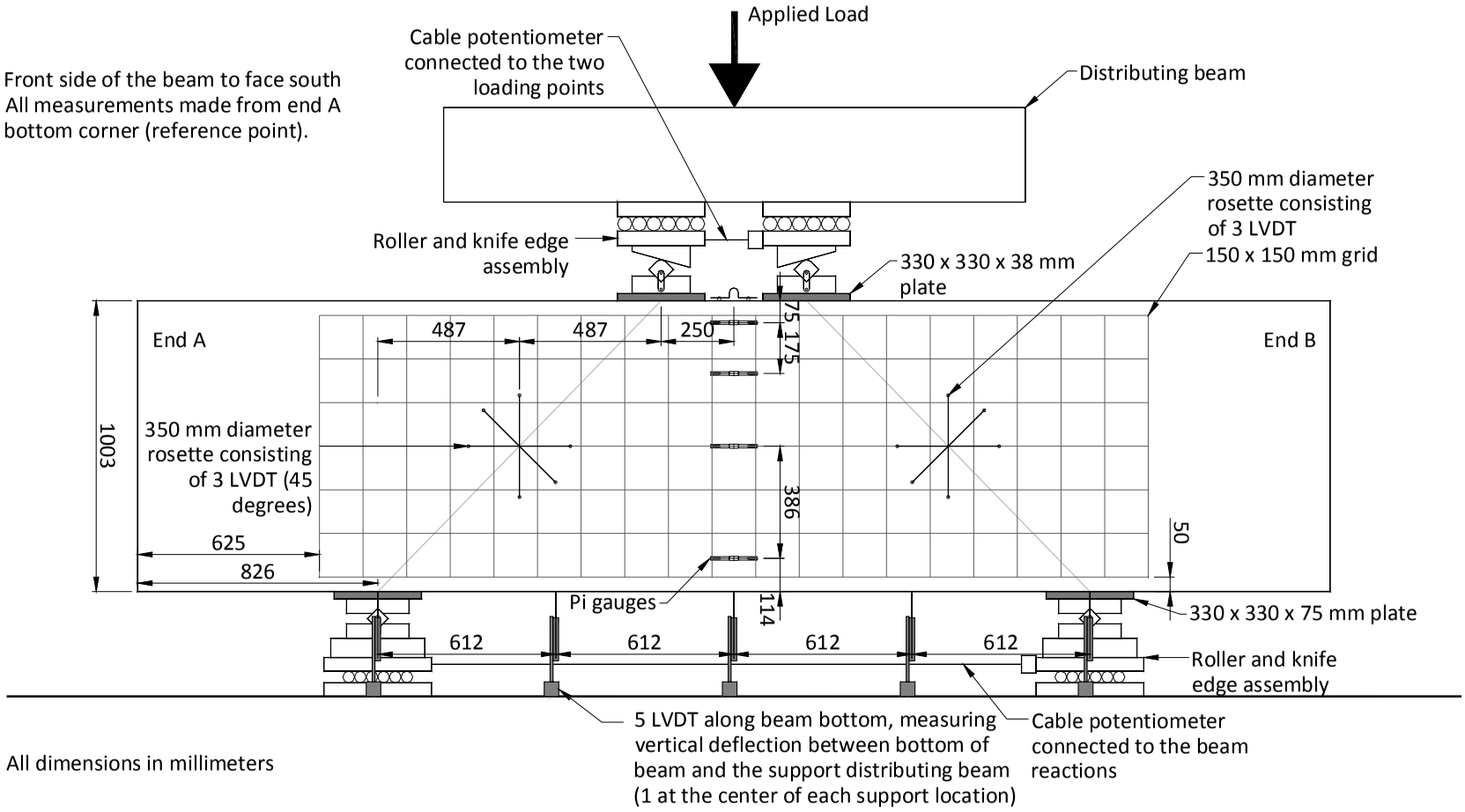

Figure C-123: Instrumentation drawing for specimen C1N.

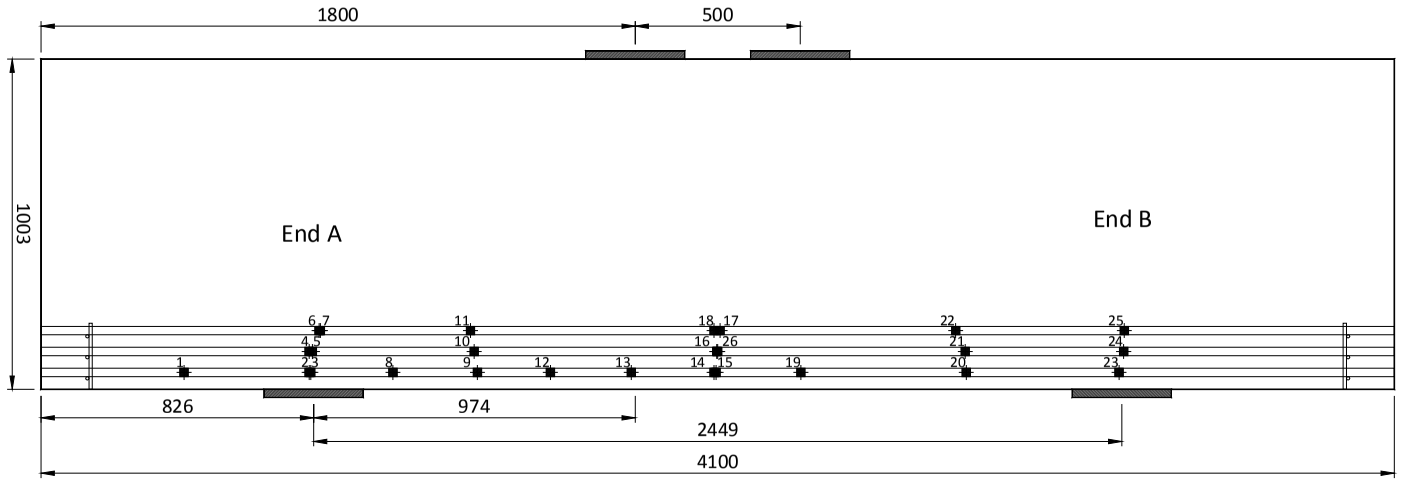

Strain Gauge Locations

Strain Gauge No.	Row	Column	Distance from End A (mm)	Strain Gauge No.	Row	Column	Distance from End A (mm)
1	B	F	422	16	M	F	2047
2	B	F	812	17	T	F	2057
3	B	C	817	18	T	B	2039
4	M	F	812	19	B	F	2302
5	M	B	822	20	B	C	2803
6	T	F	842	21	M	F	2800
7	T	B	846	22	T	F	2771
8	B	C	1066	23	B	C	3266
9	B	C	1322	24	M	F	3280
10	M	F	1312	25	T	F	3282
11	T	F	1301	26	M	B	2050
12	B	C	1543				
13	B	F	1788				
14	B	C	2039				
15	B	F	2045				

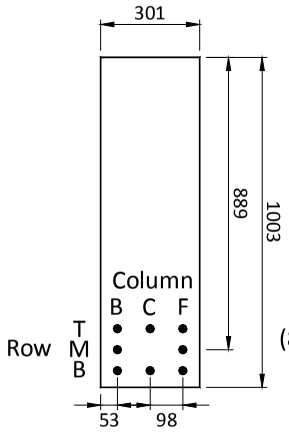

Notes:

All dimensions in mm
Clear Cover: 38.1 mm
Concrete Strength: 52 MPa
Bar Length: 4100 mm

Figure C-124: Location of the strain gauges for specimen C1N (as-built).

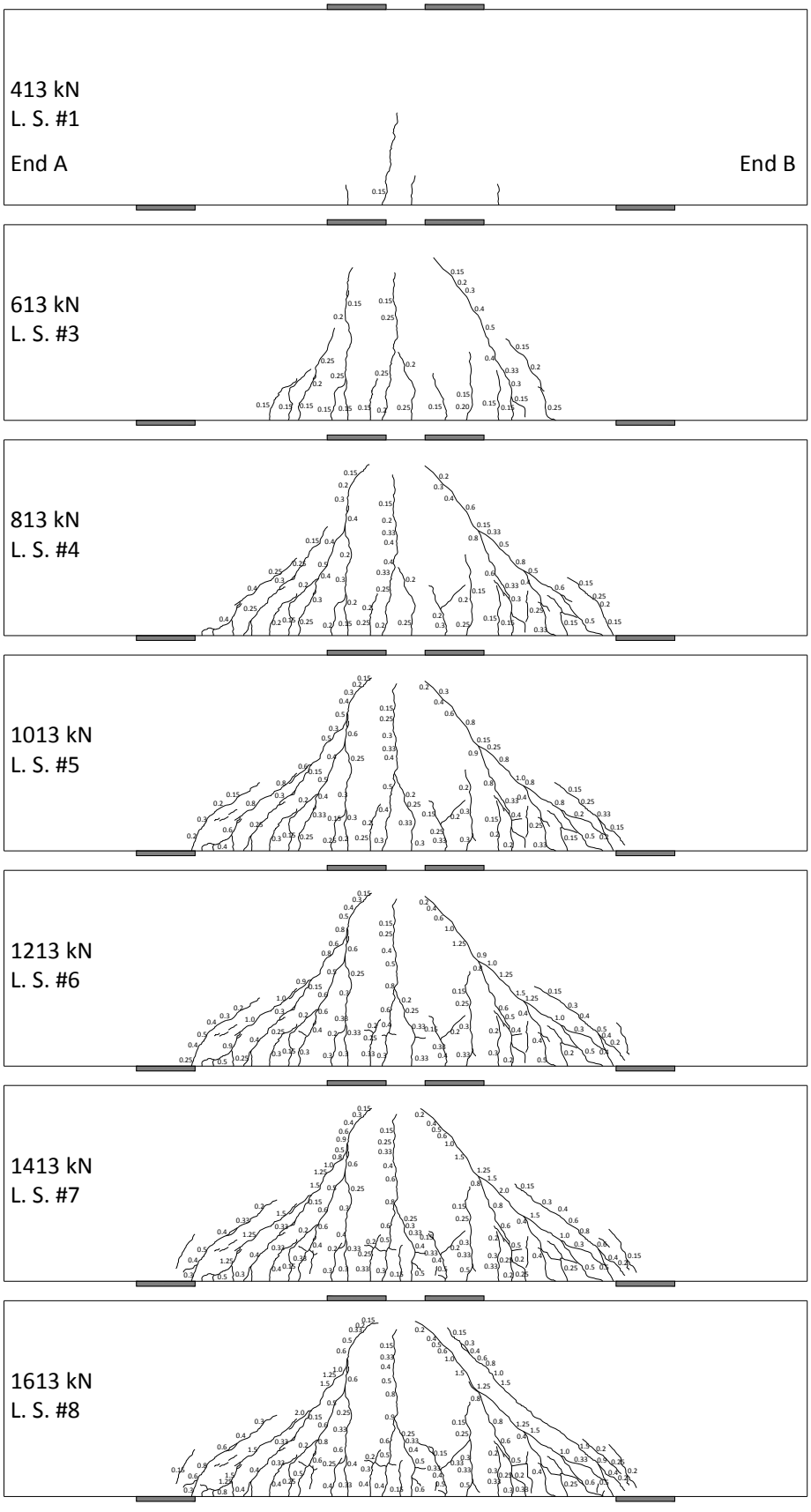
413 kN
L. S. #1
End A
End B
613 kN
L. S. #3
813 kN
L. S. #4
1013 kN
L. S. #5
1213 kN
L. S. #6
1413 kN
L. S. #7
1613 kN
L. S. #8

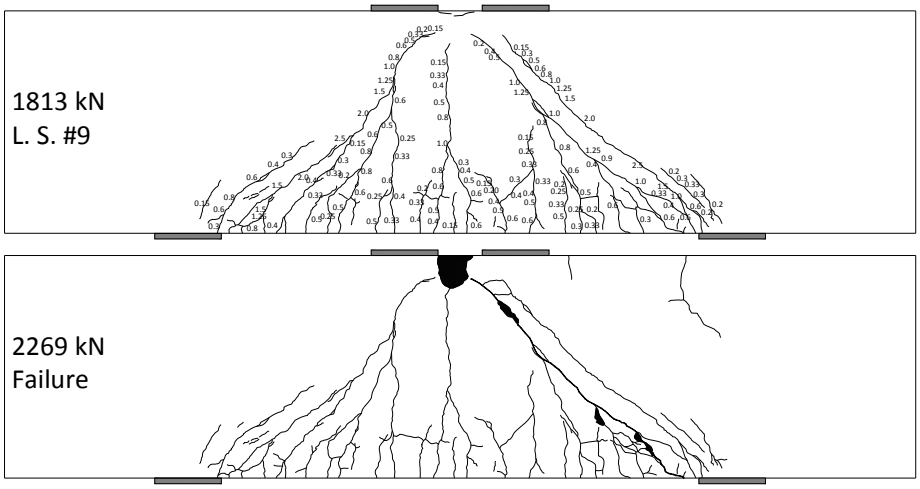

Figure C-125: Crack diagrams of specimen C1N showing the development of the cracks and the widths as loading progressed.

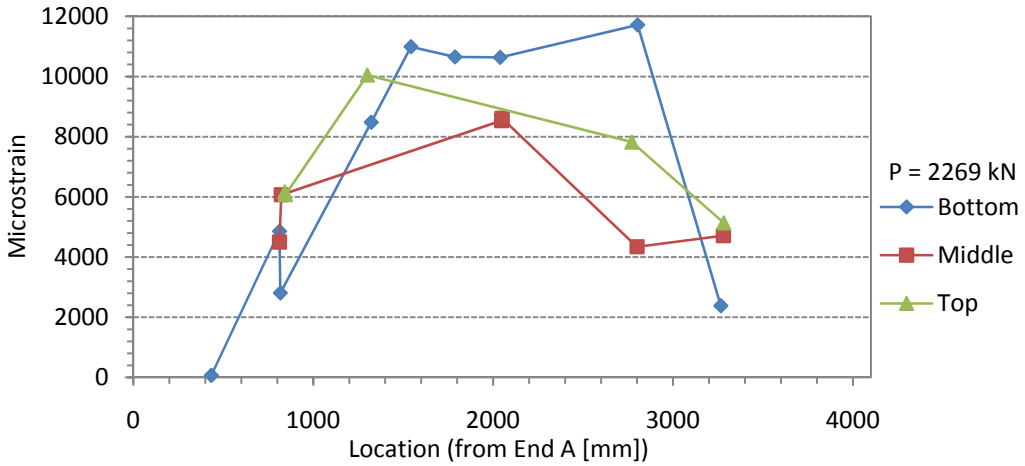

Figure C-126: Strain distribution in the bottom, middle, and top reinforcement at peak load.

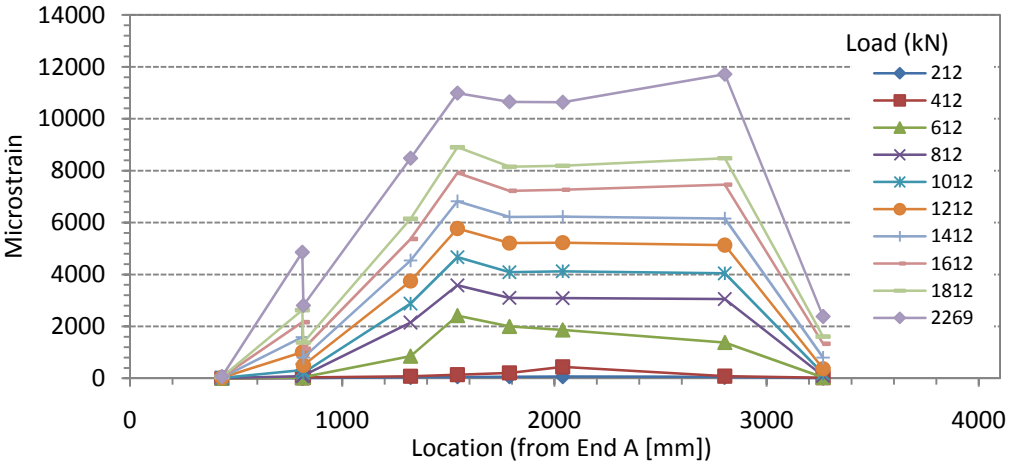

Figure C-127: Strain in the bottom reinforcement layer as loading progressed.

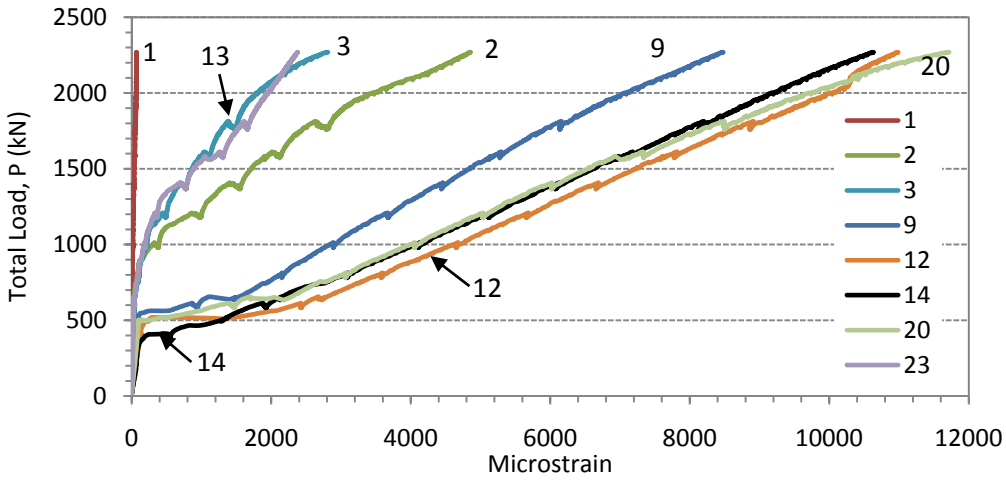

Figure C-128: Strain in the bottom reinforcement layer.

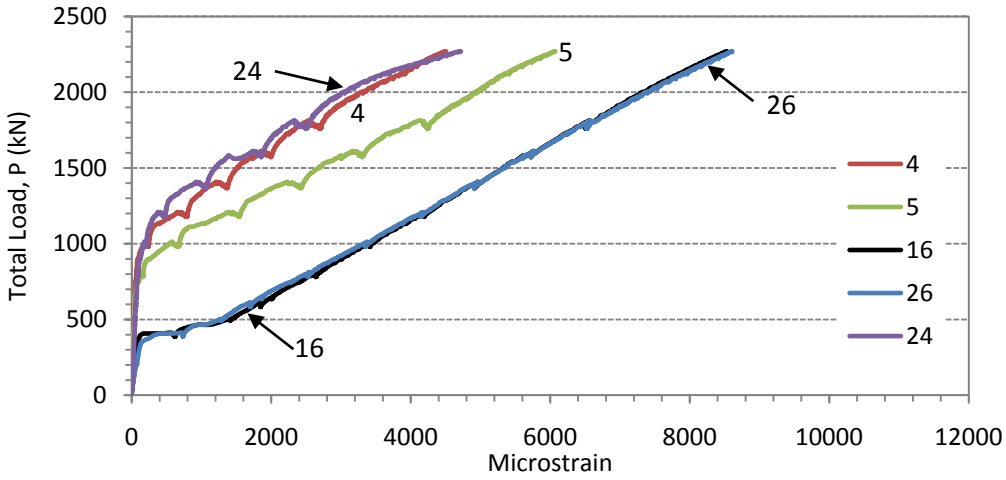

Figure C-129: Strain in the middle reinforcement layer.

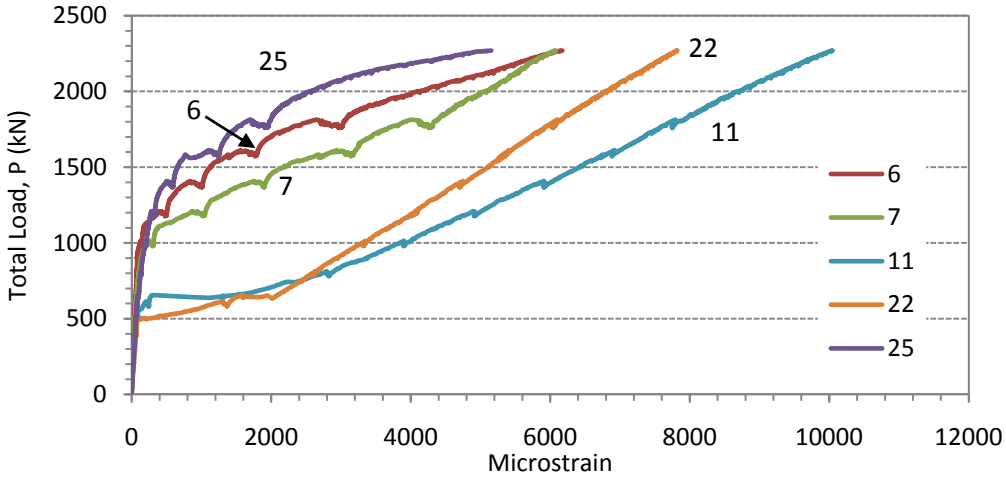

Figure C-130: Strain in the top reinforcement layer.

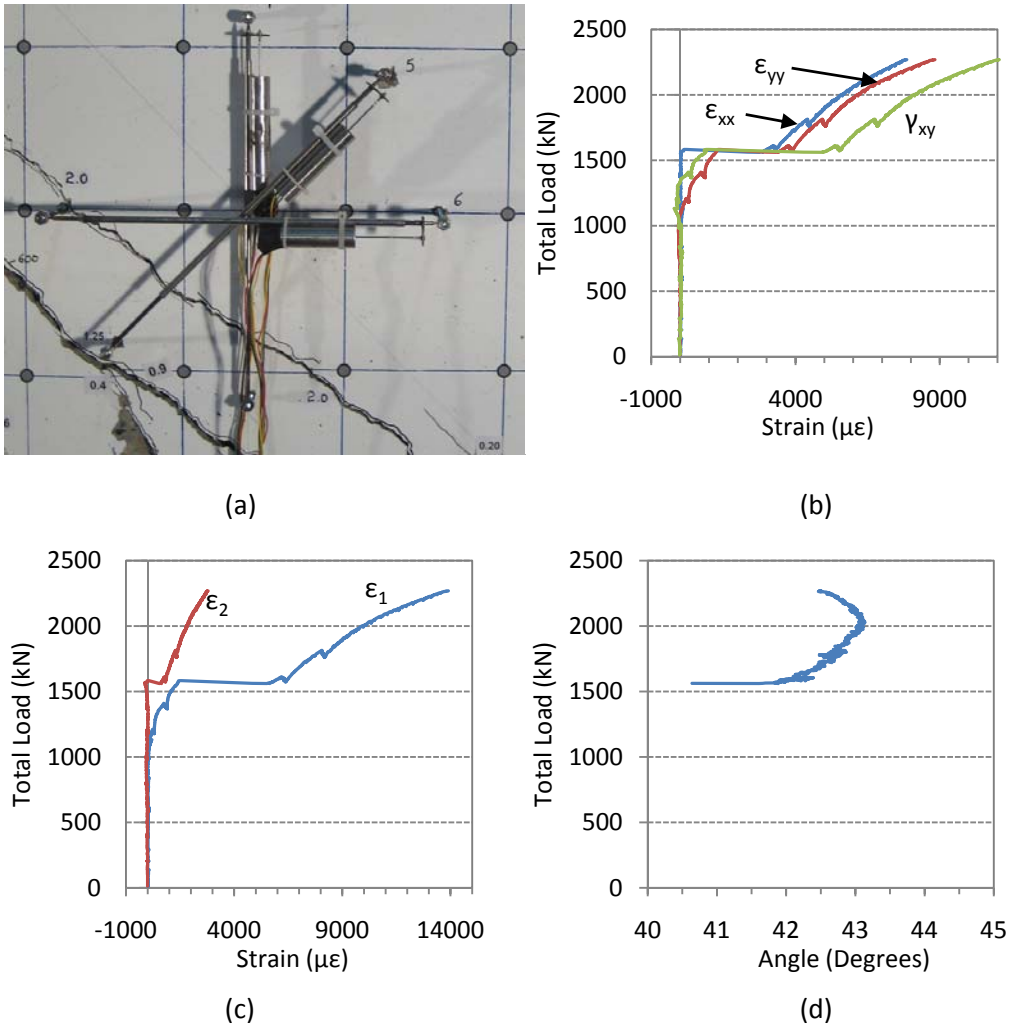

Figure C-131: (a) crack location through the rosette in shear span B at failure, (b) strain components, (c) principal strains, and (d) the direction of the minimum principal strain (angle of inclination from a horizontal line towards mid-span).

Figure C-132: Specimen C1N after failure occurred in shear span B (center of picture).

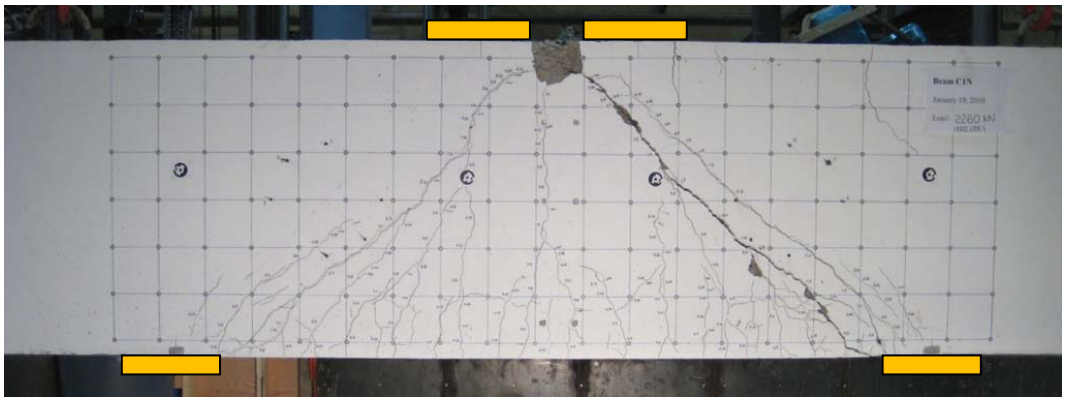

Figure C-133: Front side of specimen C1N after testing with the failure crack visible in shear span B (right).

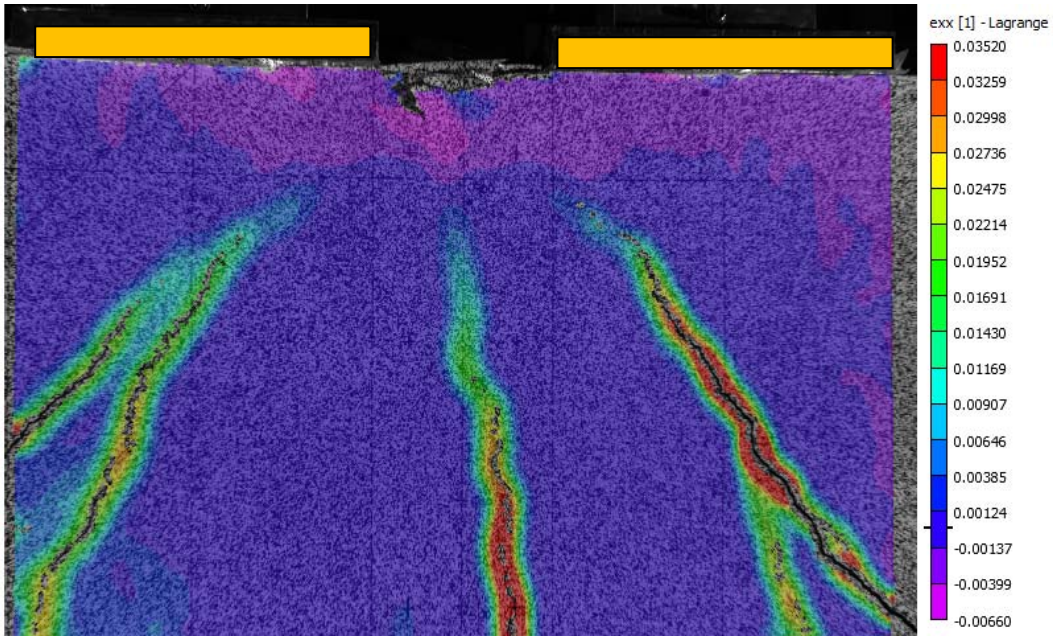

Figure C-134: Horizontal strain map at peak load showing the upper half of specimen C1N between the outer edges of the loading plate immediately prior to failure.

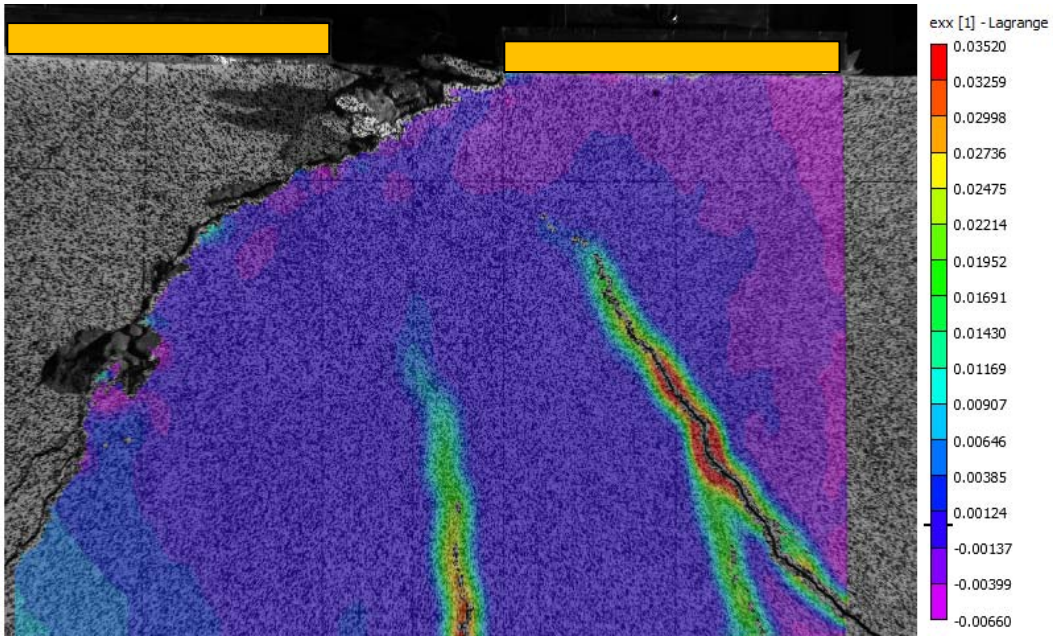

Figure C-135: Strain map showing the failure of specimen C1N. This image was taken 45 seconds after the peak load image (Figure C-134).

Table C-11: Subset of the collected data for specimen C1N.

			Displacements			Bottom Strain Gauges						
Load Stage	Time	Load, P	End A 1/4 Span	Mid-Span	End B 1/4 Span	1	2	3	9	12	14	23
(#)	(s)	(kN)	(mm)	(mm)	(mm)	(με)	(με)	(με)	(με)	(με)	(με)	(με)
	0	14	0.0	0.0	0.0	0	0	0	0	0	0	0
	250	44	0.0	0.0	0.0	0	1	3	5	8	10	2
	500	133	0.0	0.1	0.0	-1	4	11	20	35	45	7
1	660	212	0.2	0.1	0.2	0	7	18	35	59	64	12
	1060	202	0.2	0.1	0.1	0	6	17	35	60	60	10
	1310	364	0.4	0.3	0.3	1	14	31	67	112	131	20
2	1410	413	0.4	0.5	0.4	1	17	34	79	141	473	22
	2110	388	0.5	0.5	0.4	1	13	29	72	120	552	18
	2360	495	0.7	0.9	0.7	2	21	37	84	235	1268	25
	2610	542	1.0	1.4	1.1	2	24	40	112	1771	1459	27
	2860	612	1.4	1.9	1.5	2	29	45	855	2416	1864	34
3	2865	613	1.5	1.9	1.4	2	29	45	865	2424	1877	34
	4310	583	1.5	1.9	1.5	2	24	36	946	2427	1927	29
	4560	641	1.9	2.5	2.0	2	27	42	1475	2740	2136	41
	4810	711	2.4	3.0	2.4	5	47	66	1771	3077	2430	57
	5060	773	2.9	3.5	2.9	8	71	98	2024	3385	2896	86
4	5190	813	3.2	3.8	3.3	10	83	109	2156	3594	3102	96
	6870	787	3.2	3.8	3.2	10	85	106	2156	3584	3092	93
	7120	884	3.6	4.3	3.6	12	107	126	2410	3989	3474	112
	7370	956	4.1	4.8	4.1	15	222	182	2673	4376	3846	157
5	7555	1013	4.5	5.2	4.4	17	325	211	2890	4679	4134	186
	9545	984	4.5	5.3	4.5	18	387	216	2894	4653	4111	194
	9795	1088	4.9	5.8	4.9	20	443	243	3166	5070	4513	228
	10045	1168	5.4	6.3	5.3	23	709	381	3474	5460	4917	293
6	10190	1209	5.7	6.7	5.6	24	866	445	3665	5691	5151	331
	12460	1182	5.7	6.7	5.7	26	993	492	3676	5660	5118	362
	12710	1286	6.1	7.2	6.1	28	1084	539	3962	6066	5514	402
	12960	1370	6.5	7.7	6.5	30	1275	638	4286	6473	5913	569
7	13100	1409	6.8	8.0	6.8	32	1405	702	4458	6692	6126	688
	15815	1371	6.8	8.1	6.8	35	1559	783	4444	6664	6081	778
	16065	1470	7.3	8.6	7.5	37	1662	836	4740	7094	6490	848
	16315	1553	7.7	9.1	7.8	39	1843	939	5055	7501	6876	1004
	16565	1604	8.1	9.7	8.3	41	2003	1034	5277	7794	7158	1251
8	16580	1612	8.1	9.7	8.3	41	2013	1041	5296	7821	7182	1258
	18185	1579	8.2	9.8	8.4	44	2136	1125	5280	7778	7141	1313
	18435	1674	8.6	10.3	8.8	46	2245	1183	5576	8196	7532	1388
	18685	1748	9.1	10.8	9.3	47	2423	1276	5882	8574	7893	1501
9	18910	1814	9.5	11.3	9.7	50	2635	1382	6158	8913	8200	1612
	20725	1767	9.5	11.4	9.7	55	2825	1500	6136	8860	8136	1665
	20975	1865	10.0	11.9	10.1	57	2946	1558	6452	9297	8535	1745
	21225	1934	10.4	12.5	10.3	61	3158	1652	6764	9676	8875	1844
	21475	2003	10.9	13.0	10.8	64	3481	1803	7100	10055	9209	1952
	21725	2068	11.4	13.6	11.3	64	3823	1975	7418	10282	9515	2057
	21975	2117	12.0	14.2	11.7	66	4191	2160	7733	10359	9801	2148
	22225	2180	12.4	14.8	12.2	67	4463	2360	8008	10561	10112	2232
	22475	2235	12.9	15.4	12.7	67	4700	2597	8284	10809	10419	2319
Failure	22665	2269	13.4	15.9	13.2	67	4859	2812	8480	10986	10633	2381

Table C-11 continued,

		Middle Strain Gauges		Top Strain Gauges		Rosette shear span B		
Load Stage (#)	Load, P (kN)	4 (με)	16 (με)	6 (με)	11 (με)	ε_{xx} με	ε_{yy} με	γ_{xy} με
	14	0	0	0	0	14	0	-14
	44	1	7	1	3	17	-3	-14
	133	4	32	7	13	37	-3	-34
1	212	8	56	12	24	-3	0	9
	202	7	56	11	24	31	-3	-11
	364	16	93	24	48	-6	0	40
2	413	19	554	28	57	-3	0	43
	388	18	622	27	60	11	9	26
	495	25	1401	37	85	17	0	34
	542	28	1567	41	88	23	0	34
	612	34	1835	50	200	28	3	26
3	613	34	1841	50	202	31	3	23
	583	33	1847	51	245	60	6	-20
	641	36	2012	55	1307	31	0	3
	711	50	2235	62	2029	-6	-6	46
	773	63	2499	67	2558	31	-37	46
4	813	68	2662	71	2793	31	-37	46
	787	68	2645	70	2832	26	-46	14
	884	80	2939	79	3259	9	-54	34
	956	132	3217	95	3627	11	-57	34
5	1013	197	3435	126	3904	14	-54	29
	984	243	3413	145	3906	46	-31	-37
	1088	279	3729	164	4293	66	0	-94
	1168	521	4044	309	4682	-6	131	-114
6	1209	663	4221	396	4909	-9	211	-117
	1182	794	4187	500	4921	11	294	-71
	1286	863	4491	544	5294	17	343	-86
	1370	1077	4800	702	5699	14	569	109
7	1409	1211	4961	831	5908	9	717	280
	1371	1376	4919	1013	5920	14	851	386
	1470	1462	5232	1079	6302	26	931	449
	1553	1661	5527	1294	6656	14	1214	851
	1604	1847	5746	1545	6900	3202	3714	5335
8	1612	1859	5765	1561	6922	3231	3740	5366
	1579	2008	5730	1793	6893	3313	3911	5569
	1674	2114	6032	1906	7243	3707	4226	5908
	1748	2319	6318	2240	7540	4063	4583	6349
9	1814	2540	6562	2655	7794	4413	4934	6750
	1767	2717	6508	3022	7750	4487	5063	6850
	1865	2835	6815	3191	8106	4832	5389	7265
	1934	3052	7085	3640	8399	5217	5757	7672
	2003	3320	7350	4142	8715	5630	6177	8142
	2068	3595	7604	4625	9009	6048	6629	8672
	2117	3879	7861	5116	9290	6519	7157	9239
	2180	4098	8111	5495	9575	6989	7740	9889
	2235	4317	8357	5859	9843	7476	8337	10541
Failure	2269	4505	8533	6173	10047	7858	8831	11065

C.14 Specimen C2N

The displacement rate of specimen C2N was 0.25 mm/min. Flexural cracks were visually observed at load stage 1. At an applied load of 615 kN, a sudden drop in load carrying capacity to 551 kN was recorded as the main diagonal crack from the inside edge of support plate A towards the inside of loading plate A formed. At a load of 1276 kN the specimen abruptly travelled approximately 25 mm towards end A which disrupted the vertical LVDTs. The LVDTs were reset and the data was adjusted. The diagonal shear crack from the inside edge of support plate A to the inside edge of loading plate A initiated failure with the crack extending through the flexural compression zone. The failure was sudden and noisy with large chunks of concrete falling off the specimen along the diagonal crack in the lower portion of the specimen in shear span A.

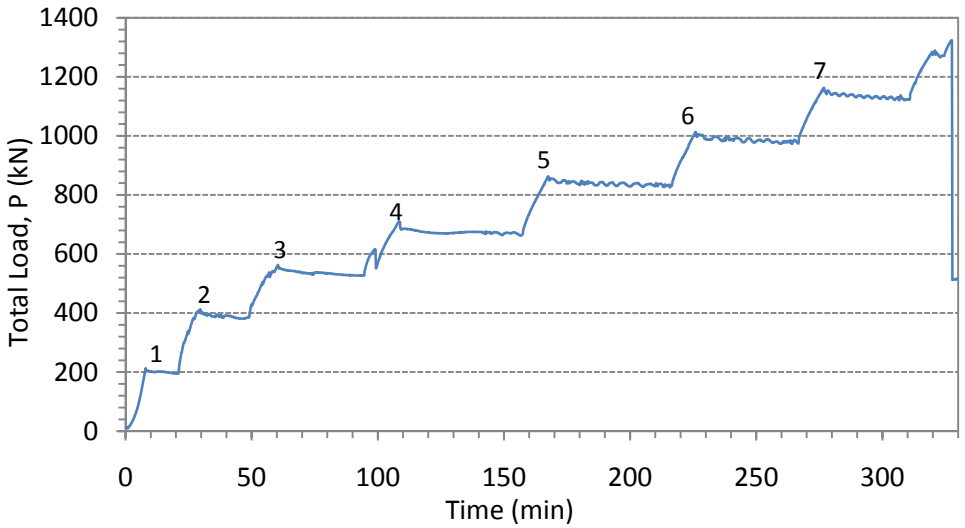

Figure C-136: Load – history of specimen C2N

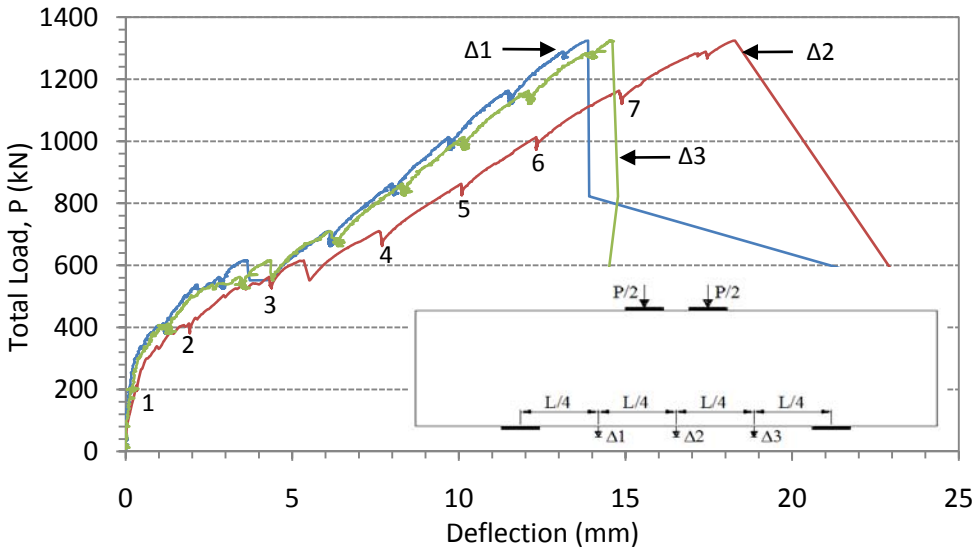

Figure C-137: Load – displacement response of specimen C2N

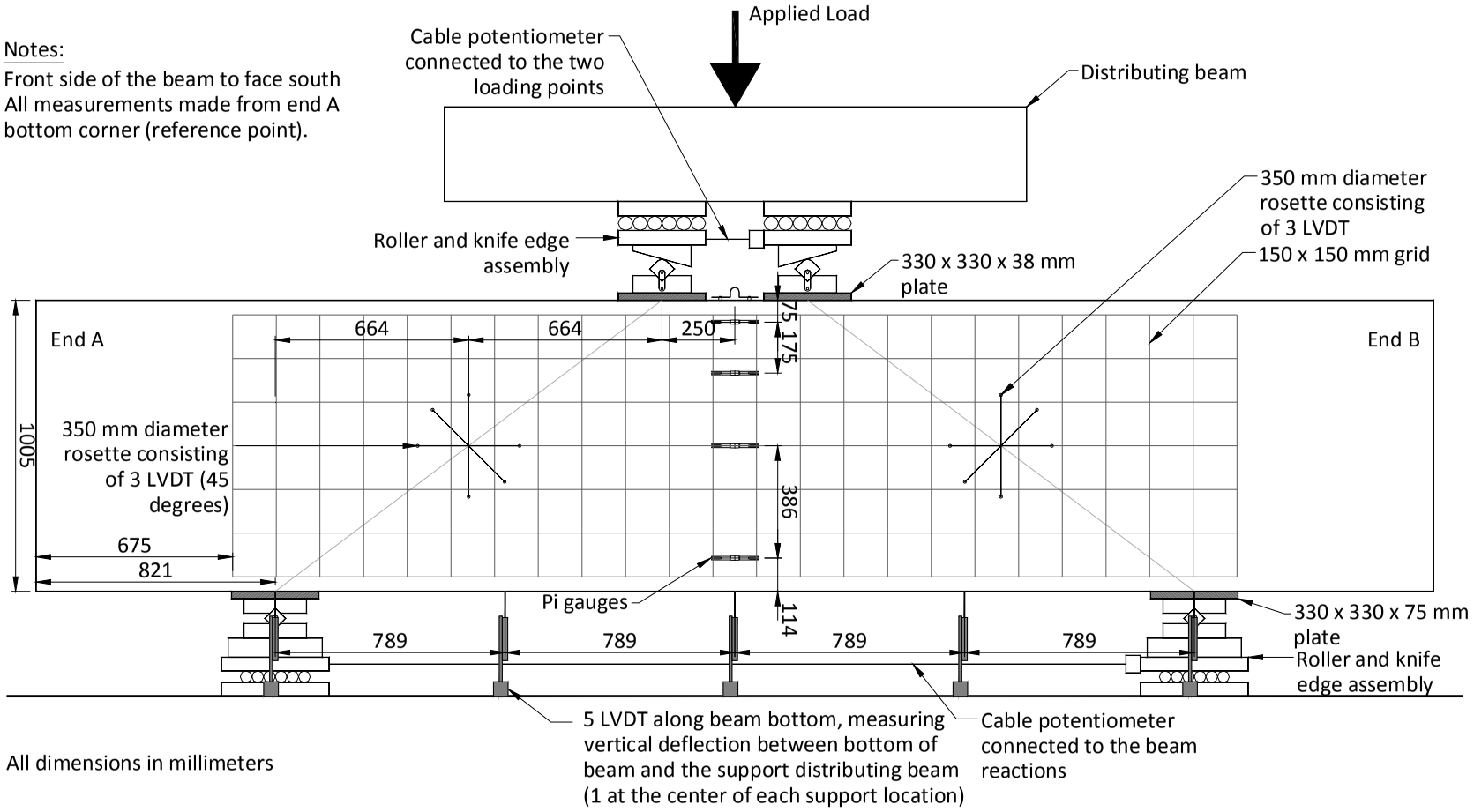

Figure C-138: Instrumentation drawing for specimen C2N.

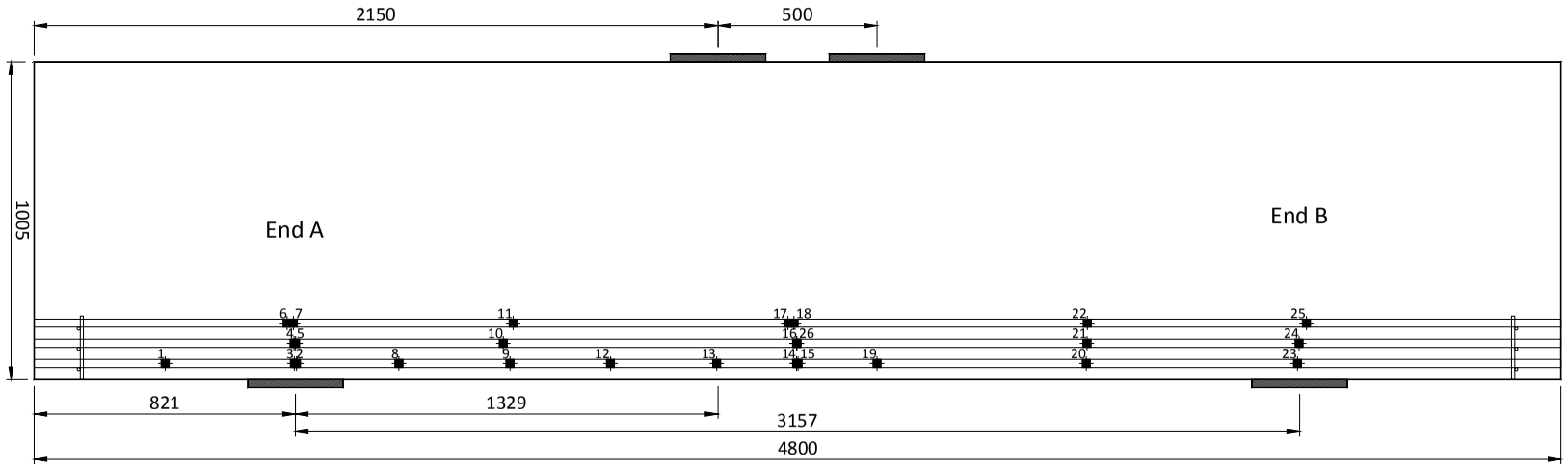

Strain Gauge Locations

Strain Gauge No.	Row	Column	Distance from End A (mm)	Strain Gauge No.	Row	Column	Distance from End A (mm)
1	B	C	412	16	M	F	2398
2	B	F	825	17	T	C	2370
3	B	C	818	18	T	F	2389
4	M	F	817	19	B	C	2650
5	M	B	822	20	B	C	3308
6	T	C	795	21	M	B	3310
7	T	F	815	22	T	F	3311
8	B	F	1147	23	B	C	3972
9	B	F	1496	24	M	F	3977
10	M	B	1475	25	T	C	4000
11	T	C	1506	26	M	B	2397
12	B	F	1812				
13	B	C	2146				
14	B	C	2397				
15	B	B	2402				

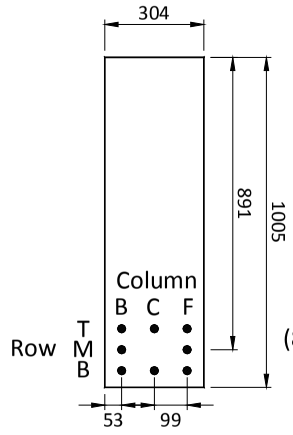

(8) - #8 GFRP Bars

Notes:

All dimensions in mm
Clear Cover: 38.1 mm
Concrete Strength: 51 MPa
Bar Length: 4800 mm

Figure C-139: Location of the strain gauges for specimen C2N (as-built).

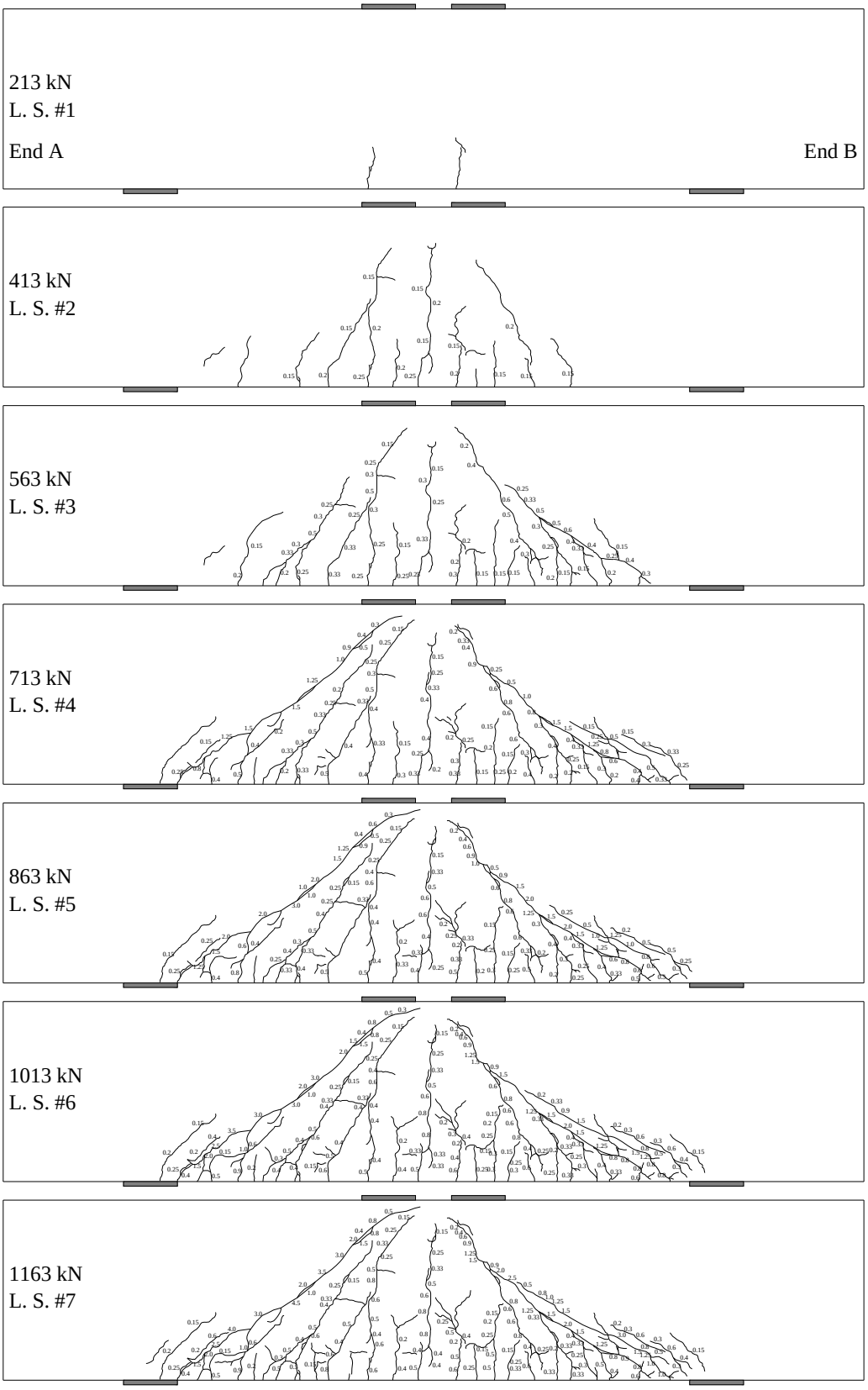
213 kN
L. S. #1
End A
End B
413 kN
L. S. #2
563 kN
L. S. #3
713 kN
L. S. #4
863 kN
L. S. #5
1013 kN
L. S. #6
1163 kN
L. S. #7

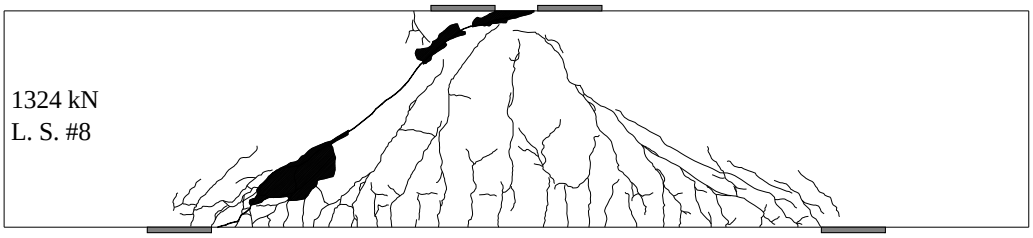

Figure C-140: Crack diagrams showing the development of the cracks and the widths as loading progressed.

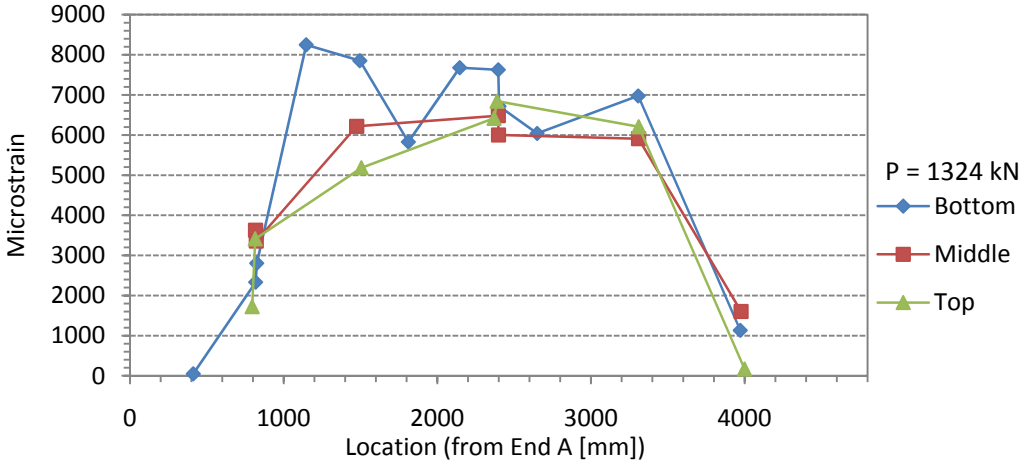

Figure C-141: Strain distribution in the bottom, middle, and top reinforcement at peak load.

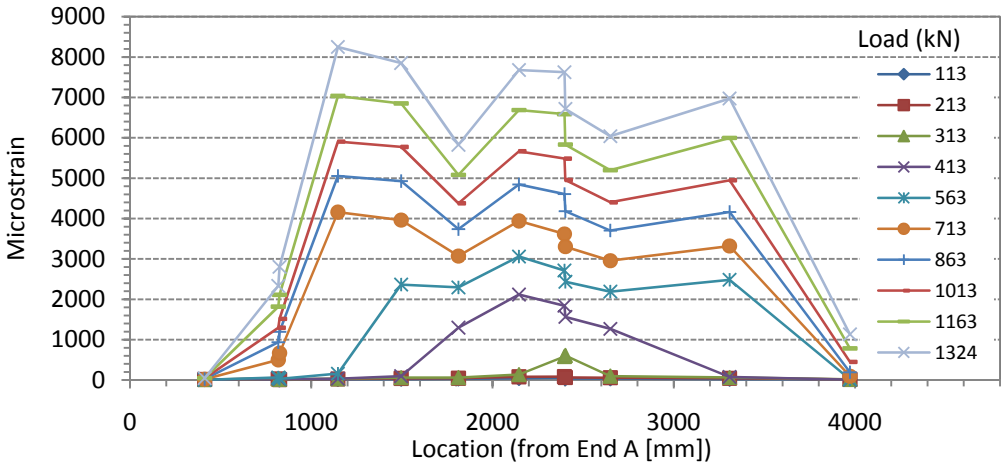

Figure C-142: Strain in the bottom reinforcement layer as loading progressed.

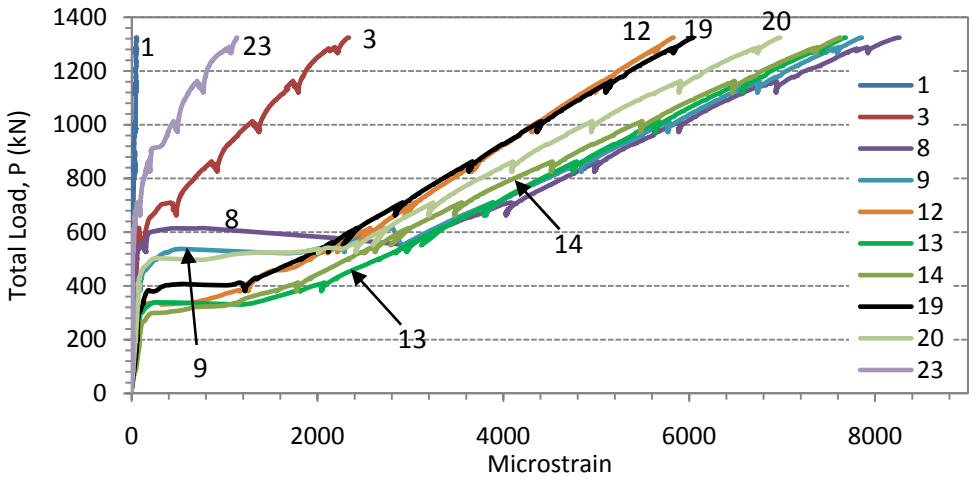

Figure C-143: Strain in the bottom reinforcement layer.

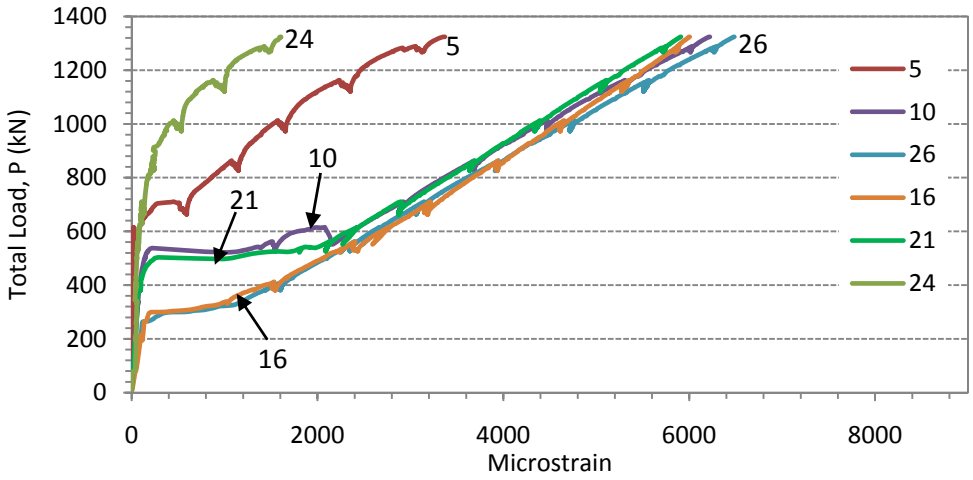

Figure C-144: Strain in the middle reinforcement layer.

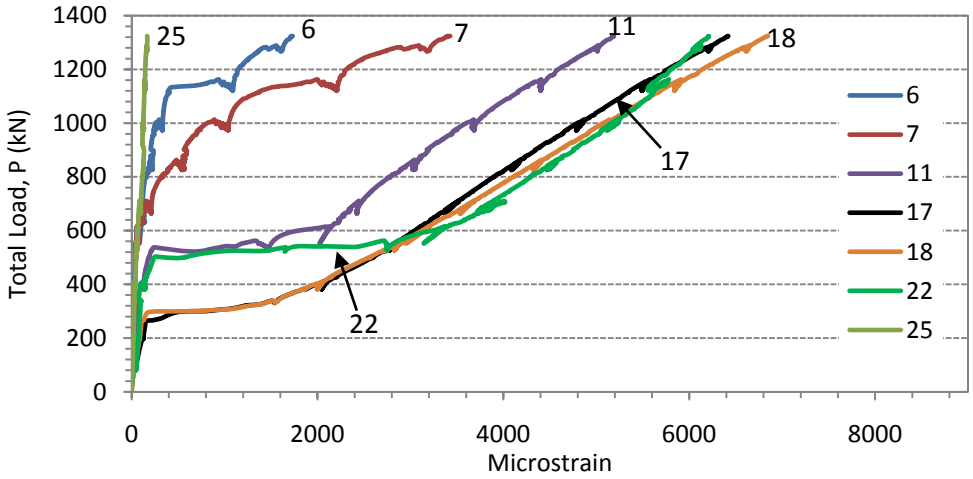

Figure C-145: Strain in the top reinforcement layer.

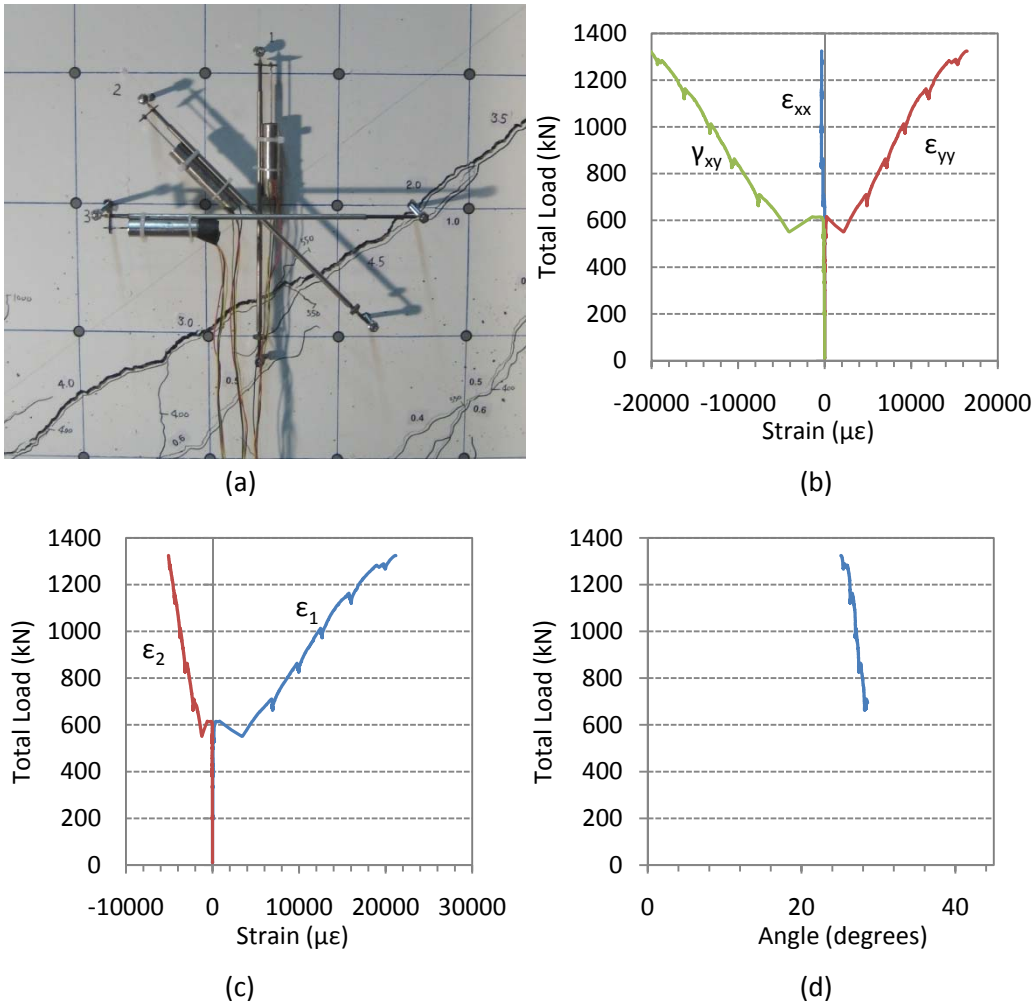

Figure C-146: (a) crack location through the rosette in shear span A at P= 1163 kN, (b) strain components, (c) principal strains, and (d) the direction of the minimum principal strain.

Figure C-147: Failure surface in shear span A from the front (a) and from the back (b) side of specimen C2N.

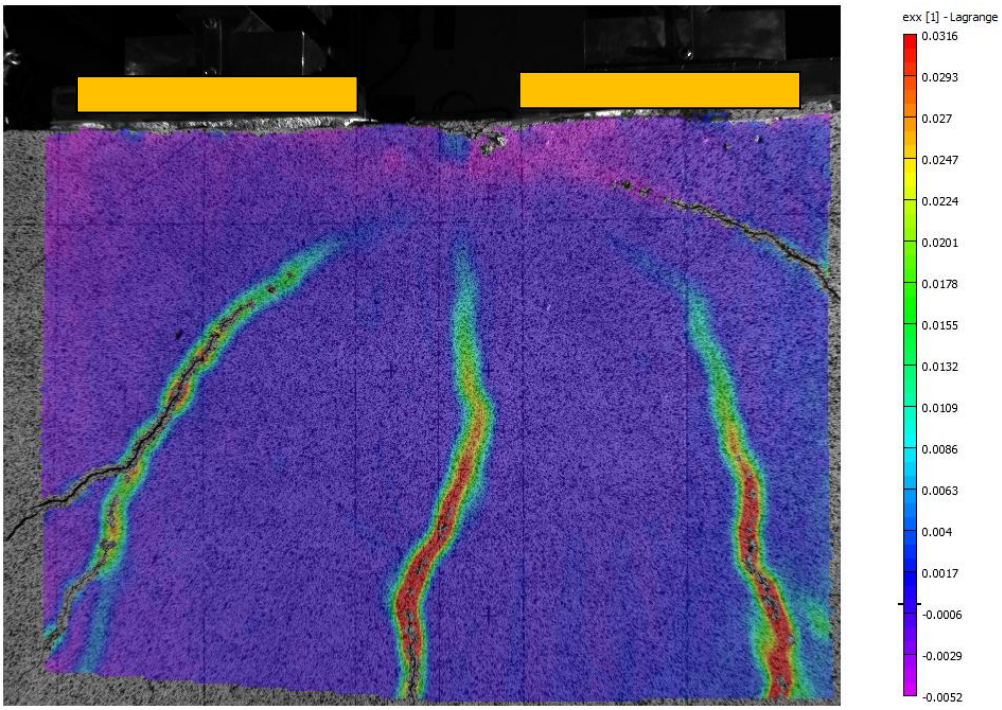

Figure C-148: Horizontal strain map in the upper portion of specimen C2N between the loading plates at maximum load (P= 1324 kN). Loading plates are shown as yellow rectangles.

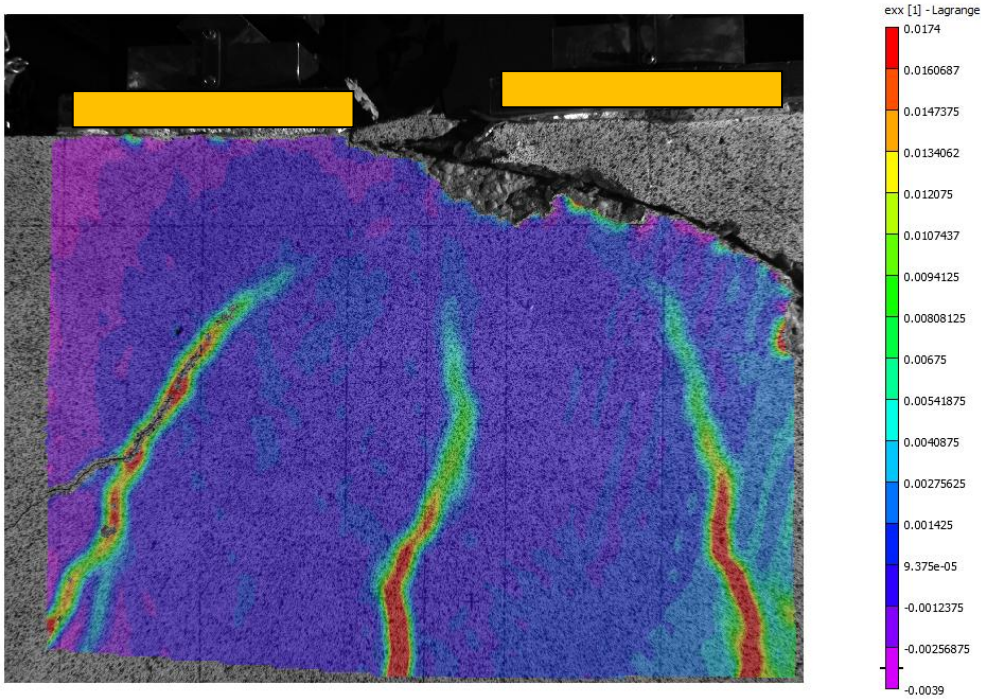

Figure C-149: Horizontal strain map showing immediately after failure. This image was taken 15 seconds after the image in Figure C-148.

Table C-12: Subset of the collected data for specimen C2N.

			Displacements			Bottom Strain Gauges				
Load Stage	Time	Load, P	End A 1/4 Span	Mid-Span	End B 1/4 Span	1	3	9	13	14
(#)	(s)	(kN)	(mm)	(mm)	(mm)	(με)	(με)	(με)	(με)	(με)
	0	13	0.0	0.0	0.0	0	0	0	0	0
	200	45	0.1	0.0	0.0	0	4	6	12	14
	400	153	0.1	0.2	0.1	16	19	31	68	71
1	480	213	0.1	0.3	0.2	15	27	42	81	86
	1260	196	0.2	0.3	0.2	14	24	41	76	84
	1460	325	0.4	0.9	0.5	14	39	63	177	966
	1660	388	0.8	1.5	1.0	4	46	69	1862	1597
2	1780	412	1.1	1.9	1.3	4	48	80	2078	1794
	2940	386	1.2	1.9	1.3	5	44	91	2040	1775
	3140	466	1.5	2.6	1.7	5	53	166	2425	2133
	3340	522	2.0	3.2	2.3	6	59	349	2802	2448
	3540	539	2.6	4.0	3.1	6	62	2100	2916	2571
3	3625	563	2.8	4.3	3.4	6	66	2256	3028	2668
	5675	527	2.9	4.4	3.5	7	60	2289	2958	2620
	5875	607	3.4	5.1	4.1	8	72	2647	3288	2927
	6075	601	4.7	5.9	4.7	14	148	3182	3292	2940
	6275	659	5.4	6.7	5.3	16	210	3536	3592	3249
	6475	704	6.0	7.5	6.0	18	326	3838	3852	3509
4	6505	711	6.1	7.6	6.1	18	416	3887	3889	3550
	9455	677	6.1	7.7	6.4	20	483	3832	3809	3490
	9655	754	6.8	8.5	6.9	21	557	4179	4151	3830
	9855	809	7.4	9.3	7.7	23	698	4523	4467	4173
	10055	863	8.0	10.1	8.3	35	860	4856	4787	4528
5	10055	863	8.0	10.1	8.3	35	860	4856	4787	4528
	12975	832	8.0	10.1	8.3	35	921	4839	4750	4516
	13175	907	8.5	10.8	8.8	24	993	5154	5070	4835
	13375	961	9.2	11.6	9.5	29	1141	5485	5389	5177
6	13550	1012	9.7	12.3	10.1	42	1295	5775	5666	5485
	16010	986	9.8	12.3	10.2	41	1372	5779	5640	5486
	16210	1061	10.3	13.1	10.8	43	1469	6129	5989	5843
	16410	1116	10.9	14.0	11.5	40	1625	6442	6308	6175
7	16605	1163	11.5	14.8	12.1	52	1736	6752	6605	6486
	18635	1123	11.6	14.9	12.1	47	1795	6735	6570	6463
	18835	1200	12.1	15.6	12.7	44	1873	7047	6881	6783
	19035	1251	12.7	16.5	13.3	46	2001	7349	7193	7106
	19235	1286	13.1	17.3	14.0	46	2173	7592	7429	7361
	19435	1271	13.2	17.5	14.1	47	2223	7590	7422	7357
	19635	1322	13.8	18.2	14.7	55	2320	7833	7660	7609
Failure	19650	1324	13.9	18.3	14.5	48	2332	7852	7678	7625

Table C-12 continued,

		Middle Strain Gauges			Top Strain Gauges			Rosette shear span A		
Load Stage	Load, P	5	10	16	6	11	18	ε_{xx}	ε_{yy}	γ_{xy}
(#)	(kN)	(με)	(με)	(με)	(με)	(με)	(με)	με	με	με
	13	0	0	4	0	0	0	0	-3	3
	45	1	5	22	3	5	11	0	-3	-3
	153	11	27	78	46	49	64	0	0	0
1	213	12	40	96	48	58	88	0	0	-11
	196	10	40	116	44	57	86	-3	11	-43
	325	13	66	906	51	84	1387	-3	9	-46
	388	10	81	1352	31	92	1894	-3	9	-63
2	412	10	91	1534	33	127	2064	0	9	-77
	386	9	91	1556	32	128	1997	0	17	-131
	466	12	118	1861	39	158	2349	3	6	-111
	522	14	164	2167	44	207	2683	3	-3	-91
	539	15	1390	2303	45	1108	2799	0	37	-77
3	563	16	1510	2403	48	1331	2915	0	57	-80
	527	15	1549	2435	47	1478	2826	-3	135	-159
	607	19	1893	2721	55	1939	3167	-3	218	-259
	601	74	2375	2724	98	2116	3133	-3	2891	-4986
	659	151	2649	2989	111	2272	3430	-9	3805	-6175
	704	279	2887	3185	116	2422	3651	-132	4635	-7342
4	711	454	2922	3213	109	2446	3680	-135	4793	-7536
	677	595	2890	3203	117	2430	3555	-198	4908	-7678
	754	698	3140	3471	128	2605	3891	-198	5534	-8555
	809	887	3409	3707	151	2811	4150	-198	6273	-9508
	863	1075	3687	3946	206	3042	4410	-198	7020	-10452
5	863	1075	3687	3946	206	3042	4410	-198	7020	-10452
	832	1151	3685	3939	223	3047	4323	-372	7172	-10720
	907	1225	3922	4185	206	3198	4631	-370	7721	-11460
	961	1388	4204	4432	234	3436	4902	-370	8434	-12330
6	1012	1567	4465	4648	294	3675	5137	-370	9112	-13132
	986	1659	4471	4624	332	3690	5072	-361	9296	-13294
	1061	1771	4745	4898	349	3909	5403	-361	9934	-14136
	1116	1974	5035	5137	402	4155	5664	-361	10710	-15028
7	1163	2230	5306	5351	931	4405	5911	-361	11707	-16123
	1123	2355	5290	5272	1089	4401	5840	-358	12037	-16229
	1200	2462	5536	5511	1148	4590	6140	-358	12684	-17051
	1251	2690	5817	5725	1304	4833	6410	-358	13621	-18063
	1286	3017	6015	5875	1535	5006	6629	-358	15017	-19181
	1271	3140	6010	5843	1617	5011	6609	-358	15405	-19330
	1322	3334	6202	5994	1724	5183	6830	-358	16264	-20094
Failure	1324	3359	6217	6002	1723	5183	6843	-358	16391	-20162